DEPARTAMENTO DE ASTROFISICA

Universidad de La Laguna

SEARCH AND CHARACTERIZATION OF STARBURST GALAXIES IN COSMOS

Thesis submitted by

Rodrigo Hinojosa Goñi

as a requirement for the degree of

Doctor of Physical Science

INSTITUTO Đ ASTROFISICA Đ CANARIAS

La Laguna, Enero de 2016

Examination date: 2016 February
Thesis supervisor: Casiana Muñoz Tuñón and Jairo Méndez Abreu

ISBN: xx-xxx-xxxx-x
Depósito legal: xx-xxxx/xxxx

Some of the material included in this document has been published in *Astronomy & Astrophysics*.

Agradecimientos

Agradezco a la colaboración ESTALLIDOS por haberme permitido colaborar y aprender entre los miembros de su equipo.
Agradezco al MINECO (Ministerio de Economía y Competitividad) la financiación concedida a través de un abeca FPI del proyecto ESTALLIDOS (AYA2010-21887-C04-04)

Resumen

El objetivo principal de esta tesis es el estudio de la evolución de galaxias con estallidos de formación estelar durante los últimos 8 Gyr. A redshift alto ($z > 1$) las galaxias muestran una gran variedad de morfologías, las cuales son inusuales en el universo local. Los principales mecanismos que permiten el cambio en la morfología de las galaxias a alto redshift están relacionados principalmente con los procesos de formación estelar, con regiones de formación estelar gigantes y masivas que alteran la morfología de las galaxias anfitrionas. El objetivo principal en este trabajo es obtener un mejor entendimiento de los procesos físicos que dominan la formación estelar y su evolución con el desplazamiento al rojo en el universo. Para esto, en esta tesis hemos estudiado galaxias desde el universo local hasta redshift intermedio ($0 < z < 1$) con el propósito de conectar la formación estelar en el universo local con el universo a alto redshift.

Esta tesis está basada en el uso extensivo del cartografiado de campo ultra profundo mas grande realizado por el telescopio espacial Hubble (HST), el cartografiado de COSMOS. Además de la alta resolución espacial, y de la profundidad en las observaciones de la Advanced Camera for Survey (ACS), el campo de COSMOS ha sido observado detalladamente utilizando telescopios espaciales y terrestres, con instrumentación que cubre una amplia región del espectro electromagnético desde ondas de radio hasta rayos X. Esta posibilidad de acceso a información en multiples longitudes de onda es la base del estudio que llevamos a cabo en esta tesis, la cual es explicada en detalle en el capítulo 2.

Un gran esfuerzo se ha puesto en la utilización de la forma mas eficiente posible de la información en multiples longitudes de onda disponibles en el cartografiado de COSMOS. A partir de esto se ha desarrollado una búsqueda y caracterización de una muestra bien definida de galaxias con estallidos de formación estelar. Para lograr este objetivo, se han desarrollado dos conjuntos diferentes de diagramas de diagnóstico: el primero es un diagrama optimizado para la búsqueda de galaxias con formación estelar hasta $z \sim 0.5$ (a partir de las líneas de emissión en Hα y [OIII]); mientras que el segundo nos permite incrementar nuestra búsqueda de galaxias con estallidos de formación estelar hasta $z \sim 1$ (a partir de la línea de emisión [OIII] y el salto de Balmer). Esta búsqueda nos ha permitido obtener un catálogo con mas de 1000 galaxias con formación estelar intensa, las cuales cubren 8 Gyr de evolución, con un amplio rango en sus morfologías (desde galaxias compactas hasta galaxias con multiples regiones de formación estelar).

La muestra resultante de galaxias abarca un rango de masas de $10^6 < M/M_\odot < 10^{10}$, con un máximo de 10^{11} $M_\odot$. La función de masa de la muestra de galaxias en COSMOS hasta $z < 0.5$ es similar a la función de masa del total de galaxias en este rango de redshift. De hecho, solo se puede apreciar una pequeña diferencia en la distribución de masas en un extremo de esta distribución, este es el sector perteneciente a galaxias masivas. Esta diferencia en la distribución se puede atribuir a galaxias rojas masivas, las cuales son comunes en el universo para este rango de redshift.

Se ha realizado una clasificación de las galaxias en nuestra muestra (capítulos 3 y 4) de acuerdo a la presencia y distribución de las regiones de formación estelar en estas galaxias. Como resultado de esta clasificación, hemos definido la morfología como: Sknot para galaxias que poseen una única región de formación estelar, que compone toda la galaxia sin tener emissión difusa. Sknot+diffuse para galaxias con una región de formación estelar rodeada por emissión difusa proveniente de la galaxia anfitriona. Por último hemos clasificado como Mknot a las galaxias compuestas por dos o mas regiones de formación estelar rodeadas por emisión difusa proveniente de la galaxia anfitriona. En total se tienen 87 galaxias Sknot, 79 Sknot+diffuse, y 54 Mknot, la distribución de estas galaxias con respecto al desplazamiento al rojo no varia para diferentes clases.

Otro aspecto importante en este estudio ha consistido en analizar las propiedades de las regiones de formación estelar, caracterizando estas mismas por sus propiedades físicas tales como la razón de formación estelar, masas, etc. Estas propiedades de las regiones de formación estelar, junto con sus propiedades morfológicas tales como sus tamaños, distribución espacial con respecto al centro de la

galaxia y la cantidad de regiones de formación estelar, han sido analizadas y discutidas con respecto a investigaciones recientes sobre posibles escenarios de formación y evolución de galaxias. En este trabajo se ha encontrado que las masas características de los brotes de formación estelar son del orden de $10^7 - 10^8 M_\odot$, con los brotes mas masivos ubicados mas cerca del centro de la galaxia. Sin embargo, la SSFR es similar para todos los brotes, lo que implica el mismo mecanismo de formación. Estos resultados están de acuerdo con escenarios que proponen la formación de regiones de formación estelar grandes y masivas en los centros de las galaxias a partir de la fusión de pequeñas regiones de formación estelar que migran hacia el centro de las galaxias provenientes de las partes externas.

Para entender mejor la evolución de galaxias con estallidos de formación estelar y las regiones que las constituyen, es fundamental comprender mas de cerca las propiedades de las galaxias anfitrionas donde encontramos estas regiones con alta formación estelar. La profundidad en las imágenes del ACS/HST, las cuales alcanzan niveles de brillo superficial del orden de las 27-28 mag arcsec^{-2} en la banda F814W, nos permite realizar un análisis detallado de la componente subyacente para las galaxias en nuestra muestra a bajo desplazamiento al rojo ($0 < z < 0.5$). En este trabajo (capítulo 5) hemos realizado el modelado del brillo superficial de las galaxias anfitrionas por medio de un algoritmo de descomposición fotométrica 2D (GALFIT). Este código realiza un ajuste a un perfil de Sersic de la distribución de brillo superficial de las componentes extendidas de las galaxias. Para poder realizar estos ajustes, hemos utilizados técnicas que nos permitan analizar los diferentes tipos morfológicos: Sknot, Sknot+diffuse y Mknot, enfocándonos principalmente en descontaminar el flujo proveniente de las regiones de formación estelar. Como resultado del ajuste al perfil de luminosidad en nuestra primera muestra, 170 galaxias han podido ser ajustados mediante esta técnica (74% Sknot, 73% Sknot+diffuse, y 89% Mknot). De estos ajustes, el 74% de galaxias poseen un perfil de luminosidad exponencial que corresponde a estructuras tipo discos. El restante 26% de galaxias poseen principalmente estructuras tipo esferoidales. Este último caso corresponde principalmente a galaxias clasificadas como Sknot. Estos resultados, presentados en el capítulo 5, junto a los resultados en el análisis de las regiones con alta formación estelar, están de acuerdo con el escenario que deja a estas galaxias clasificadas como Sknot en una fase evolutiva intermedia de galaxias con bajo brillo superficial. Las galaxias restantes, Sknot+diffuse y Mknot, son sistemas tipo discos los cuales poseen regiones con alta formación estelar. Estas regiones son mas luminosas y masivas cuanto mas cercanas al centro de la galaxia se encuentren. Estos resultados están de acuerdo con el escenario que propone a estas galaxias como sistemas que aun ahora crecen mediante gas que llega al disco y forma estrellas en brotes y que en su movimiento el la galaxia se va fusionando y migran hacia el centro de la galaxia hasta formar bulbos galácticos.

En nuestra búsqueda por entender mejor los procesos de formación estelar que dominan las galaxias con estallidos de formación estelar en el universo local, en el capítulo 6 hemos realizado un primer estudio de una muestra de galaxias, obtenida a partir de nuestra primera búsqueda ($0 < z < 0.5$), con espectros de alta resolución, obtenidos con el Intermediate dispersion Spectrograph and Imaging System (ISIS) en el William Herschel Telescope (WHT) en el Observatorio del roque de los Muchachos (ORM). Nuestro objetivo principal en este estudio es analizar las multiples componentes en la líneas de emisión Hα, con el objetivo de entender el regimen hidrodinámico en el que se encuentran las regiones de formación estelar en estas galaxias. En particular nos interesa encontrar galaxias candidatas a estar en un regimen de feedback positivo, esto es, sistemas que puedan estar enriquecidos por la caída de material producto de las explosiones de estrellas masivas de generaciones anteriores. Las luminosidades en Hα de esta muestra han sido también analizadas bajo el punto de vista de las relaciones de escala, las cuales relacionan la luminosidad en Hα en estas regiones de formación estelar con sus tamaños. Los resultados confirman la validez de esta ley, dando valores con alta precisión en los ajustes.

Summary/Abstract

The main objective of this Ph.D. thesis is to study the evolution of starburst galaxies during the last 8 Gyrs. At high redshift ($z > 1$) galaxies show a large variety of unusual morphologies that are rare to find in the local Universe. The main mechanisms transforming the appearance of high-redshift galaxies are related to star formation processes, with giant clumps of star forming stars altering the otherwise smooth shape of galaxies. This work aims to better understand the physical processes driving the evolution with cosmic time of the star formation in the Universe. Thus, we focus on intermediate redshift galaxies to bridge the gap between high-redshift starburst galaxies and the local Universe.

This Ph.D. thesis is based on the extensive use of the largest survey ever performed with the Hubble Space Telescope (HST), the COSMOS survey. Besides the high spatial resolution and deep imaging from the Advanced Camera for Surveys (ACS), COSMOS has been observed with unprecedented detail using the state-of-the-art ground- and space-based instruments. This new wealth of multiwavelenght information set the basis of the current study and it is thoroughly explained in Chapter 2.

A strong effort has been devoted to efficiently extract the information encoded in the COSMOS multiwavelength photometric dataset. Particular attention has been paid to the sample selection and characterization of a well-defined sample of starbursts galaxies. Two different sets of diagnostic diagrams have been developed to this aim: the first is optimized for targets up to $z \sim 0.5$ (sampling the Hα and [OIII] line); and the second that allow us to increase the redshift range up to $z \sim 1$ (sampling [OIII] and the Balmer break). This accurate search has produced a catalogue of over 1000 starburst galaxies covering 8 Gyrs of evolution and a large range of morphologies (from compact and smooth blue galaxies to clumpy starbursts).

The resulting sample are galaxies with masses spanning $10^6 < M/M_\odot < 10^{10}$ with a maximum at about 10^{11} $M_\odot$. The mass function of starburst galaxies in the COSMOS survey up to $z \sim 0.5$ is quite similar to that of the entire galaxies sample in COSMOS at this redshift range. In fact, only small differences at the high-mass end are found, which could be attributed to massive red galaxies that does not show up when, as it is our case, are looking for starbursts.

The galaxy sample has been classified (chapter 3 and 4) according to the presence and distribution of starburst knots/clumps within the galaxy. As a result, we classify them as: sknot when it consists of a single knot and mknots when several knots are present. Objects in which a single knot is surrounded by diffuse emission are classified as sknot + diffuse. An important part of this work is the study of the star-forming regions themselves, characterizing their physical properties such as star forming rate (SFR), masses, etc. These, together with the analysis of the starburst properties in relation with other morphological issues like their sizes and their location and number in their host galaxy, have been discussed in the framework of the more recent galaxy formation and evolutionary scenarios. Our results support a scenario were large and massive clumps at the galaxy centers would be the end product of the coalescence of surviving smaller clumps from the outskirts. Thus, making it unlikely that mergers are the reason behind the observed starburst knots.

To further understand the evolution of starburst galaxies and their constituent knots/clump, it is fundamental to know the properties of the host galaxies where they are found. The depth of the ACS/HST imaging, reaching surface brightness levels of 27-28 mag arcsec^{-2} in the F814W band, allowed us to perform an analysis of the underlying stellar component for most of the galaxies in our low redshift sample ($0 < z < 0.5$). We have carried out the detailed modeling, by means of 2D surface brightness fitting algorithm (GALFIT), of this extended structure. We have developed new techniques to deal with the variety of starburst morphologies: single knot, Sknot and diffuse and Mknots galaxies, in order to properly remove the ionized gas contamination of the host galaxy. As result, 170 of the galaxies could be reliably fit through the 2D algorithm (74% of Sknot, 73% of Sknot+diffuse, and 89% of Mknot galaxies). From the fit it results that the 74% of the host have

an exponential luminosity profile what corresponds to disc-like structures. The rest 26% however are spheroidal like. This last case corresponds mostly to Sknot galaxies. This result are presented in Chapter 5, together with results from the analysis of the bursts of these galaxies led us to propose that these are an intermediate phase of the so call low surface brightness galaxies. The rest, Sknot+diffuse light and Mknots are mostly disk systems, which are undergoing star formation now and whose starbursts are more luminous and bright the more to the center of the galaxy they are. These results also support the scenario of galaxies growing through new starburst that by coalescence may migrate to the centers to forming new bulges.

In our quest to understand the star-formation processes leading to the current population of starburst galaxies in the local Universe. in Chapter 7 we also performed an analysis of the high-resolution spectra, taken with the Intermediate dispersion Spectrograph and Imaging System (ISIS) at the William Herschel Telescope (WHT) in the Observatorio del Roque de los Muchachos (ORM), of a subsample of our low-redshift starburst galaxies. Our main goal in this study was the analysis of multi-components in the Hα emission line, to understand the hydrodynamic regimes of the star formation in these galaxies. In particular, we look for the presence of starbursts system in the negative feedback regime, i.e., systems that could be enriched by the fallback of material after the previous generation of massive stars exploded. The entire dataset and results have also been analyzed using universal scale relations like the one that relate the luminosity of the clumps or the emission line with the size. The result confirms the existence of such laws and gives more accurate values for their fit.

Index

1 Introduction **5**
1.1 Formation and evolution of star-forming clumps . . . 6
1.2 The host galaxy . . . 9
1.3 Scaling relations . . . 10
1.4 Feedback mechanisms . . . 11

2 Starburst galaxies in COSMOS at $z < 0.5$ **17**
2.1 COSMOS Databases . . . 17
2.1.1 COSMOS Intermediate and Broad Band Photometry Catalogue . . . 17
2.1.2 COSMOS Photometric Redshift Catalogue . . . 17
2.1.3 zCOSMOS . . . 18
2.2 Starburst in zCOSMOS . . . 18
2.3 Estimation of the equivalent width (EW) and the associated uncertainty . . . 19
2.3.1 Photometric EW . . . 19
2.3.2 Spectroscopic EW . . . 20
2.3.3 Statistical distribution in photometric and spectroscopic EW's . . . 20
2.4 Starburst using COSMOS Photometric Catalogue . . . 23
2.4.1 Calibration of color-color diagnostics with spectra . . . 24
2.4.2 Starburst galaxies using COSMOS photometric redshift catalogue . . . 25
2.5 Caveats to the sample selection . . . 25
2.6 K-correction and stellar mass determination . . . 26
2.7 Results and Discussion . . . 29

3 Galaxies and Star-forming regions Properties **31**
3.1 Morphology of the Starburst galaxies . . . 31
3.1.1 Surface brightness analysis and photometry . . . 32
3.1.2 Resolved star-forming regions and diffuse emission . . . 32
3.1.3 Spatial distribution of the star-forming knots in the galaxies . . . 35
3.1.4 Mass and SFR estimation of the star-forming knots . . . 36
3.1.5 Single knot galaxies . . . 44
3.2 Results and Discussion . . . 44
3.2.1 Comparison with the literature at this redshift . . . 44
3.2.2 Mknots galaxies and their link to bulge formation . . . 47
3.2.3 Two populations: the knots that are galaxies and the remaining . . . 47

4 Starburst galaxies in COSMOS at $0.3 < z < 0.9$ **49**
4.1 Selection of the sample at $0.3 < z < 0.9$ . . . 49
4.1.1 Calibration of color-color diagnostic diagrams with spectra ($0.32 \leq z \leq 0.9$) . 50
4.1.2 Starburst in the COSMOS photometric redshift catalogue $0.32 \leq z \leq 0.57$) . 51
4.1.3 Caveat to the selection and final sample . . . 53
4.2 Galaxies properties . . . 53
4.2.1 K-correction and stellar mass . . . 53
4.2.2 Hα luminosity: K-correct fit . . . 57
4.2.3 Starburst morphology . . . 57
4.3 Properties of the knots . . . 59
4.3.1 Mass of the knots . . . 61
4.3.2 Spatial distribution of multiple knots . . . 61
4.4 Luminosity function of the starburst in COSMOS ($0 < z < 0.9$) . . . 63
4.5 Results . . . 64
4.5.1 Redshift evolution of the number density of starburst . . . 64
4.5.2 Redshift evolution of the clumpy fraction . . . 68
4.5.3 Redshift evolution of the star-forming knot properties . . . 70

5 Characterizing the host galaxies: 2D modelling **71**
5.1 Luminosity profile in galaxies . . . 71
5.2 Analytical functions for the radial profiles . . . 72
5.3 GALFIT . . . 77
5.4 The fit to Sersic profiles in galaxies with star forming clumps . . . 80
5.5 Results: Sersic profile fit of the starburst galaxies in COSMOS at $z < 0.5$ . . . 81
5.5.1 Sknot galaxies . . . 82
5.5.2 Sknot+diffuse light galaxies . . . 89
5.5.3 Multiple knots galaxies . . . 98
5.6 Results and Discussion . . . 104

6 Star Formation Feedback and Scaling Relations in Starburst Galaxies **107**
6.1 Models . . . 107
6.2 SF regime diagnosis by means of photometric data . . . 108
6.3 Diagnosis by means of high spectral resolution (HSR) data . . . 111
6.3.1 Observations . . . 114
6.3.2 Data reduction and analysis . . . 114
6.4 Resolving the kinematic components of the starburst clumps . . . 119
6.5 Scaling relations . . . 126
6.5.1 Photometry . . . 126
6.5.2 Spectroscopy . . . 127
6.6 Results and Discussion . . . 128

7 Conclusions **131**
7.1 Starburst galaxies in COSMOS at $z < 0.5$ (*Chapter* 2 *and Chapter* 3) . . . 131
7.2 Starburst galaxies in COSMOS at $0.3 < z < 0.9$ (*Chapter* 4) . . . 132
7.3 The host galaxy of the starburst in COSMOS (*Chapter* 5) . . . 133
7.4 Star formation feedback and scaling relations(*Chapter* 6) . . . 134

8 Future Work **135**
8.1 WEAVE. Scaling relations in starburst galaxies up to $z \sim 1$ 136
8.1.1 Future Work using WEAVE 137
8.1.2 The sample 137
8.2 MEGARA. Star Formation Feedback in Massive systems at different redshifts. . . . 138
8.2.1 Future Work using MEGARA 139
8.2.2 Sample and observing strategy 139

A Appendix A: Main parameters for galaxies in our sample **141**

B Appendix B: Main parameters for knots in our sample **147**

C Appendix C: Main parameters for galaxies in our sample at intermediate redshift **159**

References **185**

List of Figures

1.1 Tuning Fork scheme for the classification of galaxies 5
1.2 Morphological type of galaxies 7
1.3 8
1.4 Scalin Relations 12
1.5 M82 13
1.6 Super Galactic Winds: models I 14
1.7 15
1.8 Simulations of the hydrodynamical models of superwinds 15

2.1 Comparison of the photometric and spectroscopic EW's. 21
2.2 Statistical distribution of the photometric and spectroscopic EW's. 22
2.3 Comparison of the real and the Montecarlo EW 22
2.4 Comparison of the real and simulated spectroscopic EW with Montearlo 23
2.5 Comparison of the real and simulated photometric EW with Montearlo 24
2.6 SUBARU Intermediate Band Filters 25
2.7 Color-color diagram 26
2.8 Discarded sources after visual inspection 27
2.9 Redshift distribution of starburst galaxies 28
2.10 Comparison of stellar masses 29

3.1 Classification of the starburst galaxies 32
3.2 Procedure to identify SF knots 33
3.3 Starburst morphological classes 34
3.4 Redshift distribution for the morphological classes 35
3.5 Size distribution of the galaxies and star-forming knots 36
3.6 Distribution of ellipticity of the galaxies 37
3.7 Knot sizes versus their distance to the center of the galaxy 37
3.8 Size distribution of knots 38
3.9 F606W-F814W rest-frame color for individual knots ($x-$axis) and the whole galaxy ($y-$axis). Different symbols represent different galaxies. 39
3.10 F606W-F814W rest-frame color distribution for individual knots (solid line) and the whole galaxies (dotted line). The Gaussian overplot shows the best fit to the colors distribution of the knots. 39

3.11 Distribution of both knot/clump and galaxy colors in different samples of the literature. Left: $U-V$ rest-frame color distribution using a surface mass density identification (Wuyts et al. 2012). Disk regions are shown in green and clump regions in blue. Middle: $U-V$ color distribution using a $z-$band identification (Guo et al. 2012). Disks are represented in blue and clumps in red. Right: F606W-F814W rest-frame color distribution using a F814W identification (this work), as in Fig. 3.10 of this report. . . . 40
3.12 Mass distribution of the knots . . . 40
3.13 Comparison of masses of the knots with that of their host galaxies . . . 41
3.14 Hα/continuum distribution for galaxies . . . 42
3.15 SFR, Σ_{SFR}, mass and Σ_{mass} versus galactocentric distance . . . 43
3.16 Substructures in galaxies . . . 44
3.17 Clump Surface Density and Clump Mass versus absolute $B-$band magnitude . . . 45
3.18 sSFR versus mass . . . 46
3.19 Surface brightness versus absolute magnitude in the B and V bands for Sknot galaxies 48

4.1 Color-color diagram . . . 52
4.2 Color-color diagram in the Photometric Redshift Catalogue . . . 54
4.3 Completitude of the sample . . . 55
4.4 Comparison of z_{phot} and z_{spec} . . . 56
4.5 Discarded sources after visual inspection . . . 56
4.6 Mass determination for the intermediate redshift sample . . . 57
4.7 SFR distribution . . . 58
4.8 Ellipticity of galaxies at intermediate redshift . . . 59
4.9 Starburst morphological classes at intermediate redshift . . . 60
4.10 Mass distribution in our sample at intermediate redshift . . . 61
4.11 Knot sizes versus their distance to the center of the galaxy . . . 62
4.12 Ellipticity distribution of the knots . . . 62
4.13 Mass versus distance to the center for knots . . . 63
4.14 Total Luminosity Function in the $V-$band . . . 65
4.15 Luminosity Function in the $V-$band n three different redshift ranges . . . 66
4.16 . . . 67
4.17 . . . 69
4.18 . . . 70

5.1 Sersic profiles for different values of n . . . 74
5.2 Modified Ferrer profile . . . 75
5.3 Empirical King profile . . . 76
5.4 Nuker profile . . . 77
5.5 Example of the input control parameters . . . 79
5.6 Example of the model to be used in the fit . . . 79
5.7 Diagram with the steps of the method . . . 82
5.8 Deviation of the principal parameters: r_e, m, and n (Amorin et al. 2007, Fig. 4) . . . 83
5.9 Deviation of the principal parameters: r_e, m, and n (Amorin et al. 2007, Fig. 5) . . . 84
5.10 Distribution of the goodness parameter for Sknot galaxies . . . 85
5.11 Mosaic of eight Sknot galaxies . . . 86
5.12 Luminosity Profile of the Sknot galaxy COSMOS-022 . . . 87
5.13 Distribution of the goodness parameter for Sknot+diffuse galaxies . . . 91
5.14 Distance to the center of galaxy with respect to the radius of the mask vs area of the mask with respect to the area of the galaxy . . . 92
5.15 Mosaic of eight Sknot+diffuse light galaxies in our sample . . . 94

5.16 Surface-brightness fitting of the Sknot+diffuse light galaxy COSMOS-103 95
5.17 Surface-brightness fitting of the Sknot+diffuse light galaxy COSMOS-211 96
5.18 Surface-brightness fitting of the Sknot+diffuse light galaxy COSMOS-093 97
5.19 Mosaic of eight Mknots galaxies 100
5.20 Surface-brightness fitting of a Mknot galaxy 101
5.21 Distribution of the goodness parameter for Mknot galaxies 102
5.22 Mean distance to the center of galaxy with respect to the mean radius of the mask vs mean area of the mask with respect to the area of the galaxy 103
5.23 Distribution of the Sersic index 105
5.24 Distribution of the ellipticity 106

6.1 Feedback Solution 108
6.2 Mechanical luminosity for Sknot galaxies 112
6.3 Velocity of the gas overtaken by the RS as a function of heating efficiency 113
6.4 WHT ISIS slit over the observed galaxies 116
6.5 Integrated spectrum (all spatial pixels added) of one of the galaxies observed with ISIS at the WHT telescope. A calibration CuNe+CUAR lamp is overplotted. 118
6.6 Example of the 2D image of the slit with two galaxies in the spatial axis 118
6.7 WHT reduced spectra 120
6.8 Multiple component fits to the Hα emission line 124
6.9 L(H$_\alpha$) versus diameter relation 127
6.10 L(Hα) and σ versus the diameter 129

8.1 WEAVE 136
8.2 MEGARA 138

List of Tables

2.1 Sample of starburst galaxies selected from zCOSMOS 19
2.2 Sample of starburst galaxies selected from the photometric redshift catalogue 27

4.1 Luminosity function parameters 64
4.2 Clumpy fraction at different redshifts 68

5.1 Output for the 2D fit for Sknot galaxies 88
5.2 Output for the 2D fit for Sknot+diffuse galaxies 93
5.3 Output for the 2D fit for Mknots galaxies 99

6.1 Parameters determined with Starburst 99 for Sknot galaxies 109
6.2 Observations with ISIS at the WHT 115
6.3 Results from a single Gaussian fit to the Hα emission line 119
6.4 Single Gaussian fit to the emission lines Hα, NII, and SII 122
6.5 Results of the fit to the Hα emission line with multiple components 123
6.6 Hα emission on targets with multiple components in the same central wavelength . . 125
6.7 Measurements of narrow and broad components 125
6.8 Measurements of Hα emission on targets with multiple components with different central wavelength 125

A.1 Main parameters for starburst galaxies at low redshift 142

B.1 Main parameters for star-forming knots 148

C.1 Main parameters for starburst galaxies at intermediate redshift 159

Chapter 1

Introduction

Galaxies in the Universe span a wide range of morphologies, luminosities, masses, and sizes. At low redshift, the first studies of their properties were based on a taxonomic subdivision according to their visual properties. In 1936, Edwin Hubble introduced the "Tuning Fork" scheme for the classification of galaxies (see Fig. 1.1). In this pioneering study, Hubble suggested that galaxies evolved from the left-hand to the right end of this sequence. This speculation is now discredited, but galaxies that lie at the left-hand end of the sequence are still called early-type galaxies, while those toward the right-hand end are referred to as late-type galaxies.

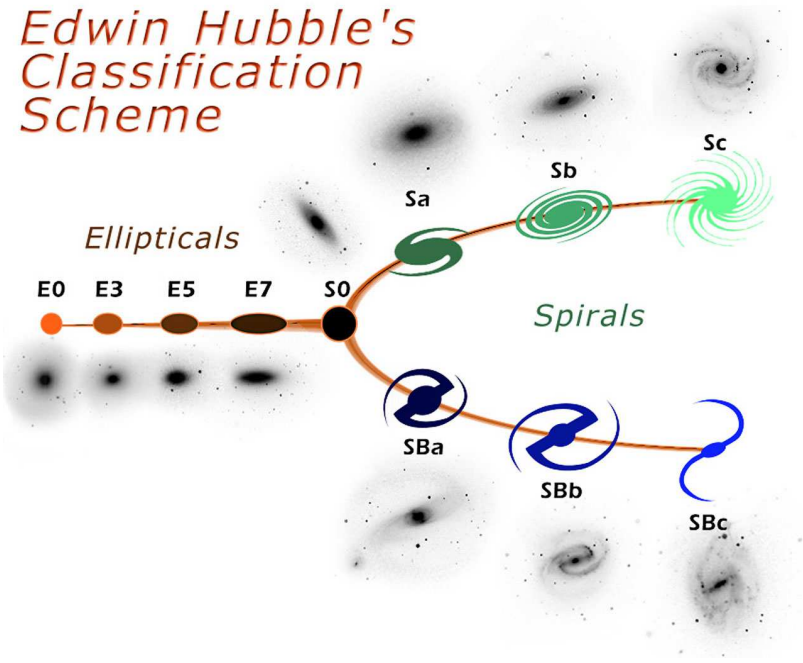

Figure 1.1: Tuning Fork scheme for the classification of galaxies, first introduced by Hubble in 1936 (figure taken from the webpage of the Hubble space telescope [2] with inverted colors).

One of the main qualitative criteria used by Hubble was the ratio between the luminosity of the spheroidal component and the total luminosity of the galaxy (B/T). On the left hand of the Hubble

diagram are placed those galaxies without a disk, therefore with $B/T \sim 1$, and which appear to be smooth and structureless. They were called elliptical galaxies due to the shape of their isophotes and they were organized as a function of their flattening. The more flattened ellipticals were positioned on the left side of the diagram. After the elliptical galaxies, Hubble's diagram bifurcates into two branches, the "normal" and the "barred" galaxies. These two types are mainly characterized by the presence of a stellar disk, and are usually called spiral galaxies due to the presence of star-forming spiral arms in their disks. A "normal" spiral galaxy contains also a central brightness condensation (the bulge or the spheroidal component) similar to an elliptical galaxy. A barred spiral contains, interior to the spiral arms, a prominent stellar structure with a bar shape. This bar often contains dark lanes produced by the absorption of the light by dust. Lenticular galaxies were placed in the transition between these two broad morphological types. Lenticular galaxies differ from ellipticals by the presence of a stellar disk. However, unlike the disk of spiral galaxies those of lenticular galaxies have no spiral structure and are not actively forming stars.

1.1 Formation and evolution of star-forming clumps

Understanding the different star formation mechanisms which lead to the variety of galaxy morphologies observed in the Universe is key to understand the formation and evolution of galaxies. With the advent of high spatial resolution images provided by the Hubble Space Telescope (HST), it has been shown that star-forming galaxies at high redshift are generally very efficient at forming stars and with irregular morphologies dominated by giant star-forming clumps (Daddi et al. 2010; Tacconi et al. 2010). Compared to local star-forming galaxies, that contain on average hundreds of relatively small HII regions (tens of parsecs scale), galaxies in the early Universe are made up of a handful of kiloparsec-sized star-forming clumps (Cowie et al. 1995; van den Bergh et al. 1996; Elmegreen et al. 2005). It has been now well established that these morphologies cannot be explained by simple spatial resolution effects, or an imaging K-correction, since artificially redshifted local star-forming galaxies produce high-redshift images with even light distributions (Elmegreen et al. 2009). This dichotomy on how the star formation proceed at high and low redshift led Elmegreen et al. (2007) to propose a new classification scheme for high-redshift systems. Besides the common spiral and elliptical morphologies new classes such as chain galaxies, clump-cluster galaxies, and tadpole galaxies were introduced. These new morphological types have in common the presence of massive $\sim 10^8 < M/M_\odot < 10^9$ star-forming clumps with different spatial distribution within the galaxy. Fig 1.2 shows examples of these morphological classes.

At high redshift, the SF in galaxies is mainly fueled by accretion of pristine gas from the cosmic web (Kereš et al. 2005; Aumer et al. 2010). In this scenario, when the dark matter halo is diffuse enough, the cool gas stream from the cosmic web can reach the inner halo, or disk, directly providing fresh gas to form stars. This mechanism is called cold-flow accretion, and it is predicted to be the main mode to trigger the SF in the early universe (L'Huillier et al. 2012). Recently, it has been proven that the accretion of metal-poor gas from the cosmic web may also activate the SF in the disk of nearby galaxies (Sánchez Almeida et al. 2013, 2014). Another scenario used to explain the growth of galaxies at high redshift invokes galaxy mergers (Conselice et al. 2003; Bell et al. 2006; Lotz et al. 2006; Bournaud & Elmegreen 2009). In this case, numerical simulations predict that major mergers can contribute up to 20% of the galaxy mass growth (wang et al. 2011) but at the cost of destroying the galactic disks of their progenitor (Naab et al. 2006, Guo et al. 2011). Therefore, several works suggest that merger-driven starbursts are less important than those triggered by gas accretion from the cosmic web (Vandevoort et al. 2011).

Recent observations and numerical simulations agree, showing that the SF at high redshift occurs mainly in giant clumps (Bournaud et al. 2015). The formation mechanism of these SF clumps is still a matter of debate. One scenario proposes that they are formed by disk fragmentation in gravitationally unstable disks (Noguchi et al. 1999, Immeli et al. 2004a, Immeliet al. 2004b,

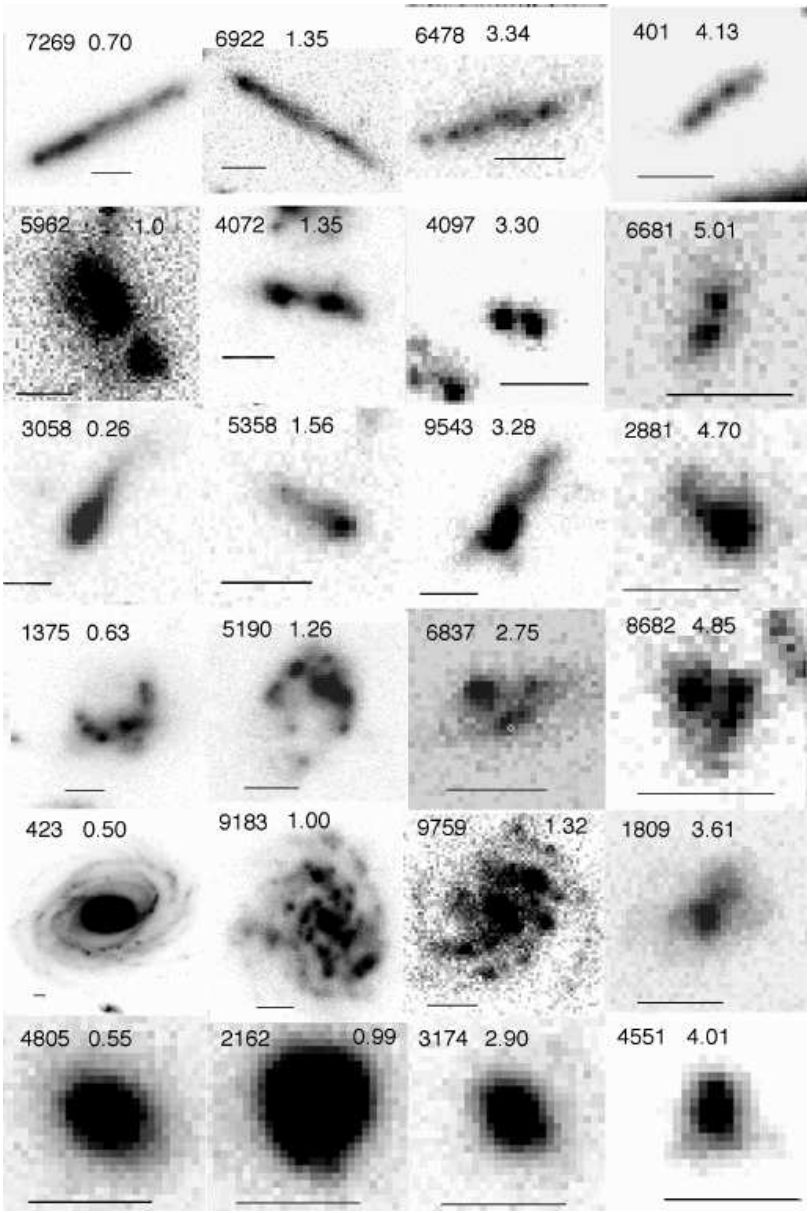

Figure 1.2: Examples of morphological type of galaxies. From top to bottom, the rows show chains, doubles, tadpoles, clump clusters, spirals, and ellipticals. The UDF catalog number is in the top left of each image, along with the redshift, which increases from left to right. The bar indicates 0.5". (Elmegreen et al. 2007)

Bournaudet al. 2007, Elmegreen et al. 2008). In this case, an intense inflow of cool gas is necessary to provide the high gas surface densities leading to the disk instabilities (Dekel et al. 2009). Contrary to this *in-situ* clump formation, (Mandelker et al. 2014) proposed that a limited number of *ex-situ* clumps might also be accreted by minor mergers into the galaxy disk.

The figure shown in Fig. 1.3 displays images of galaxies sampled at different redshift. There, it can be seen that as we move in redshift to earlier epochs in the universe the less massive galaxies and the more massive are bluer and more clumpy. Whatever model to explain the formation and evolution of galaxies has to account for this difference in age and morphologies. The recent results highlight the fact that star formation plays a main role in the growing and shaping of the galaxies we see.

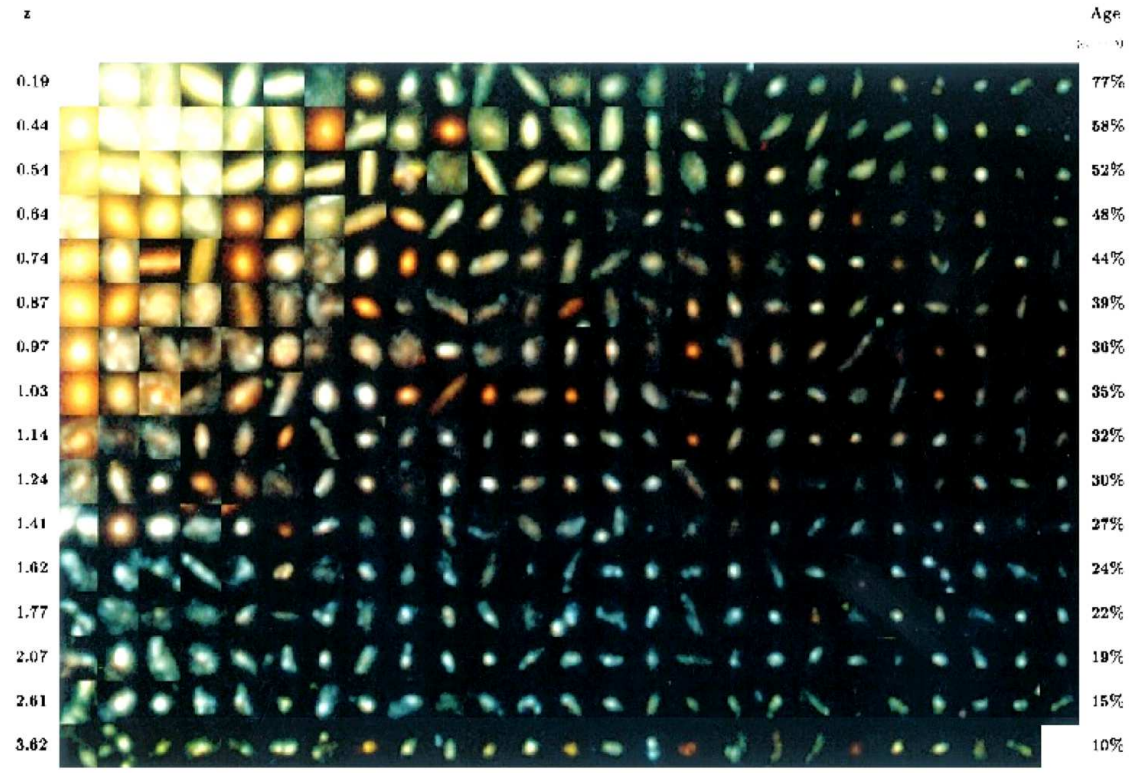

Figure 1.3: Hubble Deep Field photometric redshift sample. The sample is first sorted into redshift and divided into 16 redshift bins, each containing 25 galaxies. Within each redshift interval the galaxies are then ordered in terms of apparent magnitude (and therefore crudely in absolute magnitude). The progression down the page qualitatively reflects the process of galaxy evolution, although of course it does not correct for k-corrections and the redshift-dependent selection windows (Driver et al. 1998, Fig. 3).

Numerical simulations predict that, for a given mass, the galaxies become more clumpy at high redshift (Ceverino et al. 2010). The observations by (Elmegreen et al. 2007), including galaxies of different masses at different redshifts, confirm this tendency. These star-forming clumps are important, not only regarding the mass growth of the galaxy, but also for its morphological evolution. Numerical simulations show that star-forming clumps can migrate from the outer disk to the galaxy center, and contribute to the formation of bulges. The coalescence of clumps can take place in timescales of $\sim$4 rotation times (0.5-0.7 Gyr), therefore representing an alternative path for bulge formation at high redshift (Noguchi et al. 1999,Immeli et al. 2004a, Bournaud et al. 2007, Ceverino et al. 2010). The pre-existing thick disk and the star-forming clump migration

to the center have been considered also as responsible for the exponential profile in the luminosity of the present spiral galaxies (Bournaud et al. 2007, Elmegreen et al. 2013). As a result of this evolution, the system transforms from an initially uniform disk with high mass star-forming clumps to spiral-like galaxies with an exponential or double-exponential disk profile, a central bulge, and small remaining clumps (Bournaud et al. 2007, Ceverino et al. 2010, Elmegreen et al. 2013).

Following the predictions of numerical simulations, observational studies of clumpy galaxies have been performed using mainly high-redshift samples ($z > 1$). Deep, high-redshift surveys have proven to be a clue for studying the evolution of disk galaxies, with investigations spanning from the characterization and precise study of the star-forming knots (clumps), to their relation to the host galaxies. However, these high-redshift studies are usually severely limited by the spatial resolution of the images, even when using space-based observations with the HST Advanced Camera for Surveys (ACS). At lower redshift, studies have been mostly restricted to spectroscopic samples (Amorin et al. 2012).

All this new wealth of information at high redshift, available thanks to the advent of larger and deeper surveys as the Ultra Deep Field HST, have promoted the raise of new theories for galaxy evolution. At high redshift, this means that giant clumps of star formation - similar to those observed - might be formed within the galaxy if the adequate physical conditions are fulfilled.

1.2 The host galaxy

The host galaxy is, together with the gaseous component, the main source of the galaxy gravitational potential and therefore has strong influence on the star formation (SF) activity and SF interplay with the interstellar medium. Findings emerging from previous studies shows that the assessment of the host properties is a fundamental prerequisite for establishing the evolutionary status and the SF history of the galaxies. Furthermore, the comparison between the structural properties of the host with those of other galaxy classes is essential in order to elaborate a general view of their formation and evolution. The analysis of the underlying host stellar component of starburst galaxies has been mainly studied in the case of dwarf galaxies, and particularly, for Blue Compact Dwarf (BCD) galaxies. In fact, several deep photometric studies in the optical (e.g., Loose & Thuan (1986); Kunth et al. (1988); Telles & Terlevich (1995); Papaderos et al. (1996); Cairós et al. (2000, 2001); Amorín et al. (2007, 2009)) and in the near-infrared (e.g., James (1994); Doublier et al. (2001); Noeske et al. (2003, 2005); Cairós et al. (2003)) have demonstrated that virtually all BCDs have an older underlying stellar host in addition to the present starburst. The stellar host generally extends several kpc from the usually centrally concentrated star-forming regions. Thus, the host is generally detectable only at low surface brightness levels, showing elliptical isophotes, and displaying the red colors indicative of an old stellar population (Papaderos et al. 1996; Bergvall & Östlin 2002). The analysis of the underlying component of starburst galaxies has been also studied for other galaxy types. In a recent work, Elmegreen et al. (2013) have found that both local and high-redshift star forming galaxies have radially decreasing disk intensities when measured with ellipse-fit azimuthal averages. However, the average profiles are more irregular for high redshift clumpies (which are viewed in their restframe UV) than for local star-forming galaxies (viewed at g-band).

The faint surface brightness of the host component and the contamination caused by the starburst emission make the derivation of the structural parameters of the underlying host in starburst galaxies a complicated task. Thus, the derived structural parameters strongly depend on how well the starburst has been excluded from the fit, on the extent of the fitted host radial profile, on the quality of the dataset, and on the method and model used to parametrize the surface brightness profile. Some previous studies, in which one-dimensional models of the host component were fitted, have shown discrepant results even for the same galaxies, especially when a Sersic law was applied (see examples in Cairós et al. (2003) and Caon et al. (2005)). Moreover, during the extraction of a radial profile one can find serious limitations and ambiguities. Each of the different procedures

has its own drawbacks, resulting in information loss from the image (Baggett et al. 1998). At the present time, several well-tested two-dimensional algorithms are available. There are also several examples in the literature of studies showing that the two-dimensional method is generally more reliable than one-dimensional methods in bulge disc decompositions (de Jong 1996), as it is able to retrieve more accurate structural parameters. Particularly in starburst galaxies, a two-dimensional fit to the image may provide significant advantages over the fit to some averaged one-dimensional profile.

Despite all this progress in the field, the connection between these galaxies at high redshift ($z > 1$) and the local Universe has not been settled, mainly due to the lack of studies at intermediate redshift when the transition in the star-formation mechanism is expected to happen. The current PhD thesis is intended to fill this gap by searching and characterizing a complete sample of starburst galaxies at $0 < z < 1$. The study of the physical properties of the bursts, together with a detailed investigation of the starburst morphology, have provided new clues for galaxy formation scenarios.

1.3 Scaling relations

Extensive research has been dedicated in the literature to study the relationships among three key properties of giant HII regions and giant molecular clouds: luminosity, size and velocity dispersion (Terlevich & Melnick 1981; Larson 1981; Gallagher & Hunter 1983; Arsenault & Roy 1988; Bastian & Goodwin 2006; Rozas et al. 2006; Monreal-Ibero et al. 2007). These scaling relations contain information about the physics driving star-formation but they are still badly constrained spanning the ranges $\sigma \propto r^{1.14-3.68}$, $L \propto r^{1.92-3}$, $L \propto \sigma^{2.6-6.6}$ (see Fig. 1 Fuentes-Masip et al. 2000; Gutiérrez et al. 2011). These results were obtained by using of well-selected samples of nearby (i.e., resolved regions) measured with high spectral resolution. The previous scaling relations were formerly found for Giant HII regions by Melnick (1979, see also Terlevich & Melnick (1981) and Melnick & Quintana (1981)), and extended to HII galaxies by Melnick et al. (1988) and Telles & Terlevich (1993). The fact that giant HII regions and HII galaxies supersonic motions and follow similar scaling relations suggest that the physical mechanism behind star-formation is common. On an also important side, the scale relations were also proposed and are used as distance indicators.

Telles et al. (2001) confirmed and extended the empirical correlations found for giant HII regions and HII galaxies. This fact has profound implications both for the observations of HII galaxies and for the interpretation of their supersonic line-width. Enhanced spectral and spatial resolution seems to unveil an intricate structure in HII galaxies. Previously measured (single-aperture) supersonic motions in fact arise from regions of much smaller dimension than that occupied by the full extent of the ionized gas. HII galaxies, when resolved, present several emitting knots with a variety of shapes, luminosities, and velocity dispersion values. Telles's work show however that the global integrated value agrees very closely with the properties derived for the main emitting knot. This is because, as proposed by Munoz-Tunon et al. (1993), the intrinsic properties (luminosity, velocity dispersion) are dominated by the central (kinematical core) component. A fine calibration of these relations for local HII galaxies may be of great importance if used as a distance indicator of galaxies at large redshift, since HII galaxies are easy to find at great distances (see also Melnick et al. 2000). In particular, because the global line-emitting properties reflect the intrinsic properties of the central core component, observations even with poor spatial resolution could accurately define the luminosity and σ values of the dominant central core in every galaxy. HII Galaxies are proposed also as cosmological probes. Recently Chávez et al. (2012), using a sample of 69 HIIG and 29 Giant HII regions found a value for $H_0 = 74.3 \pm 3.1$(random) $\pm$ 2.9(systematic) km s^{-1}Mpc^{-1}, which is consistent with, and independently confirms, Riess et al. (2011) and more recent SNIa results Freedman et al. (see 2012). It will be extremely important to extend this work to $z \sim 1$. The latest, published by Wisniosky et al (2012), for a sample in the WiggleZ Dark Energy Survey (Drinkwater et al. 2010) and data for GHIIRs to simulated galaxies at $z \sim 1.9$ - 3.0, including the observational

values for galaxies at $z = 1.3$, among the Hα luminosity, size and velocity dispersion of HII regions in local star-forming galaxies and clumps in high-redshift galaxies, derived the relation for L(Hα) and σ with the size (see Fig. 1.4). Their results are in relative agreement with massive star-forming regions forming out of Toomre-unstable discs with high local velocity dispersion, with measured sizes and estimated masses in agreement with the model predictions (e.g. Noguchi 1999; Immeli et al. 2004a,b; Bournaud et al. 2007; Elmegreen et al. 2008).

The fact that the correlations are similar to the relations inherent to virialized stellar systems such as globular clusters, bulges of spiral galaxies, and the cores of elliptical galaxies led Terlevich & Melnick (1981) to propose that giant HII regions and HII galaxies are virialized systems too and then, the gas velocity dispersion (σ_{gas}) should be directly related to their total mass. In their original scenario, Terlevich & Melnick envisaged a gravitational potential that forced the collective motion of clumps of gas to present the supersonic σ values. From a theoretical point of view, virialization is now believed to have much to do with the motion of low-mass stars moving in the gravitational potential of the system while undergoing winds. This enhances their cross section and enables them to cause stirring of the gas left over from the star formation event (see: Tenorio-Tagle et al. 1993). Alternative physical reasons have also been proposed like supersonic turbulence or winds from massive stars. Chu & Kennicutt (1994), for example claimed that the supersonic line-widths could result from a plethora of unresolved expanding shells caused by the mechanical energy of the massive stars. As this hypothesis fails however to explaining the empirical correlations, and thus it has been argued that the measured line-widths follow the correlations simply due to a lack of resolution in the integrated spectra obtained from single-aperture observations (see also Tenorio-Tagle et al. 1996, for further discussion).

1.4 Feedback mechanisms

The effects of star-formation negative feedback have been invoked as an important issue in the Cold Dark Matter paradigm of galaxy formation (Dekel & Silk 1986; Scannapieco et al. 2002). However, recent theoretical results based on hydrodynamic simulations of massive star formation regions (Tenorio-Tagle et al. 2005, 2007; Wünsch et al. 2008; Tenorio-Tagle et al. 2010, 2013) have demonstrated how, in some cases, this feedback may be positive, implying that little or none of the returned matter is going to be ejected out of the system. These models have opened new scenarios of star formation. Large stellar densities may lead to strong radiative cooling causing the matter reinserted by massive stars inside the inner zones of the cluster to remain gravitationally bound.

Then, new stellar generations with different metallicities may form inside the star cluster volume (Tenorio-Tagle et al. 2005; Silich et al. 2007). As a result, star formation would be extremely efficient. This theoretical framework was developed to the light of the discovery of Super Stellar Clusters (SSCs) in the core of nearby galaxies. These studies have shown that the interplay between the thermalization of the kinetic energy provided by massive stars, radiative cooling of the thermalized plasma, and the gravitational pull of the host galaxy lead to three different hydrodynamic regimes. These are: (1) quasi-adiabatic supergalactic winds; (2) bimodal flows, with mass accumulation in the central zones and gas expulsion from the outer zones of the assembling galaxy; and (3) the gravitationally bound regime, for which all of the gas returned by massive stars remains bound to the host galaxy and is likely to be reprocessed into further generations of stars. Which of the three possible solutions takes place depends on the mass of the star-forming region, its mechanical luminosity (or Star Formation Rate; SFR), and its size.

Recently, Tenorio-Tagle et al. (2010, 2013) have provided us with a new observable to detect the existence of these different regimes. They have shown that, contrary to what previously expected, broad nebular recombination lines may have nothing to do with the expansion of the nebula. The supersonic broad emission lines result only in clusters undergoing the bimodal hydrodynamic solution. The origin of the most intense broad lines is due to the large number of re-pressurizing shocks

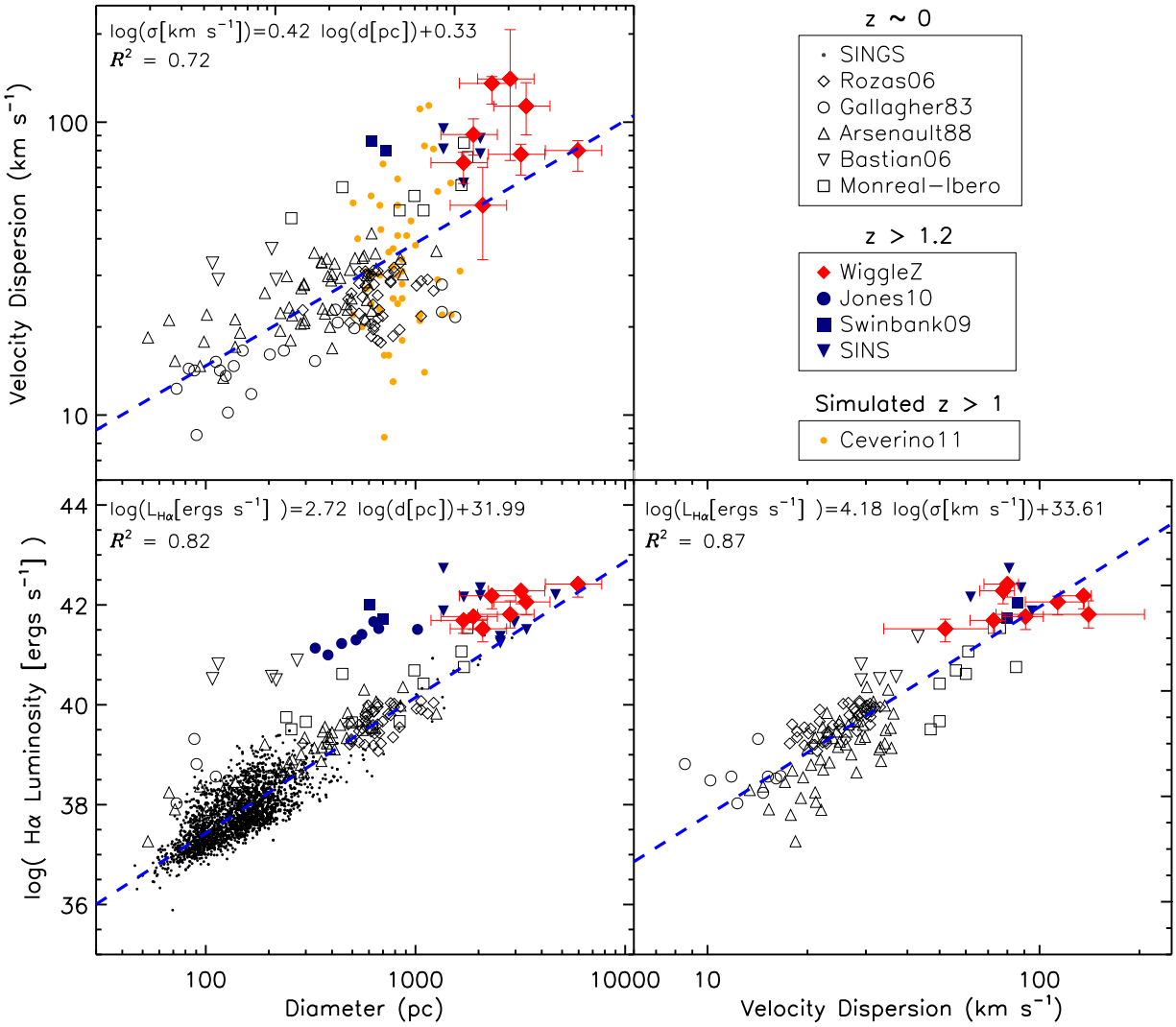

Figure 1.4: Relations among the Hα luminosity, size and velocity dispersion of HII regions in local star-forming galaxies and clumps in high-redshift galaxies. The bright red diamonds represents clumps from WiggleZ galaxies. High-redshift clumps are shown as filled symbols in blue and taken from Swinbank et al. (2009), Jones et al. (2010), Genzel et al. (2011) and Förster Schreiber et al. (2011). HII regions from local SINGS galaxies are displayed as black dots, and giant HII regions from local galaxies are shown as open black points and are taken from Gallagher & Hunter (1983), Arsenault & Roy (1988), Bastian & Goodwin (2006), Rozas et al. (2006) and Monreal-Ibero et al. (2007). The blue dashed lines show the least-squares best fits, given in the top-left corner of each panel with correlation coefficients, R^2, given directly below. Simulated clumps at 1.9 ¡ z ¡ 3.0 from Ceverino et al. (2012) are plotted in orange but have not been included in the fit. (Figure taken from Wisnioski et al. (2012).

(RS), induced within the dense thermally unstable reinserted gas as this strives to maintain pressure balance with the much hotter gaseous counterpart. The less intense, although much broader Gaussian component detected only in some cases, is shown to be caused by the cluster wind; it becomes photoionized and less dense upon its own expansion. They show also that the maximum speed of the RSs and of the cluster wind are both functions of the temperature reached at the stagnation radius. This temperature depends only on the cluster heating efficiency.

The cluster heating efficiency is a key parameter in defining the evolution of a massive and young stellar cluster. Clusters with low heating efficiency are to be much less effective in producing both kinetic energy and mass via winds to the intergalactic medium (IGM). As a consequence, their star formation efficiency is expected to be enhanced.

Fig. 1.5 shows the classical example of a nearby galaxy undergoing a supergalactic wind. M82, the cigar galaxy, a $10^9 M_\odot$ irregular that hosts a large starburst which ends up expelling the processed material to the intergalactic medium. The images have been formed from a combination of HST and WIYN H? and [N II] observations. Prominent features include loops and filaments, reflection nebulae, and "search-light" formations. Fig. 1.6 shows an schematic of the hydrodynamical models which accounts for both the energy and spectral configuration to describe an observed supergalactic wind. This is a typical case of what can be considered negative feedback of star formation.

Figure 1.5: M82, the classical example of a galaxy undergoing a supergalactic wind. The images have been formed from a combination of HST and WIYN Hα and [NII] observations (Westmoquette et al. 2005).

In many other situations, the energy of the burst, although exceeds the dimension of the starburst clusters do not reach the intergalactic medium. The material is confined in a bubble-like structure which does not break down and, after the energy of the massive stars decreases, the shell of swept up material colds down and falls again into the starburst volume.

This can be considered an intermediate case as, in time, the material will be again able to form more stars (positive SF feedback). In Fig. 1.7 the 30 Doradus cluster is shown. Different colors represent different gas and star temperatures (wavelength ranges). The same figure -right panel-

shows a sketch with the hydrodynamical evolution of a bubble and the formation of a expanding shell.

In more extreme cases, as shown by (Tenorio-Tagle et al. 2005, 2007; Wünsch et al. 2008; Silich et al. 2010; Tenorio-Tagle et al. 2010, 2013), massive assembling clumps and possible galaxies may evolve in a positive star formation feedback condition. This would imply that star formation may have a little impact on the intergalactic medium but an important effect on the formation of future generations of stars in these galaxies.

In Fig. 1.8 we show the simulations that were run to reproduce two observables which include both (positive and negative) feedback phenomena, these simulations were done considering the super winds produced by multiple super-star clusters (Tenorio-Tagle & Muñoz-Tuñón 2003). The starburst nucleus of M82, after the high resolution image of the HST unveiled the presence of a plethora of the, so call Super Star Clusters (SSC) (see Melo et al. 2005). These SSC are massive ($\sim 10^5 M_\odot$) and compact ($\sim$ 3 pc radii), and it is believed that some of them evolve in a positive feedback mode (see Silich et al. 2007,2009). Also important is that from a group of SSC which are very close each other, the self confinement of their winds produce, in a natural way the details of the filamentary structure that is observed in the Hα image of M82. Some details of the hydrodynamical models are shown in Fig. 1.8

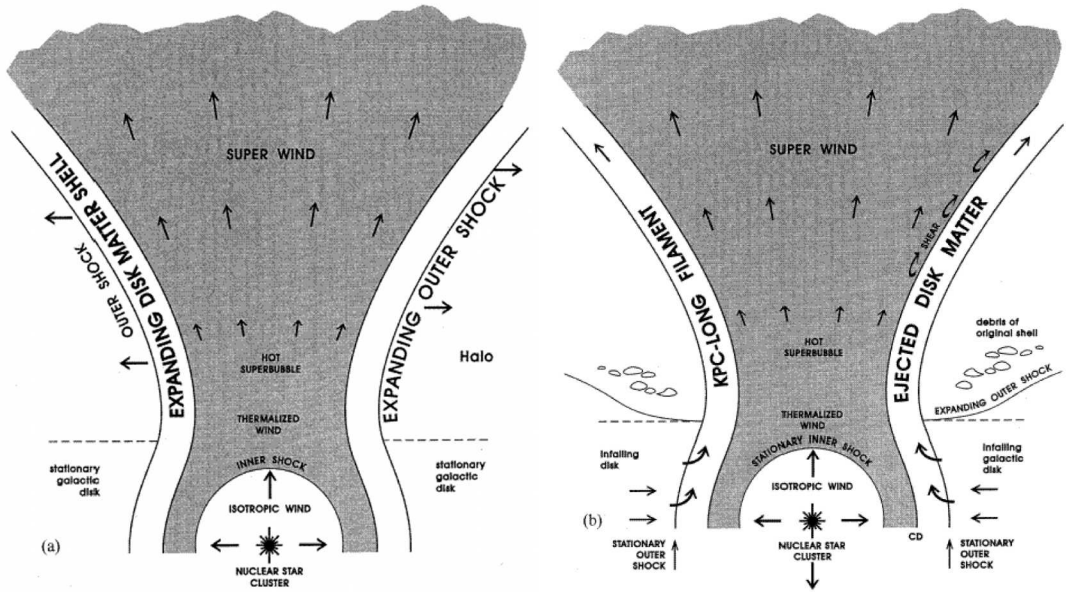

Figure 1.6: Super Galactic Winds: models I (Tenorio-Tagle & Muñoz-Tuñón 1997, 1998)

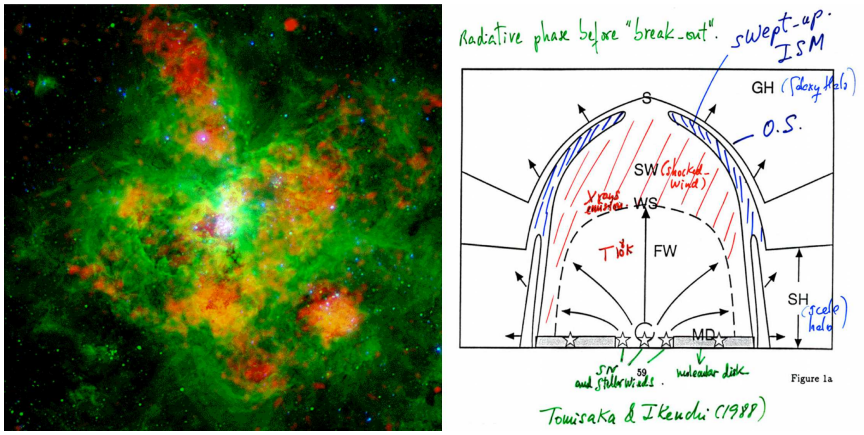

Figure 1.7: Left: 30 Dor cluster. Different colors represent different gas and star temperatures. Right: Sketch with the hydrodynamical evolution of a bubble and the formation of a expanding shell

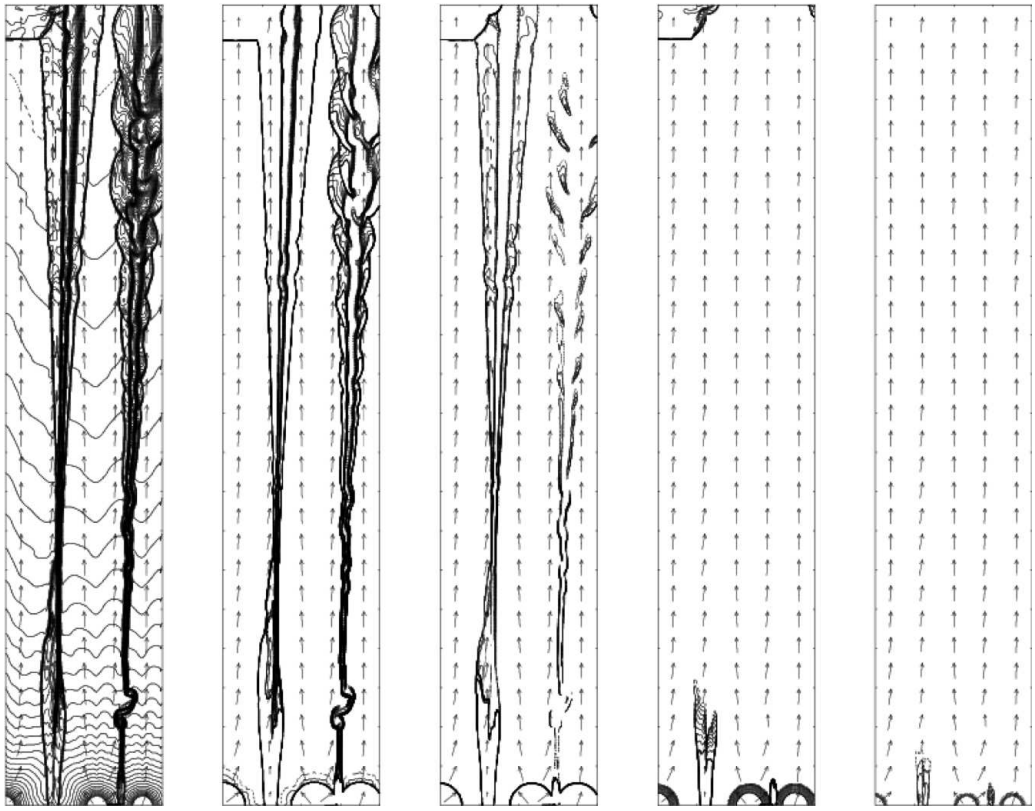

Figure 1.8: Simulations of the hydrodynamical models for supergalactic winds powered by multiple super-star clusters which reproduce two observables, which include both (positive and negative) feedback. The panels in every row represent cross-sectional cuts along the computational grid showing isodensity contours with a separation $\Delta log\rho$=0.1 and the velocity field. Each of the superwinds has a power of 10^{41} ergs s^{-1} and a radius of 5 pc (Tenorio-Tagle et al. 2003).

A brief description of this thesis

This thesis work is based mainly in the extensive use of the COSMOS survey. High spectral resolution data are also included to further study the SF feedback.

In chapter 2 we describe our methodology to find a sample of starburst galaxies at $0.1 \leq z \leq 0.48$ obtained with spectra from the zCOSMOS catalogue. Once obtained a first sample of starburst galaxies, we extend our sample to galaxies in the Photometric Redshift Catalogue, we create a methodology based in a taylor-made colo-color diagram selection. Because of the limitation wavelength coverage for the Subaru Intermediate Band Filter, our photometric catalogue of starburst galaxies is limited at the redshift ranges: $0.007 \leq z \leq 0.074$, $0.124 \leq z \leq 0.177$, and $0.230 \leq z \leq 0.274$.

In chapter 3 we analyze the star-forming region in our sample of starburst galaxies. An isophotal analysis is done to find the parameters of individual star-forming regions in the galaxies, and then we compare the properties of the star-forming regions with those of the whole galaxies.

In chapter 4 we extent in redshift our sample of starburst galaxies. First we describe the methodology to find an spectroscopic sample in the range $0.3 \leq z \leq 0.9$ with spectra from the zCOSMOS catalogue. To extent the number of galaxies we create, as in chapter 2, a taylor-made color-color diagram selection. Again, the limitation wavelength coverage for the Subaru Intermediate Band Filter, gives a limitation in redshift to the sample, this limitation allow to find galaxies from the Photometric Redshift Catalogue in the redshift range: $0.32 \leq z \leq 0.57$.

In chapter 5 we analyze the surface brightness of the host galaxies determining the morphological features of them, then we compare our results with different scenarios of galaxy formation and evolution.

In chapter 6 we analyze the hydrodynamical state of some galaxies in our sample. In this chapter we use high resolution spectra of a sample of starburst galaxies in our sample to analyze the different component of the Hα emission line. We discuss our results on the the feedback mechanism scenario and analyze a sample of galaxy candidates to be in a bimodal state.

Finally chapters 7 and 8 provide the final conclusion and future work.

Chapter 2

Starburst galaxies in COSMOS at $z < 0.5$

The Cosmological Evolution Survey (COSMOS) is the largest deep field survey ever done by the Hubble Space Telescope (HST). It covers two equatorial square degrees and about 2×10^9 galaxies have been observed in this area with the Advance Camera for Survey (ACS). The COSMOS field has been recognized as one of the Legacy cosmological fields and therefore it has been the focus of many other surveys with time. Space- and ground-based telescopes have been used to map a large range of the electromagnetic spectrum, from radio to X-ray energies. The unique combination of both the large area and multiwavelength nature of the COSMOS database lay the foundations of this Ph.D. thesis.

This chapter will introduce the available datasets and the methodology to select a well-defined sample of starburst galaxies at $z < 0.5$. The structure of this chapter is as follows: Sect. 2.1 describes the different catalogues used in this study. Sect. 2.2 shows the first subsample of starburst obtained using the available spectroscopy in the field. A thorough study of the computation of the spectroscopic and photometric emission line equivalent width (EW) is presented in Sect. 2.3. The complete sample of starbursts and its selection methodology is explained in Sect. 2.4. Possible caveats on our sample selection are exemplified in Sect 2.5. In Section 2.6 we determine the K-correction and stellar masses of the sample of starburst galaxies. A summary and final remarks of the starburst catalogues is provided in Sect. 2.7.

2.1 COSMOS Databases

2.1.1 COSMOS Intermediate and Broad Band Photometry Catalogue

Over 2 millions of sources have been observed with the HST ACS high spatial resolution camera using the F814W filter in the COSMOS field. Additional observations on 30 bands covering from the UV to the IR were done using different ground- and space-based instruments and are available in this catalogue. To perform our search we used the Intermediate Band Filters from the SUBARU telescope.

2.1.2 COSMOS Photometric Redshift Catalogue

To take spectra of thousands of sources is very time consuming, therefore, measuring redshift based only on photometric data is more efficient and have been demonstrated to be a powerful tool in recent surveys (Ilbert et al. 2009; Benítez et al. 2009). The photometric redshift (z_{phot}) in COSMOS was computed using 30 broad, intermediate and narrow band filters covering the UV, visible-NIR and mid-IR spectral ranges (Ilbert et al. 2009). This catalogue contains 385065 sources classified

as galaxies, stars, X-ray sources, faint sources or masked areas. Among them, we choose only the 305002 sources flagged as galaxies. To follow the Hα and [OIII] emission lines we need the SUBARU filters and the z_{phot}, for this reason we matched the COSMOS Intermediate and Broad Band Photometry Catalogue with the COSMOS Photometric Redshift Catalogue.

2.1.3 zCOSMOS

The spectroscopic redshift (z) was obtained with observations of the VIsible MultiObject Spectrograph (VIMOS) on the Very Large Telescope (VLT) for a subsample of the COSMOS field, as part of the zCOSMOS project (Lilly et al. 2007). This catalogue contains two parts, the first is the zCOSMOS-bright, aimed to observe ∼20000 galaxies at $0.1 < z < 1.2$ using the VIMOS red spectral range (5550-9650Å) with the R $\sim$ 600 MR grism in order to detect the strong spectral features around 4000 Å. The second part is the zCOSMOS-deep, which aims to observe ∼10000 galaxies lying at $1.5 < z < 2.5$ in the blue spectral range (3600-6800Å) to measure the strong absorption and emission features in the range between 1200 and 1700 Å. At the moment, there are 10643 published spectra corresponding to the results of the zCOSMOS-bright spectroscopic observations that were carried out in VLT Service Mode during the period April 2005 to June 2006. These have been observed using a 1 arcsec wide slit sampling roughly 2.5 Å/pixel with a velocity accuracies of the order of 100 km s^{-1}.

2.2 Starburst in zCOSMOS

Starburst galaxies show a steep rising continuum in the blue region of the spectra, combined with strong nebular emission lines. At visible wavelengths, the [OIII] and Hα emission lines are the most prominent, and we can parametrize them using the equivalent width (EW). Previous studies of starburst galaxies in the local Universe (Kniazev et al. 2004; Cairós et al. 2007, 2009a,b, 2010; Morales-Luis et al. 2011; Amorín et al. 2014) found minimum values of the [OIII] and Hα EW of about 80 Å. This value corresponds to young star-forming regions, with ages < 10 Myr (Leitherer et al. 1999; Vázquez & Leitherer 2005; Leitherer et al. 2010). Therefore, the EW turn out to be the best parameter to identify young starburst galaxies and we adopt the aforementioned EW threshold values in our work.

To measure the EW of the [OIII] and Hα emission lines we first used the spectra from zCOSMOS. The wavelength range of the spectra allows us simultaneously to measure [OIII] and Hα in the redshift range $0.1 \leq z \leq 0.47$. zCOSMOS comprises 3384 galaxies in this redshift range. To identify those with emission lines, we used the published spectroscopic redshift and the restframe wavelengths of the [OIII] and Hα emission lines (λ_c: 4959, 5007Å; 6563Å). Then, we measure the flux of the emission line (F_l) in a baseline of 30 Å, which allows us to cover the total width of the line at the continuum level. The same band-width was used to measure the flux of the continua (F_c) at rest-frame wavelengths 5053Å and 6518Å for [OIII] and Hα, respectively. The EW is defined as

$$\mathrm{EW} = \sum \frac{F_\mathrm{l} - F_\mathrm{c}}{F_\mathrm{c}} \delta\lambda \tag{2.1}$$

where $\delta\lambda$=2.5Å. The associated error is given by

$$e_\mathrm{EW} = \frac{F_\mathrm{l}}{F_\mathrm{c}} \left(\frac{\sigma_c}{med_c} \cdot \sqrt{8n} \right) \tag{2.2}$$

where both σ_c and med_c correspond to the standard deviation and the median in the continuum respectively, and n is the number of resolution elements in the selected baseline. We calculated the EW in Hα and [OIII] for all of the 3384 galaxies, covering the ranges $0.1 \leq z \leq 0.47$. We selected

Table 2.1: Starburst galaxies selected from zCOSMOS.

object	z	EW(Hα) [Å]	EW([OIII]) [Å]
cosmos-002	0.34	234 ± 43	321 ± 18
cosmos-003	0.25	104 ± 14	108 ± 28
cosmos-010	0.13	144 ± 19	100 ± 11
cosmos-014	0.38	208 ± 21	124 ± 7
cosmos-015	0.41	94 ± 21	166 ± 16
cosmos-017	0.17	177 ± 58	121 ± 12
cosmos-018	0.28	193 ± 40	174 ± 10
cosmos-021	0.19	96 ± 19	126 ± 8
cosmos-026	0.44	148 ± 70	115 ± 18
cosmos-027	0.34	190 ± 31	164 ± 6

Notes. (1) Object name (ordered by RA), (2) spectroscopic redshift, (3) Hα EW and (4) [OIII] EW.

those with EW $\geq$ 80Å in Hα and [OIII], obtaining a sample of 82 starburst galaxies. Table 2.1 shows the first few entries of the spectroscopic emission line catalogue.

2.3 Estimation of the equivalent width (EW) and the associated uncertainty

In this section we describe the methods used to estimate the EW of the galaxies in the COSMOS survey, we estimate the EW from the SUBARU Intermediate Band photometry and, if it is available, from the zCOSMOS spectroscopy, for both estimations of the EW we do an estimation of the uncertainties in the measurements. First we describe the estimation of the photometric EW, because the most of galaxies in COSMOS have available only photometric data, then for galaxies with available spectroscopy from zCOSMOS we estimate the spectroscopic EW, we compare both measurements to validate the estimation of the photometric EW, which is used for the most of the galaxies.

2.3.1 Photometric EW

To estimate the EW using the SUBARU Intermediate Band photometry, we first choose the filter corresponding to the emission line that we are measuring (Hα or [OIII]), then we close a filter corresponding to the continuum foe every emission line (5500Åfor [OIII] and 6000Åfor Hα). The equivalent width is defined as:

$$EW = (\frac{F_{linea}}{F_{cont}} - 1) \cdot \Delta W \tag{2.3}$$

In COSMOS we find the magnitudes and their associated errors for every filter, we transform these magnitudes into flux (ergs/s/cm/Å) and make an estimation of the error associated to the flux. To convert the magnitud into flux it is necessary the flux of an object with magnitude 0 in the corresponding filter (F_0), this flux for the COSMOS filters is available on the WEB (http://www.astro.caltech.edu/ capak/cosmos/filters/), also the bandwidth is available. Once obtained the F_0, the transformation from magnitude to flux is given by:

$$F = F_0 \cdot 10^{-0.4 \cdot m} \tag{2.4}$$

The associated error in flux (e_f) is estimated from the magnitude error (e_m) through an error propagation, which is given by:

$$e_f = \pm F_0 \cdot 0.4 \cdot 10^{-0.4 \cdot m} \cdot log(10) \cdot e_m \tag{2.5}$$

Once obtained the flux and bandwidth values for the filter associated to the emission line that we are measuring, we estimate the EW of that emission line using 2.3. The error associated to this EW (e_{EW}) is obtained throughout error propagation, it is given by:

$$e_{EW} = \pm \frac{F_{linea}}{F_{cont}} \left(\frac{e_{flinea}}{F_{linea}} + \frac{e_{fcont}}{F_{cont}}\right) \cdot \Delta W \tag{2.6}$$

2.3.2 Spectroscopic EW

Some galaxies in our sample were detected by their spectroscopic EW, the spectra taken with the VIsible MultiObject Spectrograph (VIMOS) at the Very Large Telescope (VLT) are available in the zCOSMOS database [1]. We used a subsample of the galaxies found from zCOSMOS, which are in the redshift range in which it is possible to de termine the photometric EW, to compare both measurements and calibrate the photometric EW. To estimate the EW we used the Splot task of IRAF, the continuum is fitted and then the EW for the emission line is calculated. For every point in the emission line we have a flux (F_t), also we have the flux value in the continuum (F_c), and the separation of every point, in wavelength, is 2.55 Å. The EW is given by:

$$EW = \sum_{j_i}^{j_f} \left(\frac{F_t}{F_c} - 1\right) \cdot 2.55 \tag{2.7}$$

where $n = j_f - j_i$ corresponds to the width of the baseline.

The error in this measurements is given by:

$$e_{EW} = \pm \frac{F_{linea}}{F_{cont}} \left(\frac{\sigma}{mediana_{cont}} \cdot \sqrt{8n}\right)^2 \tag{2.8}$$

where σ corresponds to the standard deviation.

In this work we are interested in the galaxies with EW in Hα and [OIII] $\geq$ 80 Å. These parameter represents objects with regions with young stellar formation (<10Myr). There are nine galaxies with EW $\geq$ 80 Å in Hα and [OIII] with spectra in zCOSMOS and with a redshift which allow to measure the photometric EW. The comparison of both EW(Hα) is showed in Fig. 2.1.

In Fig. 2.1 the comparison of both EW, photometric and spectroscopic, show a good relation. However, there is a point with photometric EW around 800 Å, but the spectroscopic EW is around 400 Å. For that galaxy we have checked the image, there is a close star contaminating the field, as the magnitude are determined using a fixed aperture of 3", these fact produce a discordance in the measurement of the photometric EW.

2.3.3 Statistical distribution in photometric and spectroscopic EW's

Once calibrated the methods to estimate the EW in the sample of nine galaxies with photometric and spectroscopic measurements, we extent this validations to the complete sample of galaxies. Fig. 2.2 shows the EW distribution of the all sample, the objects with photometric EW are 187, and with spectroscopic EW are 13.

[1] http://irsa.ipac.caltech.edu/data/COSMOS/spectra/z-cosmos/Z-COSMOS_INFO.html
[2] Adaptation of the error estimation in the EW from the Jorge Sánchez thesis

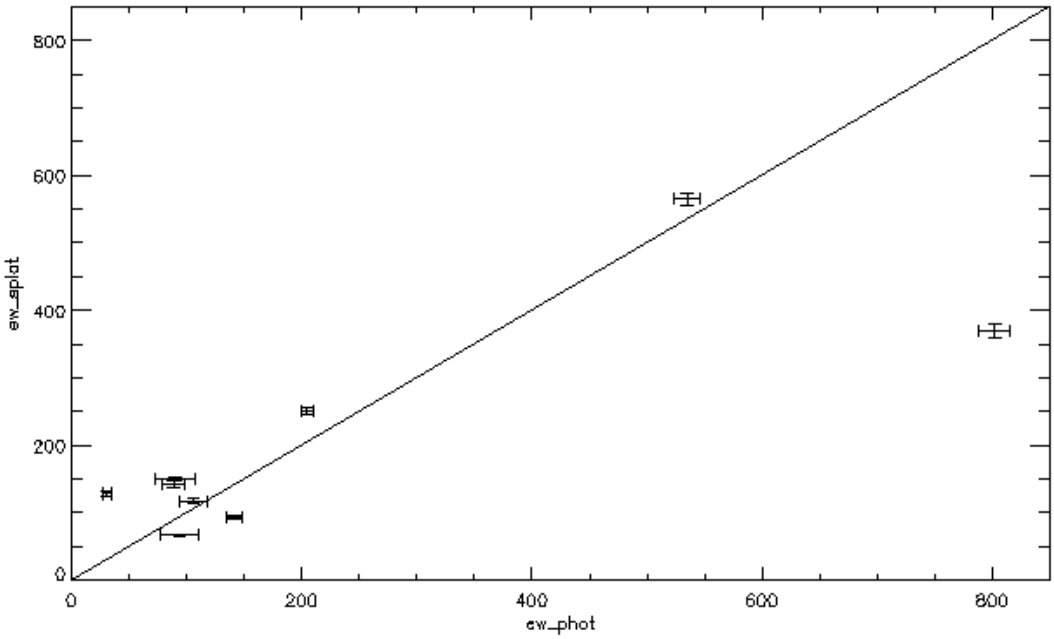

Figure 2.1: Comparison of the photometric and spectroscopic EW's.

From Fig. 2.2 we can conclude that the maximum of the distribution of both samples is similar in their values and their typical deviation. We conclude that statistically both samples have similar distribution of the EW.

We use this result as a parameter to use the photometric EW for the complete sample.

Montecarlo Simulations

The Montecarlo simulations are a method which allows to estimate errors in the measurements when the analyzed system is complex. This method is based in allow to a physical system to vary randomly, these variations allows to prevent different consequences which can affect to the system under these variations. In our search for starburst galaxies, we have identified galaxies with high EW, to estimate this EW we have used the fluxes of the objects, these fluxes have associated errors in their measurements. In this section we use the Montecarlo method to allow to the values of the EW to vary randomly in their fluxes, being their associated errors the maximum variation allowed. We compare the results obtained from the error propagation, with the stander deviation of the EW obtained from the randomly variation with the Montecarlo method.

Spectroscopic simulations

In section 2.3.2 we calculated the spectroscopic EW using the fluxes in the emission line and the continuum, and the associated errors thought error propagation. In this section we estimate the the variation in the EW using the Montecarlo method, then we compare these simulations with the errors estimated in section 2.3.2 and analyze the concordance between both methods. To do it we let to the flux to vary randomly in their associated errors, with this method we obtain a vector with values of EW, then we estimate the standard deviation for this vector, and we use this value as the associated error for the EW.

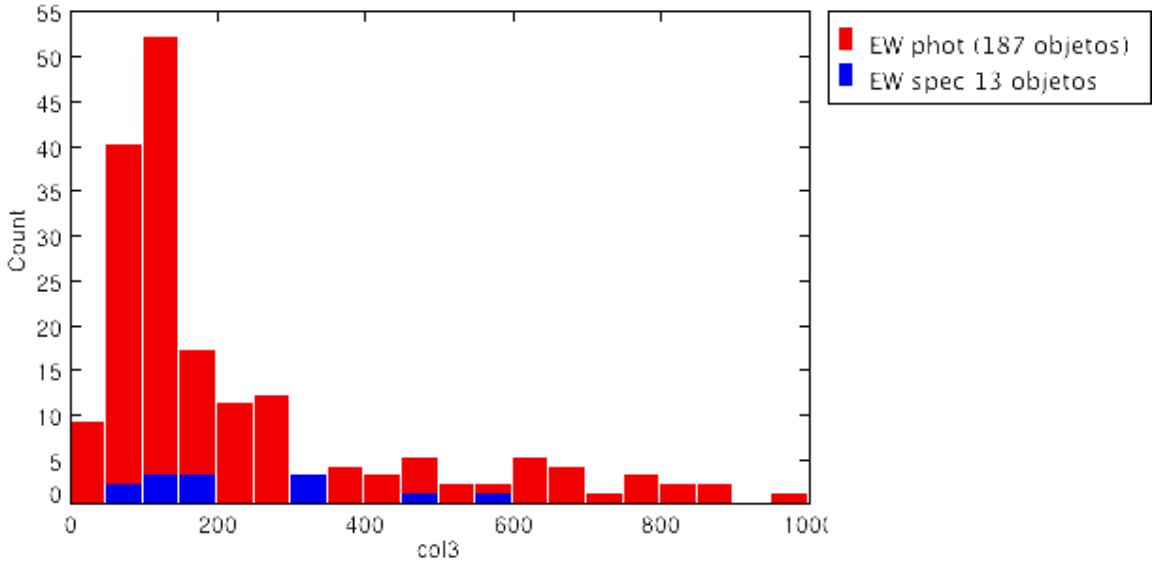

Figure 2.2: Statistical distribution of the photometric and spectroscopic EW's.

In Fig. 2.3 we show the EW obtained directly from the fluxes versus the EW obtained as the mean of the EW from the Montecarlo simulations, we include the errors, even if they are very small ($\sim 1\%$, depending on the S/N of the spectra), the errors have not a considerable importance in the comparison.

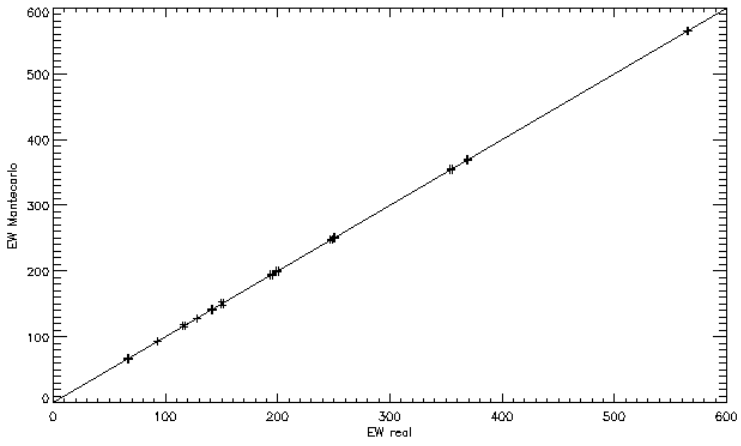

Figure 2.3: Comparison of the real and the Montecarlo EW

The errors in the measurements seem to be very small, considering error propagation and Montecarlo simulations. The reason in these small values is that we have not considerate systematic errors in the measurements. To estimate the EW we have considerate a continuum using SPLOT in IRAF, then we considerate that continuum as a fixed value. However, to calculate the EW, the definition of the continuum is very important, and a wrong estimation in this parameter could have a big influence in the result. For this reason, we should considerate the continuum with variations

according with the standard deviation, and from these variations to estimate a systematic error in the estimated EW. Using Montecarlo simulations, we consider random variations in the continuum, with the standard deviation as the maximum value for these variations. We create a vector of n elements with the EW estimated considering these variations, and from this vector determine the standard deviation, this measurements is the value for the systematic error in the EW. Fig. 2.4 shows the EW obtained with the Montecarlo method, with and without random variation in the continuum.

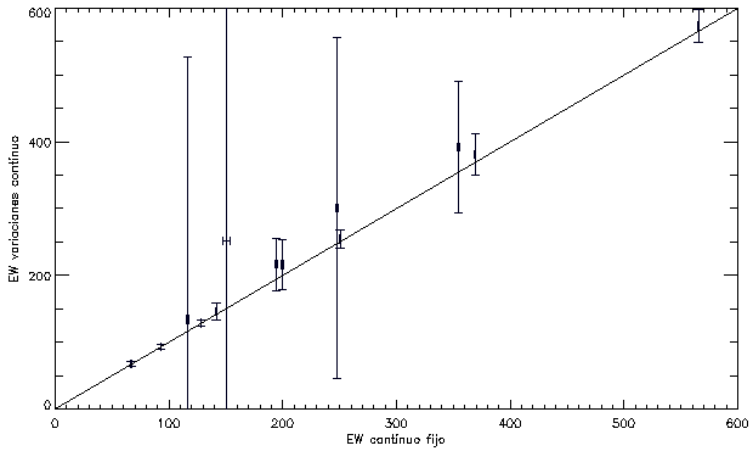

Figure 2.4: Comparison of the real and simulated with Montearlo method EW

In Fig. 2.4 we see as the error has an increment considering variations in the continuum, the size of the error bar depend on the S/N of the spectra, a typical value is of the order of the 10 %.

Photometric Simulations

In last season we studied as the errors in the determination of the EW, determined from an spectrum, depends strongly on the continuum. In this section we will see as the influence of the continuum has not much effect in the results in the case of the EW determined from the photometry.

To estimate the photometric EW, the flux was derived from the magnitude in each band, each with an associated error. The error in the EW was determined using error propagation, from the error values in magnitudes. using the Montecarlo method, we left to the continuum vary randomly with error associates as the maximum variation, then we save the values of the EW in a n dimension vector. We estimate the mean and the standard deviation of the EW from this vector, the mean as the value for the EW and the stander deviation as the systematic error in the measurement. In Fig. 2.5 we show the EW values obtained directly in comparison with the EW obtained with the Montecarlo method, depending on the precision, typical values of the errors are of the order of 5-15%

2.4 Starburst using COSMOS Photometric Catalogue

Only ∼2.8% of objects in COSMOS have spectroscopic redshift. Therefore, the use of the photometric redshift is fundamental to produce a complete catalogue of starburst galaxies. In the following we will describe the color-color selection method used to detect galaxies with EW $\geq$ 80Å in both Hα and [OIII]. We also show how we calibrate the method using the available spectral information.

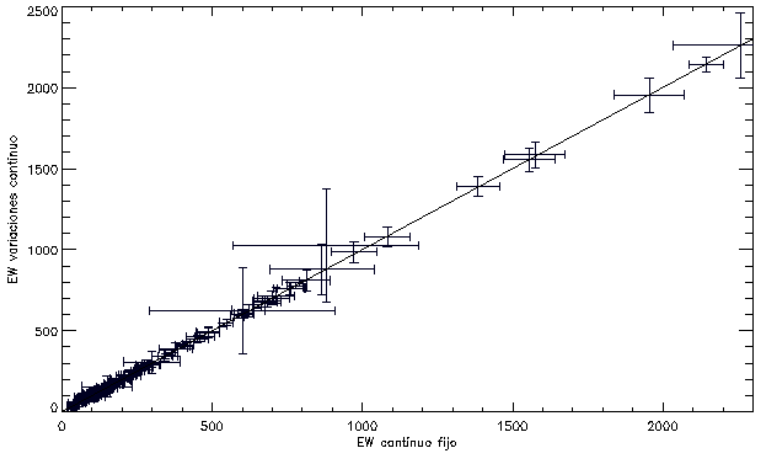

Figure 2.5: Comparison of the real and simulated with Montearlo method EW

2.4.1 Calibration of color-color diagnostics with spectra

Color-color diagrams using narrow/intermediate bands have been successfully used in the past to select sample of emission line galaxies (Sobral et al. 2013). However, the definition of the boundaries between different galaxy type, generally star-forming vs passive, is often subjective and dependent on the characteristics of the objects under study.

In order to calibrate our color-color diagnostic diagram we used the sample of confirmed starburst galaxies in the spectroscopic catalogue (see Section 2.2) as templates to search for a complete sample in the COSMOS photometric sample. These galaxies were selected as starbursts based on their EW in both Hα and [OIII]. We used the spectroscopic redshifts to locate the emission lines in the SUBARU intermediate band filters, also we selected two regions free of lines for the continuum, centered at 5500Å (C5500) as continuum for [OIII] emission line and at 6000Å (C6000) for Hα emission line. With them we constructed color-color diagrams, matching the presence of the corresponding strong line and its continuum. Therefore the colors are constructed such as (Subaru(Hα)-Subaru(C6000) v/s Subaru([OIII])-Subaru(C5500)). Fig. 2.6 shows the transmission of the SUBARU filters with an example starburst galaxy at redshift 0.25. Note that Subaru filters do not homogeneously cover the whole range, instead some gaps can be clearly seen in Fig. 2.6. The redshifts range where we are able to locate simultaneously Hα and [OIII] lines are: $0.123 < z < 0.178$ and $0.23 < z < 0.274$. The total number of galaxies in zCOSMOS within these redshifts are is 580 of which 24 are starburst galaxies. The color-color diagram (Subaru(Hα)-Subaru(C6000) v/s Subaru([OIII])-Subaru(C5500)) is shown in Fig. 2.7a. Galaxies with EW $\geq$ 80Å in both Hα and [OIII], measured from the spectra, are represented by stars. The arrow in the Fig. 2.7a shows the direction of increasing emission line EW. As expected, starburst galaxies populate a well-defined region of the color- color diagram. The use of galaxies with spectra allow us to calibrate the color excess as a function of the emission-line EWs and therefore using the easily accessible photometric data to select starburst galaxies with EW $\geq$ 80Å in both Hα and [OIII].

We use the region where Hα-C6000 $\leq$ -0.35 and [OIII]-C5500 $\leq$ -0.1 (shadow region in Fig. 2.7a) as the one with emission associated to starburst galaxies. This region is used to seek for starburst candidates using the Photometric Redshift Catalogue in the next section.

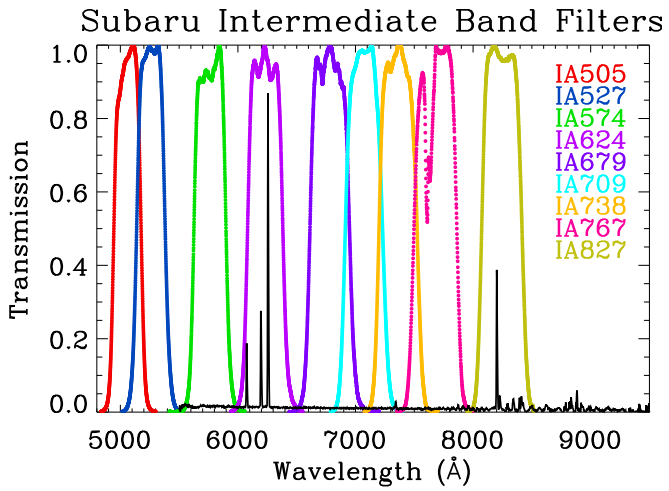

Figure 2.6: Normalized transmission curves of the intermediate-band SUBARU filters used in this study. A representative emission-line galaxy at z = 0.25 is also shown to demonstrate how the filters match simultaneously the positions of the [OIII] and Hα lines. The space between filters determine the wavelength gaps in our photometric sample.

2.4.2 Starburst galaxies using COSMOS photometric redshift catalogue

The photometric redshift allows us to match the Hα and [OIII] emission lines in the Subaru Intermediate band filters in the redshift ranges: $0.007 \leq z \leq 0.074$, $0.124 \leq z \leq 0.177$ and $0.230 \leq z \leq 0.274$. The bands including [OIII], Hα and their respective continuum at 5500Å and 6000Å have been used to build a color-color diagnostic diagram similar to the one for the spectroscopic sample. We limit our sample to galaxies with m(F814W) $\leq$ 23.5. Fainter galaxies have both photometric redshift and intermediate band magnitude errors too large for our analysis. The star symbols in Fig. 2.7a show the galaxies located in the starburst region with EW $\geq$ 80A. In order to estimate the photometric EW we used a filter in the red continuum for [OIII] and in the blue continuum for Hα. Then we used Eq. 2.1 to calculate the EW for both emission lines. In Fig. 2.7b we plot in the color-color diagram defined using the SUBARU filters for all the galaxies in the zCOSMOS catalogue. The star symbols show the locii for the starburst galaxies within the region with EW $\geq$ 80Å.

In Fig. 2.7b a smaller region is shown with a darker shadow, with Hα-C6000 $\leq$ -0.5 and [OIII]-C5500 $\leq$ -0.4. In the larger region, which we used to obtain our sample, only 33% of the photometric EW in Hα or [OIII] are less than 80Å. The smaller region exclusively comprise objects where the photometric EW in both Hα and [OIII] is $>$ 80Å. Table 2.2 shows some of the entries of the photometric emission-line catalogue, constructed using only the galaxies in the selected area (star symbols in Fig. 2.7b). The complete catalogue is available in appendix A.

2.5 Caveats to the sample selection

Several comparisons have been made to assure that our photometric sample is reliable, and to establish possible sources of uncertainty. We have detected inconsistencies in some of the photometric redshift estimations. In order to have a secure sample, other criteria have been used to filter our sample; galaxies with Hα emission-line only (without [OIII]), have been identified in Fig. 2.7b (see horizontal branch with 0<[OIII]-C5500<-0.5) and discarded. Comparing photometric and spectroscopic redshifts we have detected some inconsistencies in the photometric red- shift estimation for z

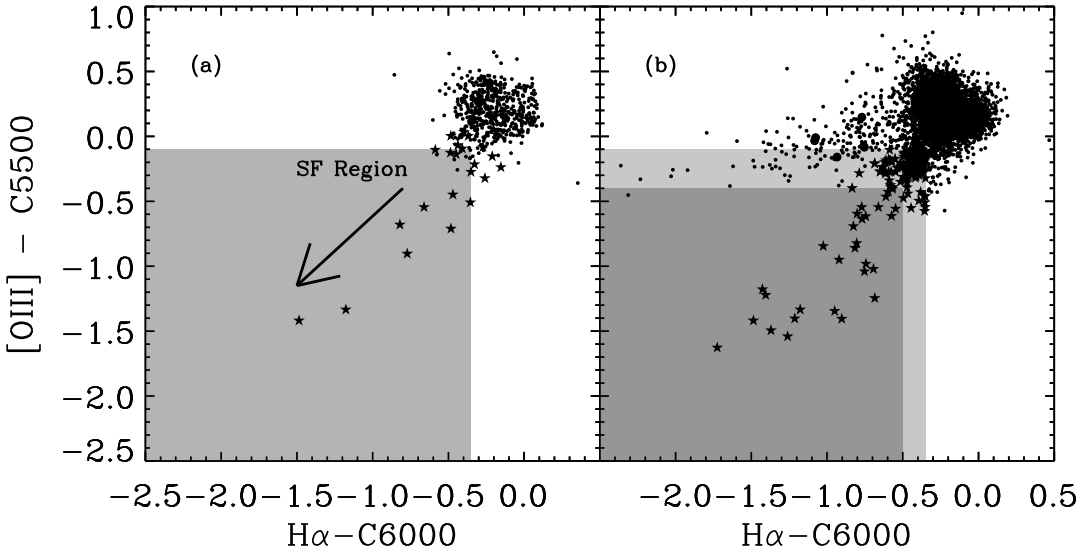

Figure 2.7: a) Color-color diagram of the 580 galaxies in zCOSMOS measured with SUBARU filters. Star symbols show the galaxies with EW $\geq$ 80Å in both Hα and [OIII], the arrow points the direction of galaxies with larger EW in both emission lines. Shadowed region in the diagram is the starburst location. b) Color-color diagram for galaxies in the photometric redshift catalogue in the redshift ranges: $0.007 \leq z \leq 0.074$, $0.124 \leq z \leq 0.177$, and $0.230 \leq z \leq 0.274$. Star symbols show the galaxies in the star-forming region defined in panel (a). We discarded galaxies with high Hα and low [OIII] emission. A subregion is showed in which the photometric EW in Hα and [OIII] is larger than 80Å for the complete sample.

≤ 0.1. As the colors shown in the diagram use the photometric redshift, the diagram is also useful to detect inconsistencies in zphot for emission-line galaxies. For these galaxies at z ≤ 0.1, the photometric redshift confused [OII] with [OIII], and [OIII] with Hα emission lines. This problem, known as "catastrophic redshift", was reported in (Ilbert et al. 2008, their Fig. 1). In summary, since we look for starburst galaxies showing simultaneously Hα and [OIII], when discarding galaxies in the color-color diagram with high Hα and low [OIII], we automatically remove galaxies with wrong photometric redshift determinations.

Altogether, in COSMOS we have identified a total number of 289 starburst galaxies with EW $\geq$ 80 Åin Hα and [OIII], either from the photometric or spectroscopic catalogues. From this sample, a total of 69 objects were rejected after a careful visual inspection. Fig. 2.8 shows some examples of fake detections, galaxies saturated by a close star, galaxies at the limit of our detection threshold, and HII regions of foreground spiral galaxies that were removed from the final sample. Our final catalogue contains 220 starburst galaxies. In Fig. 2.9 (left) we show the distribution in redshift for our sample including the gaps in redshift for the photometric sample. In Fig. 2.9 (right) the percentage of photometric and spectroscopic sample, with respect to the total number of objects in COSMOS, is shown. As it can be seen, the distribution in redshift in our sample is not homogeneous (as a consequence, our sample distribution has not a perfect completitude).

2.6 K-correction and stellar mass determination

In this section we computed the stellar masses for the 220 starburst galaxies of the sample. In order to account for redshift effects in the flux measurements for every filter of the photometric catalogue, we first calculated the K-correction for each galaxies. We used the last version of K-correct [3] (Blanton

[3] http://howdy.physics.nyu.edu/index.php/Kcorrect

Table 2.2: Starburst galaxies selected from the photometric redshift catalogue.

object	redshift	EW(Hα) [Å]	EW([OIII]) [Å]
cosmos-001	0.27	760 ± 46	770 ± 43
cosmos-004	0.26	119 ± 26	171 ± 26
cosmos-005	0.26	94 ± 10	182 ± 11
cosmos-006	0.26	124 ± 11	125 ± 10
cosmos-007	0.26	108 ± 19	112 ± 16
cosmos-008	0.16	110 ± 34	60 ± 30
cosmos-009	0.06	28 ± 10	109 ± 11
cosmos-011	0.26	351 ± 13	568 ± 16
cosmos-012	0.01	114 ± 7	55 ± 5
cosmos-013	0.26	114 ± 27	181 ± 26

Notes. (1) (1) Object name (ordered by RA), (2) photometric redshift, (3) Hα EW and (4) [OIII] EW.

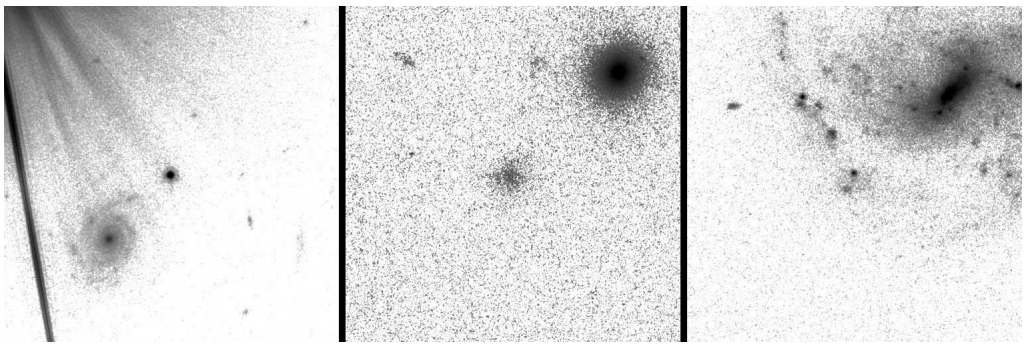

Figure 2.8: HST images with some examples of sources discarded after visual inspection. Left: saturated by a close star. Middle: galaxies at the limit of our detection threshold. Right: HII region of a foreground spiral galaxy.

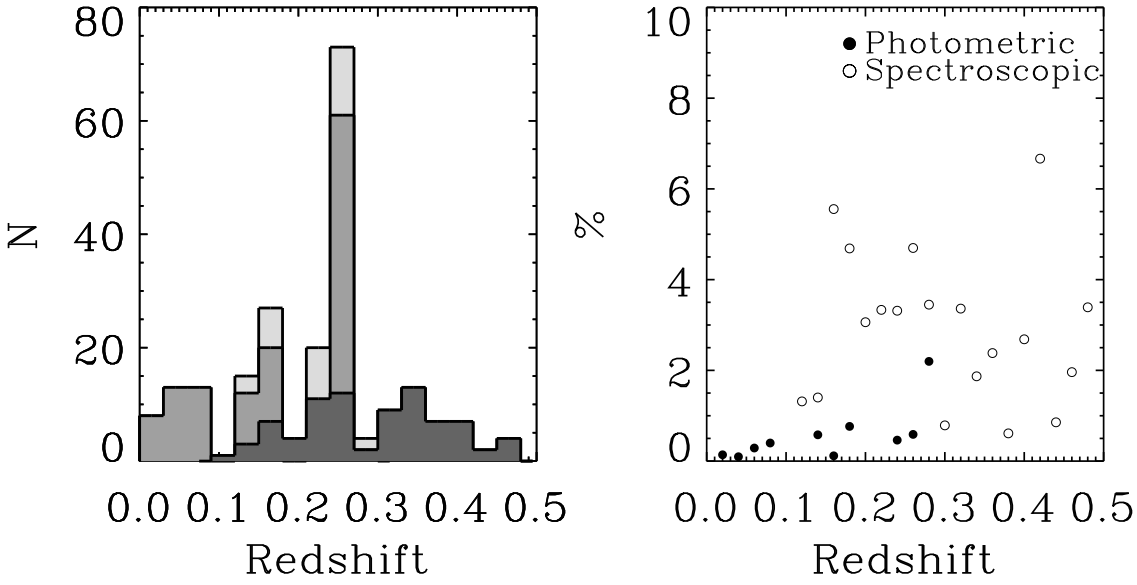

Figure 2.9: Left: Redshift distribution of the photometric (grey), spectroscopic (dark grey) and total (light grey) sample. Right: Percentage of starburst galaxies found in COSMOS, with respect to the total analyzed galaxies in different redshifts. The photometric sample is showed in filled circles, and the spectroscopic sample in open circles.

& Roweis 2007). This software use a basis set of 485 spectral templates, 450 of these are a set of instantaneous bursts from (Bruzual & Charlot 2003) models using the (Chabrier 2003) stellar initial mass function and the Padova 1994 isochrones (Alongi et al. 1991), the remaining 35 templates are from MAPPINGS-III (Kewley et al. 2001) which are models of emission from ionized gas, a crucial feature appearing in the galaxies in our sample. All our galaxies are in the Photometric Redshift Catalogue and have been mapped by COSMOS using 10 bands ($U, B, V, g, R, I, F814W, z, J$, and K), in some cases the magnitude in one of the bands was not available ($\sim$10%), the most of cases was for $K-$band, in those cases the K-correction was calculated using 9 bands. In our catalogue (Table 3) every magnitude and color are in rest frame.

We have visually analyzed every Spectral Energy Distribution (SED) of the sample to check that they are blue Emission Line Galaxies. To estimate the goodness of the fit we have defined the "goodness parameter (G)" which is expressed as $\sum(F_t - F_m)^2/F_t^2$ where F_t is the flux of the template at the wavelength of the filter and F_m is the measured flux in the filter from COSMOS. The G parameter is given in Table (galaxies-table). The best fits from K-correct show some features like blue galaxies Balmer break in the continuum and strong emission lines. In two cases the galaxies does not have those features and the fit is very poor (G very high), they appear with a value of 99 in Table 3.

The K-correct software provides also information about the stellar masses of galaxies, these are published in appendix A and are in the range $10^5 < M/M_\odot < 10^{11}$. It is worth noticing that our selection criteria does not introduce any bias on the mass distribution. The low-mass end of our mass distribution is given by the observational limits (mF814W $\leq$ 23.5) whereas the limited volume probed by the COSMOS survey produces the high-mass end. For the sake of comparison, we also computed stellar masses using the equations provided by (Bell & de Jong 2001). They use a suite of simplified spectrophotometric spiral galaxies, with SF burst, to calculate the stellar mass to luminosity ratio using colors and assuming a universal scaled Salpeter IMF. To apply these equations we used independents three colors, with magnitudes previously K-corrected, to calculate the stellar mass and to check the robustness of our results. The results are consistent with the mass

obtained with Kcorrect. Fig. 2.10 (left panel) shows the comparison between the stellar mass from K-correct and Bell & de Jong (2001); both methods to calculate the galaxy mass are consistent. Fig. 2.10 (middle panel) shows the mass distribution of the starburst galaxies determined with K-correct. Most of them are in the 10^8-10^9 $M_\odot$ range. For comparison, we also computed the stellar masses of the whole COSMOS sample with $z < 0.3$ and m(F814W)<23.5 (8650 galaxies) using the K-correct algorithm. The result is shown in Fig. 2.10 (right panel) were both distributions are plot. It is clear that the number of galaxies in the COSMOS volume at this redshift range peaks at $M/M_\odot \sim 2{\times}10^8$ with only a few galaxies with $M/M_\odot > 10^{10}$. The shape of the mass distribution is actually very similar to that of the starburst galaxies with maybe an excess of galaxies in the high-mass end. We suggest that this excess could be related to more red, elliptical-like galaxies dominating this region of the mass function.

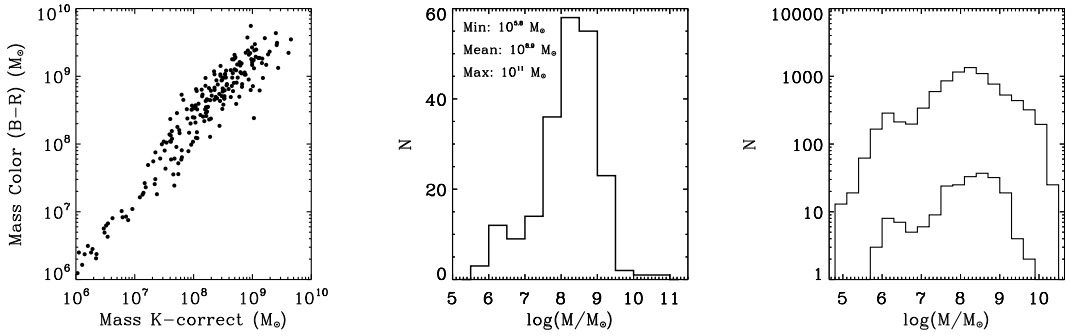

Figure 2.10: Left panel: Comparison of stellar masses estimated from the K-correct software fitting the galaxy SED, and the $B - R$ color using the prescription by Bell & de Jong (2001). Middle panel: Stellar mass distribution of the starburst galaxy sample, determined with K-correct. Right panel: Stellar mass distribution for both the entire COSMOS galaxy sample with $z < 0.3$ and m(F814W)<23.5 and the starburst identified in our paper (in logarithmic scale).

2.7 Results and Discussion

In this chapter we present an extensive, systematic, and multi-band search of starburst galaxies at redshift ($0 > z > 0.5$) in the COSMOS field. We have selected a sample of young starburst galaxies using a new tailor-made color-color diagnostic. Our methodology is based on tracing the simultaneous presence of Hα and [OIII] emission lines in the galaxies using the intermediate-band filters provided by the SUBARU telescope.

We have performed a thoroughful calibration of the color-color diagnostic by means of comparison with the spectra available in the zCOSMOS database. We have demonstrated that starburst galaxies with EW>80 Å in both Hα and [OIII] can be clearly identified in a particular loci of our diagnostic diagram.

The final catalogue presented in this chapter consists of 220 starburst galaxies. A compilation of the main parameters for the entire sample is presented in Appendix 1. The starburst sample has been identified by using both the spectra from the zCOSMOS catalogue in the redshift range $0.1 \leq z \leq 0.48$ (82 galaxies), and the photometric redshift catalogue using the SUBARU intermediate band filters in the redshift ranges $0.007 \leq z \leq 0.074$, $0.124 \leq z \leq 0.177$ and $0.23 \leq z \leq 0.274$ (138 galaxies).

The stellar masses of the galaxies were calculated using photometric data from the COSMOS database using the K-correct software. The mean and maximum mass of the starburst galaxies are $10^{8.9}$ $M_\odot$ and 10^{11} $M_\odot$. We have compared this distribution with that obtained for the whole sample of galaxies in COSMOS at the same redshift range. The resulting mean mass is 10^9 with

a (similar) lack of galaxies with $M/M_{\odot} > 10^{10}$. Therefore, the mass distribution of the starburst galaxies follows the same distribution as the whole sample of galaxies in COSMOS.

The starburst sample described in this chapter represents a benchmark sample for studies of the star-formation activity in the redshift range $0 < z < 0.5$. Up to $z < 0.3$, the photometric nature of our search implies a nearly complete sample of starburst galaxies, making it ideal for statistical studies. The current sample constitutes the basis of the next chapter, where new methodologies to analyze their physical properties have been devised and applied.

Chapter 3

Galaxies and Star-forming regions Properties

Numerical simulations predict that, at high redshift, starburst galaxies present irregular morphologies. Following these ideas, observational studies of clumpy galaxies have been performed using mainly high-redshift samples ($z > 1$). Deep, high-redshift surveys have been proven to be the key for studying the evolution of disk galaxies, with investigations spanning from the characterization and precise study of the SF knots (clumps), to their relation to the host galaxies. However, these high-redshift studies are usually severely limited by the spatial resolution of the images, even when using space-based observations with the HST Advanced Camera for Surveys (ACS). At lower redshift, studies have been mostly restricted to spectroscopic samples. We aim to bridge the gap between high-redshift galaxy studies and those in the local Universe by providing an accurate characterization of starburst galaxies at intermediate redshift, to constraint models of disk galaxy formation.

The structure of this chapter is as follows: In Section 3.1 we analyze the morphology of the galaxies, and derive the properties of the starburst knots using the HST images. Section 3.2 presents the properties of the galaxies and star-forming regions. The comparison with high-redshift galaxies is also shown. In Section **??** we provide the conclusions. A standard ΛCDM cosmology with Ω_m=0.27, Ω_Λ=0.71, and H_0=0.7 is adopted throughout this chapter.

3.1 Morphology of the Starburst galaxies

The COSMOS field has been targeted by the HST ACS camera with the F814W filter (Capak et al. 2007), this filter is centered at λ_c=8037 Å and its wavelength width is $\Delta\lambda$=1862 Å.

The F814W HST ACS high resolution images of the sample (220 galaxies), with a Full Width at Half Maximum (FWHM) of the Point Spread Function (PSF) of 0.09" and a pixel scale of 0.03"/pixel, are available in the IRSA's General Catalogue Search Service [1] and have been analyzed to identify morphological structures. A semiautomatic protocol was designed to this aim. We downloaded the images with a size of 15"x15" centered in our targets coordinates. Most galaxies are smaller than this size (see Fig. 3.1 as an example), however we found that 26 are larger than the downloaded images and they were analyzed individually. We use Source-Extractor[2] (sextractor1996) to obtain the coordinates of the galaxies and put them in the center of the images. To perform a detailed analysis, particularly to identify sub-structures like star forming regions in starburst

[1] http://irsa.ipac.caltech.edu/data/COSMOS/index_cutouts.html
[2] http://www.astromatic.net/software/sextractor

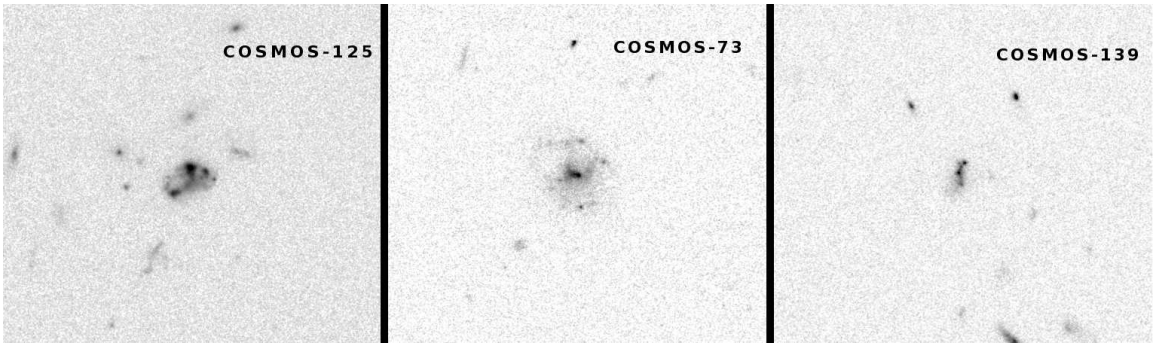

Figure 3.1: F814W HST/ACS 15"×15" high resolution images of three identified Starburst galaxies.

galaxies, we used Faint Object Classification and Analysis System (FOCAS[3]), this program offer a splitting routine which deal well with galaxy compounds.

With SExtractor we define the extension area of the galaxy. For this, throughout an iterative process, the background on the images were determined to afterwards identify objects with a signal higher or equal than three times this value. The minimal area to be considered was imposed to be 3 × FWHM of the HST ACS images to avoid the detection of spurious sources such as hot pixels and cosmic rays.

At this step different parameters are calculated for the detected objects. In particular we measured the central position and the equivalent radius, i.e., the radius of a circle with the same area than the covered for the pixels associated to the object. Then the galaxy is relocated in the center of the image using the new position and the image is resized to eight times its equivalent radius. The outermost isophote was used to obtain the flux of the galaxies, ellipticity and radius, with these quantities complemented with information from the COSMOS database we derived several parameters of the galaxies, some few entries are given in Table 3, the complete catalogue is available online.

3.1.1 Surface brightness analysis and photometry

With the resized and centered images we made an isophotal analysis with FOCAS. First, we calculated the background σ which is assumed to be constant along the image, then the objects are identified where the count level is above 3 times this value. We used the new position calculated for the objects to identify our target and separate it from other spurious sources that may be present in the field. For doing so, we define an area centered in the object and enclosed by an isophote with signal above $3\times\sigma$ (see Fig. 3.2, left panel). As a result, for each catalogued source we obtain, coordinates of the central position (maximum), total flux, nearby background, surface brightness, equivalent radius and ellipticity. In Table 3 we show the magnitude and absolute magnitude, luminous radius, colors and their errors, luminosities in Hα and [OIII] and their errors, equivalent widths in Hα and [OIII], surface brightness, ellipticity, and mass for each galaxy.

3.1.2 Resolved star-forming regions and diffuse emission

From visual inspection of the galaxies, different star-forming knots embedded in the more diffuse and extended emission are clearly visible in the galaxy images. Further analysis was carried out with FOCAS with the aim of parametrizing such structures. For doing so, we find signal over the diffuse emission of the galaxies, looking for individual regions. Besides, some regions may be overlapped and then a criteria has to be defined to separate them. The splitting of merged regions is

[3]http://iraf.noao.edu/ftp/docs//focas/focas.ps.Z

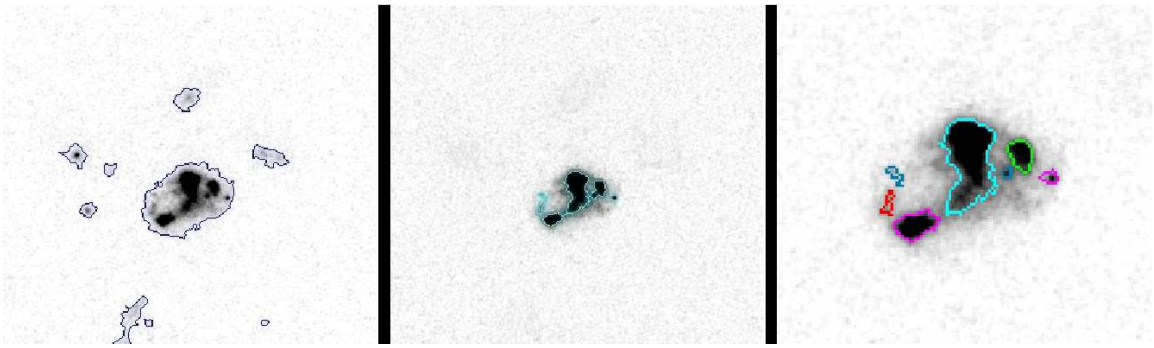

Figure 3.2: F814W HST/ACS images. Example of the procedure to identify SF knots. Left: First isophotal analysis, where the principal objects in the image are defined. Middle: Second isophotal analysis of the target galaxy, where substructures are found. Right: A zoom of the image in the middle. For clarity the detected regions are showed with different colors.

done using two main parameters: a minimal area according to the FWHM of the PSF and a signal threshold. The signal threshold has to be 3 σ the local background, which is computed iteratively from pixels that are not part of the object (see Valdes 1982, Sect. 4). A loop is entered incrementing the detection threshold level 0.2$\times\sigma$ every time, if in some level of the loop there are more than one region the analysis continue individually, the loop finish when the peak of every region is reached.

In Fig. 3.2 the process to identify substructures is shown. The left panel is the resized image with the objects detected (first isophotal analysis) in the field, with our target in the center. The middle panel shows the image with external sources in the field removed. Subregions detected within the target are overplotted. The right panel is a zoom of the middle image. Regions with a radius bigger or equal to the PSF (0.09") will be identified as subregions or knots.

All starburst galaxies in our sample were morphologically classified based on this isophotal analysis as follows: Sknot, when it consists of a single knot of star formation; Mknots, when several knots of star formation are identified within the galaxy size; Sknot+diffuse, if the single knot is surrounded by diffuse emission. Fig. 3.3 shows examples of the three morphological classes.

The F814W filter was used for the morphological classification. This assure the Hα emission is covered by the filter for all galaxies in our sample with z >1. At lower redshift, the clumpy morphological features will be detected by the continuum excess associated of the star-forming regions. The redshift distribution of the different starburst classes is presented in Fig. 3.4. They display very similar trends and they are also in good agreement with the redshift distribution for the whole sample (see Fig. 2.9). Therefore, we consider the filter bandpass is not severely limiting our study.

We measured different parameters for each substructure: area, flux, magnitude, luminous radius and ellipticity. The luminous radius was determined assuming circular symmetry for the isophotes, this is a good approximation for the core of compact star-forming knots. Fig. 3.5 shows the size distribution of galaxies and knots, the typical radius for the galaxies, sknots, sknot+diffuse and mknots are: 1-3, 1-2, 0.5-1.5 and 0.5-1.0 (kpc) (see panels a and b in figure).

In Table 4 we summarize the parameters of the knots in the starburst galaxies. As explained above they are catalogued as sknot, sknot+diffuse and mknot. When there are more than one knot in a galaxy they are sorted for their Hα luminosity from higher to lower values. The diffuse luminosity of every clump is obtained from the diffuse light considering the area of the knot, the mass is calculated using $B-R$ color using the prescriptions of (Bell & de Jong 2001) assuming the same color for the knots and its host galaxy. Distance to the center, radius and ellipticity were

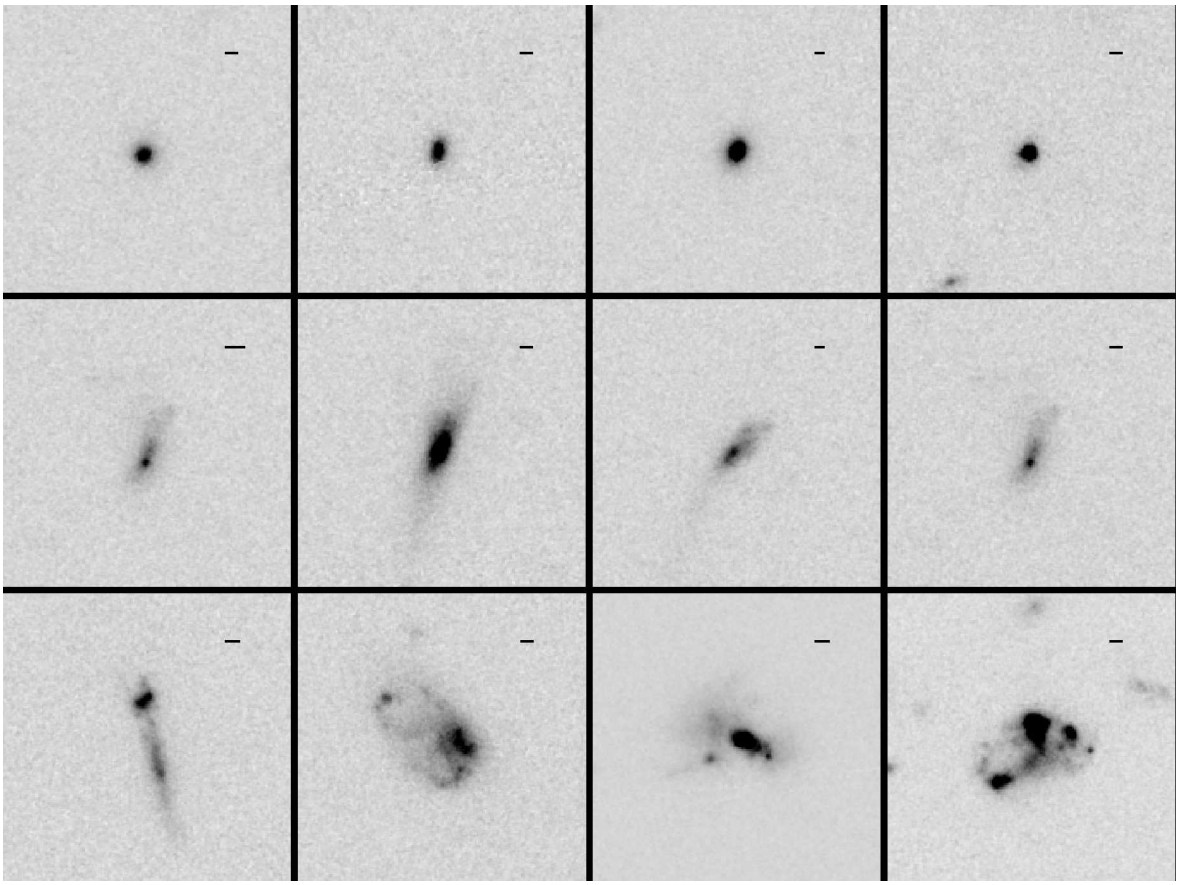

Figure 3.3: Example of the starburst morphological classes in our sample, a 1 kpc bar is showed at the top right of each image. Sknot galaxies (top row), Sknot+diffuse galaxies (middle row), and Mknots galaxies (bottom row).

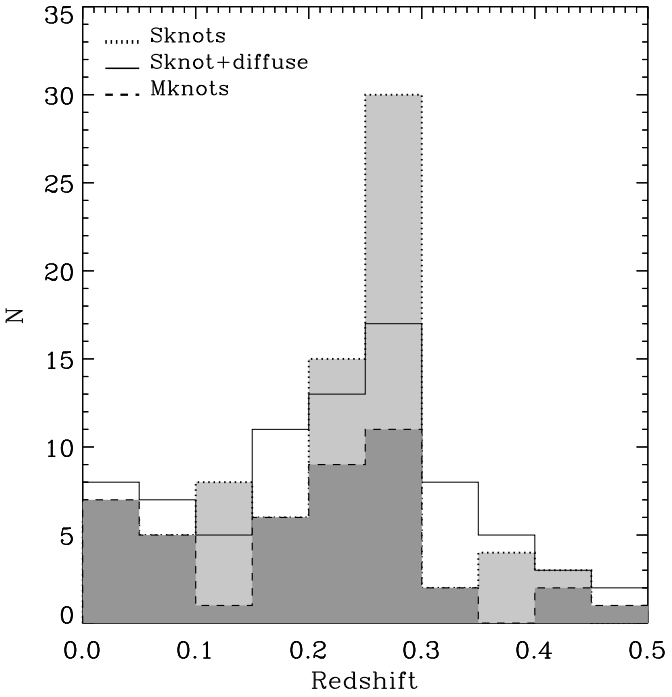

Figure 3.4: Redshift distribution for the three starburst morphological classes defined in this paper: Sknot galaxies (light grey), Sknot+diffuse galaxies (empty histogram), and Mknots galaxies (dark grey).

determined with the isophotal analysis.

In Fig. 3.6 we show the ellipticity of the galaxies for the different morphologies: sknot, mknot, and sknot+diffuse. It can be note that "sknot" galaxies are quite roundish with a mean ellipticity around 0.4. Galaxies with single knot and diffuse light and those with multiple knots are more elongated with mean ellipticities of 0.63 and 0.65, respectively.

3.1.3 Spatial distribution of the star-forming knots in the galaxies

The galaxy centers were calculated with SExtractor using the barycenter of the emission within the outer isophote; the center of the knots corresponds to the maximum luminosity of the isophote, and their radii are the equivalent to a circular shape of the isophotal area. All the projected linear scales have a resolution of 0.09" (limited by the PSF). Fig. 3.7 shows the distance to the center for each knot versus its radius. A bisector separates the knots in two classes. Knots in the upper zone (opened circles) are knots which are off-centered, whereas in the lower region (filled circles) the knots overlaps with the geometrical center of the galaxy. We call them offcenter and lopsided respectively. It is worth noting that those knots whose distance to the center is lower than their size - taking into account the spatial resolution of the HST - have been labelled as centered and plotted with a square symbol.

Fig. 3.8 shows the size distribution of the knots. Solid, dotted and dashed lines show the distribution of offcenter, lopsided and centered knots. Offcenter knots are the smaller and more abundant, lopsided and centered are generally larger but they also span a wider range in sizes. The mean radius value are 0.1, 0.5, and 2.1 kpc for offcenter, lopsided and centered knots and the mean

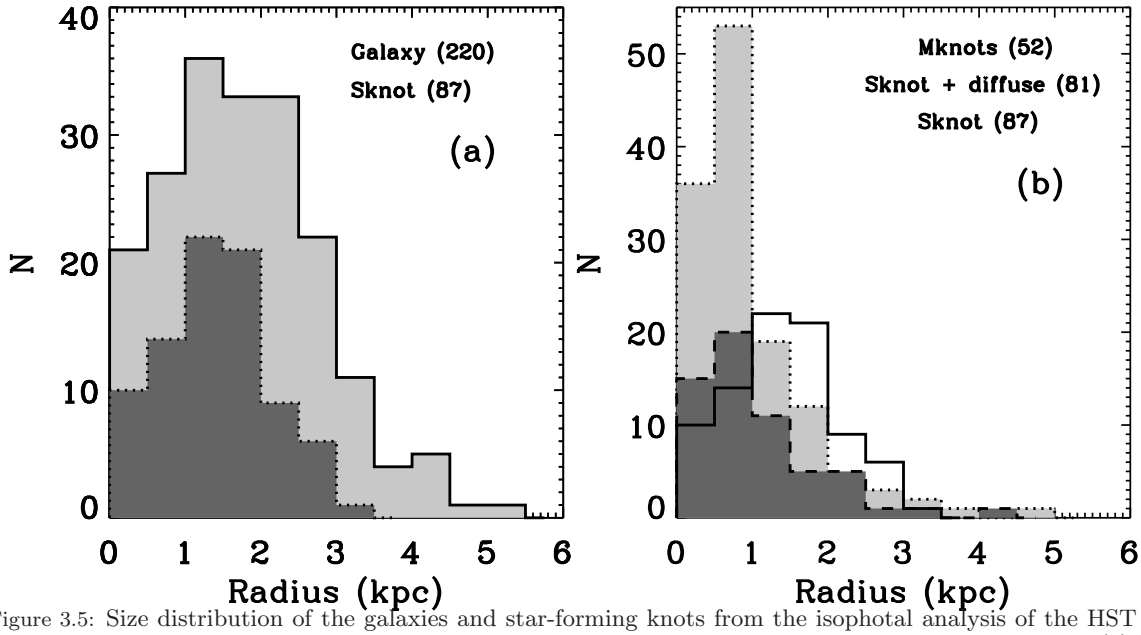

Figure 3.5: Size distribution of the galaxies and star-forming knots from the isophotal analysis of the HST high spatial resolution F814W images. Circular symmetry is assumed to estimate the radius. Panel (a), the distribution of both the total sample and Sknot galaxies is shown in light grey and grey, respectively. Panel (b), the distribution of knots in Mknot galaxies, Sknot+diffuse galaxies, and Sknot galaxies is shown in light grey, grey, and empty histogram.

distance to the center are 1.3, 1.4 and 0.6 kpc, respectively.

3.1.4 Mass and SFR estimation of the star-forming knots

Individual star-forming knots/clumps in our galaxy sample cannot be resolved using the broad-band imaging provided by the SUBARU telescope. Therefore, in order to estimate their masses using the prescriptions given by Bell & de Jong (2001, see Sect. 2.6), we need to rely on the HST imaging. Unfortunately, the COSMOS field is only covered in its entirety by the F814W filter, so a clump-scale color is not directly accessible from the observations. In order to overcome this problem we assumed that the knots and the host galaxy have the same color. Then, we used the F814W-band images to measure the luminosity of the individual knots and the SUBARU color to derive their corresponding masses.

To test the influence of our color hypothesis in the derived knot masses we carried out a search for our starburst galaxies in other multi-band HST surveys such as CANDELS (Grogin et al. 2011; Koekemoer et al. 2011) and 3D-HST (Brammer et al. 2012) surveys. The idea behind this search is to properly compare the colors of the whole galaxy with those of the individual clumps. Whether a relation will be found, this could help us to calibrate the colors of the remaining knots in order to derive more accurate stellar masses. The main drawback of this approach is that the CANDELS/3D-HST surveys only cover a small area of the full COSMOS footprint. Despite this, we found 11 starburst galaxies from our catalogue in those databases. Four of these galaxies are classified in our paper as Sknot+diffuse or Mknots galaxies, with a total of 12 knots/clumps of star formation

In this work, we used the $B-R$ color combined with the $I-$band magnitude to estimate the mass of the knots. Using the CANDELS filters we gain access to the F606W filter that we can combine with the COSMOS F814W to build a color similar to the standard $V-I$. We measured the F606W luminosity of the individual knots using the same apertures as for the F814W filter. The PSF difference between these two bands is negligible when compared to the area of the measured

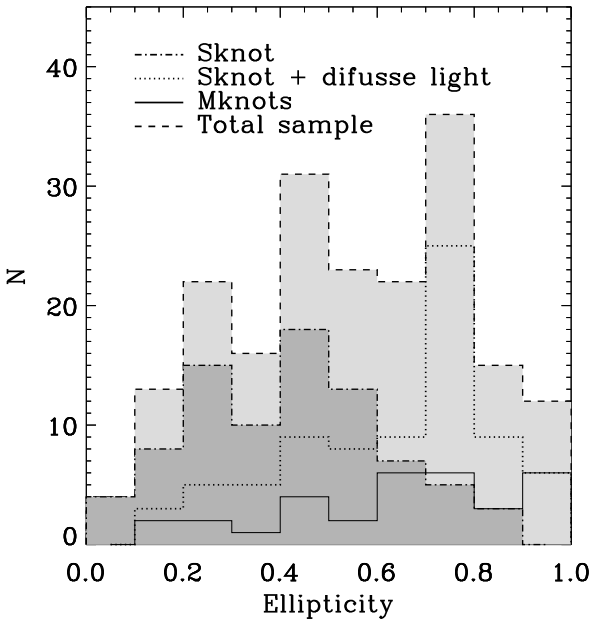

Figure 3.6: Distribution of ellipticity of the host galaxies, four cases are considered: galaxies with Sknot, Sknot+diffuse, Mknots and the total sample.

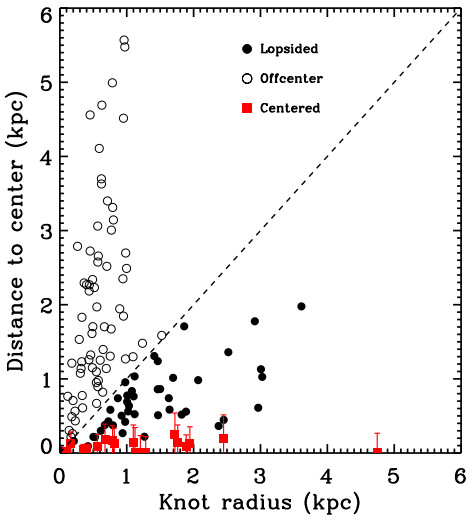

Figure 3.7: Knot sizes versus their distance to the center of the galaxy. From the diagram we separate three classes: offcenter (open circles), lopsided (filled circles) and centered (red squares with error bars) regions. A bisector separates two regions. Filled circles show regions in contact with the center of the galaxy and open circles show regions offcentered. Regions which overlap with the geometrical center of the galaxy are labeled "centered" and represented with squared symbols. Overplot bars account for the spatial resolution.

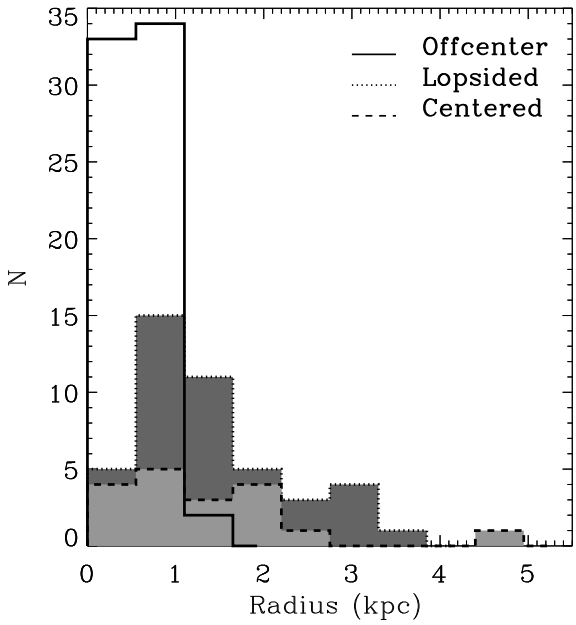

Figure 3.8: Size distribution of knots, as identified in Section 3.1.2. Solid (empty), dotted (dark grey) and dashed (light grey) lines show the size distribution of offcenter, lopsided, and centered knots. The largest star-forming knots are located in the central regions of the galaxy.

knots so further convolution steps were not necessary.

Figure 3.9 shows the comparison of the F606W-F814W (equivalent to $V-I$) rest-frame color for all the knots in the CANDELS survey ($x-$axis) and the corresponding host galaxy ($y-$axis). We used different symbols for each one of the four galaxies. This figure clearly shows how in our small sample, the starburst galaxies span a very narrow range of colors whereas the star-forming knots cover a broader range, from relatively red colors to very blue ones. To state this point more clear, in Fig. 3.10 we represent the distribution of colors for the knots (solid line) and the galaxies (dotted line). We found that, despite the variety of colors probed by knots and galaxies, they both have a similar mean color value. We fitted a simple Gaussian to the color distribution of the knot resulting a mean color (F606W-F814W) = 0.11 and σ =0.5. The mean value of the galaxy colors (F606W-F814W) is 0.14. Therefore we can conclude that the mean colors of individual knots and the whole galaxy are the similar.

Can we use the $V-I$ galaxy color as a proxy for the knot color?

Unfortunately, our previous result is based on a small subsample of starburst galaxies. Thus, in order to get a more conclusive answer to this question we look for similar studies in the literature. In particular we carefully read the two papers suggested by the referee -Wuyts et al. (2012) and Guo et al. (2012)- which we found very useful. Interestingly, we find support to our aforementioned result in both papers.

Wuyts et al. (2012) used four different strategies to separate center, disk, and clump regions in "emission–line" galaxies. The different methods were based on the identification of the galaxy regions using the surface brightness distribution of the normalized rest-frame 2800Å, $U-$band, $V-$band, and stellar mass, respectively. Since our detection band is based in the F814W filter,

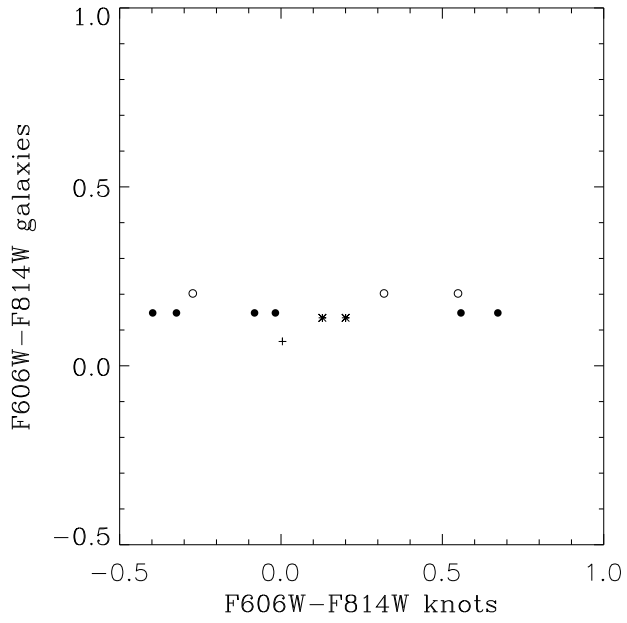

Figure 3.9: F606W-F814W rest-frame color for individual knots ($x-$axis) and the whole galaxy ($y-$axis). Different symbols represent different galaxies.

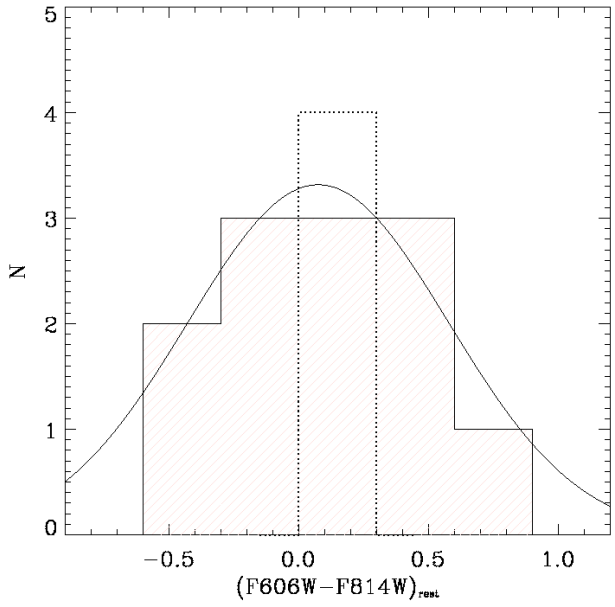

Figure 3.10: F606W-F814W rest-frame color distribution for individual knots (solid line) and the whole galaxies (dotted line). The Gaussian overplot shows the best fit to the colors distribution of the knots.

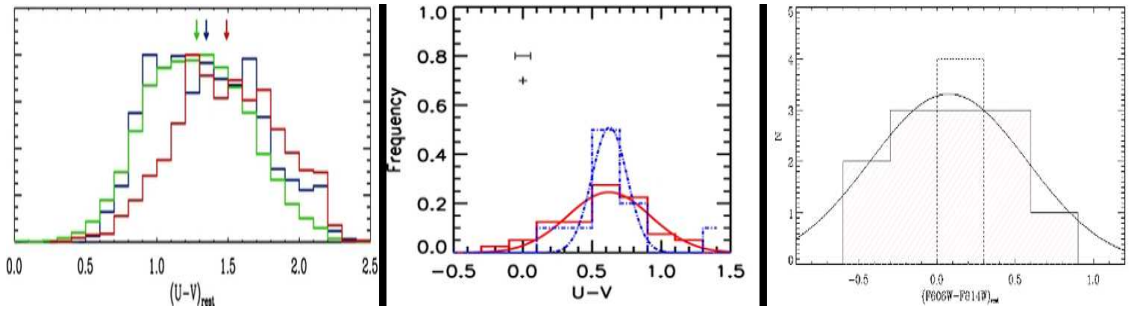

Figure 3.11: Distribution of both knot/clump and galaxy colors in different samples of the literature. Left: $U-V$ rest-frame color distribution using a surface mass density identification (Wuyts et al. 2012). Disk regions are shown in green and clump regions in blue. Middle: $U-V$ color distribution using a $z-$band identification (Guo et al. 2012). Disks are represented in blue and clumps in red. Right: F606W-F814W rest-frame color distribution using a F814W identification (this work), as in Fig. 3.10 of this report.

which roughly corresponds to $R-$band rest-frame, we consider the stellar mass detection the one closer to our methodology. In their Fig. 6 (see also Fig. 3.11) they show the $U-V$ rest-frame color distribution for the three different regions center, disk, and clumps. They claim that no difference in color is found between disk and clump regions when this detection method is used. This is in good agreement and provides additional support to our result with their -larger- sample of 323 star forming galaxies at higher z.

Guo et al. (2012) found also a similar result using a sample of 40 clumps detected using $z-$band images. Their methodology is very similar to the one used in our paper. In their Fig. 5 (see also Fig. 3.11) they compared the colors of the detected clumps with those of their surrounding disks. They claimed that the mean $U-V$ color of clumps is similar to that of disks, with the color distribution of clumps being broader. This result is remarkable in agreement with our previous one.

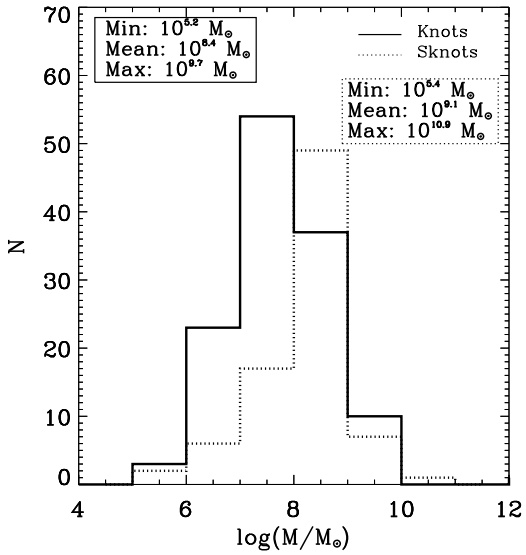

Figure 3.12: Mass distribution of the knots in Sknot+diffuse and Mknots galaxies (solid line) and Sknot galaxies (dashed line). The statistics for each kind of knots are given in the boxes with the same line code.

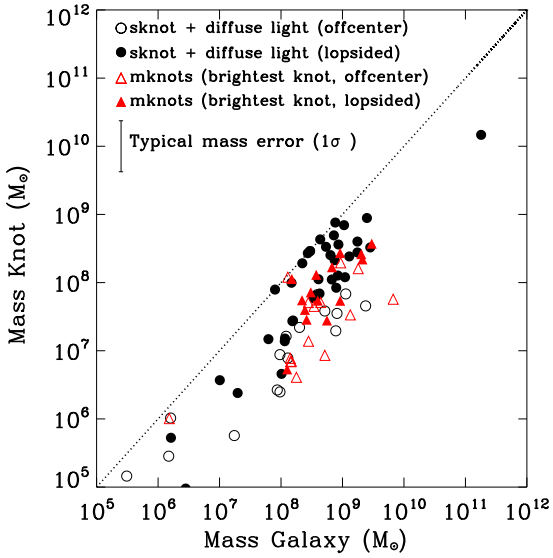

Figure 3.13: Comparison of masses of the knots with that of their host galaxies. Symbols represent the different morphologies (code inserted): One knot plus diffuse light, and the brightest knot in multiple knot galaxies. Sknot galaxies are not represented, as they would follow the bisector.

Fig. 3.11 shows the color distribution of knots/clumps and galaxies in Wuyts et al. (2012), Guo et al (2012), and this work, respectively. This figure summarizes our main conclusion, i.e., the mean color of the star-forming knots and their host galaxy is very similar. The color distribution of the knots colors is broader than that of the host galaxy. Note that our dispersion value of $\sigma \sim 0.5$ is also in good agreement with the previous studies discussed here.

For the sake of comparison, we have also compared the $U - V$ colors from our sample using the SUBARU broad-band photometry for the whole galaxy. We confirmed that we are probing the same range of colors as those in Wuyts et al. (2012). However, we decided to use the $V - I$ colors since the F814W band is our main detection filter.

Another possible caveat on our knot mass determination might be the use of different band-passes affecting our results. In order to estimate how accurate is this approximation we use our sample of Sknot galaxies. These starburst galaxies do not contain diffuse light and, therefore, the measurement using the higher resolution HST images should agree with those from the ground-based SUBARU photometry. We calculated the mass of the galaxies using the M/L ratio (Bell & de Jong 2001) with the $B - R$ color (the less affected by the background galaxy), and the luminosity in the SUBARU $I-$band and HST/ACS F814W-band with a fixed aperture of 3" (COSMOS catalogue). We find an excellent agreement between both measurements.

The masses of the knots and their corresponding errors are provided in appendix B and represented in Fig. 3.12. The mean mass for knots in Sknot+diffuse and Mknots galaxies in $10^{8.4}$ $M_{\odot}$. The minimum and maximum are $10^{5.1}$ and $10^{9.7}$ $M_{\odot}$, respectively. We also show the mass distribution of the single knot galaxies (dashed line). We compute a mean mass for Sknots of $10^{9.1}$ $M_{\odot}$, 5 times larger than the mean of knots in Sknot+diffuse and Mknots galaxies. For Sknot+diffuse and Mknots, we compare the masses and sizes of the knots and the galaxies. The comparison of the mass is shown in Fig. 3.13.

The Hα luminosity of the different star-forming galaxies in our sample was estimated following different strategies. Sknot do not require the HST/ACS spatial resolution to be measured. Therefore,

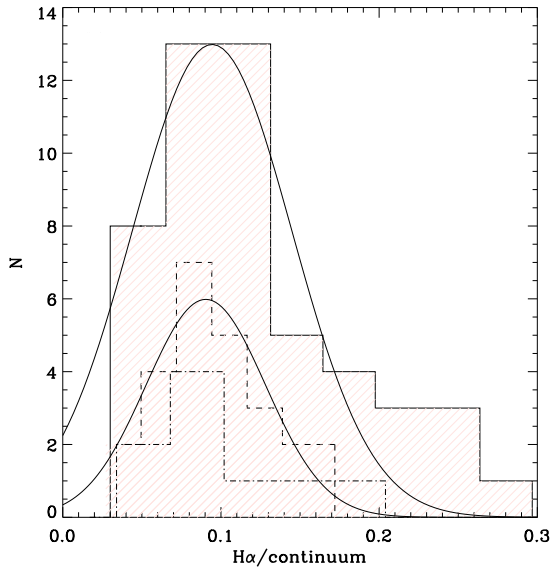

Figure 3.14: Hα/continuum distribution for galaxies in our sample with spectra in zCOSMOS. Different lines show: the distribution of the 51 Sknot+diffuse and Mknots galaxies (solid line) with a fitted Gaussian profile overplot; the distribution of a subsample of 9 galaxies with bright knots (dot–dashed line)- its luminosity twice or more that of the host galaxy, and the distribution of the 25 Sknot galaxies (dashed line) with the fit with a Gaussian overplot.

we used the SUBARU intermediate filters to determine the luminosity in Hα and continuum regions. Using these filters we were able to trace the Hα emission in the redshift ranges $0.01 \leq z \leq 0.2$ and $0.23 \leq z \leq 0.28$. 20 Sknot galaxies in our sample are in this redshift range, and nine of them have spectra in zCOSMOS. We used the difference between photometric and spectroscopic Hα luminosity of these galaxies to estimate our uncertainty, the mean of this difference is 0.66 dex.

For Sknot+diffuse and Mknots with $z > 0.1$ the F814W filter includes the Hα emission, the continuum associated to the star-forming region, and the continuum+Hα emission of the diffuse light of the host galaxy. The continuum and Hα diffuse emission from the host galaxy was removed computing the luminosity in an area equivalent to the knot but in the diffuse gas region of the galaxy and subtracting it to that of the corresponding knot.

The star-forming continuum was subtracted using an statistical value derived from the Hα/continuum ratio for 51 Mknots galaxies with spectrum in zCOSMOS. Fig. 3.14 shows the distribution of this "correction" ratio. The Gaussian fit provides a mean of 0.09, with a dispersion of 0.05. We used the mean value to correct the Hα luminosity of the knots and the dispersion was included in the error budget of the derived quantities (in particular of the SFR). A possible caveat to this method is whether Hα+continuum of the host galaxy could be present in zCOSMOS spectra. To check this issue, we used a subsample of galaxies with available spectra and with a star-forming knot/clump luminosity at least twice the luminosity of the host galaxy (9 galaxies). For this subsample we would expect to have a negligible contribution from the host galaxy due the different luminosities. We found remarkably similar results using this small sample (see Fig. 3.14, dot-dashed line). We also analyzed a subsample of 25 Sknot galaxies (galaxies without diffuse light) and with available spectroscopy in zCOSMOS. For this sub-sample we would expect our Hα/continuum distribution to be shifted towards lower values since there is no contribution from the host galaxy. However, we find again a good agreement with our initial sample of 51 galaxies. Fig. 3.14 (dashed line) show the derived distribution for Sknot galaxies. The best Gaussian fit to this distribution provides also a mean of 0.09 and a dispersion of 0.04.

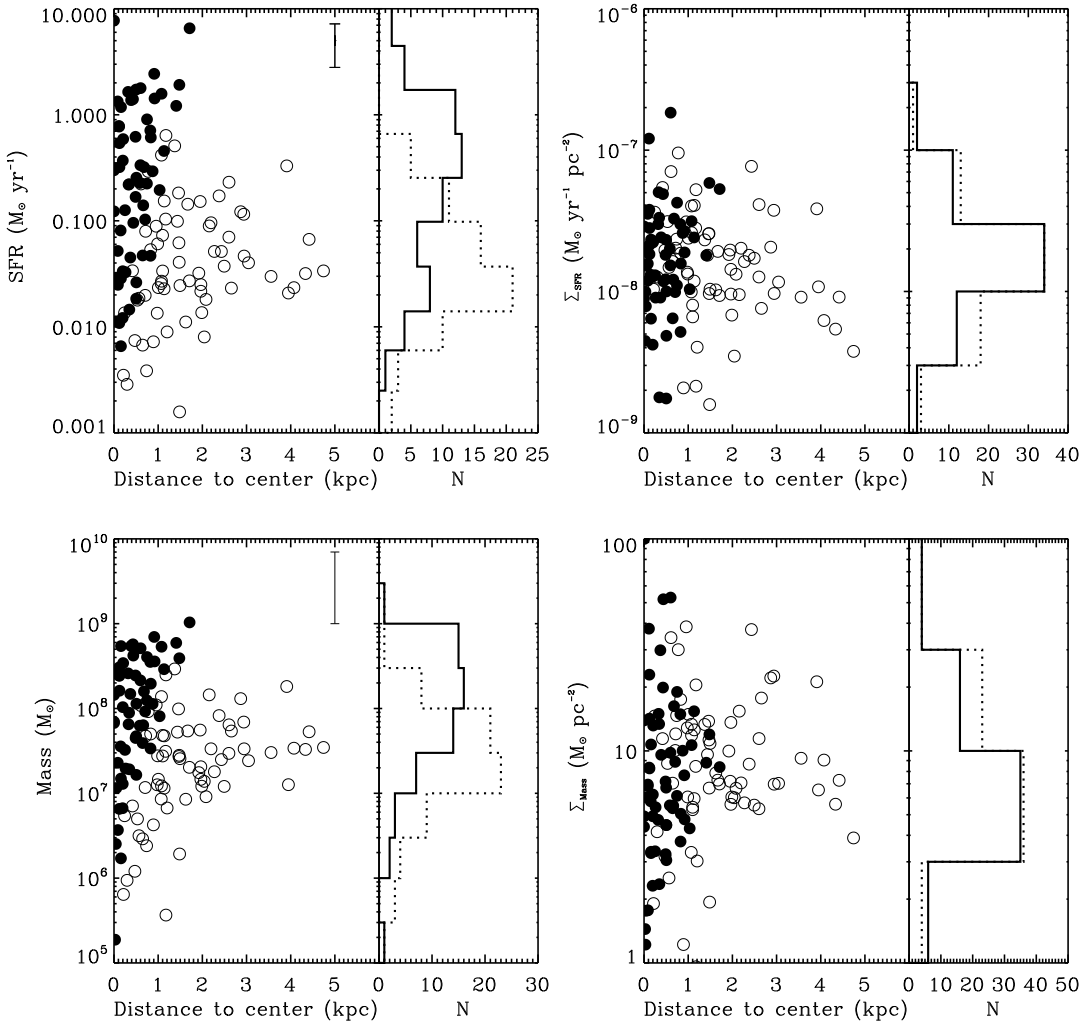

Figure 3.15: SFR and Σ_{SFR} versus galactocentric distance (top), mass and Σ_{mass} versus galactocentric distance (bottom), filled circles are centered knots and empty circles represent offcenter ones. The distribution of each quantity in the y-axis is showed at the right of each panel. The most massive and high star-forming regions are in the central part of the host galaxies.

Therefore, we consider that a Hα/continuum correction factor of 0.1 with a typical dispersion of 0.05 is a robust value even in the most extreme cases in our sample. The final luminosity in Hα, obtained as described above for Sknot, Sknot+diffuse and Mknots galaxies, is given in appendix B.

The SFR is calculated from the luminosity in Hα using the relation between L(Hα) and SFR from Kennicutt (1998). Fig. 3.15 shows the radial distribution of the SFR, SFR/area, mass and mass/area for centered, offcentered, and lopsided knots, as defined in Section 4.3. As can be seen in Fig. 3.15 (top) the knots with the highest SFR ($\sim$1 $M_{\odot}$ yr^{-1}) are only present in the central regions of the galaxies. Fig. 3.15 (bottom) shows the mass and mass/area versus the distance to the center. The more massive and largest star-forming regions are also in the central part of the host galaxies.

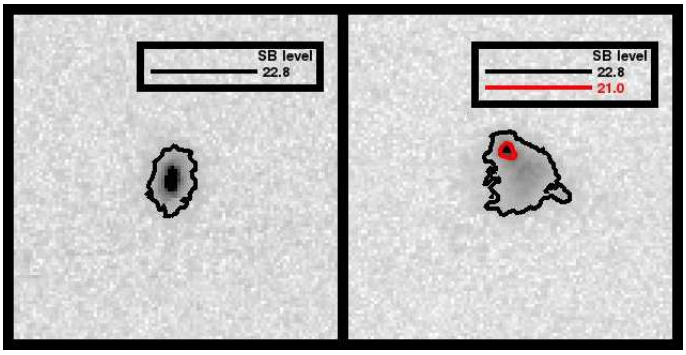

Figure 3.16: Substructures in a Sknot (right panel) and Sknot+diffuse (right panel) galaxies. Isophotes are in magnitude/arcsec^2. The analysis have not found substructures and diffuse light in the Sknot galaxy, while for Sknot+diffuse galaxy it is clearly seen how a substructure and diffuse light is found far away from the knot region.

3.1.5 Single knot galaxies

In our catalogue, 87 galaxies were classified as Sknot (∼38%), meaning that they show a resolved star-forming region and no extended diffuse emission. The minimal area used to define a substructure is 15 connected pixels, with values over 3σ the sky background. This gives us a magnitude limit of ∼26. This faint magnitude would allow us to detect very low surface-brightness sources. For this reason, and within this magnitude limit, we are confident that Sknot galaxies have no diffuse extended light. Fig. 5.11 shows two examples of the search for substructures in Sknot (left panel) and Sknot+diffuse (right panel) galaxies. The units are in magnitude/arcsec^2.

Sknot galaxies are larger (see Fig. 3.5) and more massive (see Fig. 3.12) than star-forming knots in Sknot+diffuse and Mknots galaxies. However, they have similar Σ_{SFR} and Σ_{mass}, implying that they probably share a similar SF mechanism.

The ellipticity distribution of Sknot galaxies shows that they are rounder than other starburst categories, (see Fig. 3.6). The mean is 0.4, which is in agreement with spheroidal galaxies viewed from random line-of-sights (Padilla & Strauss 2008; Mendez-Abreu 2015).

3.2 Results and Discussion

3.2.1 Comparison with the literature at this redshift

The number and properties of star-forming knots in a starburst galaxy provides important information to test the different cosmological models predicting the formation and evolution of galaxies. The availability of recent deep surveys has lead to several works aiming at quantifying the regions in the galaxies were SF is occurring. The precise definition of a starburst knot, however, is very much dependent on the particular observations. An unique definition to search for starbursts in deep fields is still lacking, and the parameters used so far have varied in the different works published in the literature. First studies were done visually (e.g., Cowie et al. 1995; van den Bergh et al. 1996; Abraham et al. 1996; Elmegreen et al. 2004a,b). More recently, Guo et al. (2014) used the excess in UV as the physical parameter to identify a clump. In particular, they classified as a star-forming clump those contributing more than 8% to the rest-frame UV light of the whole galaxy. Using this definition, they measured the knots in star-forming galaxies in the redshift range $1 < z < 3$. At lower redshift, $0.2 < z < 1.0$, Murata et al. (2014) identified the star-forming knots using the HST/ACS F814W-band in the galaxies in the COSMOS survey. The criteria used was that the detected sources must be brighter than 2σ the local background, and with a minimum of 15 connected pixels. In this paper, we have also used the HST/ACS F814W-band in the COSMOS survey to find and parametrize the star-forming knots of the starbursts identified in the COSMOS

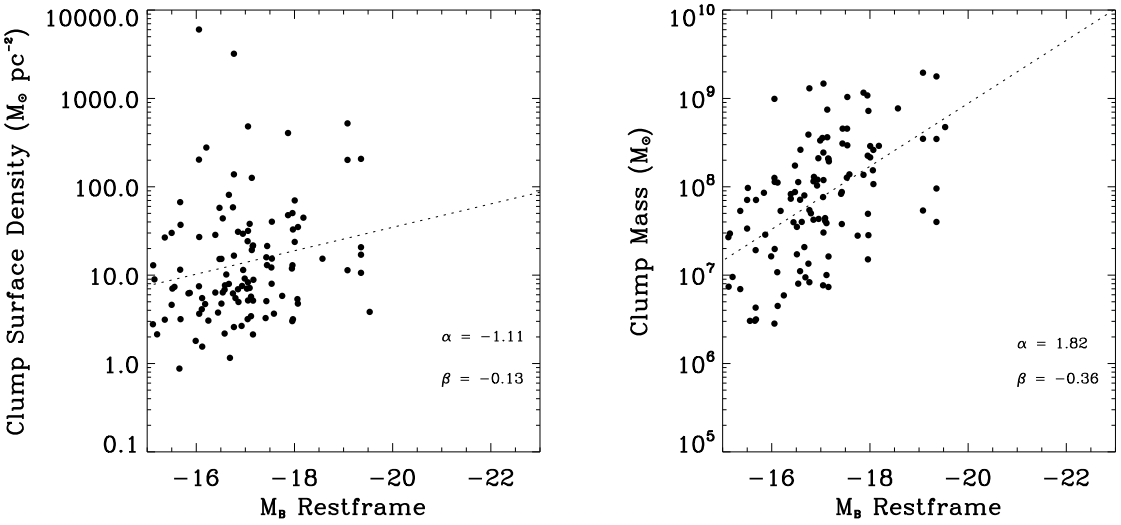

Figure 3.17: Clump Surface Density (left) and Clump Mass (right) versus absolute $B-$band magnitude of their host galaxy. The best fit to the data is shown in dotted lines. The values of slopes and intercepts are giving in the lower right corner.

survey. In particular, we calculated the emission (σ) of the host galaxies and searched for regions with 3 times this value, which is more strict than the 2σ used by Murata et al. (2014), over 15 connected pixels using FOCAS.

The clumpy fraction (f_{clumpy}; clumpy galaxies/SF galaxies) have been investigated for different redshift and mass ranges (Elmegreen et al. 2007; Overzier et al. 2009; Puech 2010; Guo et al. 2012; Wuyts et al. 2012; Guo et al. 2014; Murata et al. 2014; Tadaki et al. 2014). Despite the already mentioned differences in the clump definition, a remarkable agreement has been reached, concluding that f_{clumpy} increases with redshift. However, a direct comparison between different works is often difficult, not only because of the clump definition, but also due to the different definition of a starburst galaxy. For example, Guo et al. (2014) and Murata et al. (2014) defined their samples selecting galaxies with specific SFR (sSFR) ≥ 0.1 Gyr^{-1}. In other works, such as Guo et al. (2012), they used sSFR ≥ 0.01 Gyr^{-1}. Wuyts et al. (2012) used galaxies that need less than the Hubble time to form their masses. Tadaki et al. (2014) selected galaxies with Hα excess and Overzier et al. (2009) used Lyman Break Analog (LBA) galaxies, which share typical characteristics of high-redshift Lyman Break Galaxies (LBG). On the other hand, Puech (2010) used [OII] emission-line galaxies. The samples are then defined using a variety of criteria. In this paper we used the values of EW(Hα) and EW([OIII]) ≥ 80 Å to search for star-forming galaxies. These parameters are used in nearby HII regions and starburst galaxies, and points directly to recent (young) star formation (Kniazev et al. 2004; Cairós et al. 2007, 2009b,a, 2010; Morales-Luis et al. 2011; Amorín et al. 2014).

Using our definition of both starburst galaxy based on the EW of the Hα and [OIII] lines and star-forming clump based on light excess in the F814W filter, we calculated the clumpy fraction for our galaxies. Accounting for our entire sample up to $z \sim 0.5$ we found a value of f_{clumpy}=0.24. The mass range of the galaxies in our sample is 10^6-10^9 M$_\odot$ (Sect. 2.6), while in previous studies these values are usually larger (Overzier et al. 2009, 10^9-10^{10} M$_\odot$), (Puech 2010, $> 2{\cdot}10^{10}$ M$_\odot$), (Guo et al. 2012, $> 10^{10}$ M$_\odot$), (Wuyts et al. 2012, $> 10^{10}$ M$_\odot$), (Guo et al. 2014, 10^9-$10^{11.5}$ M$_\odot$), (Tadaki et al. 2014, 10^9-$10^{11.5}$ M$_\odot$), (Murata et al. 2014, $> 10^{9.5}$ M$_\odot$). The value obtained in this work for f_{clumpy} is larger than the value 0.08 found by Murata et al. (2014) at z=0.3. Besides the differences in the definition of the knots, the lack of agreement in the value of f_{clumpy} can be explained by the

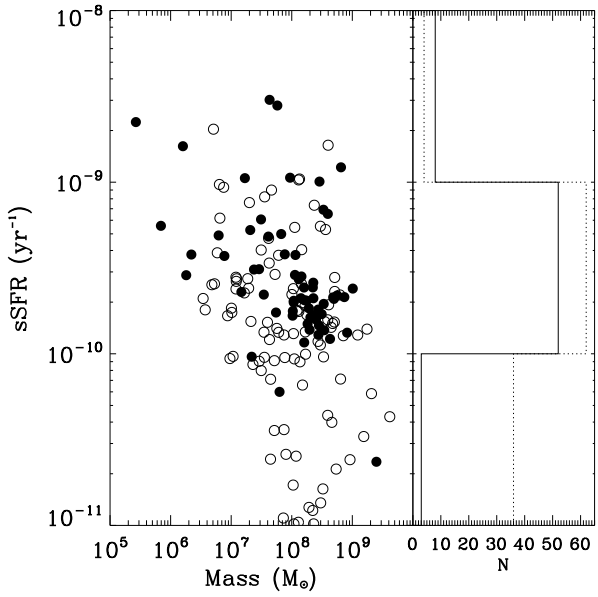

Figure 3.18: sSFR versus mass for Sknot (filled circles) and knots in Sknot+diffuse and Mknots galaxies (open circles). To the right, the distribution function (solid line is for Sknot galaxies and dotted line is for knots in Sknot+diffuse and Mknots galaxies).

difference in the mass range of the galaxy sample. On the other hand, Murata et al. (2014) defined as clumpy a galaxy with 3 or more knots, while we have considered galaxies with 2 or more knots. It is worth noting that other caveats discussed throughout this paper, such as bandpass or spatial resolution effects, would only increase our clumpy fraction.

Elmegreen et al. (2013) compared the properties of individual clumps of three different galaxy samples: knots in local spiral galaxies (obtained from the Sloan Digital Sky Survey; SDSS) massive clumps in local starbursts belonging to the Kiso Survey (Miyauchi-Isobe et al. 2010), and clumps in galaxies at high redshift from the Hubble Ultra Deep Field (HUDF). They found correlations between different parameters of the clumps and the absolute $B-$band magnitude of the host galaxy. For a comparison with Elmegreen et al. (2013), we used two properties of our sample knots: surface density and mass. In Fig. 3.17 we plot them as a function of absolute $B-$band magnitude of the galaxy. These plots are similar to those shown in Figs. 4 and 6 in Elmegreen et al. (2013). The best fit was determined for each parameter, and in the lower right corner of the figures the values of the intercept and slope are given. The surface density and mass trends are in between those provided in Elmegreen et al. (2013) for local and high-redshift massive clumps. The mass versus absolute $B-$band magnitude slopes for Kiso, HUDF and our sample are -0.54, -0.18 and -0.36, respectively. For surface density versus absolute $B-$band magnitude the values are -0.18, -0.12 and -0.13. The values suggest that for a given absolute $B-$band magnitude of the galaxy, the mass and surface density of the knots of the sample of this paper have higher values than those of clumps in local spirals, and lower than those found in high-redshift massive star-forming regions. There is a shift in the intercept of the linear regression fit of our data points, which has higher values than those provided in Elmegreen et al. (2013). This might be due to the different definitions to determine the area to retrieve the mass, surface density and SFR.

3.2.2 Mknots galaxies and their link to bulge formation

Several mechanisms have been proposed to explain the formation and evolution of galaxy bulges (Kormendy & Kennicutt 2004; Bournaud 2015). At high redshift, bulge formation is thought to be driven by either gravitational collapse (Eggen et al. 1962), major mergers (Hopkins et al. 2010), or coalescence of giant clumps (Bournaud et al. 2007). This latter scenario, in which massive star-forming clumps migrate from the outer disk to the galaxy centre forming a bulge, has been extensively discussed using numerical simulations (Noguchi 1999; Immeli et al. 2004a,b; Bournaud et al. 2007; Elmegreen et al. 2008; Ceverino et al. 2010). Recently, Mandelker et al. (2014) used cosmological simulations to provide clump properties to be compared with observations. In particular, they separated clumps formed *in-situ* (clumps formed by disk fragmentation due to violent instabilities) and *ex-situ* (clumps accreted through minor mergers), finding differences in their properties and radial gradients that could help to distinguish their origins.

In this scenario, Mandelker et al. (2014) predict that *in-situ* clumps show a radial gradient in mass, with more massive clumps populating the central regions. The aforementioned theoretical studies were focussed on massive galaxies. More recent analysis deal with less massive galaxies by means of similar theoretical simulations. In Ceverino et al (2015) they follow gas inflow that feeds galaxies with low metallicity gas from the cosmic web, sustaining star formation across the Hubble time. Interestingly, their results show clump formation in galaxies with stellar masses of $M \simeq 10^9 M_\odot$ using zoom-in AMR cosmological simulations. Although detailed simulations such as the one by Ceverino et al. (2015) for lower mass galaxies are still scarce, it is important to get observational information as the one here provided to be compare with in future theoretical works. Fig. 3.15 shows the distribution of mass and mass surface density for our clumps as a function of the galactocentric distance. Despite the errors introduced by the lack of multi-band photometry at cluster-scale resolution, it is clear how the most massive clumps in our sample are located in the galaxy center, with offcenter clumps being less massive. However, this tendency is not so clear in terms of surface mass density, where some offcentered clumps have similar surface mass densities to those located in the center, thus likely implying an *ex-situ* formation. On the other hand, numerical simulations also predict that more massive clumps of SF should appear in more massive galaxies (Elmegreen et al. 2008). This is nicely reproduced in Fig. 3.13, and it is, therefore, consistent with most of the clumps being formed at large radii, and then accreting mass from the disk as they migrate inwards.

Figure 3.15 also shows the distribution of SFR and SFR surface density versus galactocentric distance. Centered clumps show slightly higher SFR than offcentered ones. This behavior would be expected in the case of *ex-situ* formation of the clumps (Mandelker et al. 2014). However, the fairly constant radial SFR surface density, also shown in Fig. 3.15, and predicted for both scenarios, prevented us from extracting further conclusions.

In our sample we calculated the sSFR for each knot for every Sknot+diffuse and Mknots galaxy. Fig 3.18 shows the distribution of sSFR for knots in Sknot+diffuse and Mknots galaxies in our sample, with a bin width of 250 Myr^{-1}. We have also explored the sSFR for clumps which are centered and offcentered in Sknot+difffuse and Mknots galaxies. The values are similar, and no different SF mechanism can be identified based in the sSFR. Sknots and knots in Sknot+diffuse and Mknots galaxies have similar values of sSFR; the similitude in the distribution for both samples suggests the same mechanism of SF.

3.2.3 Two populations: the knots that are galaxies and the remaining

In our sample we detected two kinds of star-forming knots. One are classified as Sknot galaxies, where there is one star-forming knot, and it is not possible to detect diffuse emission. The other are knots which belong to galaxies with one or more knots of SF and diffuse emission. We detected similitudes and differences in the properties of both classes. Fig. 3.18 represents the distribution

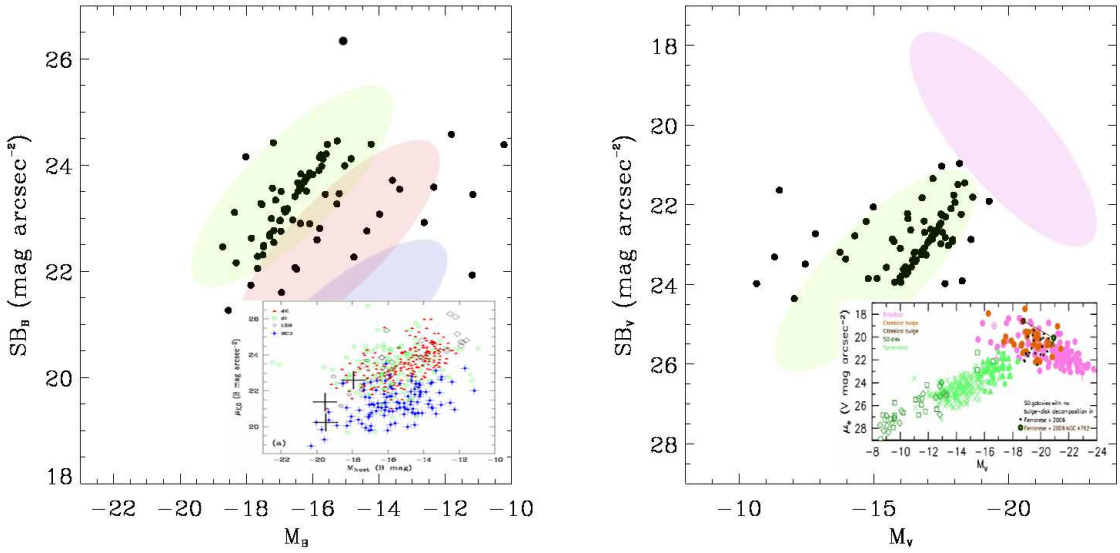

Figure 3.19: Surface brightness versus absolute magnitude in the $B-$band (left panel) and $V-$band (right panel) for Sknot galaxies. Figures are adapted from Amorín et al. (2012, their Fig. 9) for $B-$band and Kormendy & Bender (2012, Their Fig. 7) for $V-$band (the inset figure in each panel). Elliptical regions of different colors are overplotted to show the different class of galaxies, following the Amorín et al. (2012) and Kormendy & Bender (2012) diagrams.

of sSFR of both populations, showing a maximum at the same sSFR value. 1/SSFR can also be used as an estimation of age as the time scale to form the stars we see now if they would have been formed at the present SFR. With this idea, the typical time required to form both systems - starbursts spread along the disks or centered isolated ones - is around 2×10^9 years. Knots in Sknot+diffuse and Mknots galaxies do show, however, a wider range of values, with some cases that can require a formation time of up to 10^{11} years. This can be, however, a caveat of our determination of parameters, as we have explained in section 3.1.4. Overall, these results support the scenario in which the SF occurs in disk instabilities, and with larger and more massive clumps resulting from the migration to the center and coalescence processes.

For both classes we measured the surface brightness in the F814W-band. Sknot have lower values, characteristic of low surface-brightness galaxies. For Sknot galaxies we measured the surface brightness and absolute magnitude in $B-$ and $V-$band, to compare with results in the literature. In particular, we compare the photometric values of Sknot galaxies with those provided in Amorín et al. (2012, Fig. 9) and Kormendy & Bender (2012, Fig. 7), respectively. In Fig. 3.19a we show the surface brightness in $B-$band versus $B-$band absolute magnitude as in Amorín et al. (2012), and Fig. 3.19b shows the surface brightness in $V-$band versus $V-$band absolute magnitude as in Kormendy & Bender (2012). At the right upper corner of each panel, and with the same scale, we show the data points of this work. In the figures we overplotted a shadowed elliptical region where most of our points are in the plots of Amorín et al. (2012) and Kormendy & Bender (2012). A direct comparison suggests that Sknot galaxies fall in the parameter space populated by spheroidals and ellipticals (Kormendy & Bender 2012), and dwarf ellipticals and dwarf irregulars galaxies, as measured by Papaderos et al. (2008) and compiled by Amorín et al. (2012).

Chapter 4

Starburst galaxies in COSMOS at $0.3 < z < 0.9$

The cosmological evolution of the star-formation history of the Universe have been extensively discussed in the literature. Currently, it is agreed that the average star formation in the Universe had a maximum peak around $z \sim 2$ with a decrease towards both higher and lower redshifts. However, a proper understanding on the physical processes driving the evolution of the star-formation history and how to link the different observed properties of starburst galaxies at different cosmic times has still not been settled. This chapter expand on the work and analysis showed in chapters 2 and 3. Since different diagnostic diagrams have to be used in order to match the rest-frame spectral features at redshift ($0.3 < z < 0.9$), this analysis is described in a different chapter. The aim of this study is to present a comprehensive view of the star-formation mechanisms acting at intermediate redshift, bridging the gap from the early to the local Universe.

This chapter is organized as follows: Sect. 4.1 describes the selection of the sample. We used a new set of diagnostic diagrams based on the most prominent spectral features in the rest-frame optical wavelengths of starburst systems. Sect. 4.2 analyze the physical properties of the sample. The stellar masses and star-formation rates are computed as well as the classification of the starbursts morphology as in chapter 3. The properties of the individual star-forming knots and their relation with the host galaxies are explained in Sect. 4.3. In Sect. 4.4 we derive the luminosity function of the different starbursts and its evolution with cosmic time. The main conclusions of this chapter are summarized in Sect. 4.5.

4.1 Selection of the sample at $0.3 < z < 0.9$

A main objetive in our study of starburst galaxies is the understanding of the evolution with cosmic time of these systems. To do this, it is necessary to move towards bluer wavelengths to extent the sample to higher redshifts (see chapter 2). This new search for starburst galaxies will involve again the use of spectra from zCOSMOS and images from the SUBARU intermediate band filters, all of them located in the optical range of the electromagnetic spectrum. Since the Hα emission line is redshifted beyond the optical for $z \gtrsim 0.5$, it is necessary to extent at shorter wavelengths the set of strong emission lines under study, a characteristic feature of high star-forming regions.

The [OIII] emission line, together with Hα, was used to define our spectroscopic sample at lower redshift ($0.1 \leq z \leq 0.5$). In this chapter we also use the [OIII] emission line in the search for starburst galaxies at intermediate redshift, as a link between both samples. This emission line is measured with the zCOSMOS spectra (5500Å $< \lambda <$ 9700Å) in the redshift range $0.1 \lesssim z \lesssim 0.9$.

As in chapter 2, we use a cut-off limit in the EW[OIII] at 80Å to identify galaxies with young ($\leq$ 10 Myr) star-forming regions.

The EW of the Hβ emission line, as well as the EW(Hα), are good indicators of the age of star-forming regions (Madau et al. 1998; Kennicutt 1998; Leitherer et al. 1999). In order to define young ($\leq$ 10 Myr) star-forming regions and select the same kind of starburst as in chapter 2, we can use the well-known relation between both lines to calibrate our methodology. Even if the Hβ emission line is weaker than Hα, it is possible with the zCOSMOS spectral resolution (R $\sim$ 600) to measure its flux and EW. To find a cut-off value of the EW(Hβ), we used Starburst 99 models to simulate its time evolution for instantaneous and continuous star formation. We find that values of EW(Hβ) $\geq$ 20Å are representative of star-forming regions younger than 10 Myr and correspond fairly well with our previous limiting values in EW(Hα) and EW[OIII] for the lower redshift sample. Therefore, this value is used as a limit to look for galaxies with young star-forming regions.

A strong emission line at bluer wavelengths is [OII] (λ: 3727,29 Å), its excitation is very high in the diffuse ionized gas for starburst galaxies, becoming the strongest emission line in the blue part of the spectrum. Even if the flux of forbidden lines are not directly coupled to the ionizing flux, since their excitation is sensitive to abundances, the ionizing luminosity of [OII] is sufficiently well behaved with relative small effect on the [OII] calibration, and therefore it has been used as an indicator of the star formation rate in young star-forming regions (Kennicutt 1998; Kewley et al. 2004; Moustakas et al. 2006; Garn & Best 2010).

The continuum shape around the [OII] region is strongly affected by the Balmer (HI) absorption lines and Balmer jump (D4000), whose features depends on the temperature. For O stars, this region is dominated by the UV continuum. For B stars some Balmer absorption appears and D4000 starts to increase. For A stars the Balmer emission lines are strong and D4000 is very notable. Because of these features, it is difficult to calibrate the [OII] emission using the SUBARU Intermediate band filters, without having "a priori" knowledge of the spectrum. However, as this region is an indicator of the temperature and the age of a star-forming region, we can use intermediate band filters to the left, and to the right of D4000 to have an estimation of the deep of the break, and seek for starburst galaxies. Once we have found a sample of starburst galaxies, using K-correct we perform a best fit of the SED, then we use this fit to estimate the continuum in [OII], and to estimate the SFR.

4.1.1 Calibration of color-color diagnostic diagrams with spectra ($0.32 \leq z \leq 0.9$)

The short wavelength separation ($\Delta\lambda \sim$ 150Å) between the Hβ and [OIII] emission lines does not allows us to resolve them using the Subaru Intermediate Band filters. However, they are well resolved in the spectra from zCOSMOS. In order to look for a spectroscopic sample that allows to perform our color-color diagram calibration at intermediate redshift, we first measured the Hβ and [OIII] emission lines present in the spectra. Similarly as we did, in chapter 2, for [OIII] and Hα, we use a baseline of 30Å, which cover the total width of the emission lines at the continuum level. The same band width is used to measure the continuum flux. Since both emission lines are close in wavelength, we use the same continuum for both at a middle point located at $\lambda_c = 4910$Å. To estimate the EW and its corresponding error for the emission lines we used both equations 2.1 and 2.2, respectively.

We perform a first spectroscopic search of starburst galaxies in the zCOSMOS catalogue in the redshift range $0.32 \leq z \leq 0.57$. In this redshift range, it is possible to measure simultaneously the continuum at both sides of D4000, and [OIII] emission line, using the SUBARU Intermediate band filters, which will be used to build up the calibrated color-color diagram (section 4.1.2). In addition, we extended our spectroscopic search to z=0.9 (until where it is possible to measure Hβ and [OIII] with zCOSMOS), which represents an extension of our spectroscopic sample at lower redshift ($0.1 < z < 0.47$), this fact allows us to have a complete spectroscopic sample in the redshift range $0.1 < z < 0.9$. As already explained, to obtain this spectroscopic sample we looked for galaxies with EW(Hβ) $\geq$ 20Å and EW([OIII]) $\geq$ 80Å what resulted in a sample of 95 starburst galaxies in the redshift range $0.32 \leq z \leq 0.57$, and 126 in the redshift range $0.57 < z \leq 0.9$, out of the 3995 available

in zCOSMOS at these redshift ranges.

Using the SUBARU intermediate band filters, it is possible to measure simultaneously $D4000_{right}$, $D4000_{left}$, [OIII] and the continuum for [OIII], in the redshift ranges: $0.32 \leq z \leq 0.57$. To find the [OIII] emission line in this redshift range, we used four filters: IA679 ($0.32 \leq z \leq 0.38$), IA709 ($0.38 < z \leq 0.44$), IA738 ($0.44 < z \leq 0.50$), and IA767 ($0.50 < z \leq 0.57$), for each filter we used another filter to the right to estimate the continuum. In fig. 4.1, panels A, B, C, and D, we plotted for each redshift range the $D4000_{right}$-$D4000_{left}$ vs. [OIII]-continuum. Starburst galaxies are located in the lower left region of the diagram. As we did for the sample at lower redshift presented in chapter 2, this is the region that will be used to complete our sample using the photometric redshift catalogue. A total of 95 starburst galaxies were found using zCOSMOS in the redshift range: $0.32 \leq z \leq 0.57$.

4.1.2 Starburst in the COSMOS photometric redshift catalogue $0.32 \leq z \leq 0.57$)

In section 4.1.1 we demonstrated the ability of the color-color diagnostic diagram based in the D4000 and [OIII] emission line to identify starburst galaxies at intermediate redshift ($0.32 \leq z \leq 0.57$). However, due to the high incompleteness of the zCOSMOS catalogue, it is not possible to use this reduced sample of 95 starburst to infer any redshift evolution. On the other hand, the photometric redshift catalogue, used to measure the D4000 and [OIII] emission lines simultaneously, allows us to extend our sample to intermediate redshift starburst galaxies with the necessary completeness. We use the SUBARU intermediate band filters, to locate $D4000_{left}$, $D4000_{right}$ and [OIII], at a given redshift, in order to estimate their magnitudes considering the flux of the emission line and the continuum. The [OIII] emission line is considered to lie within a filter, when it is located within a filter transmission ≥ 0.5, the $D4000_{left}$, and $D4000_{right}$ continuum are located at $\lambda \sim$3200Å, and $\sim$4000Å respectively. All of them can be measured simultaneously in the redshift range: $0.32 \leq z \leq 0.57$. The diagnostic color-color diagrams defined in section 4.1.1 are used to look for star-forming galaxies. To estimate the continuum with respect to [OIII], we choose a filter located to the red ($\lambda \sim$ 5500Å: restframe) of the emission line.

In the sample at lower redshift (see chapter 2), in order to avoid large uncertainties in the color-color diagrams, we imposed a threshold of 23.5 in the F814W magnitude, which is equivalent to an absolute magnitude of -17.25 at $z = 0.28$. To study evolutionary properties of starburst galaxies, it is necessary to search for galaxies with a similar absolute magnitude in the different redshift ranges used. To locate the [OIII] emission line at an intermediate redshift we use four SUBARU Intermediate band filters, which detect this emission at: $0.32 \leq z \leq 0.38$, $0.38 < z \leq 0.44$, $0.44 < z \leq 0.50$, and $0.50 < z \leq 0.57$. At the higher redshift in each range, for an absolute magnitude of -17.25, the magnitudes are 24.3, 24.7, 25.0 and 25.4, respectively. We applied these magnitude cuts in each redshift range to search for starburst galaxies.

However, when increasing the magnitude, errors increase too. In the color-color diagrams, to define objects as located in the region of star-formation not only their values, but also their errors, have to be within this regions. As the errors increase at fainter magnitudes, many galaxies are discarded, producing a lost of completeness. We found 26913 objects catalogued as galaxies in the Cosmos Photometric Redshift Catalogue, in the redshift ranges: $0.32 \leq z \leq 0.57$, with the respective cut in magnitude for every redshift range. In Fig. 4.2, black points represent the [OIII]-continuum vs. $B4000_{right}$-$B4000_{left}$ for these galaxies in every redshift range. The 2813 galaxies from zCOSMOS located in these redshift ranges are shown with green points, and the 95 of them catalogued as starburst galaxies in section 4.1.1 are shown with blue points. Red points with their respective error bars, are galaxies from the Photometric Redshift Catalogue, located in the star-forming region.

The shape of the SED to the right of [OIII] is not constant, with variations that influence on the flux estimation of the continuum. As the distance from [OIII] to the selected continuum is not constant, depending on the chosen filter, we defined the cut in the color-color diagrams for every redshift range, as can be seen in Fig. 4.2. In Fig. 4.3 we show how faint galaxies are lost in every redshift range.

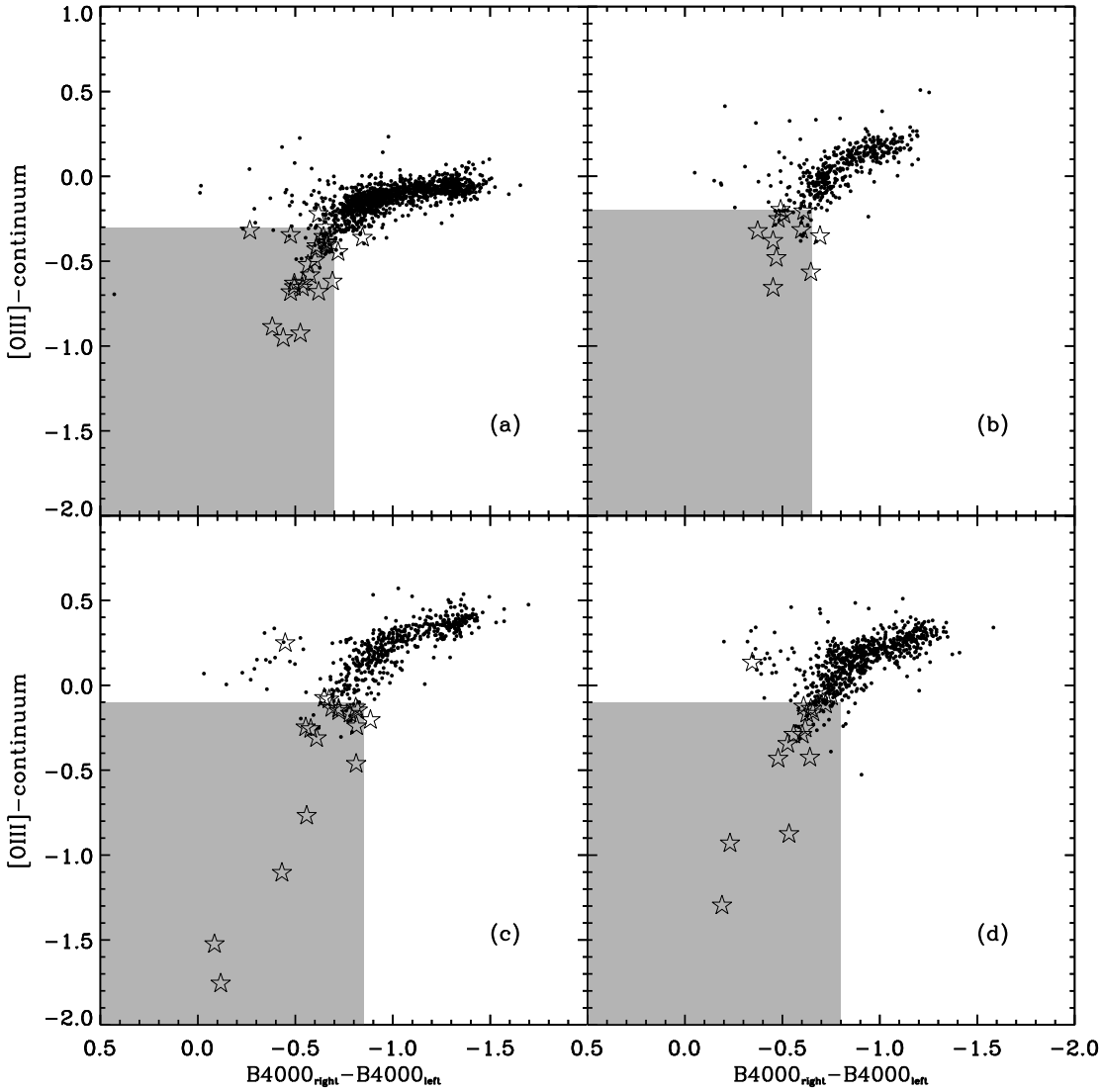

Figure 4.1: B4000$_{right}$-B4000$_{left}$ vs. [OIII]-continuum color-color diagram for the four redshift ranges in zCOSMOS. Filled circles are the galaxies from zCOSMOS that are not considered as starburst according to our criteria. Star symbols represent galaxies with EW(Hβ)$\geq$20 and EW([OIII])$\geq$80 catalogued as starburst galaxies. The shadowed zone in every redshift range ($0.32 \leq z \leq 0.38$ (panel a); $0.38 < z \leq 0.44$ (panel b); $0.44 < z \leq 0.50$ (panel c); $0.50 < z \leq 0.57$ (panel d)) represents the loccii of star-forming galaxies. Note that the shadowed zone have some differences in each panel, this difference is produced by the different filters used to estimate the magnitude, the SED have important variations in shorts wavelength ranges.

In each panel we show in grey the region where the galaxies with high star formation are located. A total of 929 starburst were found from the photometric redshift catalogue. The cuts for every redshift range are: B4000$_{right}$-B4000$_{left}$ $\leq$ -0.7 and [OIII]-continuum $\leq$ -0.3 ($0.32 \leq z \leq 0.38$), B4000$_{right}$-B4000$_{left}$ $\leq$ -0.65 and [OIII]-continuum $\leq$ -0.2 ($0.38 < z \leq 0.44$), B4000$_{right}$-B4000$_{left}$ $\leq$ -0.85 and [OIII]-continuum $\leq$ -0.1 ($0.44 < z \leq 0.50$) and B4000$_{right}$-B4000$_{left}$ $\leq$ -0.8 and [OIII]-continuum $\leq$ -0.1 ($0.5 < z \leq 0.57$). The total sample at intermediate redshift obtained as explained above, including the spectroscopic and photometric search, contains 1152 starburst galaxies.

4.1.3 Caveat to the selection and final sample

As in section 2.5, it is necessary to check our sample to establish possible uncertainties sources. Several checks were performed to avoid erroneous sources in our final sample.

Most galaxies in our sample were found from the Photometric Redshift Catalogue, being the photometric redshift a fundamental tool for this search. To test the reliability of z_{phot}, we compared the photometric and spectroscopic redshift for those galaxies with both measurements available obtaining a good agreement with 1σ of ~ 0.007, Fig. 4.4 shows this comparison. As in section 2.5, some "catastrophic redshift" detection were found (Ilbert et al. 2008, Fig. 1). 14 out of the 95 galaxies found in zCOSMOS have a wrong z_{phot} estimation. For some galaxies in the redshift range $0.3 \leq z \leq 0.4$, the [OIII] emission line is confused with Hα, and [OII] with [OIII], this produce a wrong photometric redshift determination with values $0.0 \leq z_{phot} \leq 0.1$. As we are looking for galaxies with redshift $0.32 \leq z \leq 0.57$, galaxies with this "catastrophic redshift" are not included in our photometric sample.

To avoid contaminated sources in our sample, we further performed a visual check of the 1152 galaxies. Some galaxies were discarded for being galaxies contaminated by a saturated close star, galaxies at the limit of our detection threshold, and HII regions of foreground spiral galaxies that were removed from the final sample. Fig. 4.5 is a mosaic of some galaxies discarded from our sample. A total of 49 galaxies from the sample were discarded, and our final catalogue at intermediate redshift consists on 1103 galaxies.

4.2 Galaxies properties

4.2.1 K-correction and stellar mass

The photometry from the COSMOS Photometric Redshift Catalogue is a fundamental tool for determining several parameters of the galaxies in our sample. However, since the galaxies detected in our sample are redshifted, the magnitudes in the different bands are modified because of the changes in the SED features, which is more noticeable as more redshifted the galaxies are. To take into account these changes, it is necessary to correct the magnitudes in the different filters, this correction is the so called K-correction, which was determined in our sample at low redshift in section 2.6. See this section also for a complete description of the algorithm and references.

To estimate this correction, as in section 2.6, we use the K-correct software (Blanton & Roweis 2007). In our sample we use 10 band filters (U, B, V, g, R, I, $F814W$, z, J and K) to find the best fit, using a basis of 450 spectral templates and 35 instantaneous bursts (see details in section 2.6). The best fit of the sample was visually inspected. Galaxies in our sample show the features of star-forming galaxies, like high nebular emission lines and UV continuum. The confidence parameter ($\mathfrak{C}$), which is described by $\sum(F_t - F_m)^2/F_t^2$ where F_t is the flux of the template at the wavelength of the filter and F_m is the measured flux in the filter from COSMOS, was estimated for the total sample to measure the quality of the fit.

An important parameter determined from K-correct is the stellar mass, which is calculated from the best fit of the SED. In our sample, the mass range determined with K-correct spans

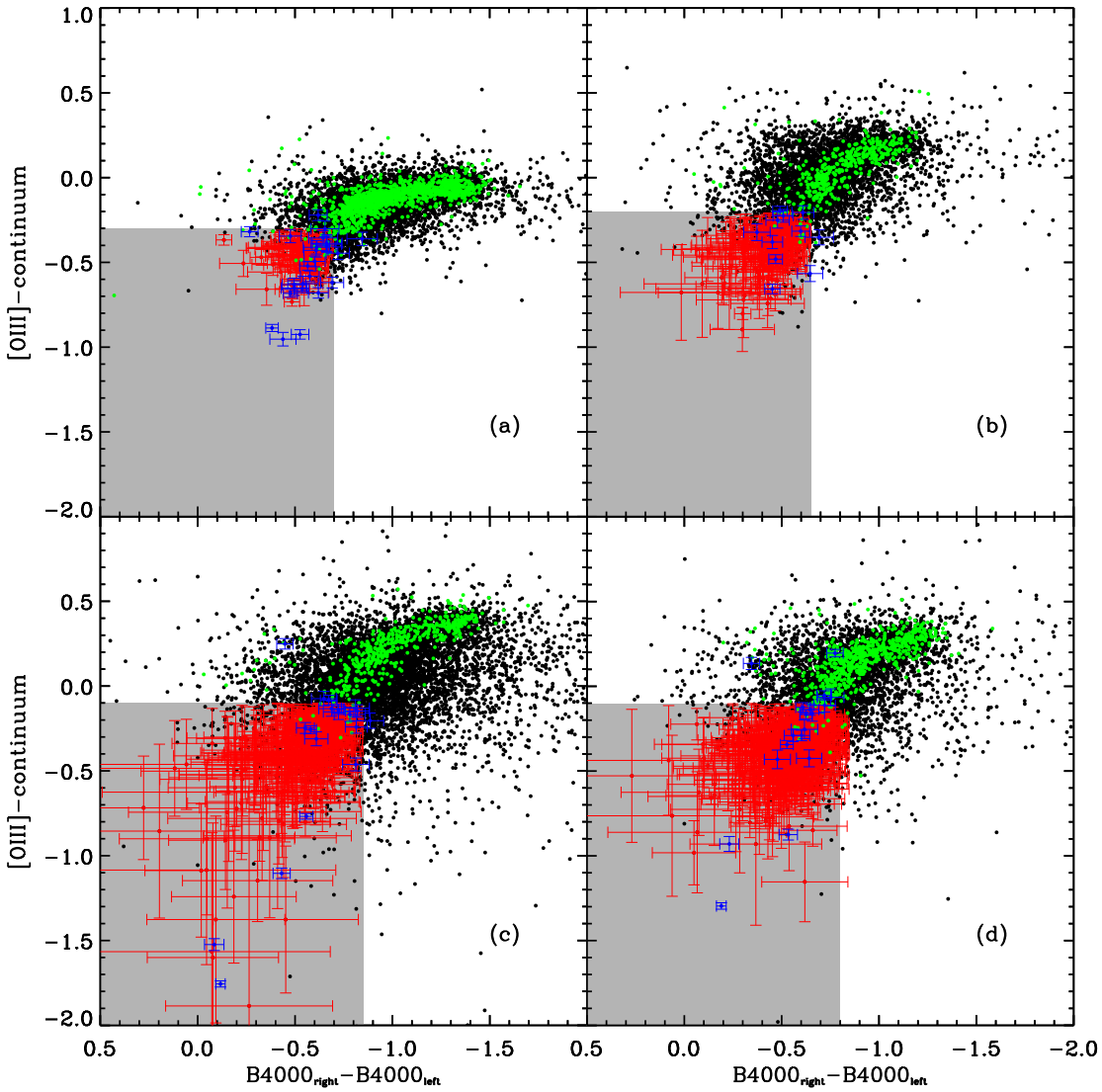

Figure 4.2: B4000$_{right}$-B4000$_{left}$ vs. [OIII]-continuum color-color diagram for the four redshift ranges in the Photometric Redshift Catalogue. Black points are galaxies in the photometric redshift catalogue that are not considered as starburst galaxies. Green points are galaxies from zCOSMOS that are not considered as starburst. Blue points with error bars are galaxies from zCOSMOS catalogued as starburst. Red points with error bars are galaxies catalogued as starburst from the Photometric Redshift Catalogue considering 1σ of error. The shadowed zone is the locii for star forming galaxies in each redshift range ($0.32 \leq z \leq 0.38$ (panel a); $0.38 < z \leq 0.44$ (panel b); $0.44 < z \leq 0.50$ (panel c); $0.50 < z \leq 0.57$ (panel d)).

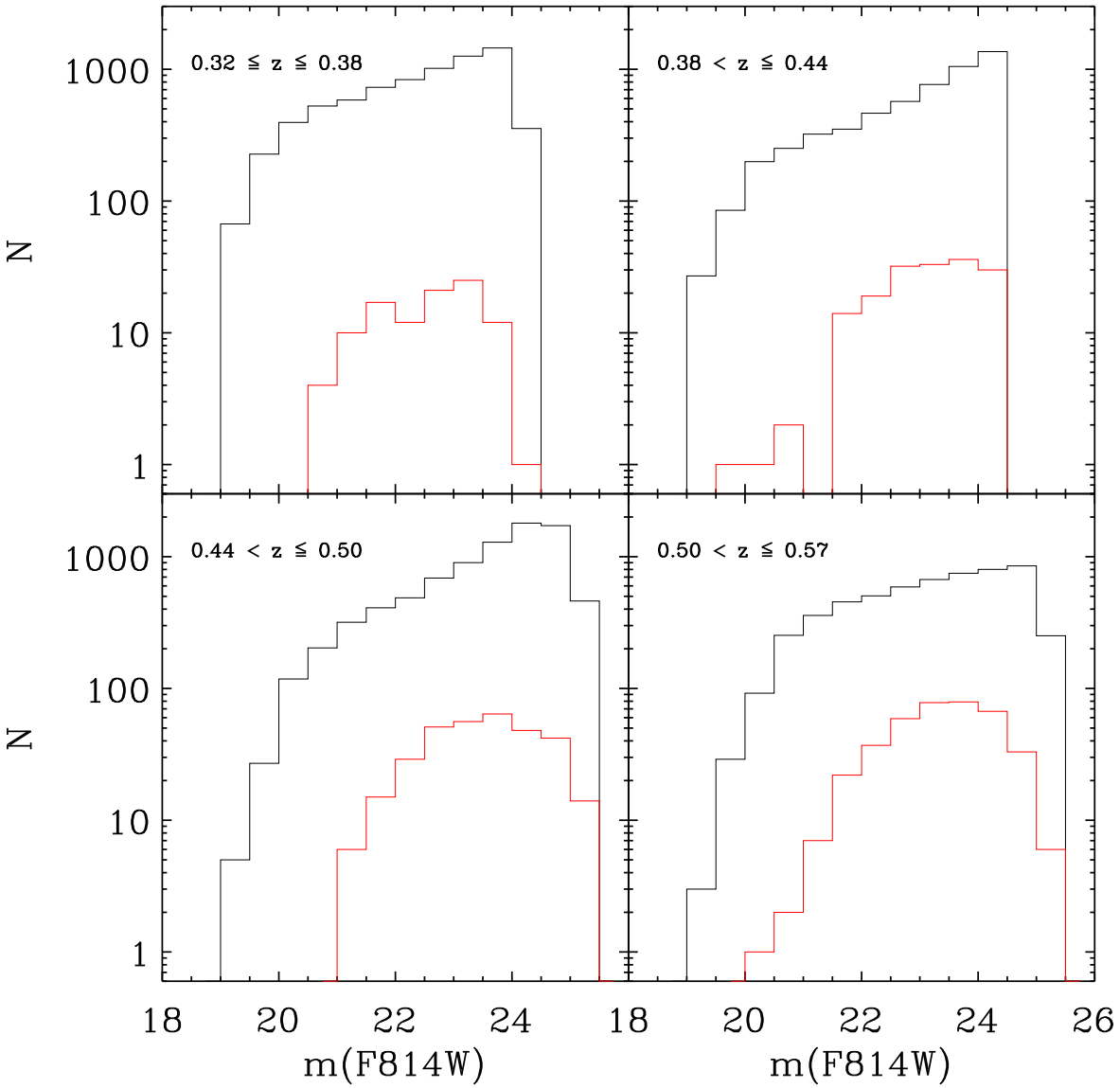

Figure 4.3: Completitude of the sample in every redshift bin. Black lines represent the total sample of galaxies in the redshift range with its corresponding cut in magnitude. Red lines represent the sample of starburst galaxies.

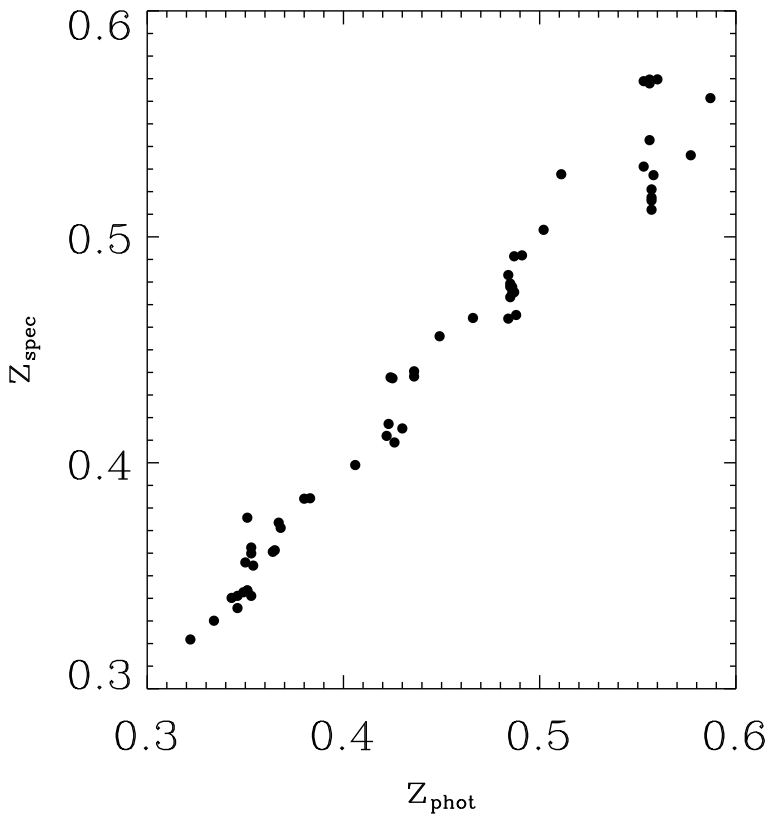

Figure 4.4: Comparison of z_{phot} and z_{spec} for galaxies found in zCOSMOS in the redshift range $0.32 \leq z \leq 0.57$.

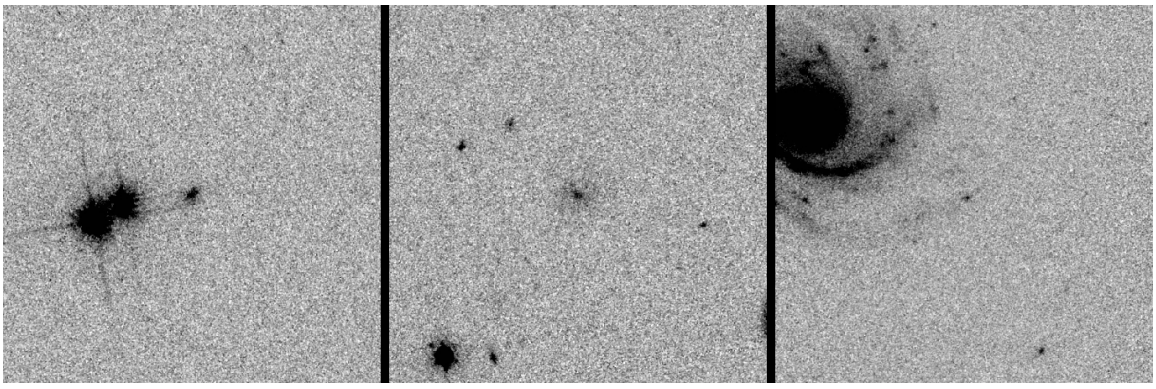

Figure 4.5: HST images with some examples of sources discarded after visual inspection. Left: Contaminated by a saturated close star. Middle: galaxies at the limit of our detection threshold. Right: HII region of a foreground spiral galaxy.

$10^{7.5} M_{\odot} < M < 10^{10.5} M_{\odot}$, with a mean of $10^{8.7} M_{\odot}$. We compared the stellar mass determined with K-correct, with the stellar mass provided by Bell & de Jong (2001), which use a simplified

set of spectrophotometric spiral galaxies with a burst of star formation to calculate the mass to light ratio. Fig. 4.6 shows the comparison of masses determined with both methods and the mass distribution using the mass from K-correct, both methods show consistent mass values.

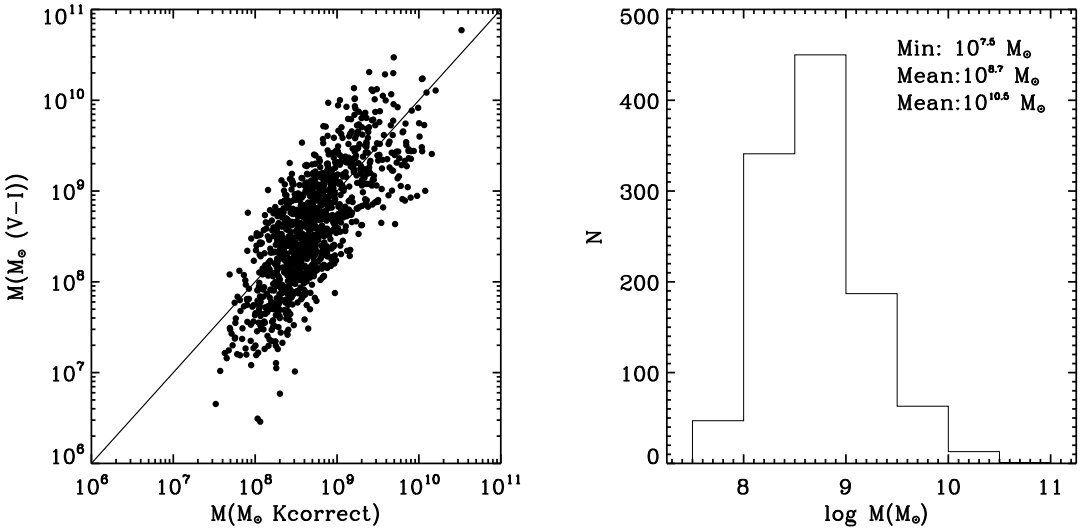

Figure 4.6: Mass determination for the intermediate redshift sample. Left: comparison of masses determined by K-correct and $V - I$ color using Bell & de Jong (2001). Right: Mass distribution obtained with the K-correct method.

4.2.2 Hα luminosity: K-correct fit

The estimation of the Star Formation Rate (SFR) in our sample of starburst galaxies at intermediate redshift is not straightforward. The Hα emission at this wavelength range is redshifted to the infrared wavelengths and it is not possible to measure with the available SUBARU Intermediate band filters. The other proxy of the SFR, the [OII] emission line, is embedded in the Balmer break, which from an observational point of view make difficult to do an estimation of the continuum.

Having mentioned the difficulties, we have however, estimate the SFR in our sample by using the best template obtained with K-correct. From the best template of every galaxy we determine the flux in Hα and the continuum, then we determine the SFR following the Kennicutt (1998) empirical relation:

$$SFR(M_\odot \cdot year^{-1}) = 7.9 \times 10^{-42} L(H\alpha)(ergs \cdot s^{-1})$$

Fig. 4.7 shows the distribution of SFR of our sample at intermediate redshift, the statistics for the SFR is: mean=0.3 $M_\odot$ year^{-1}, min=0.001 $M_\odot$ year^{-1} , and maximum=2.0 $M_\odot$ year^{-1}.

4.2.3 Starburst morphology

The F814W HST ACS high resolution images of the sample at intermediate redshift (1103 galaxies), with a Full Width at Half Maximum (FWHM) of the Point Spread Function (PSF) of 0.09" and a pixel scale of 0.03"/pixel, available in the IRSA's General Catalogue Search Service, have been analyzed to identify morphological structures. A semiautomatic protocol was designed to this aim. With SExtractor we define the extension area of the galaxy. For this, throughout an iterative process, the background on the images were determined to afterwards identify objects with a signal

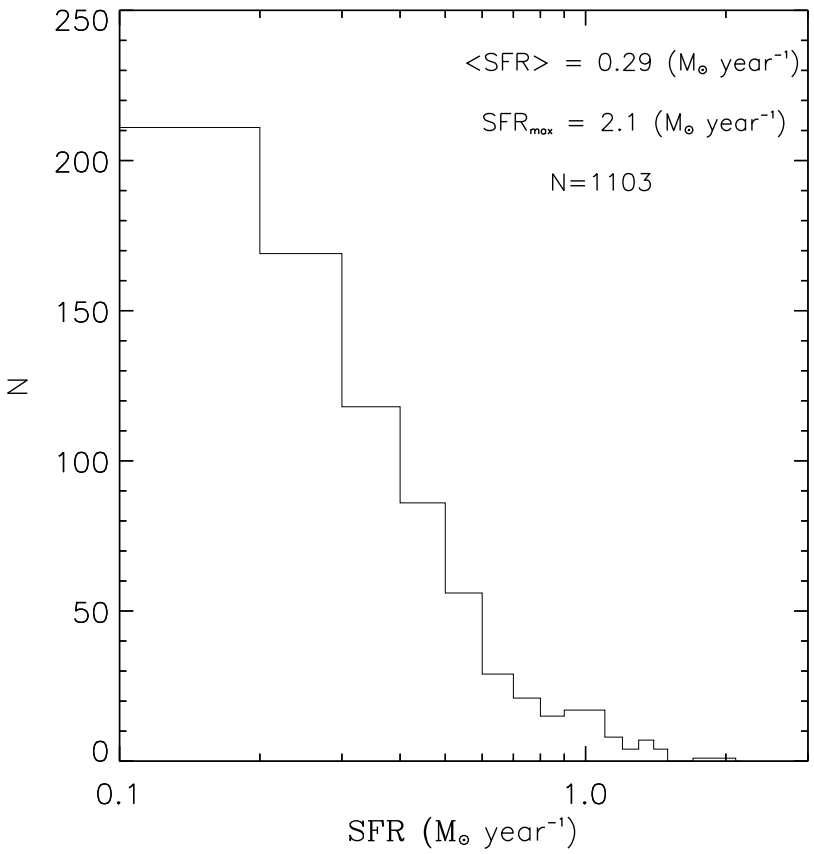

Figure 4.7: SFR distribution of the sample at intermediate redshift.

higher or equal than three times this value. The minimal area to be considered was imposed to be 3 × FWHM of the HST ACS images to avoid the detection of spurious sources such as hot pixels and cosmic rays. At this step different parameters are calculated for the detected objects. In particular we measured the central position and the equivalent radius, i.e., the radius of a circle with the same area than the covered for the pixels associated to the object. Then the galaxy is relocated in the center of the image using the new position and the image is resized to eight times its equivalent radius. The outermost isophote was used to obtain the flux of the galaxies, ellipticity and radius, with these quantities complemented with information from the COSMOS database we derived several parameters of the galaxies, some few entries are given in appendix C. Fig. 4.8 shows the ellipticity of galaxies in our sample at intermediate redshift.

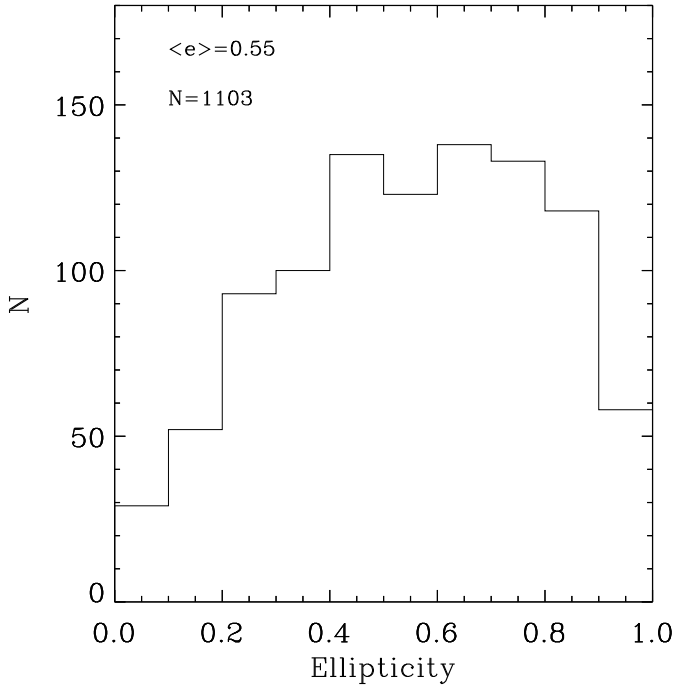

Figure 4.8: Distribution of ellipticity of the galaxies in the sample at intermediate redshift

To perform a detailed analysis, particularly to identify sub-structures like star forming regions in starburst galaxies, we used Faint Object Classification and Analysis System, this program offer a splitting routine which deal well with galaxy compounds. From this analysis we classified all galaxies as: Single Knot (Sknot), Single Knot plus diffuse light (Sknot+diffuse) or Multiple Knots (Mknots) galaxies (see section 3.1 for details). From the isophotal analysis we found 424 Sknot, 429 Sknot+diff and 126 Mknots galaxies. Fig. 4.9 shows examples of the three morphological classes. The properties of the star-forming regions are analyzed in the next section.

4.3 Properties of the knots

In this section, as we did in chapter 3, we benefit from the good spatial resolution of the HST images to go further in the characteristic of the starburst galaxies identified in section 4.1. We here applied a “trained algorithm” described in detail in chapter 3 to identify the different burst present in the

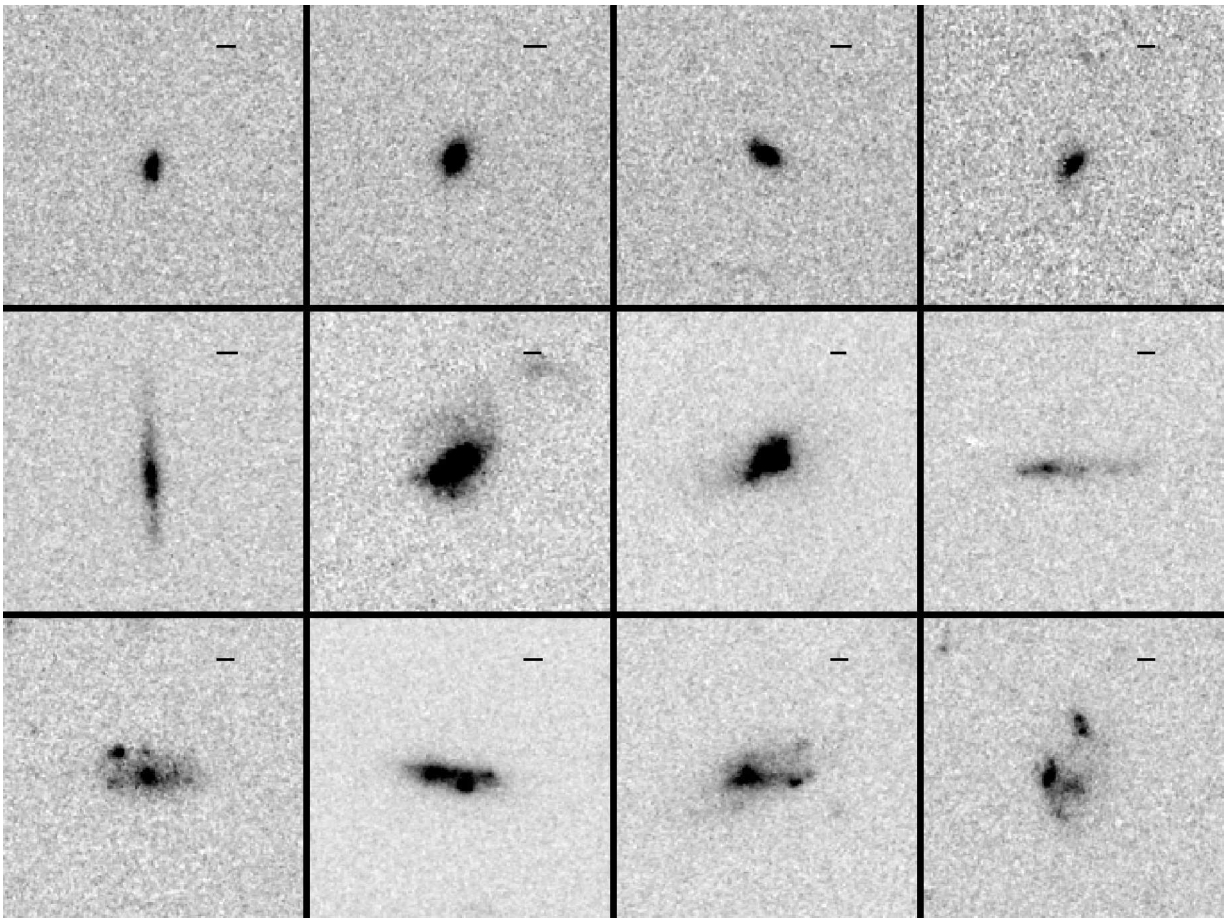

Figure 4.9: Example of the starburst morphological classes in our sample at intermediate redshift, a 2 kpc bar is showed at the top right of each image. Sknot galaxies (top row), Sknot+diffuse galaxies (middle row), and Mknots galaxies (bottom row).

galaxies. Like this we identify the presence of star forming knots and parametrize them.

We classify the galaxies according to the distribution of their SF clumps, as in chapter 3 in Sknot, Sknot+diffuse, and Mknot galaxies. Each individual knot is measured and its mass, size, and relative position in the galaxy is obtained.

4.3.1 Mass of the knots

To estimate the mass of knots in the intermediate redshift sample, we assume the same $V-I$ color for galaxies and knots, in section 3.2.4 we demonstrated that this assumption is good accurate enough for our purpose. The $V-I$ color allow us to estimate the log(M/L) of the knots (Bell & de Jong 2001), then with the F814W band luminosity we estimate the mass of the knots. The mass range for knots is $10^6 M_\odot < M < 10^{10} M_\odot$, with a mean of $10^{8.3} M_\odot$. Figure 4.10 shows the mass distribution of knots at intermediate redshift.

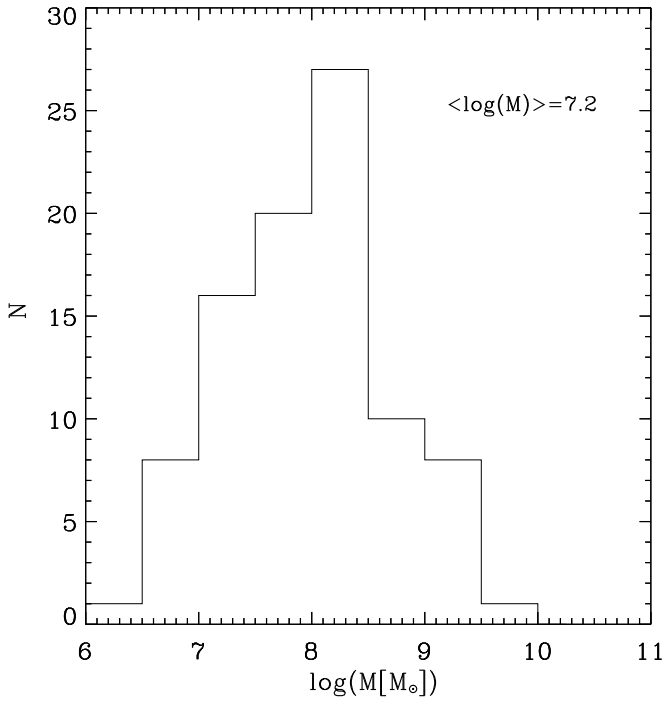

Figure 4.10: Mass distribution of the individual knots of star formation for the sample of galaxies at $0.32 \leq z \leq 0.9$

4.3.2 Spatial distribution of multiple knots

The center of the galaxies are calculated using the barycenter of the emission, within the outer isophote, with SExtractor. For each individual knot of star formation, the center is calculated as the maximum luminosity of the isophote. We also assumed a circular symmetry to estimate their radii as the equivalent to the radius of the isophotal area. Figure 4.11 shows the knot radius vs. distance to the center for knots in our intermediate redshift sample, from this figure we define the knots as: centered, lopsided, or offcenter in the same way that we did in chapter 3. In Fig. 4.12 we show the ellipticity distribution of the knots for the different classes.

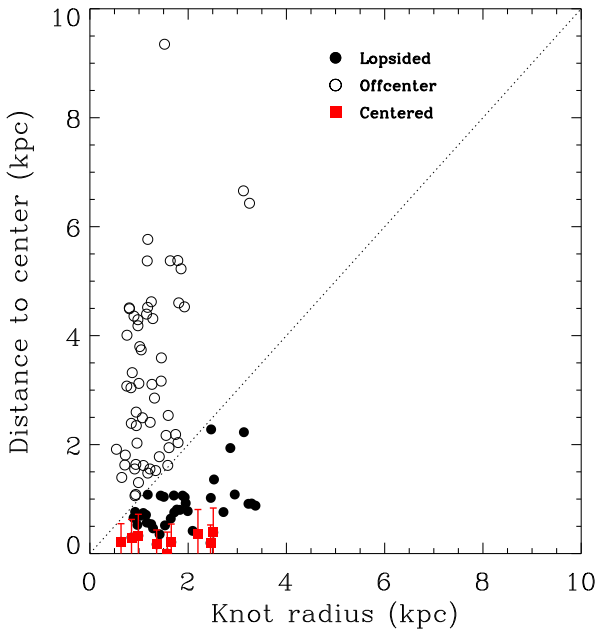

Figure 4.11: Knot sizes versus their distance to the center of the galaxy. From the diagram we separate three classes: offcenter (open circles), lopsided (filled circles) and centered (red squares with error bars) regions. A bisector separates two regions. Filled circles show regions in contact with the center of the galaxy and open circles show regions offcentered. Regions which overlap with the geometrical center of the galaxy are labeled centered and represented with squared symbols. Overplot bars account for the spatial resolution.

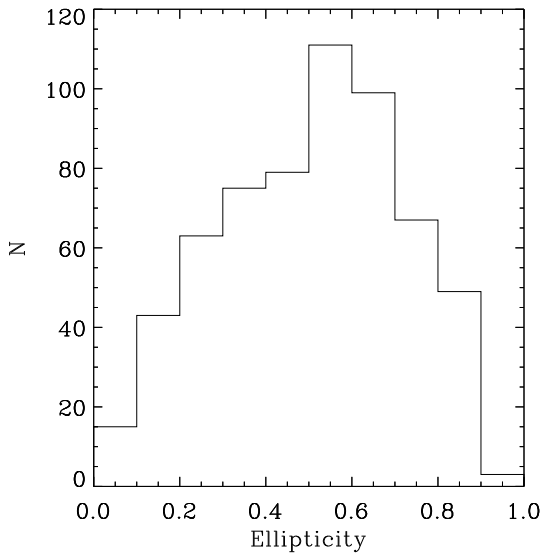

Figure 4.12: Ellipticity distribution of the SF knots.

In Fig. 4.13 we represent the mass of the knots calculated in section 4.3.1 with respect to the distance to the center of the galaxy. From this figure we can see that more massive knots of star formation are closer to the center of the galaxy.

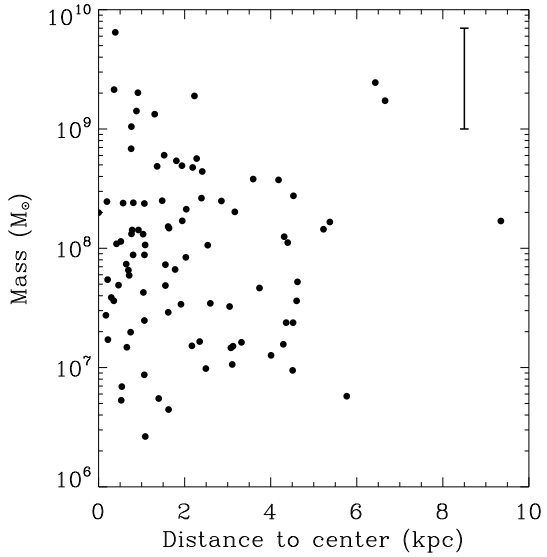

Figure 4.13: Mass vs. distance to the center for knots of the intermediate redshift sample.

4.4 Luminosity function of the starburst in COSMOS ($0 < z < 0.9$)

We estimated the luminosity function (LF) of the starburst galaxies using the $1/V_{max}$ method (Schmidt 1968; Avni & Bahcall 1980). This method assumes that for a given absolute magnitude

$$\phi(M_V) = \sum_{j=1}^{N_g} \frac{1}{V_{\max}(j)}, \tag{4.1}$$

where $V_{\max}(j)$ is the maximum volume available for a galaxy j and N_g is the total number of galaxies in the sample. For the sake of comparison with previous studies, the LF has been calculated using the $V-$band rest-frame magnitudes derived from the K-correction described in section 4.2.1. In addition, following Ilbert et al. (2009), we used as projected area covered by the COSMOS photometric redshift catalogue A=1.73 deg^2. The $1/V_{\max}$ method is widely used due to both its simplicity and because no *a priori* assumption of the LF functional form has to be made. Nevertheless, it assumes a homogeneously distributed sample of sources, and thus, effects such as cosmic variance or aggregations of starburst galaxies, can falsify this hypothesis. To test the suitability of our sample to the $V_{\max}$ method we applied the $V/V_{\max}$ statistical test developed by Schmidt (1968). The idea behind this test is to compute the ratio $V/V_{\max}$, where V is the maximum volume probed by the survey up to the source distance. Therefore, for an uniform distribution we expect

$$\langle \frac{V}{V_{\max}} \rangle = 0.5 \pm \frac{1}{\sqrt{12\,N_g}}, \tag{4.2}$$

Table 4.1: Parameters determined fitting a Schechter function to the LF for the different redshift bins.

Δz	α	ϕ^*	$M_\star$
$0 <$ z ≤ 0.28	-1.9 $\pm$ 0.4	3.98e-08 $\pm$ 3.96e-08	-19.6 $\pm$ 2.3
$0.38 <$ z ≤ 0.44	-1.5 $\pm$ 0.23	5.70e-08 $\pm$ 4.47e-08	-18.76 $\pm$ 0.59
$0.44 <$ z ≤ 0.5	-1.71 $\pm$ 0.71	2.09e-07 $\pm$ 2.93e-07	-18.37 $\pm$ 0.81
$0.5 <$ z ≤ 0.57	-1.36 $\pm$ 0.42	2.26e-07 $\pm$ 1.05e-07	-18.36 $\pm$ 0.35

and any deviation from the predicted error would imply that the hypothesis of homogeneity is not valid. We found values of $\langle V/V_{\rm max} = \rangle$ 0.45 compared to the predicted 0.5, so our results are not strongly affected by cosmic variance.

In our sample at intermediate redshift, we estimated the luminosity function for the entire photometric sample in the redshift range $0.32 \leq z \leq 0.57$. We also explored the luminosity function in the different redshift bins used in our search $0.32 \leq z \leq 0.38$, $0.38 < z \leq 0.44$, $0.44 < z \leq 0.5$, and $0.5 < z \leq 0.57$. Unfortunately, for the first redshift range $0.32 \leq z \leq 0.38$ it was not possible to do a good estimation of the LF because there were not enough of galaxies. Fig. 4.14 shows LF of the starburst galaxies at intermediate redshift in the $V-$band rest-frame for the total photometric sample. Figs. 4.15(a), 4.15(b), and 4.15(c) show the starburst galaxies at intermediate redshift LF in the $V-$band rest-frame for the redshift ranges: $0.38 < z \leq 0.44$, $0.44 < z \leq 0.5$, and $0.5 < z \leq 0.57$, respectively. Poissonian errors associated with each magnitude bin are also shown. The starburst galaxies LF was fitted adopting a Schechter function (Schechter 1976), where M* is the characteristic magnitude, ϕ^* is the characteristic number density, and α is the faint-end slope (Lin et al. 1996):

$$\phi(M) = \phi^*(0.4ln10)exp(-10^{-0.4(M-M_*)})10^{-0.4(M-M_*)(1+\alpha)}$$

The best-fit is shown in Figs. 4.14, 4.15(a), 4.15(b), and 4.15(c). For the total photometric sample best-fit parameters are given in table 4.1.

Despite the ample literature on the study of the redshift evolution of the LF of emission-line galaxies (see Sobral et al. 2013, and references therein), a proper comparison with our work is not straightforward. This is mainly due to both our strict EW limit used to separate starburst galaxies from simply emission-line galaxies, and the intermediate redshift ranges probed in this study.

Interestingly, Liu et al. (2008) studied the faint-end (α) of the LF of starburst galaxies in the COSMOS field. They selected starburst galaxies based on a SED fit, and divided their sample in redshift bins of Δz = 0.1 spanning from $0 <$ z $<$0.5. Our best-fits: α=-1.9, -1.36, -1.5, and -1.71 for the redshift ranges: $0 \leq z \leq 0.28$, $0.38 < z \leq 0.44$, $0.44 < z \leq 0.5$, and $0.5 < z \leq 0.57$, are in good agreement with those published by Liu et al. (2008) for the redshift ranges: $0.02 <$ z < 0.1 (α=-1.88), $0.1 <$ z < 0.2 (α=-1.65), $0.2 <$ z < 0.3 (α=-1.53), $0.3 <$ z < 0.4 (α=-1.35), and $0.4 <$ z $<$ 0.5 (α=-1.27).

4.5 Results

4.5.1 Redshift evolution of the number density of starburst

In this chapter we have computed the luminosity function of starburst galaxies for galaxies in the redshift range from $0.38 < z < 0.57$ (see table 4.1). For the sake of comparison, we have performed the same exercise in the low redshift sample described in chapters 2 and 3. Fig. 4.16 shows the starburst galaxies LF at redshift $0 < z < 0.27$ in the $V-$band rest-frame. Poissonian errors associated with each magnitude bin are also shown. The starburst galaxies LF was fitted adopting a Schechter function (Schechter 1976), and the best-fit is also shown in Fig. 4.16. We found as best-fit parameters α=-1.9 $\pm$ 0.4, $\log \phi_\star$=-7.4 $\pm$ 0.3, and $M_\star$=-19.6 $\pm$ 2.3.

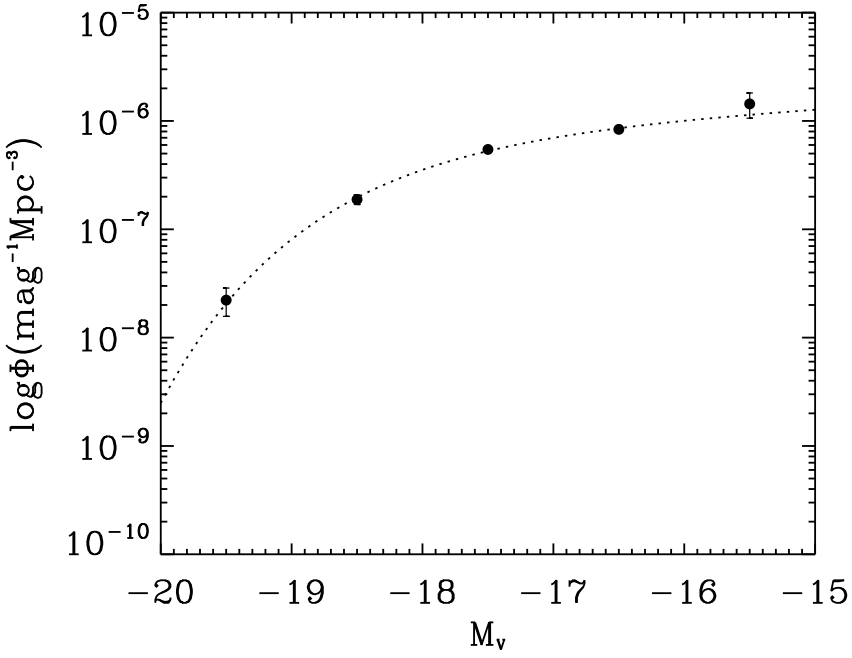

Figure 4.14: Luminosity function estimated using the $1/V_{\max}$ method in the $V-$band rest-frame of the starburst galaxies at intermediate redshift for the total photometric sample. Errors in each bin are associated to the Poissonian statistics. The dotted line shows the best-fit to the Schechter function.

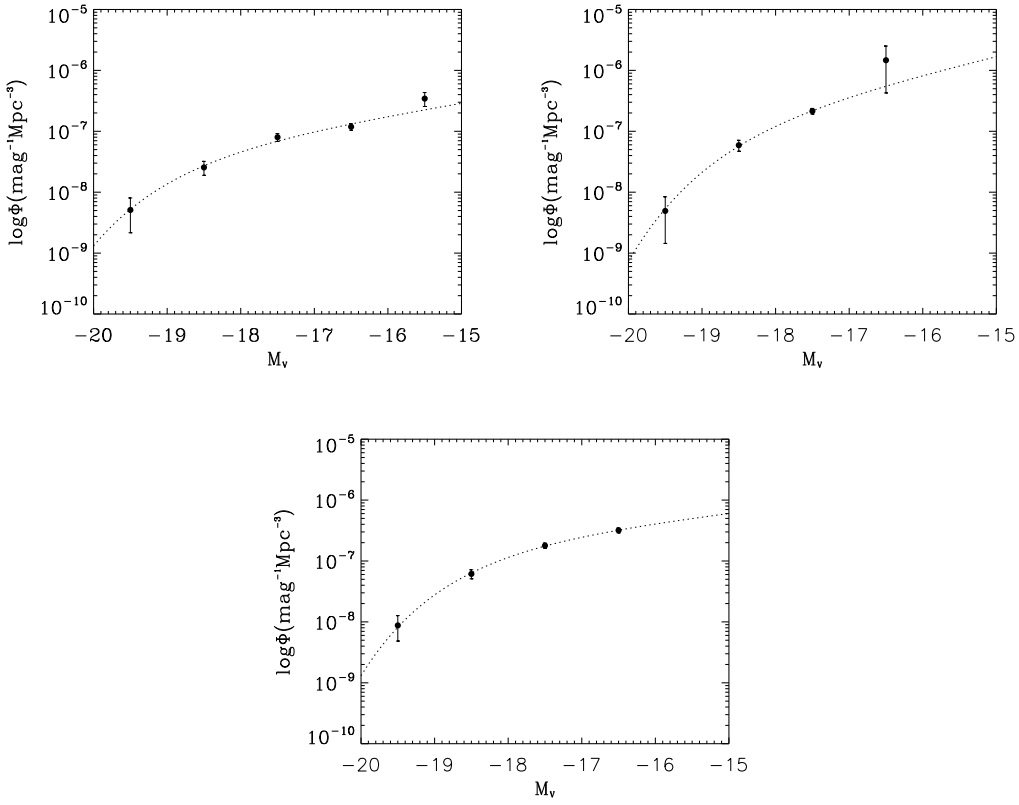

Figure 4.15: Luminosity function estimated using the $1/V_{\rm max}$ method in the $V-$band rest-frame of the starburst galaxies at intermediate redshift sample in three different redshift ranges. Top left: $0.38 < z \leq 0.44$, Top right: $0.44 < z \leq 0.5$, and Bottom: $0.5 < z \leq 0.57$. Errors in each bin are associated to the Poissonian statistics. The dotted line shows the best-fit to the Schechter function.

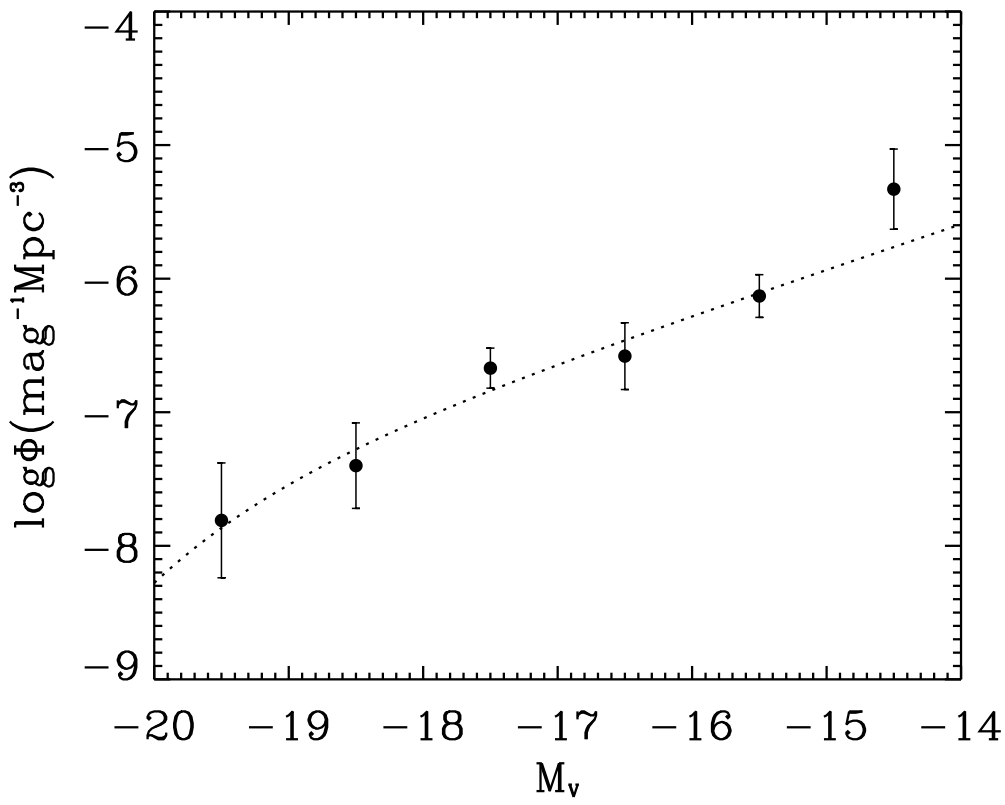

Figure 4.16: Luminosity function estimated using the 1/Vmax method in the $V-$band rest-frame of the starburst galaxies at redshift $0 < z < 0.28$.

Table 4.2: Clumpy fraction at different redshifts

redshift range	f_{clumpy}
$0 < z \leq 0.28$	0.24
$0.32 \leq z \leq 0.384$	0.20
$0.384 < z \leq 0.44$	0.12
$0.44 < z \leq 0.5$	0.11
$0.5 < z \leq 0.57$	0.13

It is evident from table 4.1 and from the results at low redshift that the values of $\phi_\star$, and $M_\star$ are poorly constrained with the available observations. However, the values of the faint-end slope are reasonable well determined and show a clear decrease of the slope from α=-1.9 at redshift $0 < z < 0.27$ to α=-1.36 at $0.5 < z < 0.57$. The faint-end slope of the luminosity function is directly related with the relative number of dwarf galaxies for a given population as a function of the magnitude. Thus, a flattening of the slope implies that there are relatively the same number of dwarf galaxies at every magnitude below the limit of the dwarf population (typically $M_* > -18$).

The observed evolution of the faint-end slope for starburst galaxies found in this work is qualitatively in agreement with the global trend of the full population of galaxies finding in the literature. The local faint-end slope of the LF obtained from two of the largest local galaxy surveys to date, 2dFGRS and SDSS found typical values of $\alpha = -1.21 \pm 0.03$ (Norberg et al. 2002) and $\alpha = -1.3 \pm 0.01$ (Blanton et al. 2005), respectively. At higher redshift, Liu et al. (2008) derived $\alpha = -1.12 \pm 0.1$ in the range $0.4 < z < 0.5$ for a portion of the COSMOS survey area. In the same paper, Liu et al. (2008) derived also the faint-end slope of galaxies with different morphological types. They selected starburst galaxies based on a SED fit, and divided their sample in redshift bins of $\Delta z = 0.1$ spanning from $0 < z < 0.5$. Our best-fit values of α listed in table 4.1 are in good agreement with those published by Liu et al. (2008, see their table 2) for all the redshift ranges $0.02 < z < 0.1$ (α=-1.88), $0.1 < z < 0.2$ (α=-1.65), , $0.3 < z < 0.4$ (α=-1.35), and $0.4 < z < 0.5$ (α=-1.27).

4.5.2 Redshift evolution of the clumpy fraction

In Sect. 3.3.1 we computed the clumpy fraction (f_{clumpy}) for all our starburst galaxy sample up to redshift ~ 0.28. We found a value of $f_{clumpy} \sim 0.24$. In this chapter, we have extended this analysis at higher redshift using the new sample described in Sect. 4.1. The clumpy fraction in the different redshift bin is shown in table 4.2.

As already explained in the previous chapter, the clumpy fraction (f_{clumpy} ; clumpy galaxies/SF galaxies) have been investigated for different redshift and mass ranges (Elmegreen et al. 2007; Overzier et al. 2009; Puech 2010; Guo et al. 2012; Wuyts et al. 2012; Guo et al. 2014; Murata et al. 2014; Tadaki et al. 2014). A common conclusion of all these works is that f_{clumpy} increases with redshift. It is clear from Table 4.2 that our result show the opposite trend, with a decrease of f_{clumpy} in our redshift range from $0 < z < 0.57$. Our values are also compatible with a constant evolution once the errors due to the number statistics are taken into account. A close look to previous works in the literature such as Murata et al. (2015) show that a distinct clumpy fraction is only seen at redshift $z > 0.8$, with many of the previous references having only one redshift bin for $z < 0.5$.

We have studied the effect of resolution as a caveat for our f_{clumpy} values. Fig. 4.17 show the knot sizes in our complete sample as a function of the redshift. The solid line represents the variation of the physical resolution for the standard HST/ACS PSF of 0.09 arcsec. From this figure it is clear that there are many clumps of star formation at low redshift that due to lack of resolution are not going to be resolved in our sample at intermediate redshift. We have done the exercise of not considering the clumps of star formation in the sample at low redshift with sizes $\leq$ 600 pc and estimate again the f_{clumpy}. This represents the limitation resolution of our intermediate redshift sample up to z$\sim$0.57. We found a value of f_{clumpy}=0.08 which is in good agreement with a constant

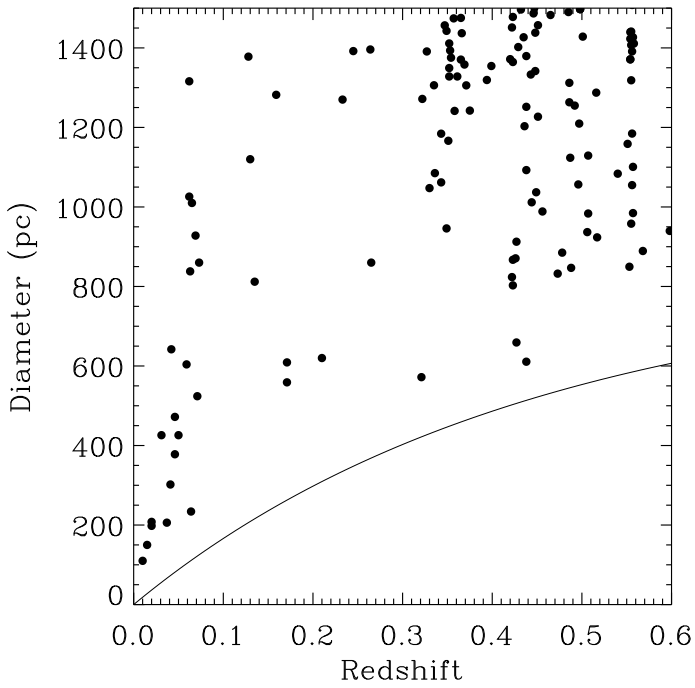

Figure 4.17: Size versus redshift of the clumps of star formation. The PSF limit is showed as a limitation in the estimation of the sizes of the clumps.

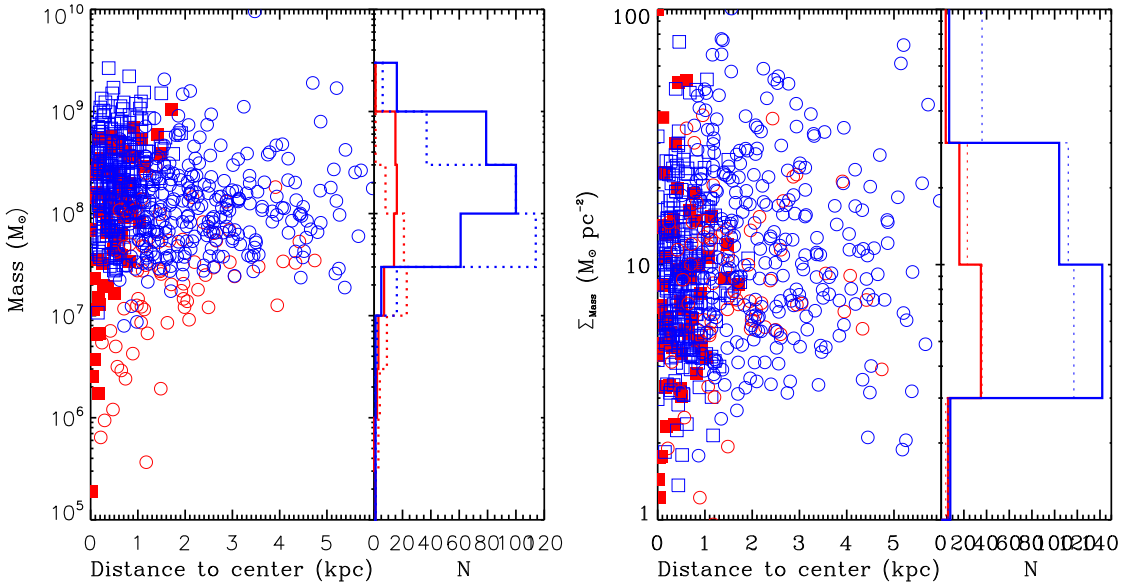

Figure 4.18: Mass and Σmass for sample at low (red) and intermediate (blue) redshift. Circles represent offcenter knots, and square are lopsided. The distribution of mass and Σmass are shown in the right of each panel, solid and dotted lines are centered and lopsided knots, respectively.

value of f_{clumpy} in our redshift range. In addition, our values are also compatible with a constante evolution once the errors are considered.

4.5.3 Redshift evolution of the star-forming knot properties

An important goal of this thesis is the study of the evolution of the properties of the star- formation clumps with the redshift. Since our sample selection procedure was devised to identify the same type of starburst galaxies, and assuming that both samples cover approximately the same mass range $10^6 < M/M_\odot < 10^{11}$ (see Fig. 2.10 and 4.6), we can study this evolution by comparing the properties of the sample found at low redshift (chapters 2 and 3) with the sample at intermediate redshift found in this chapter.

Fig. 4.18 shows the mass and surface-mass density ($\Sigma mass$), as a function of the distance to the center for the low redshift sample (red symbols) and intermediate redshift sample (blue symbols). As a general trend, the distribution of the starburst galaxies in the low and intermediate redshift samples cover roughly the same regions of the parameter space in both panels with only small differences in the both the low mass. To quantify these differences we plot in each panel the distribution of masses (panel a) and Σmass (panel b) for both sample.

Despite these small differences that can be attributed to the tails of the mass distributions. We can confirm the results obtained in chapter 3 about the relation of the knot properties and their position within the galaxy: Centered clumps show slightly higher mass than offcentered ones. In panel (a) we see that more massive clumps of star formation are closer to the galaxy center for both samples, while in panel (b) the Σmass for both samples has not important variations with respect to the distance to the center.

Chapter 5

Characterizing the host galaxies: 2D modelling

Among the main properties that characterize the galaxies, their morphology and light distribution are key to understand their evolution. The different structural components contributing to the galaxy surface-brightness, like bulges, discs, and bars provide a set of observational constraints that have to be fulfilled by whatever model aiming at explaining the formation and evolution of the galaxies.

In this chapter we apply the state of the art bidimensional algorithms to model the host galaxy of starbursts with the aim to derive reliable luminosity profiles. The question to be answered is whether the host of the starbursts in COSMOS, at redshift $z < 0.5$, are disk-like structures or not. A major challenge of this study is to decontaminate the host galaxy light from the emission from the starburst clumps. This imply to be able to identify and parametrize such structures with a high degree of accuracy therefore imposing a maximum redshift limit. In chapters 2 and 3 we have already done this parameterization and the results concerning the morphology of the starburst knots have been used in this chapter to identify and mask the corresponding areas. Only able to do so, a good modeling of the host galaxy of starburst can be done. Therefore the method here empirical can only be implemented for galaxies where starburst can be spatially resolved, and this is what have been done and presented in the chapter. The fit is performed by modeling used of the high spatial resolution data in the HST ACS F814W−*band*.

5.1 Luminosity profile in galaxies

The luminosity profile of one or various components of a galaxy is often characterized by a analytical expression which models the flux distribution through analytical functions. There are two principal techniques to fit the luminosity profile of galaxies depending on whether unidimensional or bidimensional luminosity profiles are used.

One-dimensional profile

The unidimensional profile of a galaxy, or 1D profile, represents the luminosity distribution of a galaxy as a function of its distance to the center. To obtain this profile several methods can be implemented depending on the nature of the galaxy. The most common method is to perform an elliptical isophotal analysis from a galaxy image in a given filter to obtain an average value for a

given radius. As an example of this method, the task ellipse of IRAF[1] fits elliptical isophotes to a galaxy image with the center of the galaxy as the center of the ellipse. The image is measured using an iterative method (Jedrzejewski 1987) where each isophote starts with initial values of X, Y, semi-major axis, ellipticity, and position angle, and then the best fit to an ellipse is found.

Even if 1D profiles decomposition have been used in different studies (ref. eg: Cairós et al. (2003), Caon et al. (2005)), some difficulties appear when dealing with galaxies with high star-formation starbursts. The presence of star-forming regions produce an excess of luminosity at a given radius, as a result of this excess, the value of the fitted slope of the surface-brigthness could be over estimated. Caon et al. (2005) analyzed the luminosity profile of 8 BCD galaxies using a 1D method. To deal with star-forming regions, they first identified the spatial region occupied by the starburst. Then, they defined a cutoff radius outside which the starburst emission is absent. Finally, the fit was done for radius larger than the cutoff radius.

An obvious problem with this technique arise when the starburst regions are spread all over the extent of the galaxy, i.e., when the star-forming regions cover most of the galaxy. In these case there is a significant loss of information and as a result the fit is very uncertain.

Two dimensional profile

This methodology allows us to fit a model of the luminosity distribution of galaxies directly on images. It is a pixel to pixel fit, therefore without the necessity of obtaining average values and avoiding important information loss from the image. This technique provides important advantage compared with the classical 1D profiles, for example, in the bulge/disc decomposition (see Shaw & Gilmore (1989); Byun & Freeman (1995); Wadadekar et al. (1999); Khosroshahi et al. (2000)). Some examples of algorithms codes developed to deal with 2D fitting directly from the galaxy image includes: GIM2D (Simard 1998), GALFIT (Peng et al. 2002), and GASP2D (Méndez-Abreu et al. 2008).

An important advantage of 2D fitting algorithms, when dealing with galaxies with star-forming regions, is the possibility to mask areas on the images. This allows to fit the surface-brightness distribution of galaxies without discarding the luminosity values at the star-forming region radius. A carefully selection of the mask allow to isolate the star-forming region, and therefore fit the host galaxy with a large portion of its size (see Amorín et al. 2007, 2009).

5.2 Analytical functions for the radial profiles

A number of analytical functions have been proposed to fit the radial profile of the luminosity of galaxies. Nowadays, the most commonly used profile is the Sersic profile for its ability to recover the features of several kind of galaxies and stellar structures.

In the following we will briefly describe the main analytical function used in the literature.

The **Sersic profile**, one of the most used functions to fit the luminous profile of galaxies. It was proposed by Sersic (1968) and its mathematical formulation is given by:

$$\Sigma(r) = \Sigma_e \; exp\left[-\kappa\left(\left(\frac{r}{r_e}\right)^{1/n} - 1\right)\right] \tag{5.1}$$

In this formulation r_e is the effective radius, the radius where half of the total flux is comprised. Σ_e is the surface brightness at the effective radius. The parameter "n" is known as the concentration parameter, it gives information about how concentrated is the flux of the galaxy. For high values of n, the flux is concentrated first in the center of the galaxy and then extend to large radius, for low

[1]IRAF is distributed by NOAO, which is operated by AURA Inc., under contract with the National Science Foundation.

values of n the flux is less concentrated in the center but have a truncation at larger radius. Some particular cases of the Sersic profile are the Gaussian profile (n=0.5), exponential disk-like profile (n=1) and the De Vaucouleurs profile which describes galaxy bulges (n=4).

The κ parameter is a dependent variable coupled to n such that r_e enclose half of the integrated luminosity of the galaxy in a projected area $A = 4\pi r^2$, which is given by

$$L(< r) = \Sigma_e \; r^2 \; 2\pi \; n \frac{e^\kappa}{\kappa^{2n}} \gamma(2n, \kappa) \tag{5.2}$$

The value of κ could be estimated numerically. It is also possible to have an approximation in a range of values for n (e.g., $0.5 \leq n \leq 16.5$, Caon et al. (1993)) as $\kappa \sim 2n - 1/3$. In the limit when $r \to \infty$, the gamma function could be expressed as $\gamma(2n, \kappa) \to \Gamma(2n) = (2n-1)!$ (Ciotti 1991; Graham et al. 2005), which in eq. 5.2 gives the total luminosity.

The **exponential disk profile** has been mainly used to fit the external regions of exponential disks. The common form given by Freeman (1970) is described by:

$$\Sigma(r) = \Sigma_0 exp\left(-\frac{r}{r_s}\right) \tag{5.3}$$

Here r_s is the scale length radius, the radius where the profile intensity fall e^{-1}. The exponential disk profile is a special case of the Sersic profile for n=1, in this case r_e=1.678 r_s.

The **Gaussian profile** is another special case of the Sersic profile, in this case n=4. The expression for this profile is:

$$\Sigma(r) = \Sigma_0 exp\left(-\frac{r^2}{2\sigma^2}\right) \tag{5.4}$$

In this profile, the size parameter is the FWHM instead of r_e, which is given by $FWHM = 2.354\sigma$.

Fig. 5.1 (Peng et al. 2010, Fig. 3) shows the Sersic profile for different n values, some particular cases are n=0.5 (Gaussian profile), n=1 (exponential disk profile), and n=4 (Gaussian profile).

The $\mathbf{r}^{1/4}$ **profile** was proposed by de Vaucouleurs (1948, 1953) to fit the luminosity profile of spheroidal objects such as elliptical galaxies and bulges. Its formulation is given by:

$$I(r) = I_e 10^{-3.33[(r/r_e)^{1/4}-1]} \tag{5.5}$$

I_e is the effective surface brightness. The value 3.33 was chosen to be r_e the effective radius.

The **The Ferrer profile** (bin 1987, Fig. 4) is a nearly flat core with a pronounced truncation, this profile is often used to fit galaxy bars and lenses profiles, the expression is given by:

$$\Sigma(r) = \Sigma_0 \left(1 - (r/r_{out})^{2-\beta}\right)^\alpha \tag{5.6}$$

where $r \leq r_{out}$, beyond which the function has the value 0. The α parameter defines the sharpness of the truncation, and the β parameter defines the sharpness of the central slope. Fig. 5.2 (Peng et al. 2010, Fig. 4) shows the feature of a modified Ferrer profile.

The **King profile** is often used to fit the profile of globular clusters, it has the form:

$$\Sigma(r) = \Sigma_0 \left[1 - \frac{1}{(1 + (r_t/r_c)^2)^{1/\alpha}}\right]^{-\alpha} \times \left[\frac{1}{(1 + (r/r_c)^2)^{1/\alpha}} - \frac{1}{(1 + (r_t/r_c)^2)^{1/\alpha}}\right]^\alpha \tag{5.7}$$

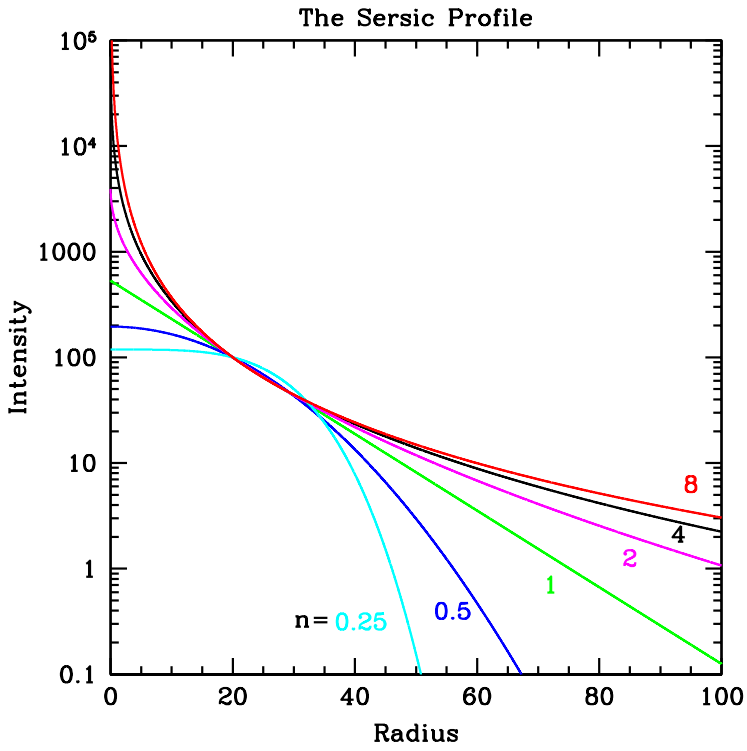

Figure 5.1: Sersic profiles for different values of n. r_e and Σ_e are held fixed. Note that the larger the n value, the steeper the central core, and more extended the outer wing. A low value for n has a flatter core and a more sharply truncated wing.

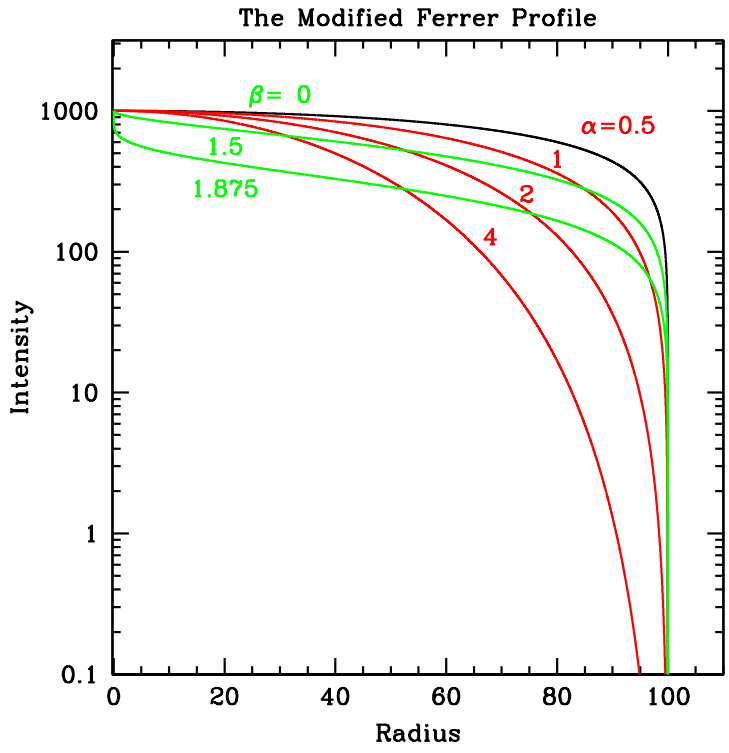

Figure 5.2: Modified Ferrer profile. The black reference curve has parameters $r_{out} = 100$, $\alpha = 0.5$, $\beta = 2$, and $\Sigma_0 = 1000$. The red curves differ from the reference only in the α parameter, as indicated by the red numbers. Likewise, the green curves differ from the reference only in the β parameter, as indicated by the green numbers.

where r_c and r_t are the core and truncation radius. The α parameter has a value 2 in the standard empirical King profile. Fig. 5.3 (Peng et al. 2010, Fig. 5) shows the feature of the King profile.

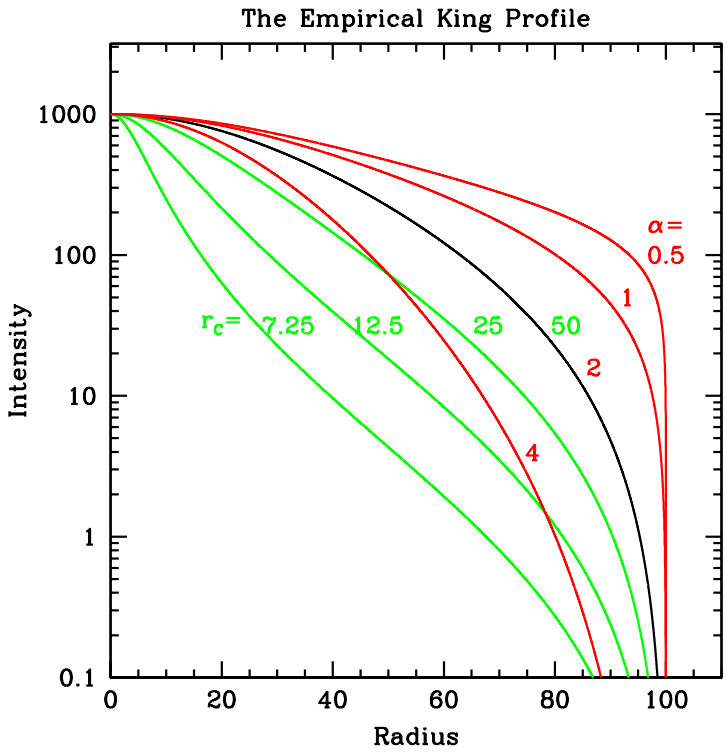

Figure 5.3: Empirical King profile. The black reference curve has parameters $r_c = 50$, $r_t = 100$, $\alpha = 2$, and $\Sigma_0 = 1000$. The red curves differ from the reference curve only in the α parameter, as indicated by the red numbers. Likewise, the green curves differ from the reference only in the r_c parameter, as indicated by the green numbers.

The **Nuker profile** (Lauer et al. 1995) is often used to fit the nuclear profile of nearby galaxies. This profile has the form:

$$I(r) = I_b 2^{\frac{\beta-\gamma}{\alpha}} \left(\frac{r}{r_b}\right)^{-\gamma} \left[1 + \left(\frac{r}{r_b}\right)^{\alpha}\right]^{\frac{\gamma-\beta}{\alpha}} \tag{5.8}$$

This profile has a double power-law, where β is the outer power-law slope, γ is the inner slope, and α controls the sharpness of the transition. Fig. 5.4 (Peng et al. 2010, Fig. 7) shows the feature of the Nuker profile profile.

The **Edge-On disk profile** is used to fit the surface brightness for flattened galaxies viewed edge on, it has the form:

$$\Sigma(r,h) = \Sigma_0 \left(\frac{r}{r_s}\right) K_1 \left(\frac{r}{r_s}\right) sech^2 \left(\frac{h}{h_s}\right) \tag{5.9}$$

where r_s is the disk scalelength, h_s is the perpendicular disk scale-height, and K_1 is the Bessel function.

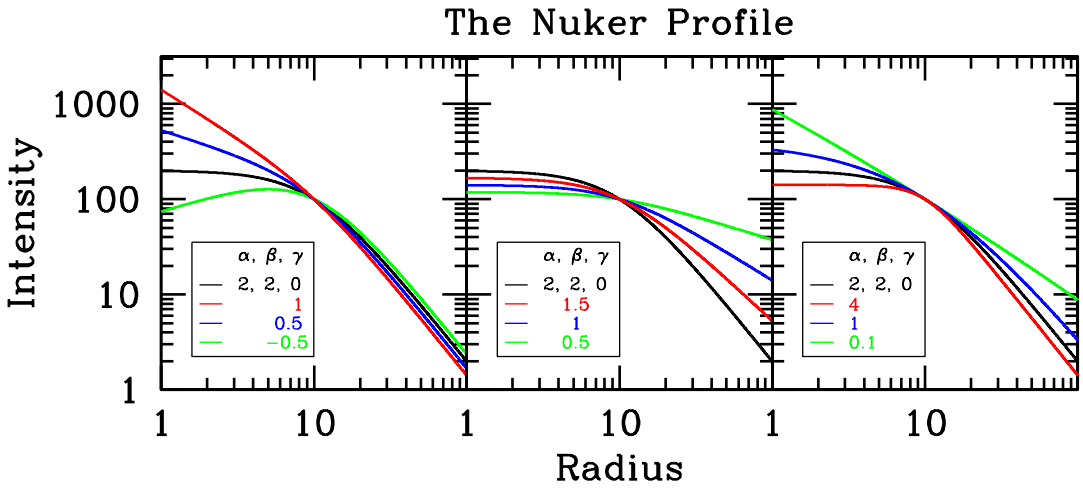

Figure 5.4: Nuker profile. The black reference curve has parameters $r_b = 10$, $\alpha = 2$, $\beta = 2$, $\gamma = 0$, and $I_b = 100$. For the other colored lines, only one value differs from the reference, as shown in the legend.

5.3 GALFIT

GALFIT [2] (Peng et al. 2002) is a 2D algorithm based on the Levenberg-Marquardt minimization method (Press et al. 1997). It is written in C language and designed to fit the luminosity profile of well resolved galaxies. The ability for simultaneously fit the luminosity profile with an arbitrary number of components (e.g. bulge, disk, bar), or splits merged components allowing to separate their individual profiles, combined with an optimized computer speed makes this algorithm a powerful tool for the analysis of the luminosity profile of galaxies and their components.

GALFIT fits analytical functions, most of them described in section 5.2, combining them simultaneously to fit the luminosity profile of galaxies and point sources directly over digital images. This analysis allows to obtain parameters like: luminosity, size, concentration of the central profile, position angle, axis ratios, etc.

When running GALFIT the user has the option to mask a region of the image, then excluding pixels from the fit. The optional masked area was first introduced by Peng et al. (2002) to avoid for dust lane regions seen on some galaxies which can affect the luminosity profile, or bad pixels regions on the images. Amorin et al. (2007, 2009) implemented the method of masked areas to Blue Compact Galaxies (BCGs) or Dwarfs with star-forming regions. They studied simulated Amorín et al. (2007), and real (Amorín et al. 2007, 2009) BCGs masking regions with star-formation using ellipses with different sizes. They find a stability region where the masked area covers the starburst emission and the area of the host galaxy with a good S/N is enough to do the fit. As a result of this study, they defined a method to analyze the luminosity profile on galaxies with star-formation. The details of this method will be given in section 5.4. To fit the luminosity profile of our sample (chapter 2) we used GALFIT with masks on the star-forming regions defined in section 3.1.2.

To run GALFIT we need a series of initial data. In the following we will detail which are the input data we have used. Basically GALFIT needs: the CCD image of the galaxy, an image with the sigma noise pixel to pixel (sigma image), a Point Spread Function (PSF) image, a mask image (optional), and one or several models for the fit.

[2] http://users.obs.carnegiescience.edu/peng/work/galfit/galfit.html

Science Image

The input data image is a FITS file. Our selected catalogue was obtained from the COSMOS database. One of the principal advantage of this database is the high spatial resolution images from the HST ACS F814W band. A total of 575 frames of 203"×203" were observed four times, with equal-length exposure time of 507 seconds, obtaining an integrated time of 2028 seconds for every frame.

For every galaxy in our sample, we found its respective frame, then we cut an image with a size of 201×201 pixels as an initial size with the galaxy in the center, this is the image used for the fit as science image. At the moment of running the algorithm we resize the image according to the size of the galaxy in the image.

Sigma Image

To obtain a good CCD image of an astronomical object, several processes have to be done, from obtaining the data to the final calibrated image. These processes, including the instrumental noise, produce statistic random noise that is different at every pixel of the image. To estimate the flux at some pixel of the image, the sigma value of the statistic random noise in that pixel should be considered. GALFIT uses a χ^2 method to estimate the best luminosity profile of a galaxy, this χ^2 is a sum of deviations between the data flux and the best fitting model, relative to the expected deviation (σ) at each pixel, which is defined as:

$$\chi^2_\nu = \frac{1}{N_{dof}} \sum_{x=1}^{nx} \sum_{y=1}^{ny} \frac{(flux_{x,y} - model_{x,y})^2}{\sigma^2_{x,y}} \tag{5.10}$$

Where N_{dof} is the number of degrees of freedom in the fit. GALFIT uses as input file a sigma map image, which gives relative weights to the pixels during the fit, this image can be estimated with GALFIT or can be add by the user. To choose a good sigma image improves considerably the results of the fit.

In COSMOS there is a sigma image for every tile, which takes into account the different processes to obtain the final image (Koekemoer et al. 2007). For every galaxy we downloaded the tile and the sigma image, then we cut in the same position over the detector, so that it coincides with the size and coordinates of the Science Image.

Point Spread Function (PSF) Image

The PSF is an important input for the fit, GALFIT convolves the model with the PSF to obtain the luminosity profile. A wrong choice of the PSF affects directly to the output model.

To obtain a good PSF from the HST ACS camera is not easy, particularly because the geometrical variations along the CCD and temporal variations in the focus. To deal with these difficulties, we made use of a method previously implemented by Rhodes et al. (2007) for images of the ACS WFC camera in the COSMOS field. To cover the complete COSMOS field with the ACS WFC camera, it was necessary to observe 575 frames, each of them observed four times with an observation time of 507 (s). To deal with the spatial variations of the focus along the CCD, we choose a circle around the galaxy with a radii of 500 pixels, then we search for bright stars in the 575 frames of COSMOS inside that circle. To take into account the temporal variation of the focus, we used the values of the focus, for each frame, obtained by Rhodes et al. (2007), and then we look for tiles with a similar focus ($\pm$ 1 μm) to the frame where our galaxy is located. With these two criteria we found several stars ($\sim$ 30) to construct the PSF for every galaxy.

Mask Image

To model the luminosity profile of the host galaxy in presence of star-forming regions it is necessary to mask the area of the starburst. To construct a mask of this region we used FOCAS. Star-forming knots embedded in the more diffuse and extended emission were found as explained in sect. 3.1.2. Then we assign the value 1 to the region corresponding to the knot and 0 to the rest of the frame. In summary, we used all the star-forming knots catalogued and presented in chapter 3.1.2 as the mask images to be used with GALFIT.

Input file

To run GALFIT an input file is used, in this file the user introduces the images, parameters and models to be used in the fit. There are two principal blocks, the control parameters and the models to be used. Fig. 5.5 shows the block were the input images and region of the science image where the fit is done are introduced. In this example we show a galaxy from our sample. Fig. 5.6 shows an example of a model to be ran by GALFIT, in this case we used a Sersic profile. To the right of most parameter in Fig. 5.6, we put a number 1. It means that the parameters are allowed to vary while the fitting is done, if that number is 0 the parameter is fixed.

```
# IMAGE and GALFIT CONTROL PARAMETERS
A) cosmos_37_sci.fits     # Input data image (FITS file)
A1) I                     # Band labels
A2) 8140                  # Band wavelengths
B) cosmos_37_out.fits     # Output data image block
C) cosmos_37_wht.fits     # Sigma image name (made from data if blank or "none")
D) psf_cosmos_037.fits    # Input PSF image and (optional) diffusion kernel
E) 1                      # PSF fine sampling factor relative to data
F) mask_cosmos_37.fits    # Bad pixel mask (FITS image or ASCII coord list)
G) none                   # File with parameter constraints (ASCII file)
H) 51   151  51   151     # Image region to fit (xmin xmax ymin ymax)
I) 100    100             # Size of the convolution box (x y)
J) 25.96                  # Magnitude photometric zeropoint
K) 0.03                   # Plate scale (dx dy)    [arcsec per pixel]
O) regular                # Display type (regular, curses, both)
P) 0                      # Choose: 0=optimize, 1=model, 2=imgblock, 3=subcomps
```

Figure 5.5: Example of the input control parameters. Data, sigma, PSF and mask images to be used in the fit are defined in this section, also some parameters as the band, region to fit, and plate scale are defined here.

```
# Object number: 1

 0) sersic      # Object type
 1) 101.      1 # position x [pixel]  (constant with wavelength)
 2) 101.      1 # position y [pixel]
 3) 20.       1 # total magnitude in each band
 4) 10.       1 # R_e in each band
 5) 1.        1 # Sersic exponent in each band
 9) 0.5       1 # axis ratio (b/a) in each band
10) 0.        1 # position angle (PA), same value in each band
 Z) 0          #  Skip this model in output image?  (yes=1, no=0)
```

Figure 5.6: Example of the model to be used in the fit, in this case a Sersic model is used to fit the luminosity profile of a galaxy. Position and the model parameters are defined here, to the right of most parameter we introduce a number 1, it means that the parameters are allowed to vary while the fitting is done, if that number is 0 the parameter is fixed.

To fit the luminosity profile, GALFIT minimize the χ^2 defined in equation 5.10. The algorithm assume that the surface-brigthness profiles are axially symmetric and described by generalized el-

lipses (Athanassoula et al. 1990) first proposed to model galaxy bars. When the axis of the ellipse are aligned with the coordinates axis, the radial coordinate is given by:

$$r = \left(\mid x \mid^{c+2} + \mid \frac{y}{q} \mid^{c+2} \right)^{1/(c+2)} \tag{5.11}$$

Where $q = b/a$ is the ratio between the semi-major axis (a) and semi-minor axis (b) of the ellipses, c is the exponent which describes the shape of the isophote (c $<$ 2 Disky; c$>$ 2 Boxy).

5.4 The fit to Sersic profiles in galaxies with star forming clumps

In our sample, the starburst galaxies present one or more star-forming knots surrounded (Sknot+diffuse and Mknots) or not (Sknot) by diffuse light. To fit the luminosity profile of the host galaxy in Sknot+diffuse and Mknots galaxies is not simple. The presence of the star-forming knots produces an excess of luminosity, which may result in an overestimation on the slope of the profile, and therefore in a wrong result.

The evaluation of the uncertainties and errors in the fit of such systems was studied by R. Amorin in his PhD. work, and published in Amorín et al. (2007, 2009). They studied the profile of the host galaxy in a sample of 8 (Amorín et al. 2007) and 28 (Amorín et al. 2009) BCDs. To do this, they used a set of masks of the starburst regions in GALFIT, using a Sersic profile. This function is used for many studies, covering the features of many kind of galaxies, in ellipticals (from dwarfs to brightest cluster members, Caon et al. (1993); Young & Currie (1994); Graham et al. (1996); Graham & Guzmán (2003); Aguerri et al. (2005)) and spiral bulges (Prieto et al. 2001). Figure 5.7 (Amorín et al. 2007, Fig. 2) shows the diagram with the main steps to fit the luminosity profile of their sample.

To mask a region of a galaxy before fitting the surface brightness distribution could influence the results. The derived parameters may strongly depend on the masked area. For example, if the masked area is smaller than the real size of the star-forming knot, then some flux from the knot will contaminate the luminosity of the host galaxy, producing an excesses of luminosity. On the other side, if the masked area is too large, the galaxy area used to fit the luminosity profile will be small, which could produce an underestimation of the luminosity. In the search for stability of the derived parameters, Amorín et al. (2007, 2009) used two variables: the transition radius (R_{tran}) as the minimal mask radius where the presence of the starburst flux is negligible, and the maximum radius (R_{max}) as the radius where the galaxy luminosity is too faint to include further information. The quantity $R_{max} - R_{tran}$ indicates the radial interval where the fit is stable.

In order to test the reliability of their method and determine the robustness, Amorín et al. (2007) used synthetic galaxies with Sersic index 1 and 4 to test the radial stability interval. They determined the R_{tran} and the stability for different sizes of R_{mask} with respect to R_{tran}. The parameters studied are: Sersic index (n), magnitude (m) and equivalent radius (R_e). Figure 5.8 (Amorín et al. 2007, Fig. 4) shows the deviation of the output parameters with respect to R_{mask} (upper scale) and the ratio R_{mask}/R_e (bottom scale) for synthetic galaxies with n=1 (left) and n=4 (right) Sersic profile. Red line correspond to models with the sky left as a free parameter, black line is for a fixed sky value. The error bar corresponds to the statistical uncertainties estimated by GALFIT in the χ^2 minimization. Grey bands correspond to deviations of 10% and 20% in the output R_e and n parameters for n=1 and n=4 respectively, and 0.1 mag deviation for m_{tot} in both cases. Asterisks in all cases show an estimation of the transition radius R_{tran}. As can be seen, the stability in the output results is reached when $R_{mask} = R_{tran}$, followed by a more or less extended stability region. For small masks ($R_{mask} < R_{tran}$) a systematic overestimation in n and luminosity is produced. This fact also depends on the starburst luminosity. For large masks ($R_{mask} > R_{tran}$) the parameters uncertainties grow up showing no systematic effects.

The size of the masked area plays an important role to reach the R_{tran}. Fig 5.9 (Amorín et al. 2007, Fig. 5) shows the deviation of the output parameters, as in Fig 5.8, with respect to R_{mask} (upper scale), and R_{mask}/R_e (bottom scale), for galaxies with n=1 (left) and n=4 (right). In this case, three different synthetic starburst sizes were used to estimate R_{tran}, varying between $\sim$1 R_e (black line), $\sim$ 1.5 R_e (red line), and 2 R_e (green line). The error bars and and the grey bands are the same as in Fig 5.8. As can be seen in the figure, R_{tran} depends on the size of the star-forming region.

As a result of their simulations, they conclude that:

- For $R_{mask} < R_{tran}$, a systematic overestimation in the Sersic parameters are produced.
- For $R_{mask} = R_{tran}$, the Sersic parameters are recovered.
- For $R_{mask} > R_{tran}$, the Sersic parameters are recovered, but uncertainties grow up.
- The n parameter is the most sensitive to the choose of a correct mask.
- The stability in the parameters is generally reached when $R_{tran} \gtrsim R_e$

With all of these considerations, they fitted a Sersic profile to a sample of 8 blue compact dwarf galaxies. The results are published in (Amorín et al. 2007, Table 2). The same considerations were used in Amorín et al. (2009) to fit a Sersic profile to 28 blue compact dwarf galaxies (Amorín et al. 2009, Table 4). Most of them turned out to be disc like galaxies.

5.5 Results: Sersic profile fit of the starburst galaxies in COSMOS at $z < 0.5$

As described in chapters 2 and 3, we have identified 220 galaxies in COSMOS catalogued as starburst galaxies. Among them, 87 are catalogued as Sknot galaxies, 79 Sknot+diffuse, and 54 Mknots (see Fig. 3.5).

In this chapter we apply GALFIT to get the best luminosity profile. In our sample of starburst galaxies we do not know a priori the kind of luminosity profile of the host galaxy, for this reason we should select a profile able to determine the luminosity profile in a wide range of possibilities. As we have explained in section 5.2, the Sersic profile has a good flexibility to different kind of profiles, being the Sersic index (n) the parameter which describes the shape of the profile. For this adaptability to different kind of profiles, we choose the Sersic profile to fit our sample of galaxies. There are some drawbacks that can influence the output results when fitting this profile with a two dimensional fit. As explained in section 5.3 (Sigma Image), a bad sigma image produce a wrong sky-subtraction. Too faint surface brightness, principally in the outer part of the galaxy where the Sersic index is very sensitive do also result in inaccurate fit, and a wrong masking of the star-forming region in starburst galaxies is also an important caveat for the result. In Cairós et al. (2003), they discussed at some length the applicability of a Sersic profile over a sample of BCDs galaxies, one of their main conclusion is that these drawbacks are most probably due to the observational uncertainties/limitations of the data, and that do not imply that the Sersic profile is inadequate to describe the profile of the host galaxy in BCDs. In all this section we have first taken into careful consideration all posible sources of error when dealing with observations. Moreover, and after the

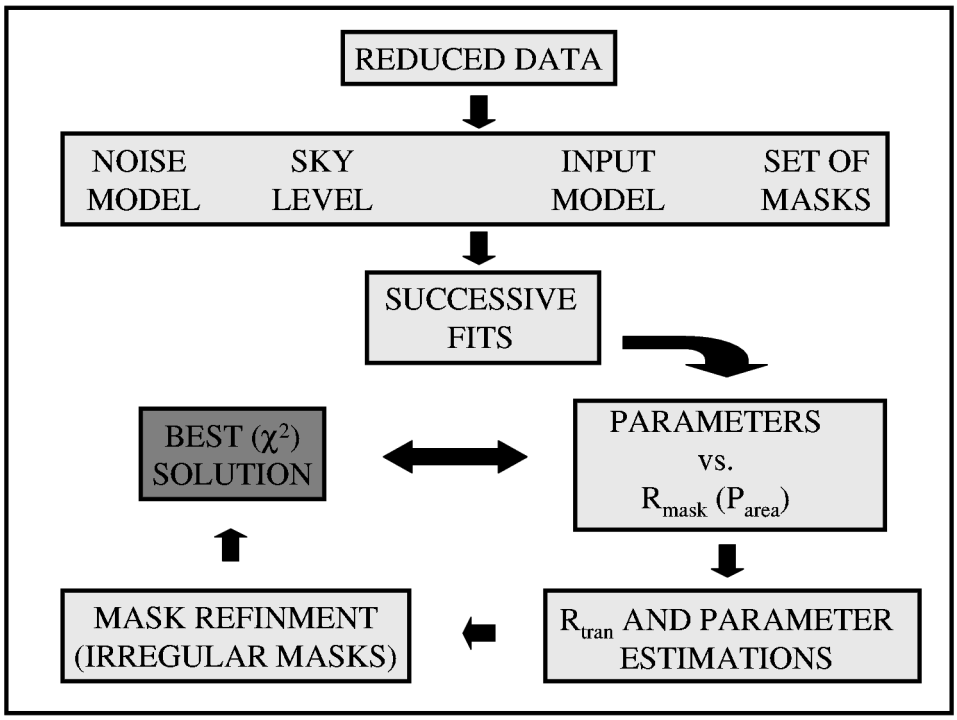

Figure 5.7: Diagram with the steps of the method from input to output parameters (from Amorin PhD, and Amorín et al. (2007)).

above have been taken into account, we do perform different fits and tests and defined a goodness parameter that is used to discard the results that are not reliable enough.

In this section we present the results of the luminosity profile fit to each one of the different starburst classes (Sknot, Sknot+diffuse and Mknots) in our sample.

5.5.1 Sknot galaxies

In our sample, 87 galaxies were catalogued as Sknot galaxies. They are galaxies with just one knot of star formation without diffuse emission. Fig. 5.11 shows a mosaic with examples of eight of these galaxies, the bar at the upper right corner represents 1 kpc scale. This kind of galaxies are the simplest cases to fit a 2D luminosity profile in our sample, since it is not necessary to make masks for star-forming regions as. To do this 2D fit, we have used a Sersic profile in GALFIT, the main output parameters of the fit for Sknot galaxies have been summarized in Table 5.1. Column 1 shows the name of the galaxies as in section 2. Column 2 gives the observed surface brightness (erg s^{-1} cm^{-2} $Å^{-1}$ kpc^{-2}) of the galaxies in the F814W ACS/HST band. Column 3 gives the nearby background (erg s^{-1} cm^{-2} $Å^{-1}$) surrounding the galaxies in the F814W ACS/HST band. Columns 4, 5, 6, and 7 are the Sersic index (n), effective radius (R_e), position angle (PA), and ellipticity ($e = 1 - \frac{b}{a}$) given by GALFIT, where b is the semi-minor axis and a is the semi-major axis determined from the fit using a Sersic profile. Column 8 provides the goodness parameter defined latter on.

The quality of the images used to fit the luminosity profile of the galaxies is an important factor to obtain a good fit since bad S/N ratio increases the uncertainties. To do an estimation of the goodness of the fit we analyze the output image given by GALFIT. This is an image cube composed by 4 images: (1) The galaxy image resized to the area used for the fit, (2) the final model of the

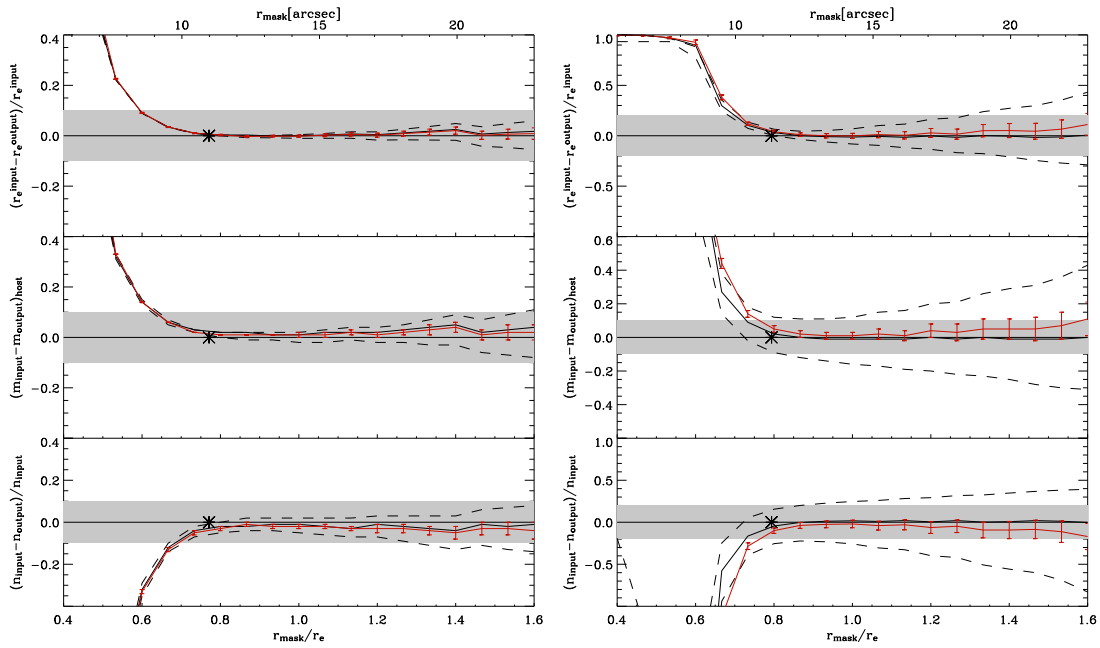

Figure 5.8: Deviation of the principal parameters: r_e, m, and n, as a function of r_{mask} (upper scale) and r_{mask}/r_e (bottom scale). Left panel shows the n=1 model, and right panel is the n=4 model. Red line correspond to models with the sky left as a free parameter, black line is for a fixed sky value. The error bar corresponds to the statistical uncertainties estimated by GALFIT in the χ^2 minimization. Grey bands correspond to deviations of 10% and 20% in the output R_e and n parameters for n=1 and n=4 respectively, and 0.1 mag deviation for m_{tot} in both cases. Asterisks in all cases show an estimation of the transition radius (R_{tran}). Figure taken from (Amorín et al. 2007, Fig. 4).

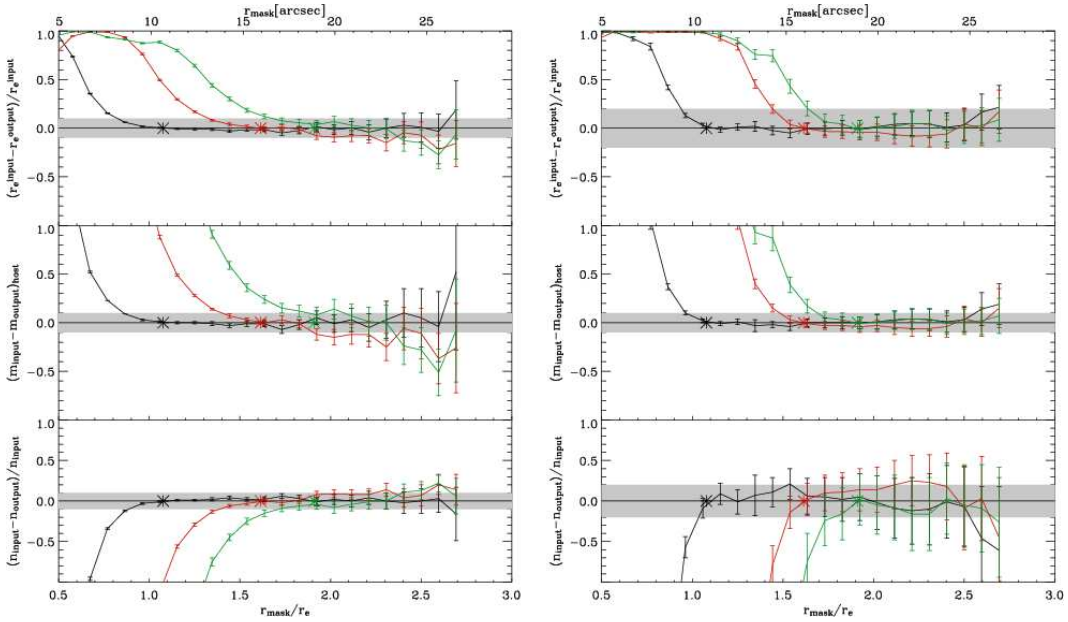

Figure 5.9: Deviation of the principal parameters: r_e, m, and n, as a function of r_{mask} (upper scale) and r_{mask}/r_e (bottom scale), and the simulated starburst size. Left panel shows the n=1 model, and right panel is the n=4 model in synthetic galaxies with starburst size $\sim$1 R_e (black line), $\sim$ 1.5 R_e (red line), and 2 R_e (green line). The error bars and and the grey bands are the same as in Fig 5.8. Asterisks in all cases show an estimation of the transition radius (R_{tran}). Figure taken from Amorín et al. (2007, Fig. 5).

galaxy in the fitted area, (3) the residual image resulting from subtracting (2) from (1), and (4) a PSF image. As Sknot galaxies have not substructures embedded in the more diffuse light, it is not necessary to construct masks. For a good fit, the residual image should be the flux from the sky without emission from the galaxy, which should be totally included in the model image. We analyzed the residual image from the fit. First we determined the mean value for the area corresponding to the sky, then we looked for emission which deviate 3 $\times\sigma$ from this value, which can be positive or negative, and quantified this deviation value as an excess of emission in the residual map. We estimated the ratio of the absolute value of this emission excess in the residual map over the flux from the galaxy used to do the fit as an estimation of the goodness ($\mathfrak{G}$) on fitting the luminosity profile as:

$$\mathfrak{G} = \frac{\sum |F_{residual}| - \sum F_{sky}}{\sum F_{galaxy} - \sum F_{sky}}$$

Fig. 5.10 shows the distribution of the parameter $\mathfrak{G}$ for our sample of Sknot starburst. We have used the $\mathfrak{G}$ to quantify how good is the fit and to define a threshold to select results that we consider reliable. We have discarded fits with $\mathfrak{G} > 0.1$. This means that the integrated residual flux is larger than ten percent of the emission of the galaxy. 23 galaxies have a fit value $\mathfrak{G} > 0.1$ and where discarded. In table 5.1 we give the parameter for the 87 galaxies, 64 with a good luminosity profile fit, and 23 (shadowed) with a bad fit.

The results of the fit can be plotted as a luminosity profile. Fig. 5.12 shows an example of the fit to the galaxy COSMOS-022. To the left of the figure three panels show the procedure of the fit. Top left panel shows the science image of the galaxy, top right panel shows the 2D best fit model using a Sersic profile, and the bottom left panel shows the residuals of the fit. Scales are in magnitudes/arcsec^2, X-axis is RA and Y-axis is DEC. Using 2D images it is also possible to build a

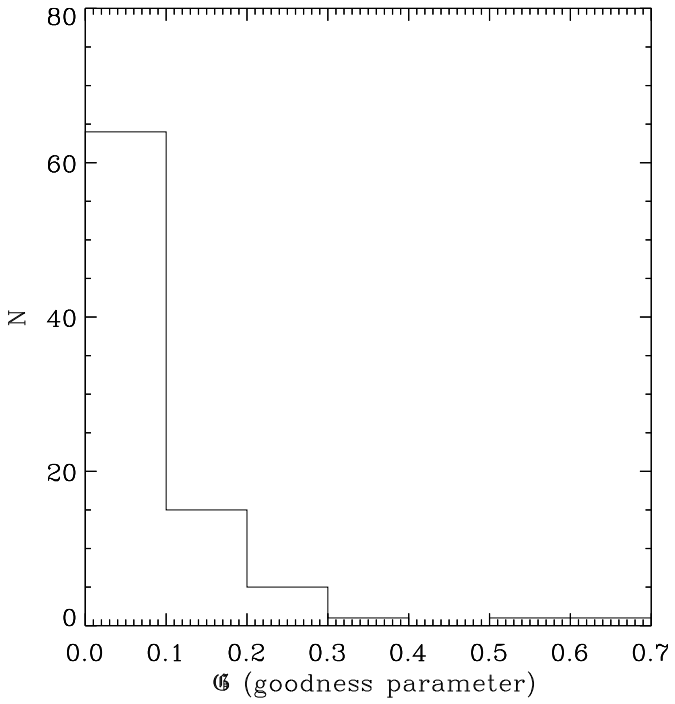

Figure 5.10: Distribution of the goodness parameter for Sknot galaxies.

1D luminosity profile by doing ellipse fitting, we used the task ellipse of IRAF to do this 1D profile. As input parameter for the ellipse task we used the ellipticity, axis ratio, and equivalent radius obtained with the best 2D fit. To the right of Fig. 5.12, in the upper panel, we show this fit for the galaxy (black dashed line), the Sersic profile (red line) obtained with the best fit with GALFIT, and the PSF (black dotted line). Lower panel shows the residual of the model with respect to the galaxy. The x-axis shows the radius in kpc scale (top) and arcsec scale (bottom). The y-axis shows the surface brightness μ (mag arcsec^{-2}) in the F814W ACS/HST band.

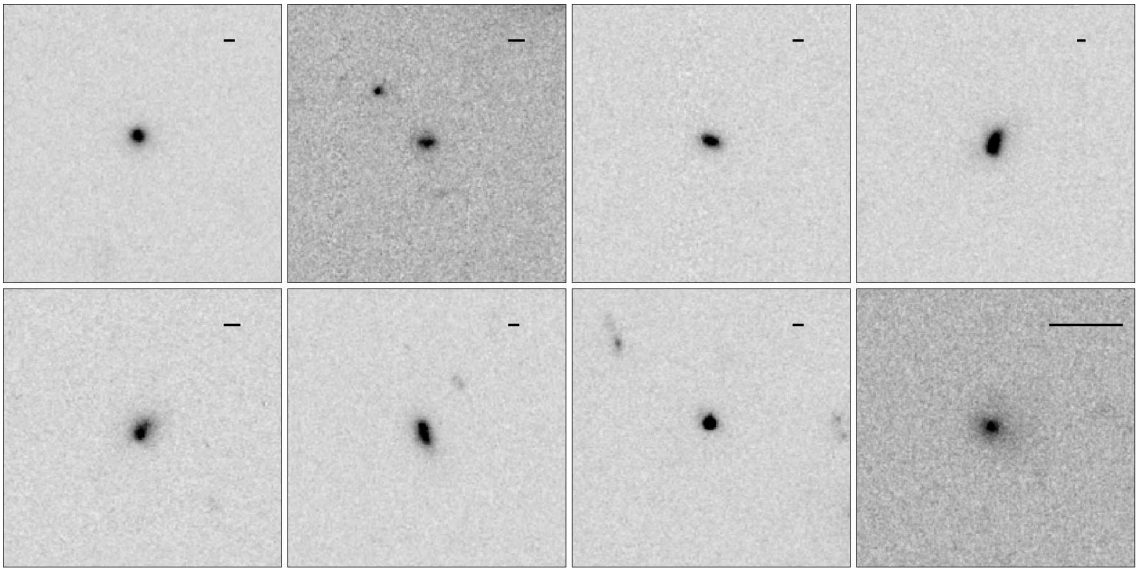

Figure 5.11: Mosaic of eight Sknot galaxies in our sample. At the upper right corner a bar with 1 kpc size is showed. Boxes size is 15"x15".

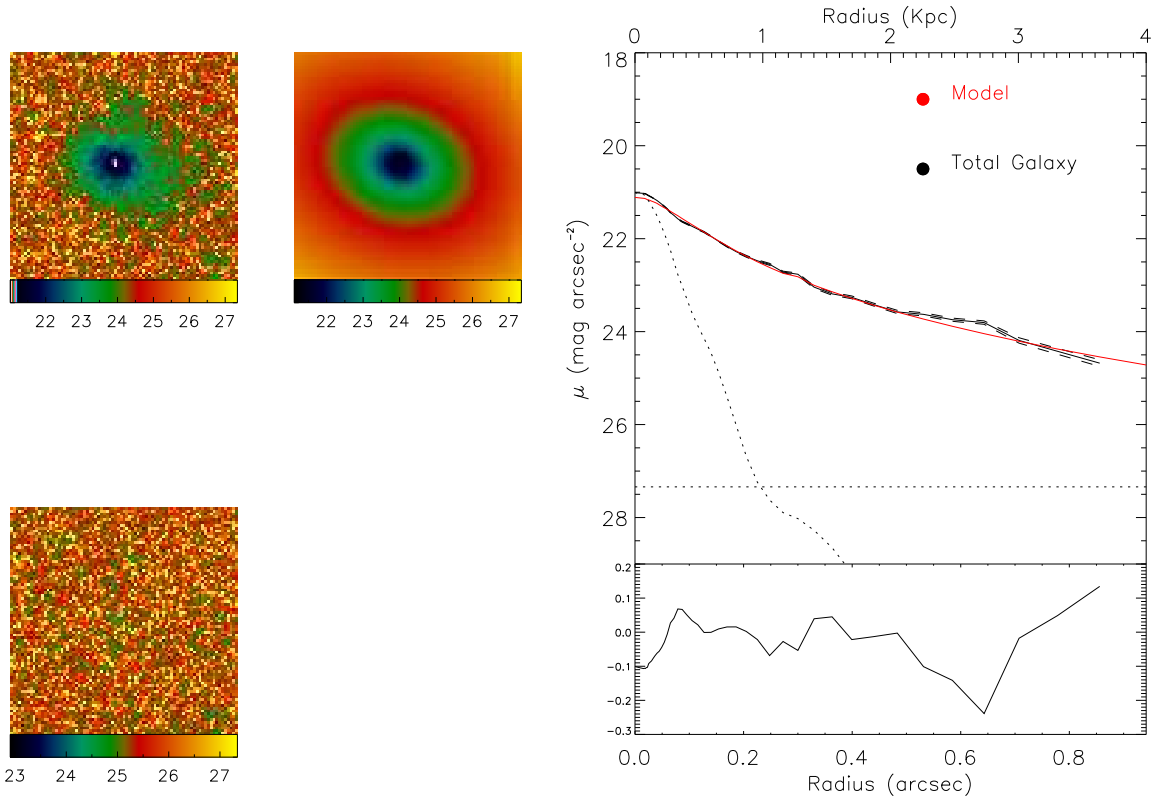

Figure 5.12: Example of the luminosity profile of the Sknot galaxy COSMOS-022. The three panels to the left show: the galaxy, 2D fit and residuals. Scales are in magnitudes/arcsec^2, X-axis is RA and Y-axis is DEC. The right panel shows the 1D profile of the galaxy (black dashed line), the Sersic profile fit (red line), and PSF (black dotted line) at the upper panel. Lower panel shows the residual of the model with respect to the galaxy. X axis shows the radius in kpc scale (top) and arcsec scale (bottom). Y axis shows the surface magnitude μ (mag arcsec^{-2}) in the F814W ACS/HST band.

Table 5.1: Output for the 2D fit with GALFIT of the Sknot sample.

Object	SB	NB	n	R_e	PA	e	𝔊
	(erg s^{-1}cm^{-2}Å^{-1}kpc^{-2})	(erg s^{-1}cm^{-2} Å^{-1})		(pixels)			
(1)	(2)	(3)	(4)	(5)	(6)	(7)	(8)
cosmos-004	3.86E-24	2.68E-13	1.57 ± 0.02	4.5	25	0.12	0.04
cosmos-008	4.62E-22	1.58E-13	1.20 ± 0.04	6.6	86	0.34	0.02
cosmos-013	4.93E-24	2.27E-13	0.83 ± 0.02	5.1	70	0.53	0.03
cosmos-014	2.90E-25	1.92E-13	0.99 ± −−	9.9	-31	0.34	0.57
cosmos-017	3.02E-24	2.15E-13	1.54 ± 0.03	8.0	-35	0.31	0.09
cosmos-018	1.24E-24	2.50E-13	0.62 ± 0.02	7.8	17	0.6	0.07
cosmos-020	1.74E-24	2.79E-13	2.96 ± 0.08	1.9	-55	0.12	0.07
cosmos-022	8.15E-22	2.21E-13	3.67 ± 0.15	33.8	71	0.24	0.01
cosmos-023	1.10E-21	7.63E-14	1.22 ± 0.04	12.6	-42	0.71	0.05
cosmos-026	2.17E-25	4.41E-13	2.19 ± 0.03	4.3	56	0.5	0.04
cosmos-027	4.81E-26	2.06E-13	3.13 ± 0.04	6.6	-26	0.33	0.07
cosmos-035	1.36E-23	9.56E-14	1.12 ± 0.03	5.4	-12	0.35	0.03
cosmos-039	3.62E-24	1.41E-13	2.46 ± 0.06	2.3	-42	0.13	0.04
cosmos-047	1.94E-24	4.09E-13	1.17 ± 0.02	15.0	-47	0.71	0.04
cosmos-048	1.42E-25	2.62E-13	0.81 ± 0.01	10.5	6	0.57	0.09
cosmos-050	9.93E-25	2.94E-13	2.27 ± 0.03	6.9	20	0.52	0.04
cosmos-052	8.82E-23	3.10E-13	0.97 ± 0.02	7.6	32	0.43	0.04
cosmos-053	5.29E-25	2.10E-13	1.29 ± 0.02	8.6	-80	0.34	0.06
cosmos-055	3.79E-23	3.74E-13	10.85 ± 0.94	91.3	-15	0.54	0.03
cosmos-057	6.05E-25	2.88E-13	0.99 ± 0.01	6.9	84	0.34	0.08
cosmos-059	2.64E-25	2.89E-13	1.74 ± 0.03	6.6	-90	0.07	0.14
cosmos-063	3.75E-24	2.39E-13	0.58 ± 0.01	7.9	66	0.67	0.04
cosmos-067	3.88E-23	1.77E-13	2.77 ± 0.08	11.9	-45	0.28	0.04
cosmos-072	2.37E-20	2.54E-13	3.15 ± 0.21	31.6	26	0.27	0.02
cosmos-077	4.79E-23	1.55E-13	1.53 ± 0.10	7.1	53	1.0	0.33
cosmos-078	4.12E-26	3.41E-13	3.57 ± 0.05	6.5	34	0.03	0.06
cosmos-079	5.33E-25	1.18E-13	3.16 ± 0.04	7.7	76	0.1	0.04
cosmos-080	9.90E-25	2.32E-13	1.36 ± 0.02	5.7	31	0.0	0.15
cosmos-086	2.67E-25	2.73E-13	0.88 ± 0.01	7.9	-53	0.23	0.06
cosmos-087	1.21E-24	3.79E-13	1.77 ± 0.02	11.4	49	0.51	0.02
cosmos-094	1.33E-24	3.05E-13	1.79 ± 0.04	16.6	11	0.59	0.04
cosmos-096	6.88E-23	2.59E-13	2.52 ± 0.11	10.4	32	0.47	0.01
cosmos-099	4.02E-22	1.03E-13	2.11 ± 0.09	10.7	76	0.56	0.02
cosmos-106	5.81E-23	9.53E-14	0.83 ± 0.04	7.7	-16	0.53	0.03
cosmos-108	2.59E-24	7.02E-14	2.33 ± 0.05	12.1	81	0.39	0.01
cosmos-110	1.42E-24	2.77E-13	2.92 ± 0.03	6.7	18	0.45	0.02
cosmos-117	4.39E-21	7.45E-14	4.68 ± 0.42	28.3	38	0.36	0.02
cosmos-119	1.79E-24	2.62E-13	1.15 ± 0.01	4.6	-50	0.33	0.02
cosmos-126	2.97E-24	1.80E-13	0.92 ± 0.02	5.2	-2	0.21	0.02
cosmos-128	1.08E-26	2.48E-13	2.63 ± 0.02	10.2	64	0.35	0.04
cosmos-129	8.54E-24	2.72E-13	1.56 ± 0.03	8.6	2	0.27	0.04
cosmos-133	9.22E-25	2.93E-13	1.83 ± 0.03	7.2	-3	0.56	0.03
cosmos-141	8.83E-27	1.63E-13	2.26 ± 0.01	8.7	6	0.58	0.05
cosmos-142	4.83E-24	6.99E-14	1.52 ± 0.03	17.8	2	0.62	0.02

Table 5.1: continued.

Object	SB	NB	n	R_e	PA	e	$\mathfrak{G}$
(1)	(2)	(3)	(4)	(5)	(6)	(7)	(8)
cosmos-145	1.14E-24	2.57E-13	1.52 ± 0.02	6.7	-55	0.59	0.10
cosmos-152	5.97E-26	2.00E-13	0.68 ± 0.01	12.0	39	0.78	0.06
cosmos-153	3.00E-23	2.60E-13	0.80 ± 0.02	8.1	-81	0.39	0.03
cosmos-154	7.92E-23	2.46E-13	0.90 ± 0.03	9.1	-19	0.4	0.03
cosmos-155	4.87E-21	3.41E-13	5.95 ± 0.32	11.0	12	0.33	0.05
cosmos-157	2.20E-23	2.71E-13	3.76 ± 0.12	5.9	-64	0.47	0.08
cosmos-158	3.37E-24	2.88E-13	2.06 ± 0.03	7.8	85	0.51	0.03
cosmos-160	3.40E-24	2.34E-13	1.25 ± 0.02	6.5	90	0.29	0.05
cosmos-164	2.12E-26	2.59E-13	3.19 ± 0.10	5.0	90	0.15	0.23
cosmos-174	2.26E-23	3.87E-13	2.31 ± 0.07	4.9	26	0.36	0.01
cosmos-182	1.40E-20	3.50E-13	0.91 ± 0.05	5.7	-64	0.55	0.01
cosmos-190	1.91E-23	2.12E-13	0.34 ± 0.01	6.3	-86	0.51	0.10
cosmos-192	6.38E-25	2.78E-13	1.25 ± 0.02	7.5	-3	0.52	0.05
cosmos-195	8.30E-24	2.74E-13	0.46 ± 0.02	7.0	29	0.64	0.06
cosmos-198	2.06E-25	4.49E-13	4.13 ± 0.06	7.4	63	0.5	0.05
cosmos-204	2.38E-26	3.04E-13	0.12 ± 0.14	79.6	41	0.95	0.61
cosmos-205	5.17E-24	2.83E-13	0.53 ± 0.03	5.9	-55	0.57	0.05
cosmos-206	3.01E-21	7.81E-14	4.20 ± 0.72	4.6	-36	0.57	0.02
cosmos-210	1.61E-23	8.13E-14	2.85 ± 0.08	27.0	90	0.3	0.02
cosmos-214	6.77E-24	6.89E-14	2.45 ± 0.05	9.8	38	0.18	0.02
cosmos-215	1.50E-25	2.62E-13	2.01 ± 0.03	5.6	48	0.08	0.14

Results of the 2D fit using a Sersic profile to the galaxies classified as Sknot (Sec. 5.5.1). Column 1: Name of the galaxies as was catalogued in our sample. Column 2: Surface brightness (erg s^{-1} cm^{-2} $Å^{-1}$ kpc^{-2}) of the galaxies in the F814W ACS/HST band. Column 3: Nearby background (erg s^{-1} cm^{-2} $Å^{-1}$) surrounded the galaxies in the F814W ACS/HST band. Columns 4: Sersic index (n) from the fit with its associated error. Column 5: Equivalen radius (R_e). Column 6: Position angle (PA). Column 7: Ellipticity (e). Column 8: Goodness parameter ($\mathfrak{G}$).

5.5.2 Sknot+diffuse light galaxies

In our catalogue, 79 galaxies were classified as Sknot+diffuse light. Fig. 5.15 shows examples of eight of them, the bar at the upper right corner corresponds to a 1 kpc scale. As we have explained in Sect. 5.4, to fit the 2D surface brightness distribution of galaxies with star-forming regions is not direct, and it is necessary the use of masks to remove the knots of star formation before fitting the host galaxy. In this section, we deal with galaxies with one star-forming region embedded in a more diffuse emission, so for every galaxy we constructed a mask of this region and performed the luminosity profile fit of the host galaxy.

To construct the masks of the star-forming regions we used FOCAS. We used the task splits to separate the star-forming region from the host galaxy looking for signal over $3\times\sigma$ the local background of the galaxy (see Sect. 3.1.2).

The fit was done with GALFIT using a Sersic profile. For every galaxy we ran the model using the mask of the corresponding star-forming region. The output parameters are given in table 5.2.

The use of a mask reduce the effective area of the galaxy to perform the fitting. Amorín et al. (2007) studied how the size of the mask with respects to the effective radius (r_e) of the galaxy could influence on the estimation of the output results, the derived parameters may strongly depend on

the masked area. We show three example of the influence of the mask in the estimation of the output parameters of the profile. Figs. 5.16, 5.17 and 5.18 show the fitted profile of COSMOS-103, COSMOS-211 and COSMOS-093 as an example of how the mask can affect the output parameters. In each figure, the upper fit was done using a mask (parameters in Table 5.2), and the lower fit was done without the use of a mask. To the left of each figure we show the 2D fit: galaxy, mask (for the masked fit), model, and residual. To the right of each figure, for clarity, we show the 1D fit over the model obtained with a 2D fit, the total galaxy profile, the PSF profile, and for those fits with performed within a mask we also show the host galaxy and knots profile.

In COSMOS-103 (Fig. 5.16), the presence of a central star-forming region produce an overestimation of the luminosity in the central region, as can be seen in the right panels. For masked fit we obtained a Sersic index n=0.98, which is an expected value for disk profile. For unmasked profile, the overestimation on the luminosity produce an overestimation in the Sersic index n=1.87. In this case the use of a mask is essential to obtain a good fit of the profile.

In COSMOS-211 (Fig. 5.17), the star-forming region is located close to the border of the galaxy, and its size is small in comparison to the galaxy size. In this case the use of a mask have not much effect on the output result, for masked fit the Sersic index is n=0.85, and for unmasked fit n=0.82. The residual in both cases are similar, and correspond to the star-forming region.

In COSMOS-093 (Fig. 5.18), the star-forming region is located in the center of the galaxy, and the size is enough to cover a large area of the profile. Masking a large area in the central region, produce an under estimation on the luminosity in the central region of the galaxy, as can be seen in the masked fit. The obtained Sersic index for the masked fit is n=0.18, but without masking n=0.96, which is an expected value for disk like galaxies.

The inadequate consideration of the starburst contamination - which can be efficiently solved by masking it - is not the only source of error. As explained in the introduction of this section, the quality and depth of the images at low Surface Brightness (SB) areas is important to obtain a good fit. To estimate the goodness of the fit, as in section 5.5.1, we use the residual image. As we are dealing with galaxies with one knot of star formation, using a mask to cover the area of the knot, the residual map should contain the flux corresponding to the star-forming region. To have an estimation of the flux from the star-forming region we multiply the mask of this area, which has value 1 in this region and 0 out of this, first (1) with the galaxy, and second (2) with the model obtained from the fit. Then we estimate the difference between (1) and (2) to obtain the flux, which for a good fit should corresponds to the flux of the star-forming region only. We estimated the ratio between the difference of the estimated flux for the star forming region and the residual, and the flux of the galaxy used to do the fit (excluding the star-forming region), this ratio give us the excess of flux in the residual with respect to the flux of the galaxy used to do the fit. This is the $\mathfrak{G}$ parameter, that for a galaxy with star-forming region is given by:

$$\mathfrak{G} = \frac{\sum(|F_{residual}| - F_{knot}) - \sum F_{sky}}{\sum F_{galaxy} - \sum F_{sky}}$$

In Fig 5.13 we show the distribution of the $\mathfrak{G}$ values for Sknot+diffuse galaxies. From this result we select galaxies with $\mathfrak{G} < 0.1$ as those where 2D fit is reliable. As in the previous section, we have used the $\mathfrak{G}$ to quantify how good is the fit and to define a threshold to select results that we consider reliable. We have discarded fits with $\mathfrak{G} > 0.1$, what means that the residual is larger than ten percent of the emission of the galaxy 18 galaxies were discarded using this criteria.

Beside the goodness parameter there are more issues to be considered. The area of the mask for the star-forming region with respect to the area of the galaxy used to fit the luminosity profile, and its distance to the center of the galaxy, are two important factors to consider for the fitting of the galaxy surface brightness. A centered mask produce a loss of information from the center to a given radius if the same mask (starburst) is in the periphery of the galaxy, the information at that given radius can be obtained from the same radius in other sectors of the galaxy. Then for the same

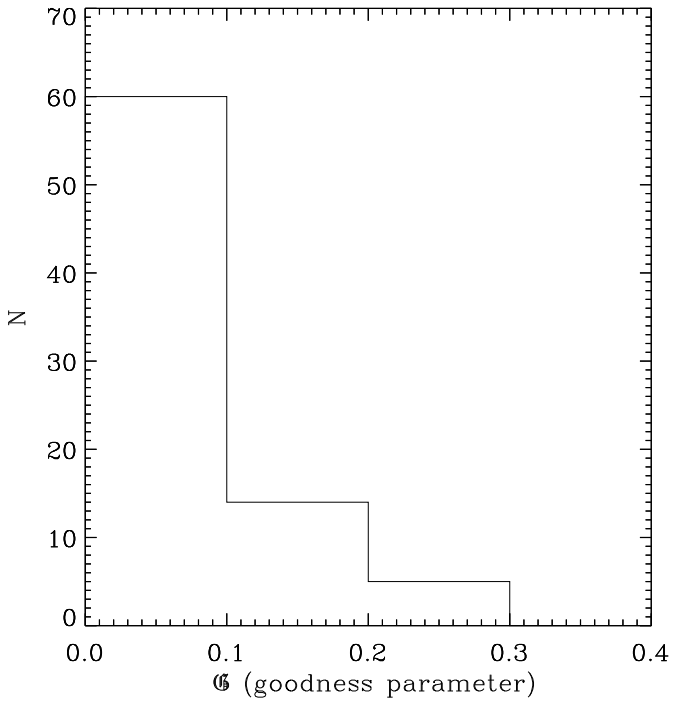

Figure 5.13: Distribution of the goodness parameter for Sknot+diffuse galaxies.

galaxy and the same starburst, those are centered tend to influence more the fit. On the other side, the larger the mask of the star-forming region, the smaller the area of the galaxy that remains. To explore the influence of both the size of the mask and its distance to the center of the galaxy in the best fit, we computed the ratio of the mask to the galaxy area and compared it with the distance of the mask to the center of the galaxy with respect to its size. Fig. 5.14 we shows this relation. A dotted line in the x-axis separate the lopsided of the offcenter knots. From this figure we discarded 3 centered galaxies with a ratio of areas ≥ 0.5 (red points), for these galaxies the output results for masked and unmasked fits show strong deviations. Table 5.2 shows the principal results from the fit of the luminosity profile for 79 Sknot+diffuse galaxies in our sample.

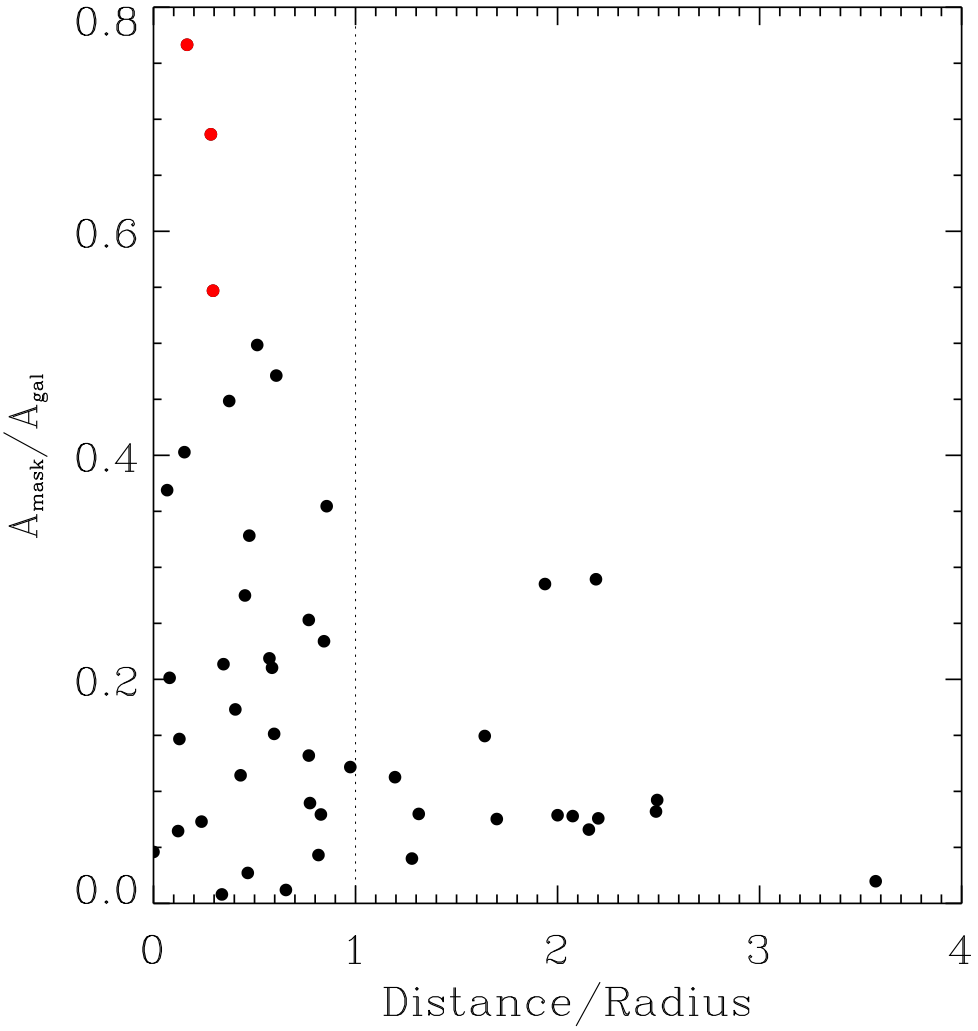

Figure 5.14: Distance to the center of galaxy with respect to the radius of the mask vs area of the mask with respect to the area of the galaxy. The vertical dashed line in the x-axis separates the lopsided of the offcenter knots. Red points are centered knots with a large area, this kind of knots does not allow to do a good fit, and are discarded for the statistics.

Object	Area gal pixels^2	Area mask pixels^2	SB (erg s^{-1}cm^{-2}Å^{-1}kpc^{-2})	NB (erg s^{-1}cm^{-2} Å^{-1})	n	R_e (pixels)	PA	e	label	$\mathfrak{G}$
(1)	(2)	(3)	(4)	(5)	(6)	(7)	(8)	(9)	(10)	(11)
cosmos-002	926	61	1.06E-24	2.09E-13	0.81 ± 0.02	9.2	90	0.06	0	0.07
cosmos-003	1903	702	1.42E-25	1.90E-13	0.44 ± 0.03	23.1	77	0.43	0	0.22
cosmos-010	736	20	2.41E-24	2.51E-13	1.52 ± 0.04	30.6	24	0.42	0	0.02
cosmos-024	502	178	1.85E-20	9.18E-14	0.92 ± −−	2.0	-1	0.97	0	0.13
cosmos-025	871	40	3.31E-23	2.39E-13	1.11 ± 0.03	15.1	10	0.51	1	0.02
cosmos-030	1156	91	1.67E-24	2.20E-13	0.88 ± 0.02	14.3	-7	0.52	0	0.02
cosmos-031	763	114	9.92E-24	2.10E-13	0.64 ± 0.03	16.5	-25	0.75	0	0.04
cosmos-034	1542	267	2.42E-22	2.26E-13	1.01 ± 0.08	31.3	61	0.43	0	0.05
cosmos-038	2268	186	6.69E-25	2.30E-13	0.26 ± 0.01	0.9	63	0.94	0	0.08
cosmos-040	1715	74	9.94E-24	1.99E-13	0.57 ± 0.01	24.4	43	0.69	1	0.02
cosmos-042	664	50	1.22E-21	3.80E-13	1.08 ± 0.05	27.4	-15	0.19	1	0.005
cosmos-043	1705	225	8.86E-26	1.88E-13	0.56 ± 0.01	16.4	16	0.46	0	0.03
cosmos-044	3005	24	3.98E-27	2.25E-13	0.99 ± 0.01	19.8	71	0.69	0	0.12
cosmos-051	235	68	7.72E-22	2.69E-13	0.30 ± −−	1.9	3	0.90	0	0.06
cosmos-061	3177	695	7.00E-27	2.248E-13	0.94 ± 0.02	21.1	-63	0.06	0	0.22
cosmos-070	1094	256	2.97E-24	8.73E-14	0.43 ± 0.02	22.8	64	0.65	0	0.05
cosmos-074	1718	564	2.35E-25	2.98E-13	0.76 ± 0.03	30.1	-21	0.63	1	0.11
cosmos-076	1241	314	4.90E-18	2.58E-13	0.59 ± 0.02	29.1	-56	0.63	0	0.02
cosmos-081	2258	1235	1.88E-25	2.09E-13	2.63 ± 0.25	20.8	17	0.85	0	0.54
cosmos-090	1172	172	4.76E-25	3.93E-13	0.44 ± 0.02	13.0	2	0.52	0	0.04
cosmos-093	1375	392	1.64E-25	2.76E-13	0.18 ± 0.01	27.8	-76	0.81	1	0.07
cosmos-111	2220	447	3.87E-26	3.46E-13	0.12 ± 0.01	38.0	67	0.79	0	0.06
cosmos-114	1799	72	2.14E-25	4.59E-13	0.56 ± 0.01	17.0	-52	0.61	1	0.03
cosmos-116	548	40	6.01E-20	2.28E-13	3.60 ± 0.54	82.1	-38	0.69	0	0.05
cosmos-120	1503	18	5.26E-25	2.77E-13	0.91 ± 0.02	10.5	45	0.00	1	0.10
cosmos-121	1530	137	1.38E-24	1.92E-13	0.51 ± 0.01	15.8	55	0.25	0	0.01
cosmos-123	1652	250	2.62E-26	3.62E-13	0.43 ± 0.01	18.2	44	0.68	0	0.02
cosmos-124	759	15	1.03E-23	7.46E-14	0.54 ± 0.02	10.9	-52	0.56	1	0.03
cosmos-139	1277	146	6.24E-24	2.22E-13	0.79 ± 0.02	19.6	71	0.60	0	0.02
cosmos-146	741	568	1.23E-23	3.57E-13	0.14 ± 0.03	16.4	34	0.33	0	0.37
cosmos-147	3285	256	1.17E-25	2.56E-13	0.74 ± 0.01	20.9	7	0.16	0	0.01
cosmos-148	1062	98	5.17E-24	3.19E-13	0.72 ± 0.02	12.4	65	0.44	1	0.02
cosmos-149	914	59	4.20E-22	1.64E-13	1.62 ± 0.06	14.8	-70	0.31	0	0.001
cosmos-159	1208	147	4.29E-23	3.44E-13	0.96 ± 0.03	24.4	-84	0.33	0	0.60
cosmos-163	1793	202	2.08E-26	1.81E-13	0.26 ± 0.01	18.3	-37	0.63	0	0.07
cosmos-171	1371	646	1.23E-25	2.97E-13	0.13 ± 0.01	26.0	32	0.44	0	0.12
cosmos-172	1357	373	5.67E-25	2.69E-13	4.27 ± 0.43	16.5	37	0.72	0	0.22
cosmos-175	3632	1463	4.39E-27	1.99E-13	1.36 ± 0.10	24.9	-63	0.34	0	0.36
cosmos-178	2504	1123	7.53E-26	2.74E-13	0.78 ± 0.04	59.9	-53	0.49	0	0.06
cosmos-183	1545	325	2.41E-24	3.24E-13	0.63 ± 0.03	21.7	66	0.59	0	0.10
cosmos-184	658	328	3.42E-22	2.02E-13	2.43 ± 0.59	155.6	-72	0.61	0	0.07
cosmos-186	1564	334	1.21E-26	2.46E-13	0.41 ± 0.02	22.8	-45	0.45	1	0.08
cosmos-196	1753	140	2.47E-22	3.02E-13	0.69 ± 0.02	28.8	-32	0.42	1	0.001
cosmos-199	567	45	8.39E-21	2.01E-13	6.33 ± 1.68	1762.9	76	0.30	0	0.03
cosmos-207	1391	955	3.74E-26	9.01E-14	0.47 ± 0.05	35.7	14	0.66	0	0.94
cosmos-211	1054	80	2.29E-23	1.58E-13	0.85 ± 0.02	15.2	-9	0.28	1	0.001

Table 5.2: Results of the 2D fit using a Sersic profile to the galaxies classified as Sknot+diffuse (Sec. 5.5.2). Column 1: Name of the galaxies as was catalogued in our sample. Column 2: Area of the galaxy used for the fit (pixels^2). Column 3: Area of the masked region (pixels^2). Column 4: Surface brightness (erg s^{-1} cm^{-2} Å^{-1} kpc^{-2}) of the galaxies in the F814W ACS/HST band. Column 5: Nearby background (erg s^{-1} cm^{-2} Å^{-1}) surrounded the galaxies in the F814W ACS/HST band. Columns 6: Sersic index (n) from the fit with its associated error. Column 7: Equivalen radius (R$_e$). Column 8: Position angle (PA). Column 9: Ellipticity (e). Column 10: Label: 0 for lopsided knots; 1 for offcenter. Column 11: Goodness parameter ($\mathfrak{G}$).

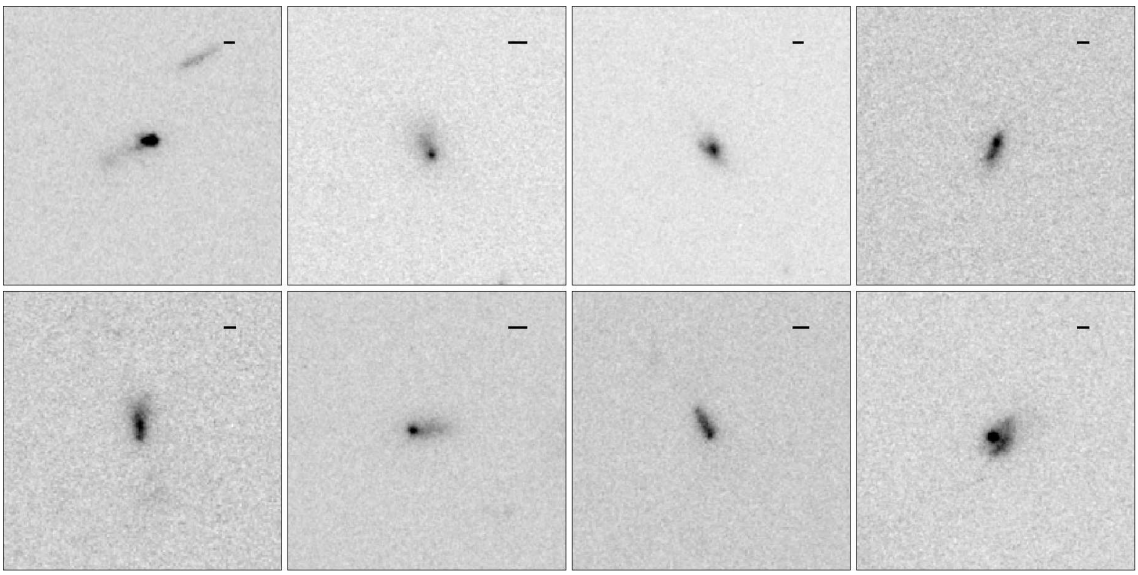

Figure 5.15: Mosaic of eight Sknot+diffuse light galaxies in our sample. At the upper right corner a bar with 1 kpc size is shown. Boxes size is 15"x15".

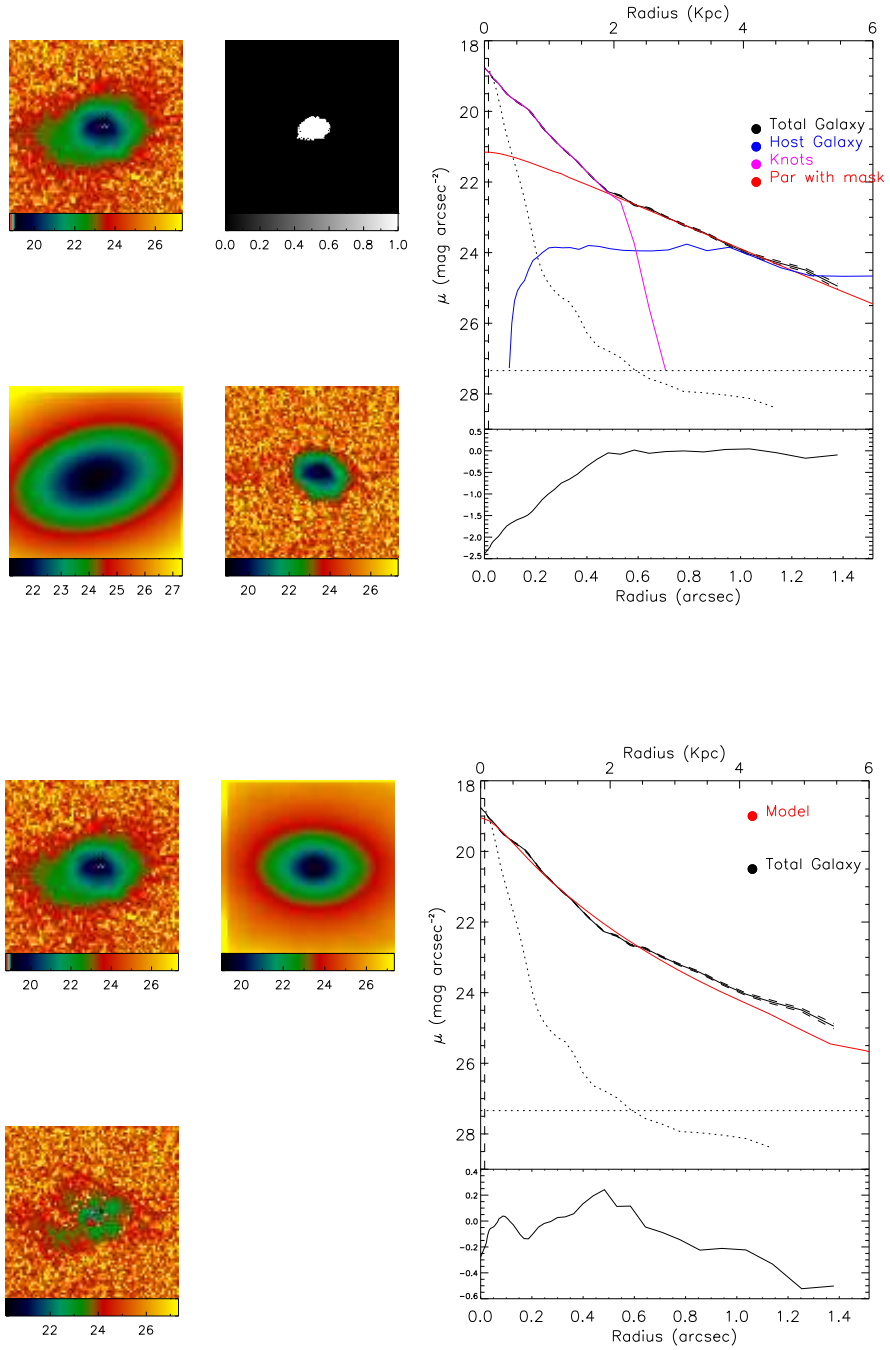

Figure 5.16: Surface-brightness fitting of a Sknot+diffuse light galaxy. In the top a fit using a mask is showed, in the bottom the fit without a mask. In the left of each fit, panels show the galaxy, mask (for the fit including a mask), 2D model and residual of the fit. In the right the luminosity of the galaxy, model, and PSF versus radius is showed on the top for every fit, for masked fit also the profile of the host galaxy and knots are showed. In the bottom the residual of the model with respect to the galaxy is showed. In this case the presence of a central star-forming region produce an overestimation of the luminosity. For masked fit we obtained a Sersic index n=0.98, which is an expected value for disk profile. For unmasked profile, the overestimation on the luminosity produce an overestimation in the Sersic index n=1.87. In this case the use of a mask is essential to obtain a good fit of the profile.

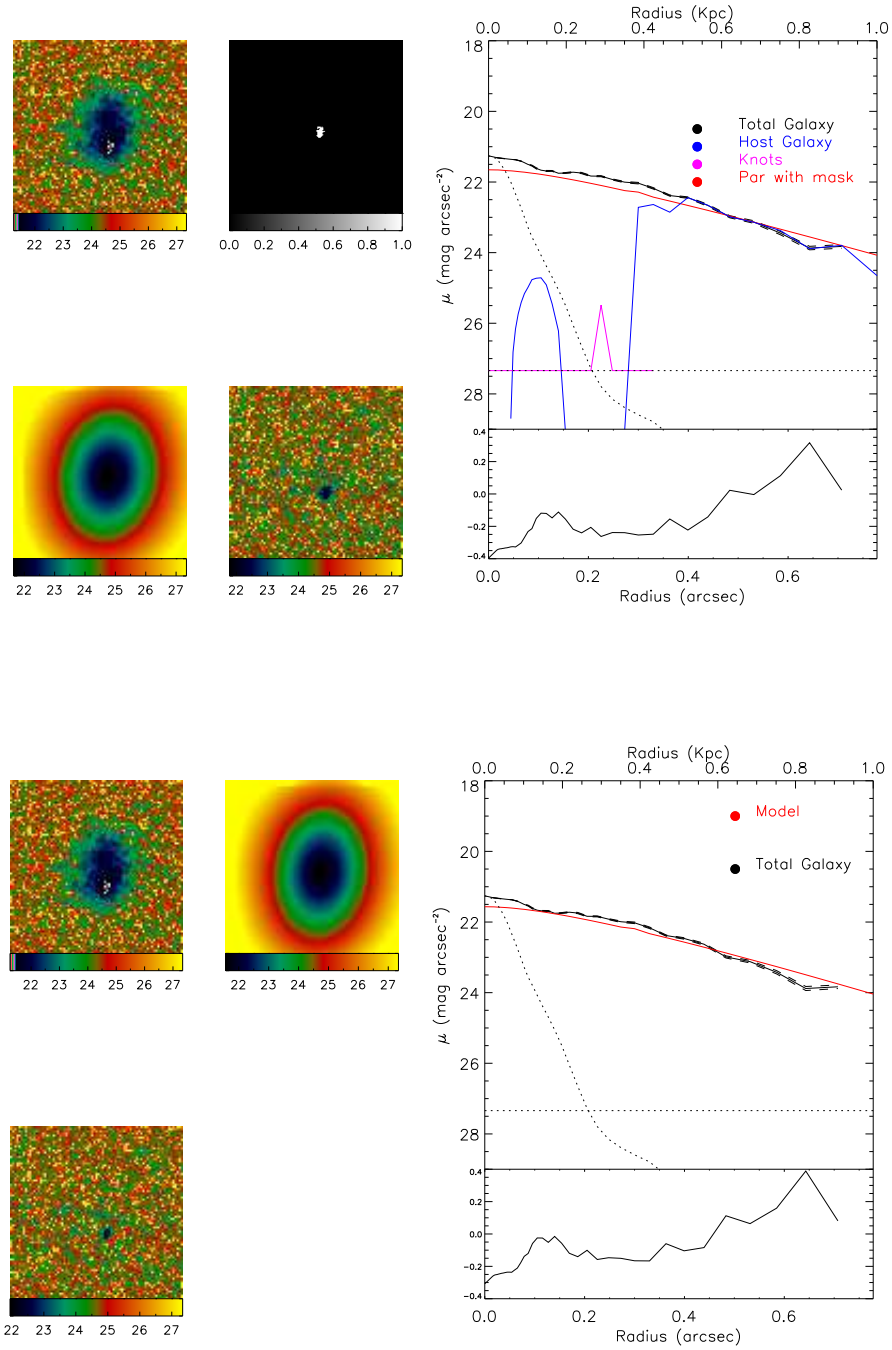

Figure 5.17: Surface-brightness fitting of a Sknot+diffuse light galaxy. In the top a fit using a mask is showed, in the bottom the fit without mask. In the left of each fit, panels show the galaxy, mask (for the fit with mask), 2D model and residual of the fit. In the right the luminosity of the galaxy, model and PSF versus radius is showed on the top for every fit, for masked fit also the profile of the host galaxy and knots are showed. In the bottom the residual of the model with respect to the galaxy is showed. In this case the star-forming region is located close to the border of the galaxy, and its size is small in comparison to the galaxy size. The use of a mask have not much effect on the output result, for masked fit the Sersic index is n=0.85, and for unmasked fit n=0.82. The residual in both cases are similar, and correspond to the star-forming region.

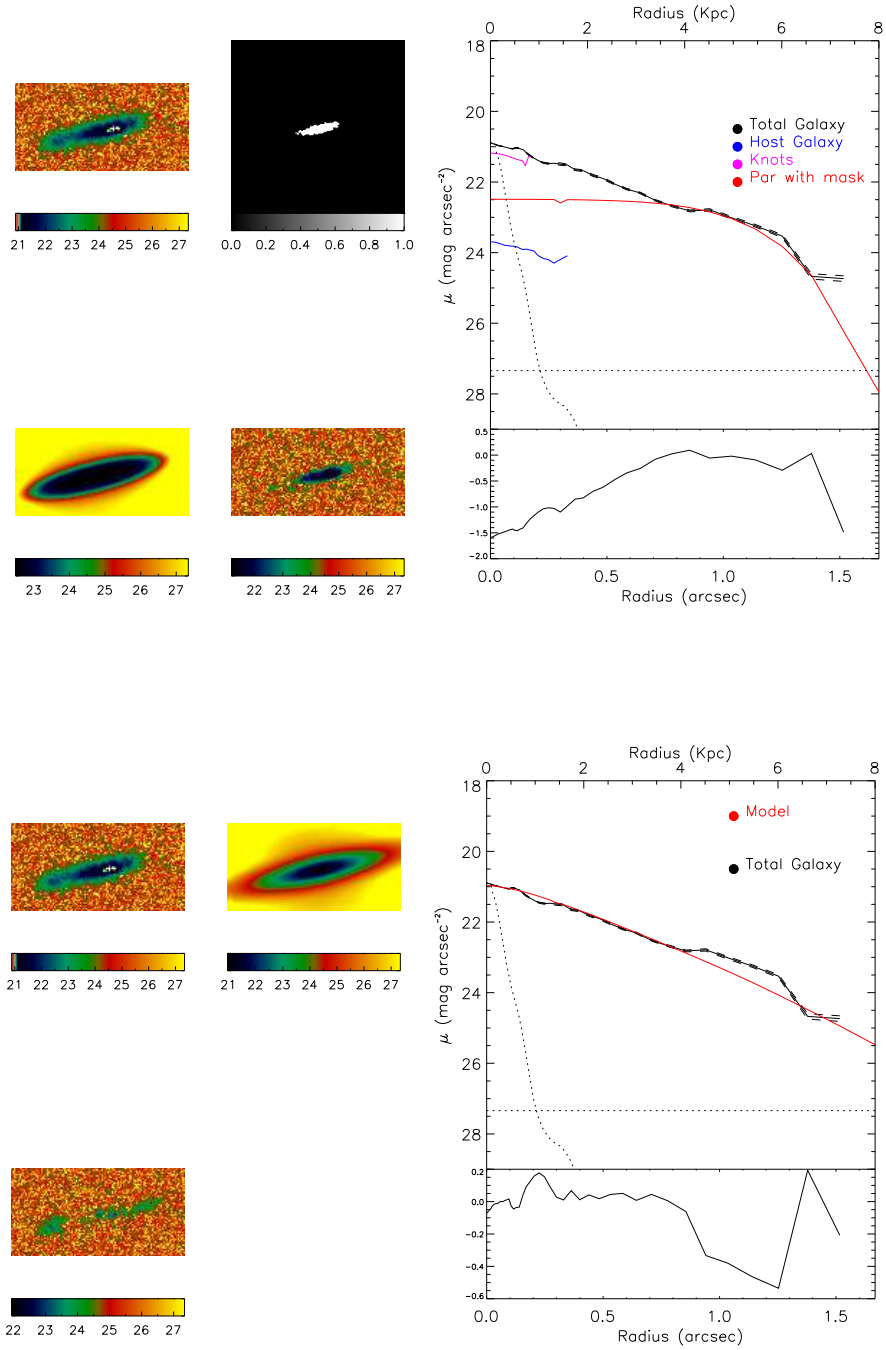

Figure 5.18: Surface-brightness fitting of a Sknot+diffuse light galaxy. In the top a fit using a mask is showed, in the bottom the fit without mask. In the left of each fit, panels show the galaxy, mask (for the fit with mask), 2D model and residual of the fit. In the right the luminosity of the galaxy, model and PSF versus radius is showed on the top for every fit, for masked fit also the profile of the host galaxy and knots are showed. In the bottom the residual of the model with respect to the galaxy is showed. In this case the star-forming region is located in the center of the galaxy, and the size is enough to cover a large area of the profile. Masking a large area in the central region, produce an sub estimation on the luminosity in the central region of the fit. The Sersic index for the masked fit is n=0.18, but without masking n=0.96, which is an expected value.

5.5.3 Multiple knots galaxies

In our catalogue of starburst galaxies, 54 of them are classified as Mknots galaxies. They are galaxies with two or more star-forming regions surrounded by diffuse emission. Fig. 5.19 shows examples of eight Mknots galaxies in our sample, the bar at the upper right corner corresponds to a 1(kpc) scale. In this section we present the results for the fit of the luminosity profile of these galaxies.

For every Mknots galaxy, we constructed a mask with the knots of star formation. As in the previous section for Sknot+diffuse light galaxies, to construct the mask for the star-forming regions we used FOCAS with the task splits to separate embedded regions of star formation. For Mknots galaxies the situation is similar to Sknot+diffuse galaxies, but with more knots of star formation. We estimate the flux from the star-forming region using the mask, the galaxy and the output model. We estimated the ratio between the difference of the flux for every pixel from the star-forming region and the flux from the residual image, with respect to the flux from the galaxy used to fit the luminosity profile. Galaxies fits with a goodness parameter ($\mathcal{G}$) > 0.1 were discarded. Fig. 5.20 shows an example of the fit to the galaxy COSMOS-091 classified as Mknot galaxy. To the left of the figure four panels show the procedure of the fit. Top left panel shows the science image of the galaxy, top right panel shows the mask used in the fit. Bottom left show the 2D best fit model using a Sersic profile, and the bottom right panel shows the residuals of the fit. Scales are in magnitudes/arcsec^2, x-axis is RA, and y-axis is DEC. To the right of Fig. 5.20, in the upper panel, we show this fit for the galaxy (black dashed line), the Sersic profile (red line) obtained with the best fit with GALFIT, the PSF (black dotted line), the host galaxy (blue line), and the knots (pink line). Lower panel shows the residual of the model with respect to the galaxy. X axis shows the radius in kpc scale (top) and arcsec scale (bottom). Y axis shows the surface magnitude μ (mag arcsec^{-2}) in the F814W ACS/HST band.

The ratio of the masked area over the galaxy area was also estimated and compared with the distance to the center of the galaxy. To do it we have considered the sum of every mask area for each galaxy over the galaxy area with respect to the mean distance of the knots to the galaxy center. In Fig. 5.22 we show this comparison, one galaxy was discarded from this test. Table 5.3 shows the principal parameters from the luminosity profile fit for the 54 Mknots galaxies.

For the total sample of Mknot galaxies, the mean of the Sersic index of the luminosity profile is $< n > \sim 1$, which are similar to the values found for Sknot+diffuse galaxies. From these statistical results, we induce that the most of the Mknots galaxies have a disk like luminosity profile. As in previous section, the presence of an star-forming region produce an overestimation on the luminosity profile of the host galaxy, this effect is more pronounced when the star-forming region is located in the center of the galaxy.

Object	Area gal pixels^2	Area mask pixels^2	SB (erg s^{-1}cm^{-2}Å^{-1}kpc^{-2})	NB (erg s^{-1}cm^{-2} Å^{-1})	n	R_e (pixels)	PA	e	𝔊
(1)	(2)	(3)	(4)	(5)	(6)	(7)	(8)	(9)	(10)
cosmos-005	3788	190	4.24E-26	2.03E-13	1.10 ± 0.01	28.0	83	0.62	0.07
cosmos-006	2280	454	3.66E-26	1.63E-13	0.61 ± 0.01	22.4	21	0.54	0.04
cosmos-011	1954	92	1.71E-26	3.494E-13	0.61 ± 0.01	10.9	90	0.39	0.13
cosmos-012	6257	355	99.0	99.0	1.02 ± 0.01	33.2	21	0.55	0.01
cosmos-019	4454	236	8.78E-26	2.02E-13	0.99 ± 0.01	33.2	22	0.41	0.01
cosmos-021	1750	194	1.09E-24	3.16E-13	0.73 ± −−	0.4	12	0.83	0.31
cosmos-032	2937	548	5.97E-27	2.22E-13	0.40 ± 0.01	27.8	8	0.67	0.00
cosmos-054	2380	1105	1.32E-20	1.93E-13	1.40 ± 0.02	23.6	-5	0.72	0.07
cosmos-056	802	246	3.17E-23	1.41E-13	1.48 ± 0.07	39.3	20	0.44	0.02
cosmos-058	4110	257	99.0	99.0	0.67 ± 0.01	44.0	7	0.60	0.01
cosmos-062	5680	94	99.0	99.0	0.94 ± 0.01	105.2	46	0.68	0.02
cosmos-068	4394	564	6.06E-27	2.16E-13	0.37 ± 0.01	25.0	-62	0.32	0.02
cosmos-071	1142	134	8.98E-26	3.33E-13	0.21 ± 0.01	16.5	-68	0.72	0.04
cosmos-082	5073	543	7.01E-28	2.03E-13	0.65 ± 0.01	26.7	-30	0.47	0.04
cosmos-083	451	104	3.48E-24	3.02E-13	0.20 ± 0.02	8.1	-28	0.55	0.01
cosmos-084	3714	210	5.60E-26	2.31E-13	1.42 ± 0.02	23.4	26	0.61	0.09
cosmos-085	2571	369	1.24E-25	2.91E-13	0.68 ± 0.02	40.3	71	0.78	0.01
cosmos-089	1062	861	99.0	99.0	0.82 ± 0.01	103.4	19	0.59	0.00
cosmos-091	1302	70	5.60E-25	2.85E-13	1.13 ± 0.02	23.1	-53	0.83	0.05
cosmos-098	7127	459	99.0	99.0	1.39 ± 0.02	100.5	-85	0.89	0.01
cosmos-104	3379	651	99.0	99.0	1.30 ± 0.03	60.6	-68	0.36	0.03
cosmos-107	1850	222	1.42E-20	3.15E-13	0.45 ± 0.01	21.1	55	0.16	0.03
cosmos-109	1172	76	8.91E-24	3.33E-13	1.00 ± −−	0.0	19	0.50	0.17
cosmos-113	1888	152	6.87E-26	2.96E-13	0.84 ± 0.01	33.5	-32	0.71	0.02
cosmos-125	3765	856	1.11E-27	3.12E-13	0.22 ± −−	0.4	15	0.87	0.5
cosmos-131	1897	431	7.50E-26	4.05E-13	0.51 ± 0.02	15.2	-56	0.16	0.09
cosmos-132	1303	165	3.06E-25	3.81E-13	0.69 ± 0.02	14.3	32	0.51	0.02
cosmos-134	3169	626	99.0	99.0	0.41 ± 0.01	40.5	35	0.51	0.04
cosmos-143	3346	471	1.98E-25	2.08E-13	0.75 ± 0.01	24.9	-8	0.52	0.00
cosmos-144	2103	588	99.0	99.0	1.06 ± 0.02	50.5	17	0.51	0.00
cosmos-156	13964	647	99.0	99.0	0.73 ± 0.00	56.8	-30	0.52	0.03
cosmos-161	1669	497	2.27E-25	2.08E-13	0.49 ± −−	0.0	49	0.52	0.04
cosmos-162	1972	187	1.23E-25	2.91E-13	0.35 ± 0.01	17.6	-9	0.46	0.03
cosmos-166	1665	369	1.01E-24	2.73E-13	0.40 ± 0.01	15.8	-18	0.28	0.04
cosmos-167	1427	83	3.14E-24	2.50E-13	0.10 ± −−	1.4	0.4	0.80	0.34
cosmos-176	2151	516	5.31E-26	7.03E-13	0.31 ± 0.01	26.9	-81	0.76	0.04
cosmos-177	2149	415	8.868E-26	1.89E-13	0.57 ± 0.01	19.3	90	0.32	0.08
cosmos-179	2679	552	1.60E-25	1.49E-13	2.40 ± 0.17	65.3	90	0.50	0.04
cosmos-181	2596	163	7.46E-26	3.54E-13	0.33 ± 0.01	17.5	-28	0.28	0.02
cosmos-189	1754	246	3.35E-25	3.46E-13	0.44 ± 0.02	16.1	-90	0.34	0.00
cosmos-193	874	215	2.68E-24	2.89E-13	0.93 ± 0.05	19.6	-36	0.38	0.05
cosmos-216	4325	229	99.0	99.0	0.81 ± 0.01	52.3	64	0.55	0.00

Table 5.3: Results of the 2D fit using a Sersic profile to the galaxies classified as Mknots (Sec. 5.5.3). Column 1: Name of the galaxies as was catalogued in our sample. Column 2: Area of the galaxy used for the fit (pixels^2). Column 3: Area of the masked region (pixels^2). Column 4: Surface brightness (erg s^{-1} cm^{-2} Å^{-1} kpc^{-2}) of the galaxies in the F814W ACS/HST band. Column 5: Nearby background (erg s^{-1} cm^{-2} Å^{-1}) surrounded the galaxies in the F814W ACS/HST band. Columns 6: Sersic index (n) from the fit with its associated error. Column 7: Equivalen radius (R_e). Column 8: Position angle (PA). Column 9: Ellipticity (e). Column 10: Goodness parameter (𝔊).

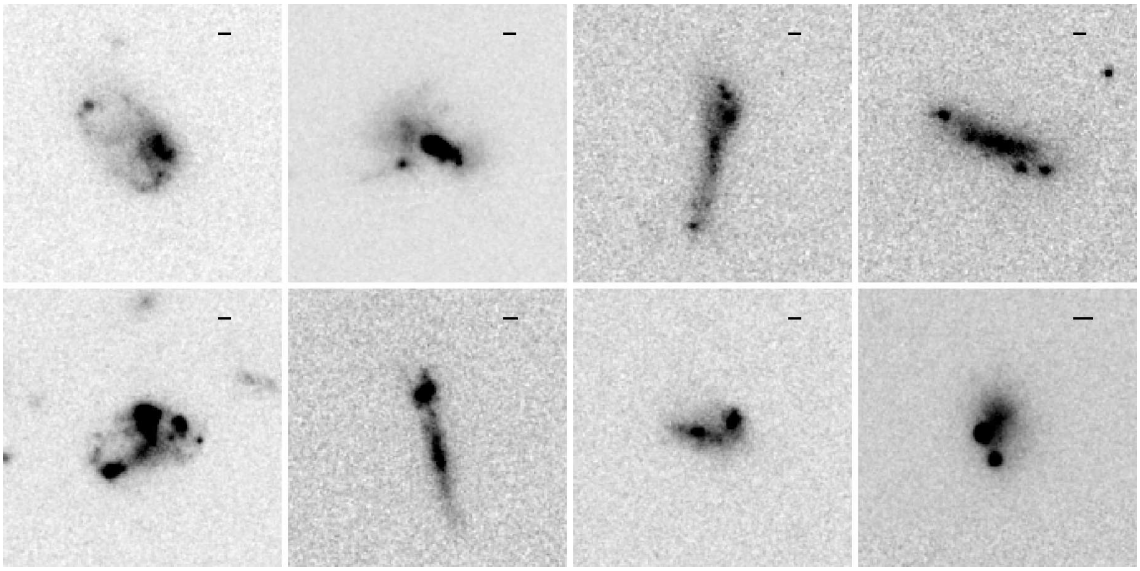

Figure 5.19: Mosaic of eight Mknots galaxies in our sample. At the upper right corner a bar with 1 kpc size is showed.

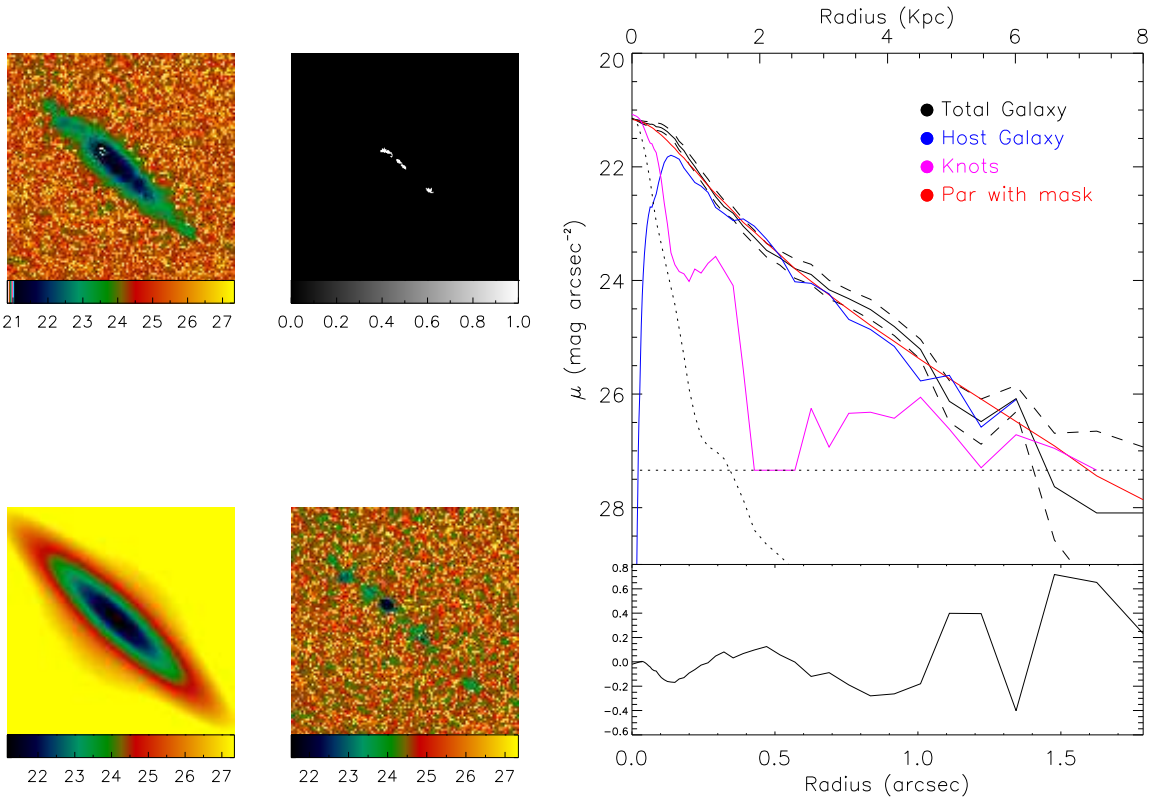

Figure 5.20: Surface-brightness fitting of a Mknot galaxy using a mask for the star-forming regions. In the left panels we show the galaxy, mask, 2D model and residual of the fit. In the right the luminosity of the galaxy, model, knots and PSF versus radius is showed. In the bottom we show the residual of the model with respect to the galaxy.

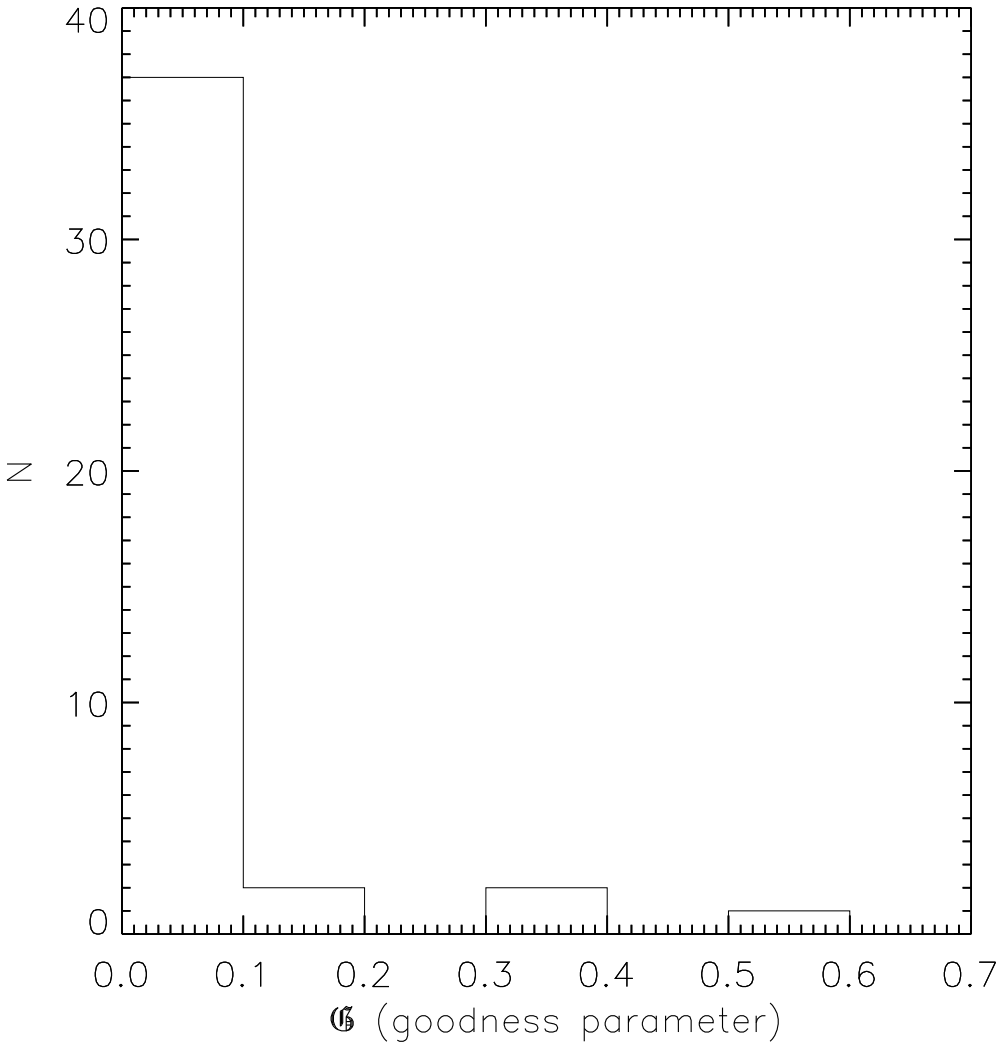

Figure 5.21: Distribution of the goodness parameter for Mknot galaxies.

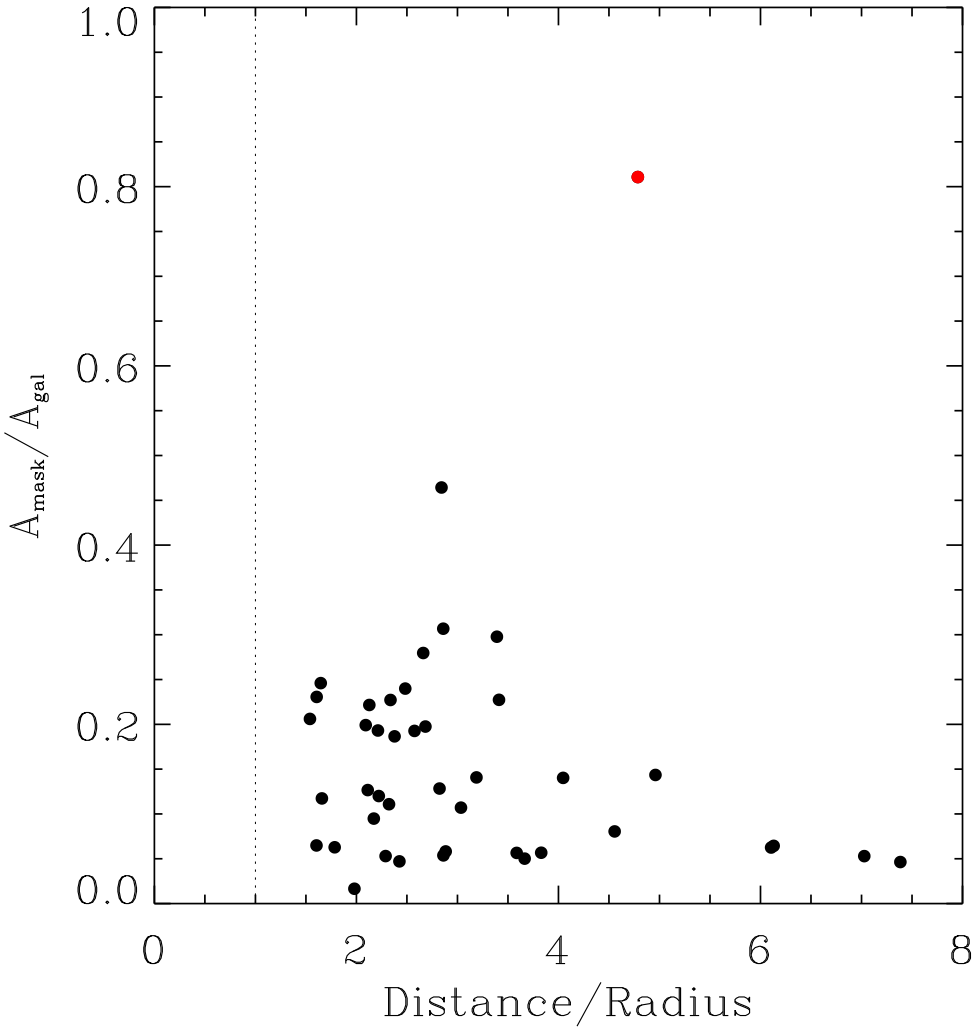

Figure 5.22: Mean distance to the center of galaxy with respect to the mean radius of the mask vs mean area of the mask with respect to the area of the galaxy. A The vertical dashed line in the x-axis separates the lopsided of the offcenter knots. Red points are knots with a large area, this kind of knots does not allow to do a good fit, and are discarded for the statistics.

5.6 Results and Discussion

The host galaxy is the main source of the galaxy gravitational potential and therefore has strong influence on the SF activity and SF interplay with the interstellar medium. Previous studies show that the assessment of the host properties is a fundamental pre-requisite for establishing the evolutionary status and the SF history of the galaxies. Furthermore, the comparison between the structural properties of the host with those of other galaxy classes is essential in order to elaborate a general view of their formation and evolution.

The faint surface brightness of the host component and the contamination caused by the starburst emission make the derivation of the structural parameters of the underlying host in starburst galaxies a complicated task. Thus, the derived structural parameters strongly depend on how well the starburst has been excluded from the fit, on the extent of the fitted host radial profile, on the quality of the dataset, and on the methodology and models used to parametrize the surface brightness distribution. In this chapter we have analyzed the high spatial resolution images in the F814W-band obtained with the ACS camera in the HST available in the COSMOS database. The possibility of using these images with a high spatial resolution is fundamental to study the faint surface brightness of the host galaxies.

In this chapter we have performed a careful 2D fit to the three morphological classes (see chapter 3) of the starburst in COSMOS. We have restricted the analysis to the sample at $z < 0.5$ which, as presented in chapters 2 and 3, comprises 220 galaxies.

We have defined a new statistics to quantify the goodness of the fit to the galaxy surface brightness. This goodness parameter ($\mathfrak{G}$) uses the residual image from GALFIT. Based on the goodness parameter we have been able to discard not reliable fits and obtain a final sample of properly fit host galaxies.

GALFIT also allows for identifying areas of the image which should not be included in the fit. This feature has permitted us to use the star forming regions, identified in chapter 3, to construct masks to be used to do not contaminate the emission from the host by the light from the starburst.

We have also explained the influence of these masks in the accurate of the resulting luminosity profile. We have included morphological parameters like the ratio of the masked area to that of the galaxy and the precise position of the mask, centered or lopsided.

After a careful inspection of the results and uncertainties, from the total sample of 220 galaxies, 171 have been successfully (and) reliability fit using GALFIT. Among the three classes of galaxies, Sknot, Sknot+diffuse, and Mknot galaxies, the percentage of the galaxies that have been successfully fit is 73%, 73% and 91% respectively. The 49 remained fits were analyzed and the principal parameters were given in tables 5.1, 5.2 and 5.3.

Fig. 5.23 shows the distribution of the Sersic index for the three different types of starburst galaxies under study: Sknot, Sknot+diffuse, and Mknots. We have removed from the distribution those galaxies with a poor fit based on the $\mathfrak{G}$ parameter. The Sersic distribution for Sknot galaxies is clearly different from that of Sknot+diffuse and Mknots galaxies. Sknot galaxies shows an extended distribution that gets towards n values ~ 4, Sknot+diffuse and Mknots are far more concentrated in the range $0 < z < 2$ with a peak in $n \sim 1$.

Summarizing, the host galaxy in Sknot+diffuse and Mknots is well described by an exponential profile typical of a galaxy disk. Sknot galaxies are fit with a wide range of n values, including n=4 which corresponds to an exponential distribution as that for an elliptical-like galaxy.

It is important however to emphasize that Sknot galaxies emission includes the host and the burst. As we have not been able to separate both light distribution (see chapters 2 and 3), the fit can not be interpreted as for the Mknots and Sknot+diffuse galaxies samples.

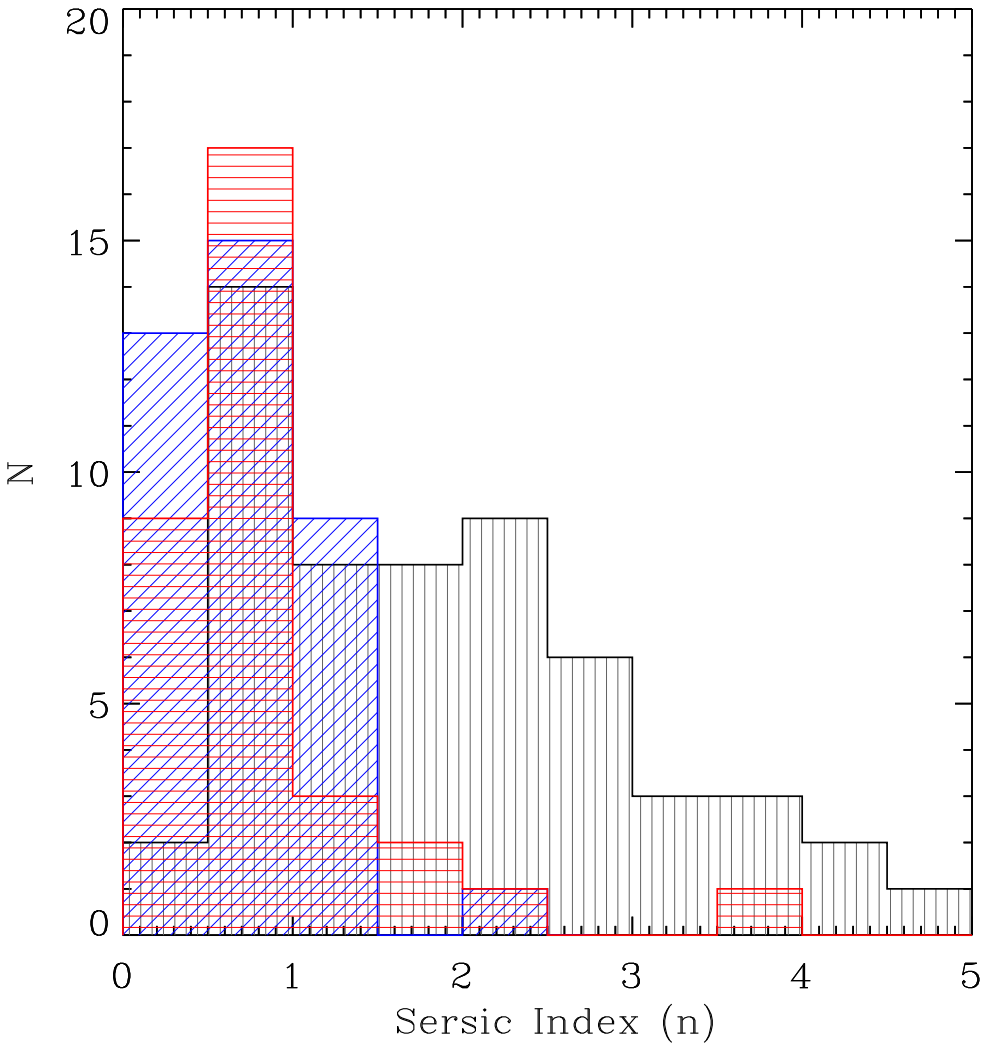

Figure 5.23: Distribution of the Sersic index for the three categories: Sknot (black), Sknot+diffuse (red), and Mknot (blue).

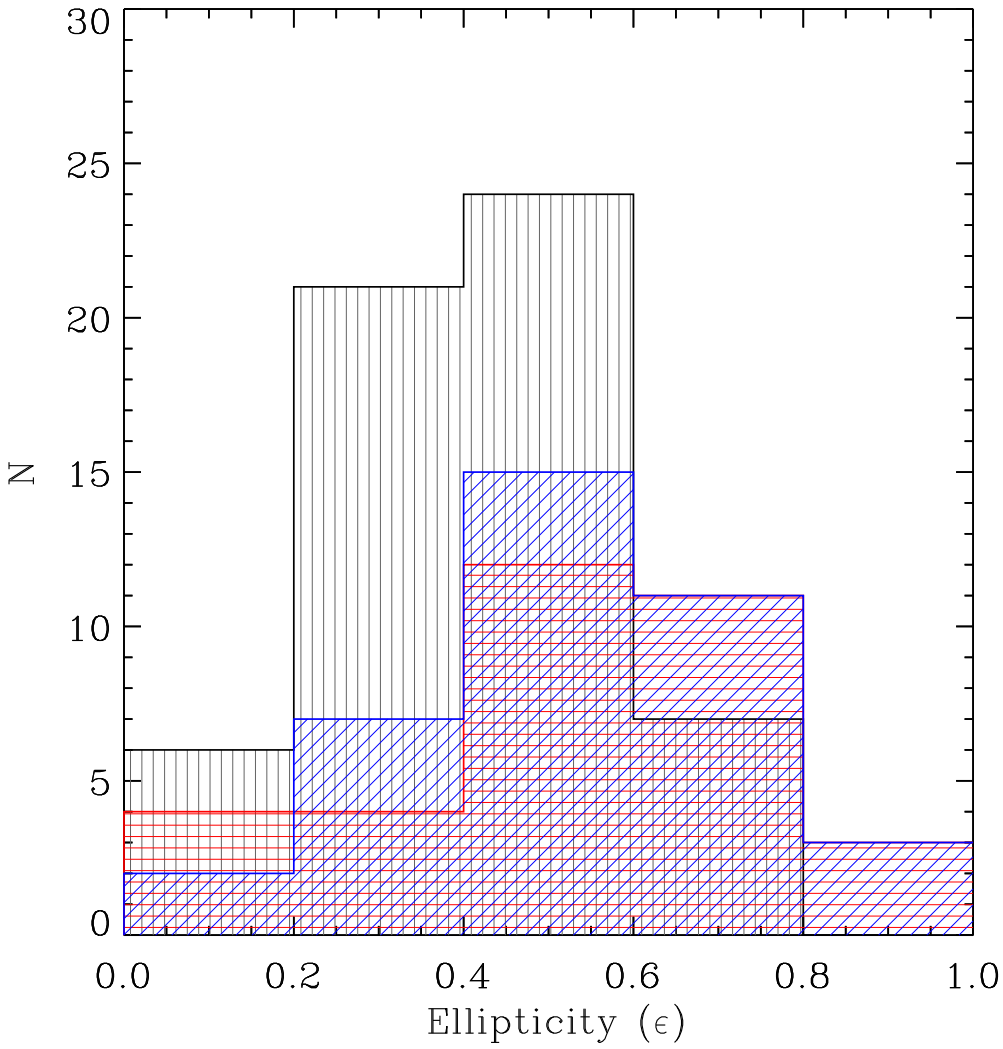

Figure 5.24: Distribution of the ellipticity for the three categories: Sknot (black), Sknot+diffuse (red), and Mknot (blue).

Chapter 6

Star Formation Feedback and Scaling Relations in Starburst Galaxies

The role of star formation (SF) negative feedback is central in galaxy formation studies (Dekel & Silk 1986; Scannapieco et al. 2002; Erb, 2015). In fact, the current state-of-the-art models of galaxy formation are only able to match the observations by tuning the amount of negative feedback produced by SNe in star-forming regions (Governato et al. 2010). The basic principle behind negative feedback is that massive stars, which produce photons and mechanical energy, drive Super Galactic Winds (SGW). SGW remove the material from the galaxy and, together with the ionization, inhibit further SF (Heckman et al. 1990; Tenorio-Tagle & Muñoz-Tuñón, 1997, 1998).

In this chapter we explore different diagnostic tools to explore the starburst feedback of the starburst (clumps) identified in our photometric search. A small sample has also been observed via spectrography of high resolution to seek for more detailed predictions of the hydrodynamical models. Sect. 6.1 describes the physical models which explain the different hydrodynamical solutions derived from the star formation. In section 6.2 we analyze the photometric data from the COSMOS database in the different hydrodynamical scenarios in order to look for galaxies candidates to be in the so-call bimodal phase. Section 6.3 describes the high resolution spectra obtained with the WHT, the data reduction, and the main parameters obtained from the spectral analysis. The multiple components of the H_α emission are analyzed in section 6.4 in order to find different components for the same star-forming region corresponding to the gas in the central region and the gas expulsion from the outer zone. In section 6.5 we analyzed the universality of the scaling relations of luminosity and σ of H_α with the diameter for star-forming regions.

6.1 Models

Theoretical works have shown that the interplay between the thermalization of the kinetic energy injected by massive stars, the radiative cooling of the thermalized plasma, and the gravitational pull of the host galaxy lead to three different hydrodynamic regimes. these are: (1) quasi-adiabatic supergalactic winds; (2) bimodal flows, with mass accumulation in the central region and gas expulsion from the outer zone of the assembling galaxy; and (3) the gravitational bound regime, for which all the gas returned by massive stars remains bound to the host galaxy and it is likely reprocessed into further generations of stars. Which of the three possible solutions takes place depends on the mass of the star-forming regions, its mechanical luminosity (or star formation rate), and its size (Silich et al. 2010: Tenorio-Tagle et al. 2010). In case (2) the value of the stagnation radius defines the volume in which the reprocessed material is retained. Outside the stagnation radius, the classical

adiabatic wind solution holds (Chevalier & Clegg, 1985).

More recent works include also the cooling from the dust produced by Supernovae in the cluster. Like this the threshold line separating the free wind solution and the bimodal phase is as presented in Tenorio-Tagle et al., 2013 and shown in Fig. 6.1. Within more energetic or more massive SSCs, which will fall above the threshold line, the deposited matter suffers frequent thermal instabilities. This depletes the pressure and causes the stagnation radius to move towards the cluster surface, leading to a bimodal solution. In these cases the outer cluster regions produce a stationary wind while the matter deposited in the central regions accumulates and becomes ready to participate in further episodes of star formation.

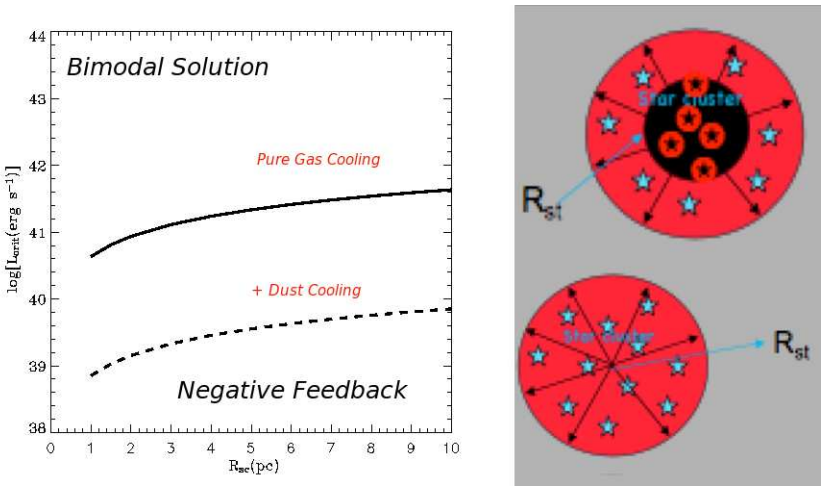

Figure 6.1: Threshold mechanical luminosity. L_{crit} calculated for $V_A\infty$=1000 km s^{-1} under the assumption of pure gas cooling (solid lines) and when gas and dust cooling are added (dashed lines). In all cases, dust grains were assumed to have a radius a=0.1μm.

Bellow the threshold line, the star formation feedback is negative, that is the classical wind or super wins scenario in which matter and energy is thrown out of the cluster to the intergalactic medium.

6.2 SF regime diagnosis by means of photometric data

In order to relate the star cluster mass with the star cluster mechanical luminosity we use an approximate relation to the results of Starburst 99 (Leitherer et al. 1999). This is based on synthesis model for coeval cluster with a Salpeter initial mass function with sources between 1 M$\odot$ and 100 M$\odot$ and ages in the range 4-10 Myr. We assume an instantaneous star formation law and solar metallicity. Like this the mechanical energy of a cluster of mass M_{SC} is given by:

$$L_{SC} = 3 \times 10^{40} \frac{M_{SC}}{10^6 M_\odot} ergs^{-1} \tag{6.1}$$

To derive the age, we use the EW(Hα) as the input parameter. For the galaxies in our sample the EW(Hα) is obtained from the whole galaxy. Only for Sknot galaxies, the EW represents the burst. For this reason we restrict the analysis in this section to the Sknot galaxies only. In Fig. 6.2 we show the mechanical luminosity vs. the radius for Sknot galaxies, the values are provided in table 6.1. Fig. 6.2 shows also the location of the threshold line derived when using only gas cooling from a gas in collisional ionization equilibrium (see Silich et al. 2004 ; Tenorio-Tagle et al. 2007; Tenorio-Tagle et al. 2013) compared to the critical line when one adds gas and dust cooling (dotted line). As

seen in the figure, dust cooling lowers the threshold in the cluster mechanical luminosity (or cluster mass) by about 2 dex or more, depending on the assumed value of $V_{A\infty}$. Thus, many massive (M_{SC} $\geq 10^5 M_\odot$) clusters that appear to be quasi-adiabatic when only gas cooling is considered, are now well above the threshold line, and thus in the bimodal regime.

The calculations show that at the critical line, the fraction of the injected energy that clusters return to the ISM is $L_{out}/L_{SC} \approx 0.69$. As demonstrated by Tenorio-Tagle et al. (2007), this decreases monotonically as one selects more massive clusters with a larger excess energy above the critical value (L_{out}/L_{SC}; see Figure 5 of Tenorio-Tagle et al. 2007). Thus, radiative cooling may strongly deplete the mechanical energy output from massive clusters and thus reduce their negative star formation feedback into the ISM.

Overplot in the figure with the threshold lines from the models, solid line is derived when using only gas cooling from a gas in collisional ionization equilibrium, and dotted line is derived when gas and dust cooling are considered, we have plot the values of the L_{mech} versus the size for Sknot galaxies. The shadow area is the locii of the clusters which evolve in the negative feedback regime if the curve which take into account dust cooling is considered. From them, all the mechanical luminosity and mass from the stars of the clusters have to be released as a classical wind. Note that depending on whether or not dust cooling is important, the family of the clumps of our sample that will undergo a bimodal (+ feedback) situation will vary. From Fig. 6.2 there are two galaxies which are in the bimodal phase if only gas cooling is considered. Many more (50 included the two mentioned above), a total of 63% of the total sample of Sknot galaxies, would be in the bimodal phase and the hydro-solution which accounts for dust cooling is taken account. The results, statistically would be very important and would mean that the standard values used for feedback in the modes should, at least have to be revised. If confirmed, then 63% of the targets would return to the interstellar medium less energy than that predicted by Starburst 99. Red points in the figure are Sknot galaxies which were observed with the WHT and will be analyzed in section 6.4.

Table 6.1: Parameters for Sknot galaxies used to determine the star formation regime, assuming an instantaneous star formation law and solar metallicity. (1) Target name, (2) radius of the galaxy, (3) log of the mechanical luminosity, and (4) mass of the galaxy.

Target	Radius	L_{mech}	mass
	parsecs	ergs s^{-1}	$M_\odot$
(1)	(2)	(3)	(4)
COSMOS-001	1.56	43.25	2.87e+08
COSMOS-004	1.53	42.76	1.59e+08
COSMOS-007	1.65	43.05	3.12e+08
COSMOS-008	0.64	42.30	5.50e+07
COSMOS-009	0.66	41.75	2.18e+07
COSMOS-013	1.43	42.87	2.03e+08
COSMOS-014	2.51	43.54	9.86e+08
COSMOS-016	1.70	43.09	3.37e+08
COSMOS-017	1.19	42.17	4.12e+07
COSMOS-018	1.73	42.93	2.44e+08
COSMOS-020	1.37	43.27	3.34e+08
COSMOS-022	0.21	40.76	1.60e+06
COSMOS-023	0.70	42.57	1.04e+08
COSMOS-026	2.77	43.77	1.71e+09
COSMOS-027	2.62	43.61	1.16e+09
COSMOS-029	4.92	44.81	1.85e+10
COSMOS-035	1.10	42.79	1.76e+08

Table 6.1: continued.

Target	Radius	$\log(L_{mech})$	mass
(1)	(2)	(3)	(4)
COSMOS-037	2.22	43.31	5.62e+08
COSMOS-039	0.69	42.35	4.30e+07
COSMOS-046	1.32	42.61	1.14e+08
COSMOS-047	1.90	42.80	1.83e+08
COSMOS-048	2.65	43.54	9.57e+08
COSMOS-049	−−	40.83	1.91e+06
COSMOS-050	1.82	43.07	3.44e+08
COSMOS-052	0.46	40.97	3.50e+06
COSMOS-053	2.26	43.21	4.68e+08
COSMOS-055	1.50	43.99	2.74e+09
COSMOS-057	1.87	42.91	2.27e+08
COSMOS-059	2.99	43.53	9.86e+08
COSMOS-060	2.17	43.24	4.83e+08
COSMOS-063	1.37	42.60	1.15e+08
COSMOS-067	1.18	42.68	1.31e+08
COSMOS-072	0.19	40.79	1.81e+06
COSMOS-077	1.16	42.57	1.03e+08
COSMOS-078	2.52	43.56	1.02e+09
COSMOS-079	1.81	43.26	4.97e+08
COSMOS-080	1.69	42.52	9.39e+07
COSMOS-086	1.89	43.19	4.29e+08
COSMOS-087	2.47	43.22	4.80e+08
COSMOS-088	1.55	42.79	1.52e+08
COSMOS-092	2.46	43.21	4.51e+08
COSMOS-094	1.71	42.94	2.51e+08
COSMOS-096	1.08	42.38	6.70e+07
COSMOS-099	0.86	42.74	1.61e+08
COSMOS-103	2.52	43.68	1.33e+09
COSMOS-106	1.04	42.59	1.08e+08
COSMOS-108	1.20	42.91	2.38e+08
COSMOS-110	0.93	42.53	9.76e+07
COSMOS-115	1.21	42.04	3.22e+07
COSMOS-117	0.26	41.44	7.72e+06
COSMOS-119	1.51	42.99	2.73e+08
COSMOS-126	1.44	42.99	2.82e+08
COSMOS-127	0.76	42.14	4.02e+07
COSMOS-128	2.14	43.33	5.99e+08
COSMOS-129	1.52	42.77	1.62e+08
COSMOS-130	3.28	43.81	1.85e+09
COSMOS-133	2.00	43.49	1.51e+09
COSMOS-138	−−	43.58	1.06e+09
COSMOS-141	2.11	43.43	7.38e+08
COSMOS-142	1.32	42.77	1.62e+08
COSMOS-145	1.65	43.49	8.21e+08
COSMOS-150	2.74	43.36	6.54e+08
COSMOS-152	2.36	43.43	7.38e+08
COSMOS-153	1.37	42.84	1.92e+08

Table 6.1: continued.

Target	Radius	log(L_{mech})	mass
(1)	(2)	(3)	(4)
COSMOS-154	0.87	42.00	2.89e+07
COSMOS-155	0.10	39.98	2.67e+05
COSMOS-157	0.80	41.77	1.68e+07
COSMOS-158	1.57	42.89	2.27e+08
COSMOS-160	1.54	42.91	2.28e+08
COSMOS-164	2.19	43.56	6.50e+08
COSMOS-174	1.20	42.59	1.08e+08
COSMOS-182	0.10	40.39	6.92e+05
COSMOS-190	0.42	41.92	2.38e+07
COSMOS-192	2.58	43.60	1.10e+09
COSMOS-195	1.41	42.44	7.67e+07
COSMOS-198	1.53	43.94	2.50e+09
COSMOS-202	1.60	42.69	1.42e+08
COSMOS-204	2.25	43.20	4.54e+08
COSMOS-205	1.46	42.83	1.97e+08
COSMOS-206	0.41	42.25	6.29e+07
COSMOS-209	2.78	43.26	5.08e+08
COSMOS-210	0.50	41.63	1.47e+07
COSMOS-212	1.19	42.48	8.88e+07
COSMOS-214	0.86	41.95	3.46e+07
COSMOS-215	1.30	42.38	5.78e+07
COSMOS-218	0.24	41.31	5.99e+06

6.3 Diagnosis by means of high spectral resolution (HSR) data

An observable to distinguish among the different hydrodynamical regimes summarized in 6.1 by measuring emissions line profiles was proposed in Tenorio-Tagle et al. (2010). They predicted two components when the starburst evolves in the bimodal regime. One of them, more intense, from gas within the stagnation radius and a second one, broader and less intense, due to the cluster wind near the cluster surface. In these models, the origin of the most intense Gaussian component is the huge amount of repressuring shocks (RS), induced within the dense thermally unstable reinserted gas as maintains pressure balance with the much hotter gaseous counterpart. The less intense, although much broader Gaussian component, should be caused by the cluster wind, as it becomes photoionized and less dense upon its own expansion. Tenorio-Tagle et al. (2010) and Muñoz-Tuñón et al. (2012), also showed that the maximum speed of the RSs and the cluster wind are both functions of the temperature reached at the stagnation radius. This temperature depends only on the cluster heating efficiency (η), which defines the amount of energy that remains in the flow despite the cooling. Both speeds, that of the RSs and that of the cluster wind, attain a unique value for every η, and these should correspond to the largest speeds at the Half Width at Zero Intensity (HWZI) that one could infer from the Gaussian components used to fit the observed lines. If one measures the HWZI of the observed line and assume that the largest detected speed is due to the wind emanating from the cluster, then η could be calculated. This is a unique tool to measure directly the heating efficiency of the star-forming region.

Low η implies that much of the energy is radiated away while high η means an efficient transformation into kinetic energy as a powerful, high temperature wind that extends far beyond the cluster radius (Muñoz-Tuñón et al. 2012), see Fig. 6.3.

Our goal was to obtain high-resolution spectra of a sample of well-selected massive starbursts

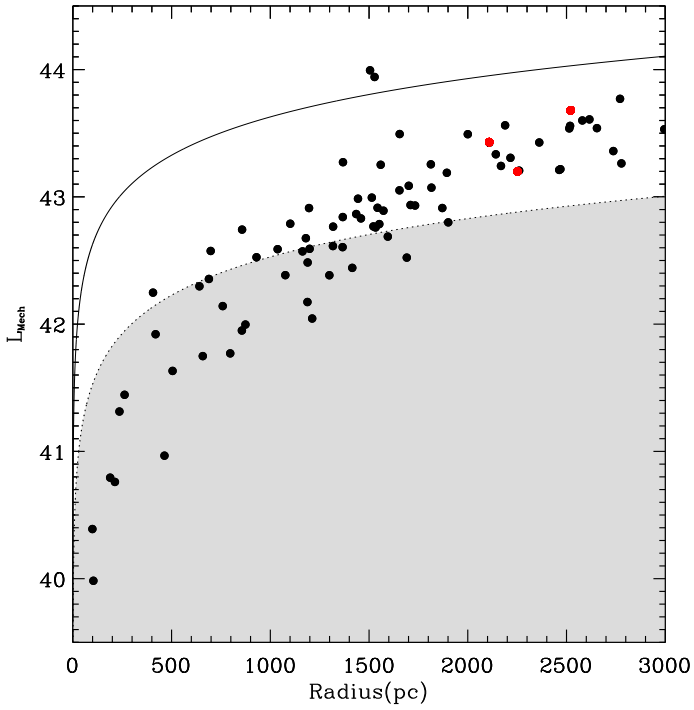

Figure 6.2: Mechanical luminosity for Sknot galaxies, determined using Starburst 99 (Leitherer et al. 1999) assuming an instantaneous star formation law. The threshold line derived when using only gas cooling from a gas in collisional ionization equilibrium (solid line) is showed, compared to the critical line when one adds gas and dust cooling (dotted line) (Tenorio-Tagle et al. 2010). Red points are Sknot galaxies which were observed at the WHT candidates together with oner cadidatesto be in the bimodal phase.

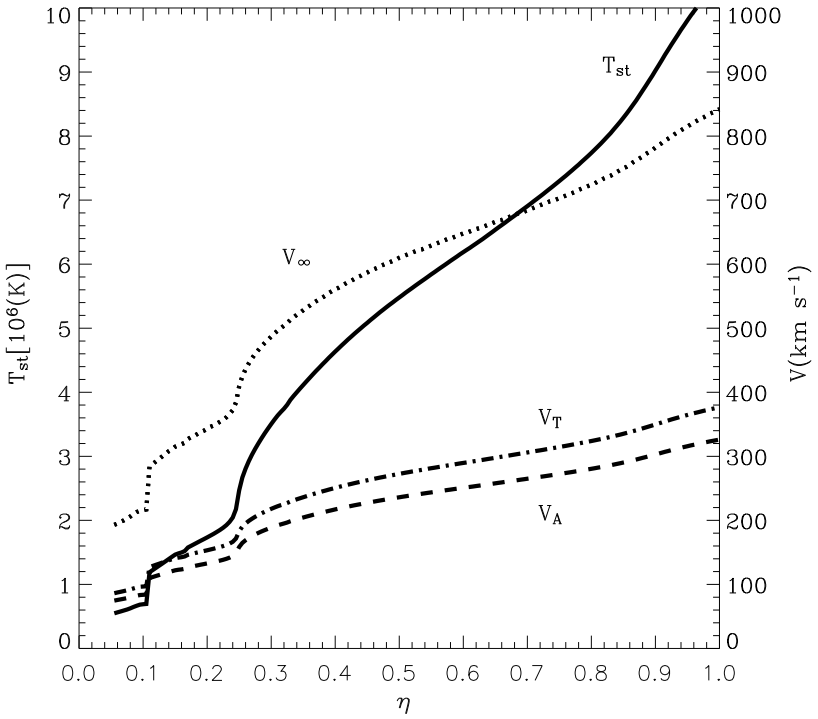

Figure 6.3: Velocity of the gas overtaken by the RS as a function of heating efficiency. The solid line marks the temperature at the stagnation radius (T_{st}), the dashed lines indicate the velocity of the gas overtaken by the RS_S under the adiabatic (1) and isothermal (2) approximations, and the dotted line indicates the terminal speed of the cluster wind (V_∞), all of them plotted as a function of the heating efficiency, η. High η means powerful wind whereas lower η imply that much of the energy is radiated away and much material is to be captured within the stagnateion radius. Fifure taken from Temorio-Tagle et al. (2010).

taken from our catalogue in chapters 2 and 3, candidates to be in the positive feedback regime, to apply our diagnostic plots and study the details of their hydrodynamical status based in the analysis of the Hα emitting line-profiles. The work, presented in this chapter will further establish the pathway to future studies with more extensive samples at and different z. That will be a step towards continuing the work developed in this thesis, in the future (see more in chapter 8). We started by making a telescope proposal aiming at obtaining long slit high resolution spectroscopy ($\sigma \sim 15$ km/s) in order to resolve the Hα (6563 Å) emission line of a subsample of star-forming galaxies from the catalogue at low redshift (chapter 2). The resolved emission line profiles of the star-forming regions were analyzed looking for the presence of a single or double component in the velocity space that will give us important insights on the hydrodynamical state of these objects. We will determine which feedback regime applies (positive or negative) to each star forming complex and find the net contribution of the clumps to the enrichment of the ISM.

6.3.1 Observations

The observations were taken at the WHT during the nights 02 and 03 of February of 2013 using ISIS/WHT mounted with the grim R1200R. It covers a spectral range of 1055 Å with a blaze angle centered at 7200 Å. This gives an instrumental velocity dispersion of $\sigma_{inst} \sim 15$ km/s for a slit width of 1.0 arcsec. This instrumental configuration allows us to map the Hα emission line at the redshift of the galaxies with the required spectral resolution. Typical seeing during the observations was 1 arcsec and the nights were classified as photometric. We selected a subsample of the targets selected from COSMOS in the redshift range $0 < z < 0.3$. We finally obtained long-slit spectroscopy for 11 massive star-forming galaxies selected from the 1.4×1.4 degrees field of view of COSMOS with confirmed spectroscopic redshift from the low resolution spectra in zCOSMOS (see chapter 2).

The details of the observations including the total exposure time, extinction, etc. are provided in table 6.2 together with the target name, exposure time, central wavelength of Hα, seeing, z from the observations and from COSMOS, and the class of galaxy defined in chapter 3.

In Fig. 6.4 we show the HST images of the sample of the galaxies observed with the ISIS slits overplotted. The slit was aligned in the paralactic angle unless in cases where it was possible to observe more than one galaxy with the same slit. For example, COSMOS-204 and COSMOS-209 were obtained with the same slit. In Fig. 6.6 we show as example the 2D image of the detector with the two galaxies that were detected by the slit. For both galaxies the [SII] (doublet), and Hα emission lines can be distinguished.

6.3.2 Data reduction and analysis

To obtain the final spectra, several calibration images were taken in along the observation nights. In particular, bias frames, dome flats, sky flats, arc spectra, object spectra and template stars were taken.

Pre data reduction

The data reduction was performed with standard tasks of the Image Reduction and Analysis Facility (IRAF) software for long slit spectra data reduction. IRAF [1] is a collection of software written at the National Optical Astronomy Observatory (NOAO) geared towards the reduction of astronomical images in pixel array form. First we performed a pre data reduction, the steps followed to do it and the IRAF tasks used were:

- Calculate the average BIAS (Zerocombine)
- Calculate the average DOME FLAT (Flatcombine)

[1] http://iraf.noao.edu/

Target	Exposure time (sec)	Central wavelength Å	Seeing	Redshift WHT	Redshift COSMOS	Class
(1)	(2)	(3)	(4)	(5)	(6)	(7)
COSMOS-44	1800 1800 1800	8001.6	1.1	0.22	0.22	Sknot+diffuse
COSMOS-61	1800 1800	8312.9	1.5	0.27	0.26	Sknot+diffuse
COSMOS-82	1800 1800	8208.3	2.1	0.25	0.25	Mknots
COSMOS-97-a	1800 1800	8030.8	2.1	0.22	0.22	Mknots
COSMOS-97-b	1800 1800	8030.4	0.9	0.22	0.22	Mknots
COSMOS-103	1800 1800	8114.6	2.1	0.24	0.24	Sknot
COSMOS-125	2700 2700	8298.4	1.4	0.26	0.26	Mknots
COSMOS-130	2700 2700		1.4		0.38	Sknot
COSMOS-135	1200 1200		1.2		0.05	Mknots
COSMOS-137	1200 1200	8303.6	1.2	0.28	0.26	Sknot+diffuse
COSMOS-141	1800 1800	7772.7	1.1	0.18	0.17	Sknot
COSMOS-144	1800 1800		1.1		0.26	Mknots
COSMOS-164	1800 1800	8198.8	0.8	0.25	0.25	Sknot
COSMOS-204	2700 1800	7987.3	1.25	0.22	0.22	Sknot
COSMOS-209	2700 1800	82265.5	1.25	0.26	0.26	Sknot

Table 6.2: Observations with the ISIS longslit spectra from WHT. (1) Target name, (2) exposure time, (3) central wavelength of Hα, (4) seeing, (5) redshift determined with the WHT spectra, (6) redshift from COSMOS (zCOSMOS when available), and (7) morphological classification (chapter 3).

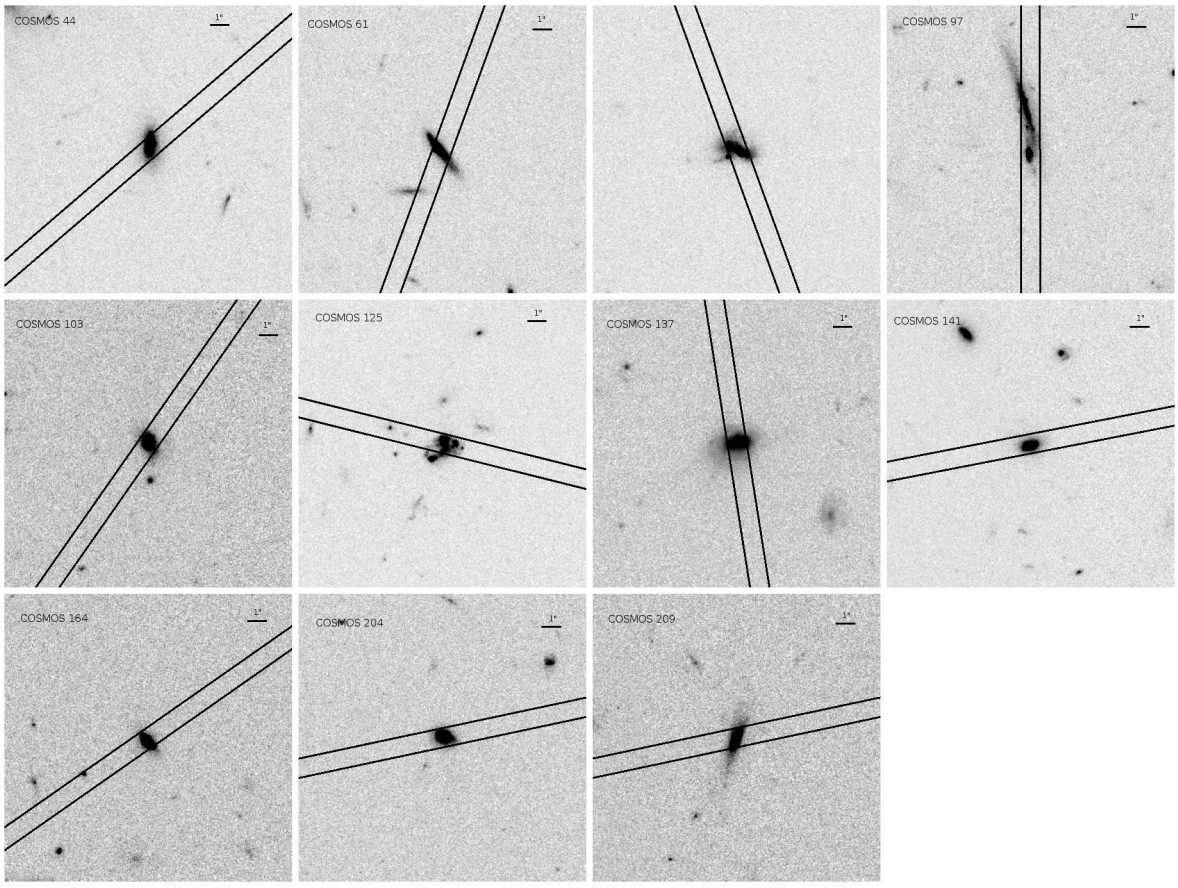

Figure 6.4: WHT ISIS slit over the observed galaxies, the slit was configured with a width of 1 arcsec. Images were taken from the HST ACS F814W−band available in the COSMOS survey.

- Remove BIAS from DOME FLAT (ccdproc)
- Normalize DOME FLAT (Response)
- Correct DOME FLAT for illumination (Illumination)
- Calculate the average SKY FLAT (Flatcombine)
- Remove BIAS from SKY FLAT (ccdproc)
- Normalize SKY FLAT (response)
- Get illumination correction from SKY FLAT (Illumination)
- Build MASTER FLAT (Imarith)
- Correct OBJECTS for BIAS and FLAT (ccdproc)
- Correct TEMPLATE STARS for BIAS and FLAT (ccdproc)
- Correct ARCS for BIAS and FLAT (ccdproc)
- Correct OBJECTS for COSMIC RAYS (lacos_spec)
- Correct TEMPLATE STARS for COSMIC RAYS (lacos_spec)
- Correct ARCS for COSMIC RAYS (lacos_spec)

In Fig. 6.5 we show a typical spectrum with the calibration lamp used for wavelength calibration overplotted.

Resize the spectra along the spatial axis

The CCD image along the spatial axis has geometrical variations which are hard to correct, to avoid this effect we trim the image before sky subtraction, this trimming is done in a base 6 $\times$ the half width at the base of every side, from the middle point of the galaxy in our spectrum.

Wavelength and Flux calibration

After of the pre data reduction steps and the resize of the spectra, we performed a wavelength calibration, the step followed to do it and the tasks used were:

- Identify features on middle column of REFERENCE ARC (Identify)
- Reidentify features on the ARCS (Reidentify)
- Fit wavelengths to pixels on ARCS (Fitcoords)
- Wavelength calibration of ARCS (Transform)
- Wavelength calibration of OBJECTS (Transform)
- Recalibrate with the sky lines (Splot)

Finally we performed the flux calibration with the observed standard stars, the step followed to do it and the task used were:

- Determine SENSITIVITY FUNCTION (Sensfunc)

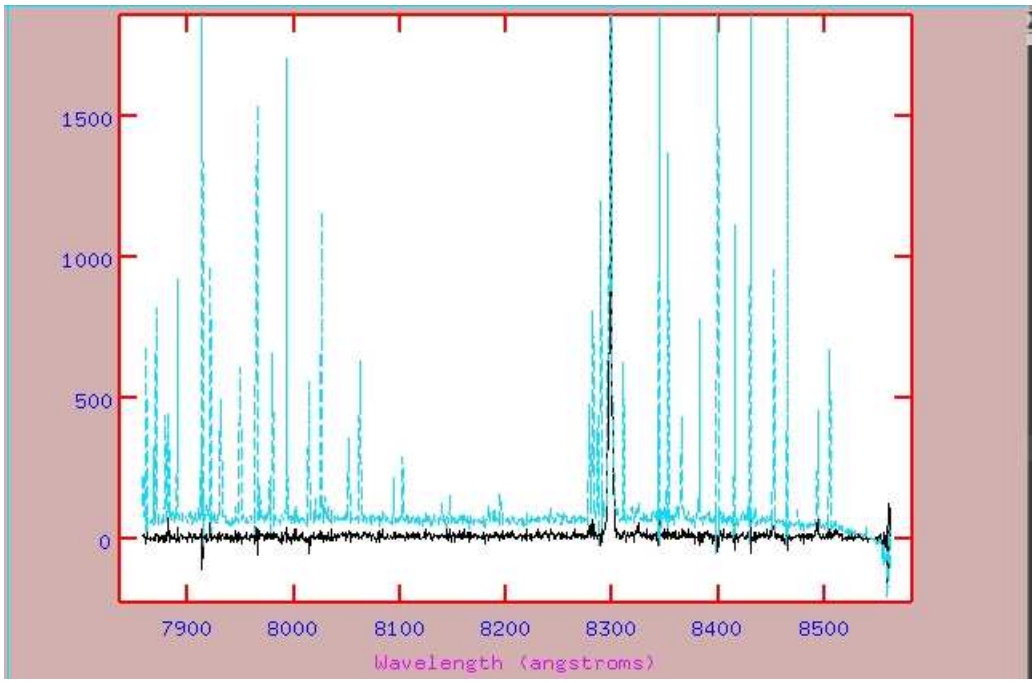

Figure 6.5: Integrated spectrum (all spatial pixels added) of one of the galaxies observed with ISIS at the WHT telescope. A calibration CuNe+CUAR lamp is overplotted.

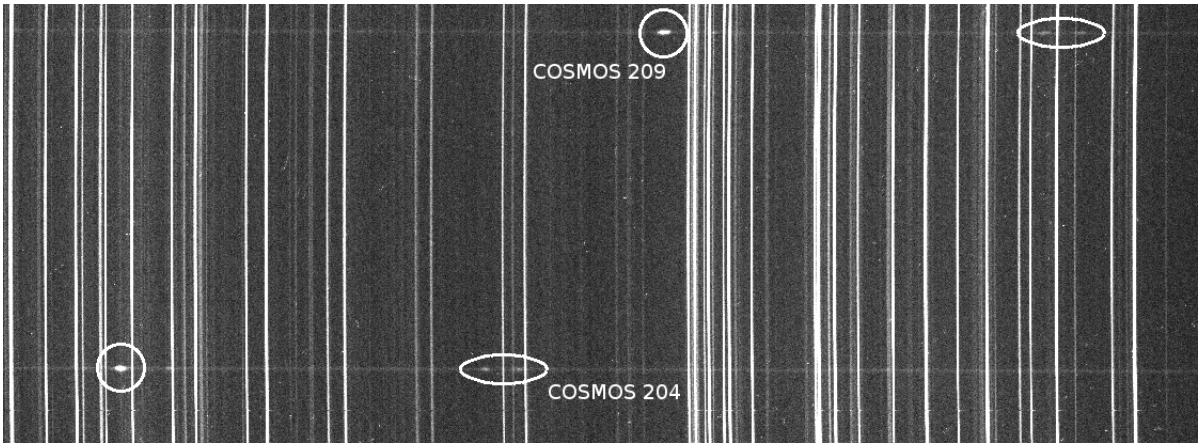

Figure 6.6: Example of the 2D image of the slit with two galaxies in the spatial axis, for both galaxies the Hα and [SII] emission lines are showed.

Object	Redshift WHT	Hα extent	L(Hα)× 10^{40}	EW (Hα)	Redshift	L(Hα)× 10^{40}	EW (Hα)	Type
		(kpc)	(ergs·s^{-1}) (WHT)	Å(WHT)	zCOSMOS	(ergs·s^{-1}) (zCOSMOS)	Å(zCOSMOS)	
(1)	(2)	(3)	(4)	(5)	(6)	(7)	(8)	(9)
COSMOS-044	0.22	14.3	1.03	172	0.22	4.53	220	Sknot+diff
COSMOS-061	0.27	15	0.32	118	−−	−−	−−	Sknot+diff
COSMOS-082	0.25	24	8.6	271	0.25	9.96	316	Mknots
COSMOS-097	0.22	16	1.01	84	0.22	5.11	176	Mknots
	0.22	19.7	1.29	208				
COSMOS-103	0.24	19	0.6	161	0.24	3.19	112	Sknot
COSMOS-125	0.26	18.7	5.12	233	0.27	23.58	572	Mknots
COSMOS-137	0.28	26.5	5.8	152	0.27	23.20	402	Sknot+diff
COSMOS-141	0.18	15	0.91	71	0.19	3.22	113	Sknot
COSMOS-164	0.25	18	2.84	231	−−	−−	−−	Sknot
COSMOS-204	0.22	18	1	141	0.22	3.60	130	Sknot
COSMOS-209	0.26	18.7	0.53	189	−−	−−	−−	Sknot

Table 6.3: Results from a single Gaussian fit to the Hα emission line in the spectra of our targets for the WHT and zCOSMOS spectra. (1) Target name, (2) redshift determined with the WHT spectra, (3) Hα extent in the spatial axis, (4) Hα luminosity determined with the WHT spectra, (5) Hα equivalent width, (6) redshift from zCOSMOS (when available), (7) Hα luminosity from zCOSMOS (when available), (8) Hα equivalent width from zCOSMOS (when available), and (9) the morphological classification of the galaxy from chapter 3.

- Flux calibration and extinction correction of TEMPLATE STARS (Calibrate)
- Flux calibration and extinction correction of GALAXIES (Calibrate)

In Fig. 6.7 we show a mosaic with the 2D reduced WHT spectra, centered at the Hα emission. The x-axis corresponds to the spatial axis and the y-axis to the spectral axis. In this sample there are three galaxies catalogued as Mknots (COSMOS-082, COSMOS-097 and COSMOS-125), however the spatial resolution of the spectra, limited by the seeing, does not allow to separate the regions that were identified from the HST image (see chapter 3 and appendix B). Only for the case of COSMOS-097 it is possible to detect the emission from two separated clumps in the spatial axis.

Once obtained the 2D reduced spectra, we integrated in the spatial axis to obtain a 1D spectra and measure parameters like, z, Hα flux, or EW from the galaxies. These parameters, within errors are in very good agreement with those obtained from zCOSMOS. It confirms that our galaxies, selected from COSMOS as described in chapter 2 do show strong emission lines, adding reliability to the goodness of our selection criteria.

In table 6.3 we provide the redshift, the spatial extent of Hα emission, Hα luminosity, and EW(Hα) after fitting a single Gaussian profile to the Hα emission of the integrated 1D spectra obtained with WHT. For the sake of comparison we also show the redshift, Hα luminosity, and EW(Hα) obtained with spectra from zCOSMOS.

In table 6.4 we present the result of a single Gaussian fit to all emission lines in the spectra of our targets. The table includes fit central wavelength, line width (FWHM), peak intensity and flux of the fit profile. The fit has been performed by means of DIPSO[2] software. The errors in the parameters are also included in the table. Numbers in the column "Line" of table 6.3 corresponds to Hα, [NII], [NII], [SII] and [SII].

6.4 Resolving the kinematic components of the starburst clumps

In section 6.3.2 we carried out the standard procedure on fitting a single Gaussian to the line profiles. This, in turns is the only possible approach when the spectra are taken with moderate to poor resolution. Our observations however allows for a more detailed analysis of the line profile. To start one may question if the presence of multiple components as identified by splitting emission lines lines reflects the presence of different stellar cluster- not resolved in the image.

[2]http://www.starlink.rl.ac.uk/docs/sun50.htx/sun50.html

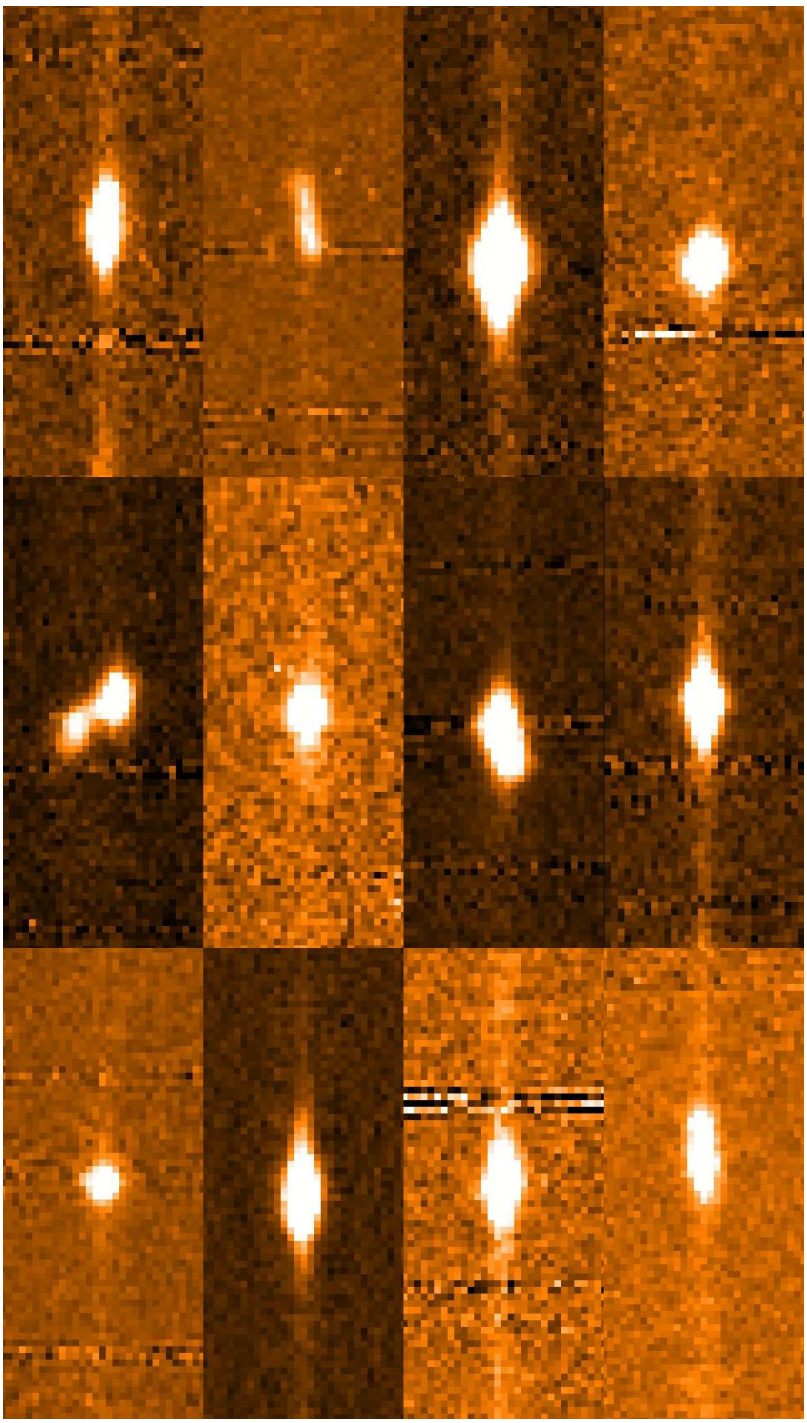

Figure 6.7: Mosaic of the 2D reduced WHT spectra centered in the Hα emission, the X and Y axis show the spatial and spectral axis respectively. Galaxies are shown in the same order as presented in table 6.1 and 6.2 from left to right, top to bottom.

Also and, as explained below, the line profile analysis is also compulsory to be able to determine the kinematic status of the ionized nebula. Moreover, the so call scaling relations (see chapter 1) do not account for the presence of the winds, which are expected from the adiabatic expansion of the winds and SN remnants which leave the cluster volume and produce the, more extended ionized nebula.

To address the above-mentioned issues we have performed a more detailed line analysis allowing for more than one component to match the line profiles. The results for Hα line are summarized in table 6.4. In Fig. 6.8 we show the analysis of the components in the Hα emission lines.

In this figure we see in a black circle five cases where we found multiple components with the same central wavelength, we interpret this result as two different hydrodynamical regimes in the same star-forming region, the first being more intense and narrow belong to the gas within the stagnation radius, and the second one, broader and less intense, is due to the cluster wind near the cluster surface. In table 6.4 we summarize the emission of both components fitting a Gaussian profile. The fits are given in the different rows for every component (broad and narrow). Three of the five galaxies with multiple components and the same central wavelength are catalogued as Sknot galaxies, which allow us to find them in the L_{mech} versus radius diagram (Fig. 6.2) explained in section 6.2. These three galaxies are marked in red color in this diagram and are candidates to be in the bimodal regime. Assuming that the different components belong to the photoionized cluster wind (broad component) and the gas condensed within the stagnation radius (narrow component), we constructed table 6.4 to give the parameters of the different regions.

The other six spectra show multiple components with different central wavelength. We interpret this result as spatially different star-forming regions which in some cases (Sknot) can not be spatially resolved by the HST images, but they are resolved spectroscopically. For Sknot+diffuse galaxies one component could be from the emission of the star-forming region, and the other component could be from the diffuse emission. If this should be the case this component must be fainter than the component from the star-forming region. Other possibility, if both components have comparable intensity is that the second component comes from another star-forming region which is not resolved spatially. For Mknot galaxies we interpret these components as the emission from the star-forming regions which can be resolved spectrally and spatially. The six cases of multiple components with different central wavelength corresponds to: Sknot galaxies (COSMOS-164 and COSMOS-209), Sknot+diffuse galaxies (COSMOS-044 and COSMOS-061), and Mknot galaxies (COSMOS-097 and COSMOS-125). In chapter 3 we identified the star-forming regions in galaxies. From that classification we found two star-forming regions in COSMOS-097 and four in COSMOS-125. For COSMOS-097 we identified two components, in COSMOS-125 we identified three, then we interpret these components for COSMOS-097 as the emission from the different knots of star formation, and for COSMOS-125 as the emission from the three brighter star-forming regions catalogued in chapter 3.

Of the six spectra with multiple component with different central wavelength mentioned in the last paragraph, we want to emphasize the case of COSMOS-164, which shows three components, two centered at the same wavelength and one with different central wavelength. The HST image gives us a radius of 2.2 kpc for this object, which is typically a large radius, then we suggest that there are more than one star-forming region, which is confirmed from the component with different central wavelength. From the resolved spectra of this object we conclude that there are two star-forming region, one of them with just one component, and the other one with two components. For the star-forming region with two components, one of them is narrow and the other broad, with FWHM: 2.723 and 7.643 Å respectively, with the flux of the narrow component $\sim 3 \times$ the flux from the broad one, as expected for a region with two different hydrodynamical regimes.

The results of the fits for galaxies with components with the same central wavelength are shown in Fig. 6.6. For each of the galaxy (columns) it shows in three rows: the values of the fit to the broader and the narrower components, respectively. The parameters provided by the gaussian fit are: flux, the central wavelength and the FWHM in Å. For these galaxies the less intense and

Target	Line	Center	Error center	Width	Error Width	Peak	Error Peak	Flux	Error Flux
(1)	(2)	(3)	(4)	(5)	(6)	(7)	(8)	(9)	(10)
cosmos-044	1	7983.770	0.335	3.234	0.782	4.455E-18	9.503E-19	1.538E-17	3.228E-18
	2	8001.744	0.012	3.491	0.032	1.234E-16	9.214E-19	4.586E-16	3.481E-18
	3	8026.910	0.100	3.286	0.248	1.531E-17	c9.448E-19	5.356E-17	3.374E-18
	4	8189.598	0.157	4.305	0.342	1.096E-17	7.897E-19	5.024E-17	3.681E-18
	5	8207.085	0.154	3.611	0.370	1.001E-17	8.827E-19	3.849E-17	3.444E-18
cosmos-061	1	8312.847	0.064	4.765	0.145	2.804E-17	7.895E-19	1.433E	4.079E-18
	2	8338.186	0.560	3.471	1.172	3.449E-18	9.386E-19	1.274E-17	3.687E-18
	3	8507.766	0.513	4.875	1.130	3.723E-18	7.736E-19	1.932E-17	4.181E-18
	4	8526.303	0.930	5.127	1.566	2.229E-18	6.947E-19	1.217E-17	4.109E-18
cosmos-082	1	8189.947	0.505	3.767	1.153	1.394E-17	3.741E-18	5.591E-17	1.533E-17
	2	8208.314	0.007	3.269	0.021	8.331E-16	4.242E-18	2.899E-15	1.500E-17
	3	8234.047	0.159	3.361	0.422	4.216E-17	4.226E-18	1.508E-16	1.529E-17
	4	8400.633	0.149	2.671	0.365	3.977E-17	4.561E-18	1.131E-16	1.319E-17
	5	8418.523	0.214	2.849	0.504	2.885E-17	4.418E-18	8.749E-17	1.339E-17
cosmos-97-A	1	8030.230	0.018	3.599	0.044	1.300E-16	1.323E-18	4.979E-16	5.157E-18
	2	8217.843	0.179	3.579	0.468	1.258E-17	1.333E-18	5.192E-18	3.273E-17
	3	8235.771	0.312	3.900	0.761	7.885E-18	1.265E-18	3.273E-17	5.386E-18
cosmos-97-B	1	8030.806	0.015	2.624	0.034	1.184E-16	1.315E-18	3.306E-16	3.715E-18
	2	8056.199	0.320	2.665	0.586	5.269E-18	1.221E-18	1.494E-17	3.443E-18
	3	8218.736	0.318	4.330	0.868	6.868E-18	1.052E-18	3.165E-17	5.128E-18
	4	8236.821	0.229	2.534	0.497	7.203E-18	1.307E-18	1.943E-17	3.517E-18
cosmos-103	1	8114.638	0.020	2.321	0.058	6.088E-17	1.161E-18	1.504E-16	2.905E-18
	2	8304.543	0.259	2.643	0.691	5.109E-18	1.038E-18	1.437E-17	3.058E-18
	3	8322.663	0.175	1.515	0.407	5.865E-18	1.325E-18	9.457E-18	2.199E-18
cosmos-125	1	8298.395	0.014	3.647	0.035	4.429E-16	3.507E-18	1.719E-15	1.383E-17
	2	8324.307	0.585	4.028	1.207	1.101E-17	3.111E-18	4.721E-17	1.378E-17
	3	8492.537	0.299	3.679	0.715	2.074E-17	3.487E-18	8.124E-17	1.365E-17
	4	8510.600	0.504	4.557	1.035	1.428E-17	2.894E-18	6.927E-17	1.488E-17
cosmos-137	1	8285.430	0.354	2.479	1.026	1.317E-17	3.993E-18	3.475E-17	1.057E-17
	2	8303.558	0.009	2.680	0.025	4.949E-16	3.593E-18	1.412E-15	1.038E-17
	3	8329.797	0.128	2.545	0.331	3.407E-17	3.616E-18	9.229E-17	9.936E-18
	4	8498.086	0.101	2.313	0.268	4.201E-17	3.853E-18	1.034E-16	9.630E-18
	5	8516.149	0.164	2.745	0.499	2.825E-17	3.826E-18	8.252E-17	1.102E-17
cosmos-141	1	7772.688	0.026	2.129	0.075	1.114E-16	3.136E-18	2.524E-16	7.182E-18
	2	7797.000	0.580	3.455	1.812	6.923E-18	2.681E-18	2.546E-17	9.802E-18
	3	7954.612	0.257	2.694	0.510	1.430E-17	2.554E-18	4.101E-17	7.447E-18
	4	7971.840	0.657	3.543	1.748	6.347E-18	2.563E-18	2.394E-17	9.343E-18
cosmos-164	1	8189.805	0.015	3.769	0.036	2.791E-16	2.264E-18	1.120E-15	9.220E-18
	2	8215.874	0.596	4.365	1.469	7.571E-18	2.180E-18	3.518E-17	9.799E-18
	3	8381.325	0.436	2.939	1.059	8.465E-18	2.541E-18	2.648E-17	8.122E-18
	4	8399.371	0.339	2.598	0.899	1.078E-17	2.865E-18	2.981E-17	8.013E-18
cosmos-204	1	7969.590	0.152	1.141	0.324	6.408E-18	1.715E-18	7.784E-18	2.059E-18
	2	7987.326	0.014	2.929	0.034	1.194E-16	1.135E-18	3.722E-16	3.586E-18
	3	8012.314	0.216	3.602	0.494	8.245E-18	9.835E-19	3.161E-17	3.830E-18
	4	8174.321	0.143	3.086	0.339	1.135E-17	1.066E-18	3.728E-17	3.571E-18
	5	8191.524	0.237	3.562	0.686	7.803E-18	1.106E-18	2.959E-17	4.248E-18
cosmos-209	1	8247.771	0.857	4.099	2.030	2.759E-18	1.120E-18	1.204E-17	5.072E-18
	2	8265.487	0.049	4.495	0.114	4.731E-17	1.054E-18	2.264E-16	5.136E-18
	3	8290.855	0.562	4.427	1.426	4.191E-18	1.100E-18	1.975E-17	5.295E-18
	4	8458.731	0.364	3.824	0.723	5.896E-18	1.095E-18	2.400E-17	4.522E-18
	5	8477.498	0.514	3.267	1.297	3.937E-18	1.173E-18	1.369E-17	4.650E-18

Table 6.4: Single Gaussian fit to the emission lines Hα, [NII], [NII], [SII] and [SII] in the spectra of our targets. (1) Target name, (2) Identified single emission line, (3) central wavelength of the emission line, (4) error in the estimation of the central wavelength, (5) FWHM of the emission line, (6) error on the estimation of the FWHM, (7) Peak in the flux, (8) error in the estimation of the peak of the flux, (9) integrated flux, and (10) error in the flux estimation.

Target (1)	Line (2)	Center (3)	Error center (4)	Width (5)	Error width (6)	Peak (7)	Error peak (8)	Flux (9)	Error flux (10)
COSMOS-44	1	8001.573	0.041	2.624	0.156	9.870E-17	1.487E-17	2.757E-16	5.692E-17
	2	8804.119	0.095	1.411	0.269	1.532E-17	4.598E-18	2.302E-17	1.032E-17
	3	8002.054	0.149	5.119	0.649	3.196E-17	1.554E-17	1.742E-16	6.423E-17
COSMOS-61	1	8311.920	0.106	2.672	0.216	3.038E-17	1.196E-18	8.640E-17	6.850E-18
	2	8314.893	0.179	2.472	0.319	1.899E-17	7.473E-19	4.997E-17	6.283E-18
COSMOS-82	1	8208.369	0.008	2.384	0.048	5.775E-16	2.098E-17	1.465E-15	8.086E-17
	2	8208.143	0.031	5.024	0.138	2.944E-16	2.170E-17	1.574E-15	7.668E-17
COSMOS-97-A	1	8027.495	0.221	2.448	0.378	1.887E-17	3.230E-18	4.916E-16	1.196E-17
	2	8030.361	0.042	3.186	0.088	1.328E-16	1.322E-17	4.503E-16	1.322E-17
COSMOS-97-B-1	1	8030.803	0.033	2.388	0.188	9.457E-17	2.783E-18	2.403E-16	1.574E-17
	2	8030.803	0.033	3.393	0.885	2.364E-17	6.957E-19	8.538E-17	2.343E-17
COSMOS-97-B-2	1	8030.294	0.000	2.034	0.183	5.922E-17	4.531E-18	1.282E-16	1.557E-17
	2	8031.232	0.000	2.451	0.135	7.317E-17	4.659E-18	1.909E-16	1.646E-17
COSMOS-103	1	8114.639	0.017	1.762	0.054	5.300E-17	1.398E-18	9.939E-17	4.580E-18
	2	8114.139	0.139	6.752	0.514	1.224E-17	1.216E-18	8.799E-17	5.682E-18
COSMOS-125-1	1	8296.433	0.046	1.773	0.105	1.119E-16	7.231E-18	2.112E-16	2.306E-17
	2	8298.734	0.017	2.198	0.051	3.463E-16	7.876E-18	8.105E-16	3.186E-17
	3	8298.302	0.074	5.000	0.000	1.376E-16	8.898E-18	7.323E-16	4.736E-17
COSMOS-125-2	1	8296.207	0.074	1.981	0.157	1.441E-16	9.556E-18	3.038E-16	3.495E-17
	2	8298.691	0.033	2.757	0.073	4.641E-16	5.429E-18	1.362E-15	3.755E-17
COSMOS-137	1	8303.633	0.014	1.858	0.068	3.524E-16	1.896E-17	6.970E-16	6.080E-17
	2	8303.331	0.046	4.368	0.228	1.738E-16	2.003E-17	8.080E-16	5.514E-17
COSMOS-141	1	7772.686	0.025	1.765	0.101	9.847E-17	5.847E-18	1.850E-16	1.983E-17
	2	7772.867	0.263	5.114	1.029	1.684E-17	5.992E-18	9.169E-17	1.886E-17
COSMOS-164	1	8188.229	0.045	1.375	0.137	9.109E-17	1.220E-17	1.333E-16	2.714E-17
	2	8190.085	0.050	2.723	0.116	2.412E-16	3.188E-18	6.992E-16	2.940E-17
	3	8190.199	0.237	7.643	0.478	4.020E-17	5.313E-19	3.271E-16	2.161E-17
COSMOS-204	1	7987.282	0.027	2.400	0.057	9.919E-17	1.381E-18	2.534E-16	4.700E-18
	2	7987.628	0.150	5.246	0.270	2.480E-17	3.453E-19	1.385E-16	7.567E-18
COSMOS-209	1	8262.281	0.151	1.164	0.383	5.211E-18	1.707E-18	6.454E-18	3.111E-18
	2	8265.140	0.053	3.339	0.208	4.971E-17	8.820E-19	1.767E-16	9.747E-18
	3	8267.894	0.088	1.802	0.200	1.965E-17	2.220E-18	3.770E-17	7.413E-18

Table 6.5: Results of the fit to the Hα emission line with multiple components using DIPSO. (1) Target name, (2) identified components in the Hα emission line, (3) central wavelength for each components, (4) error in the estimation of the central wavelength, (5) FWHM for each components, (6) error on the estimation of the FWHM, (7) Peak in the flux, (8) error in the estimation of the peak of the flux, (9) integrated flux, and (10) error in the flux estimation.

broader component comes from the cluster wind and the narrower and more intense of the two lines is produced by the repressurizing shocks within the star-forming regions. Both line arise from matter associated to the star-forming regions and thus they are centered at almost the same radial velocity. The radial velocity differences for these galaxies are given in Table 6.7. In table 6.8 we shows the parameters for the galaxies with components with a different central wavelength.

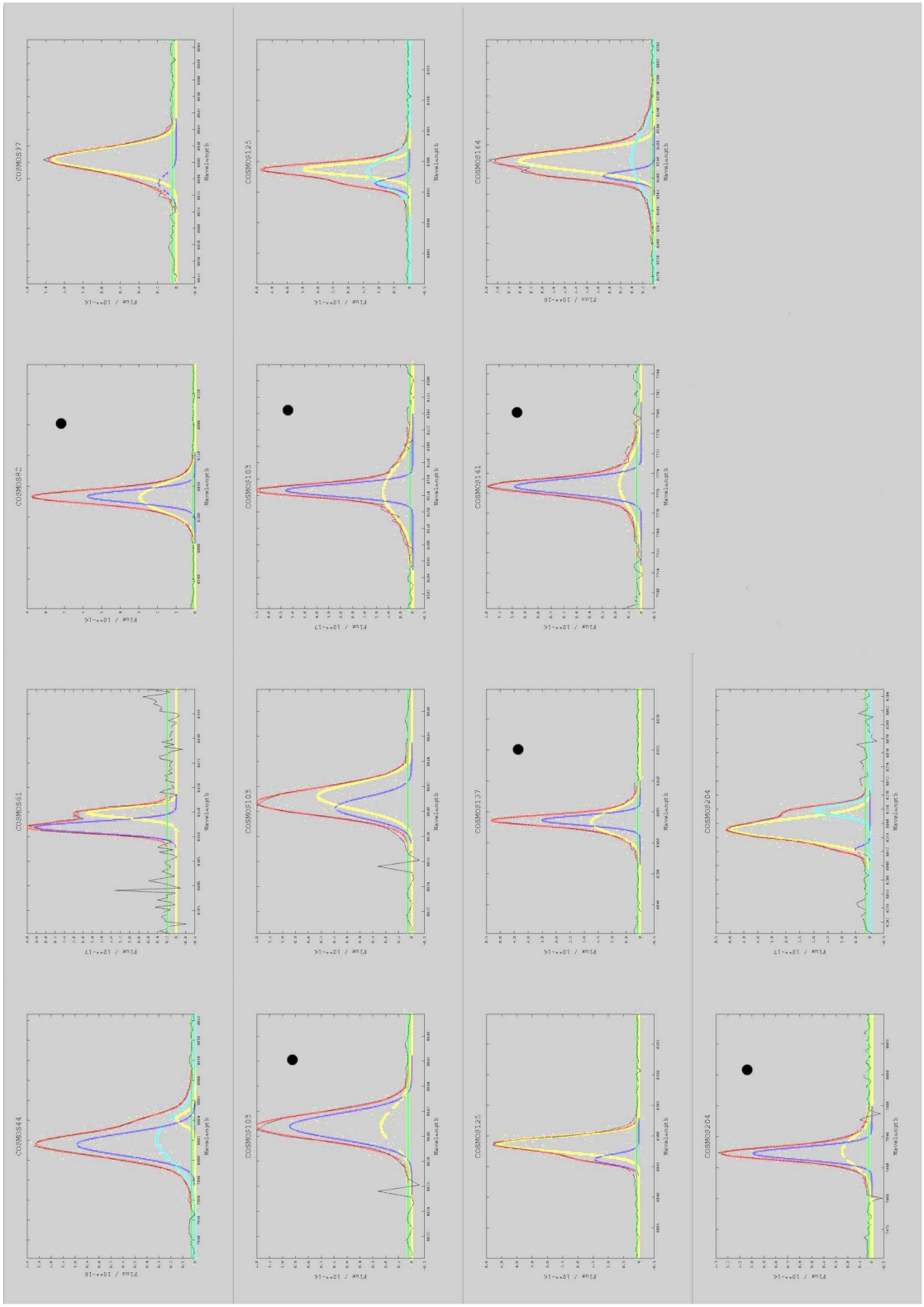

Figure 6.8: Multiple component fits to the Hα emission line with DIPSO. Six galaxies show multiple components with the same central wavelength - This galaxies - (marked with a black circle) are then candidates to be in a positive feedback stage. The multiple components shown in the other (8) cases at different central wavelength we interprete as signatures of different starburst knots, not resoleved spatially but distinguishable in the velocity pattern.

Component		COSMOS-082	COSMOS-103	COSMOS-137	COSMOS-141	COSMOS-204
GAUSS2 (BROAD)	Flux	1.574E-15	1.216E-18	2.003E-17	5.992E-18	3.453E-19
	center	8208.143	8114.139	8303.331	7772.867	7987.628
	FWHM	5.024	6.752	4.368	5.114	5.246
GAUSS1 (NARROW)	Flux	1.465E-15	1.398E-18	1.896E-17	5.847E-18	1.381E-18
	center	8208.369	8114.639	8303.633	7772.686	7987.282
	FWHM	2.384	1.762	1.858	1.765	2.400

Table 6.6: Results of the measurements of Hα emission on targets with multiple components in the same central wavelength. The results of the two gaussians of the fit are given in the different rows for every galaxy (columns).

Target	LineV($_{wind}$) km s^{-1}	V($_{RS}$) km s^{-1}	Width Ratio	$\Delta\lambda$
COSMOS-082	918	361	0.47	0.226
COSMOS-103	2577	359	0.14	0.1
COSMOS-137	1215	394	0.33	0.5
COSMOS-141	1403	347	0.25	0.0
COSMOS-204	995	411	0.41	0.2

Table 6.7: Line measurements on targets corrected by thermal and instrumental broadening. (1) Target name, (2) velocity of the broad component, (3) velocity of the narrow component, (4) ratio of the width between both components, and (5) delta wavelength between components.

Component		COSMOS-044	COSMOS-061	COSMOS-097	COSMOS-125	COSMOS-164	COSMOS-209
1	Flux	2.757E-16	8.640E-17	4.916E-16	2.112E-16	6.992E-16	1.767E-16
	center	8001.573	8311.920	8027.495	8296.433	8190.085	8265.140
	FWHM	2.624	2.672	2.448	1.773	2.723	3.339
2	Flux	2.302E-17	4.997E-17	4.503E-16	8.105E-16	3.271E-16	3.770E-17
	center	8804.119	8314.893	8030.361	8298.734	8190.199	8267.894
	FWHM	1.411	2.472	3.186	2.198	7.643	1.802
3	Flux	1.742E-16			7.323E-16	1.333E-16	6.454E-18
	center	8002.054			8298.302	8188.229	8262.281
	FWHM	5.119			5.000	1.375	1.164

Table 6.8: Results of the measurements of Hα emission on targets with multiple components with different central wavelength. The results of the gaussians of the fit are given in the different rows for every galaxy (columns).

6.5 Scaling relations

Line widths have been used as a powerful tool for deriving fundamental parameters for star forming systems. From the seminal work by Smith and Weedman (1970) in Giant HII regions, it is known that the emission line profile in these systems are supersonic and can reflect the mass of the ionizing stellar cluster. Numerous studies have been devoted to trying to understand the physical mechanisms that provide the energy to the ionized gas as well as to connect its movement as reflected by the line width to the virial mass of the stellar system. From the purely observational point of view much effort has been paid on establishing the line width versus size relation which is important as a scale relation itself and also as it would provide an easy tool to derive masses by just measuring "easy" parameters like the size and the width of the emission line. Lately, as we have been setting more information in the high z universe the scale relations are been used for star forming galaxies in deep surveys. The latest, published by Wisniosky et al (2012), for the sample in the WiggleZ Dark Energy Survey (Drinkwater et al. 2010), there and making use of a large parameters range, from data for GHIIRs to simulated galaxies at $z \sim 1.9 - 3.0$ and including the observational values for galaxies at $z = 1.3$ a new law is obtained for σ versus radii, given by:

$$log(L_{H\alpha}) = (2.72 \pm 0.04) \times log(d) + (31.99 \pm 0.08) \tag{6.2}$$

where $L_{H\alpha}$ is the luminosity in Hα in $ergsseg^{-1}$, and d is the diameter in parsec of the star-forming region.

6.5.1 Photometry

In our sample, we took advantage of the HST high spatial resolution images, which allow us to spatially resolve the clumps of SF, providing an accurate estimation of their sizes. Furthermore, it allows us to estimate the L(Hα) for individual clumps and explore the L(Hα) vs. diameter relation without further hypotheses. We estimated the L(Hα) for clumps in galaxies with $z \geq 0.1$, for which we can detect the Hα emission in the F814W-band. With these values obtained in chapters 2 and 3 we plotted the L(Hα) vs. diameter to explore this scaling relation. Fig. 6.9 shows the Hα luminosity versus diameter of knots in our sample. Blue points are Sknot galaxies. Some Sknot galaxies do show field objects within the fixed SUBARU aperture (Φ=3"). These objects are shown enclosed by a circle, and have been discarded for the fit. Sknot with spectra in zCOSMOS were used to estimate errors associated with the luminosities. Green points are these objects, and the error bar is the difference between the spectroscopic and photometric Hα luminosity. The mean value of this difference is taken as the error for the blue points. The continuum corrected Hα emission for Sknot+diffuse and Mknots is also represented in Fig. 6.9 (red points). The errors associated to each knot were computed by propagating the uncertainties. In order to estimate how the uncertainties associated with these Hα measurements can influence the best-fit of the scaling relation, we ran a set of Monte Carlo experiments. We created 100 simulated distributions of Hα luminosity of the knots. Each individual galaxy was allowed to vary its luminosity within the 1σ correction. The best-fit for each distribution was obtained, and it is represented in Fig. 6.9 (red line). The mean slope and dispersion obtained from this method was 2.46 and 0.04, respectively. The value of the slope is an important parameter to under- stand the universality of the L(Hα) vs. diameter scaling relation. In our sample we found the relation:

$$log(L_{H\alpha}) = (32.2 \pm 0.1) + (2.48 \pm 0.05) \cdot log(d) \tag{6.3}$$

for Sknot, Sknot + diffuse and Mknots galaxies. Fuentes-Masip et al. (2000) obtained a value for the slope of 2.5 for giant HII regions in NGC4449, and Wisnioski et al. (2012) found a value of 2.78 using local giant HII regions and high-redshift clumps.

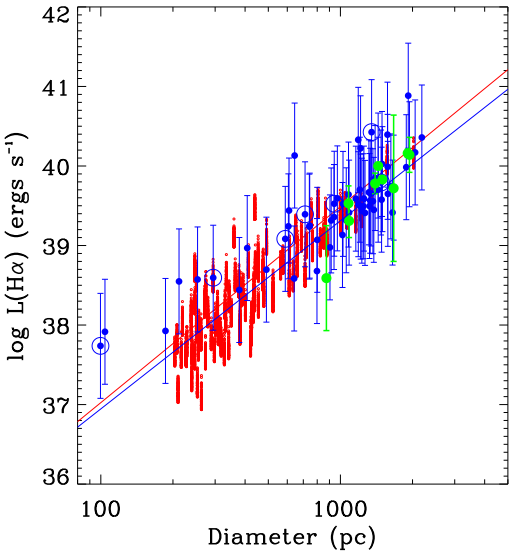

Figure 6.9: L(H_α) versus diameter relation. Blue points are Sknot galaxies. Circled enclosed points were discarded for the fit because of contamination in the flux. Green points are Sknot, with L(H_α) determined photometrically and spectroscopically (from zCOSMOS spectra); the error bar is the difference in luminosities. The mean value of the errors is taken as proxy error for the measurements (error bar for blue points). Red points are estimations of L(H_α) of clumps with a Monte Carlo simulation. The solid red line is the best fit for red points and solid blue line is the best fit for Sknot galaxies.

6.5.2 Spectroscopy

In Fig 6.10 we show the Hα luminosity and σ versus diameter for galaxies and star-forming regions derived from the high resolution spectra obtained with the WHT. To compare our analysis with previous studies we overplot the scaling relations derived by Fuentes-Masip et al. (2000), and for the L(Hα) versus diameter overplot our derived scaling relation (see section 6.5.1).

In Secs. 6.3 and 6.4 we analyzed the spectra of a subsample of 11 galaxies with a total number of 22 knots. We performed two fitting procedures, one consisting in a single gaussian fit to the Hα emission line a second fit with several components to the line width. In some cases (5 galaxies), the different components fit shared the same central wavelength what made us to conclude that we are sampling different temperature regimes of the gas around the clusters. Some other cases (6 galaxies) however do show that the output components fit to Hα in emission have different central wavelength and our interpretation is that the different clumps (clusters) can not be spatially resolved with the HST images but it is possible with the high resolution spectra obtained with the WHT.

From the spectroscopy we are able to resolve different components with different rest frame velocity and central wavelength. The overploted red line in the panel a is our scaling relation determined from the photometric data in our sample at low redshift. In panel b the overploted green line is the scaling relations from Fuentes-Masip et al. (2000). Black points are the whole galaxies, blue points are regions in galaxies classified as Sknot but showing multiple components in the spectra with different central wavelength, the flux was obtained from each component, and to determine the size of this regions we dive the total size by the number of components found. Green points are star forming regions in galaxies classified as Sknot+diffuse which show multiple components in the spectra, the flux was obtained from each component, and to determine the size we divide the size of the star-forming region in the galaxy by the number of components. Red points are star-forming regions in galaxies classified as Mknots, we determine the floc from each component

and the size from the star-forming regions size determined in chapter 3.

6.6 Results and Discussion

In this chapter we have analyzed the photometric data from the COSMOS database, and the long slit high resolution spectra ($\sigma \sim 15$ km/s) for a subsample of starburst galaxies in our catalogue, obtained with ISIS at the WHT at the observatory "Roque de los Muchachos", in order to study the hydrodynamical regime of the galaxies.

We have analyzed in two different section the photometric and spectroscopic data. First, for the photometric data analysis , we measured the equivalent width of the galaxies catalogued as Sknot in chapter 3. Using the Starburst 99 models, we can combine the mass and EW in our targets to do an estimation of the mechanical luminosity. For the galaxies in our sample the EW(Hα) is obtained from the whole galaxy. Only for Sknot galaxies, the EW represents the burst. For this reason we restrict the analysis of the mechanical luminosity with respect to the radius to the Sknot galaxies only. The analysis of the mechanical luminosity with the size of star-forming regions allow to determine the hydrodynamical regime. As result, in section 6.2 we found that 63% of Sknot galaxies are candidates to be in a bimodal regime if cooling by dust produced by SN is taken into account to define the threshold line.

We analyzed the high resolution spectra obtained with ISIS at the WHT, in order to look for different components in the velocity space in the Hα emission line, corresponding to the different hydrodynamical state of the star-forming region. In section 6.3 we analyzed 11 high resolution spectra with multiple components, five of them have multiple component with the same central wavelength, and six of them have multiple component with different central wavelength. In case of multiple components wit the same central wavelength, the two components correspond to different states of the gas in the star-forming region. The broad component is the expandding wind gas through the outer zone. The narrow component corresponds to the gas confined in the star-forming region within the stagnation radius which remains bound to the cluster. In case of multiple components with different central wavelength, we interpret them as corresponding to different star-forming region not necessary resolved spatially.

Of the five galaxies with multiple components with the same central wavelength, three of them correspond to Sknot galaxies. As in section 6.2 we analyzed the L_{mech} with the size of Sknot galaxies, in Fig. 6.2 we show in red points these galaxies, which are candidates to be in the bimodal regime. From the photometric plot shown in Fig. 6.2 and the results from the high spectral resolution data we can conclude that cooling by dust scheme is more surely the one applicable.

In section 6.5 we studied the scaling relation of L($H\alpha$) and σ with the size of the star-forming regions. Using the photometric data for Sknot galaxies and the knots of star formation in Sknot+diffuse and Mknot galaxies, we confirm the value of the slope in the L(Hα) versus diameter obtained by Fuentes-Masip et al. (2000). From the high resolution spectra, in Fig. 6.10 (a) we confirm our photometric relation for L(Hα) versus diameter using galaxies and their components. In Fig. 6.10 (b) we confirme the relation in the σ versus diameter obtained by Fuentes-Masip et al. (2000) with our galaxies and their components.

In this chapter we have analyzed photometric and spectroscopic data in order to study the hydrodynamical in same starburst galaxies in our sample. This study present preliminary make result to seek for the factibility of the cases for the MEGARA and WEAVE with the targets identified in COSMOS (this is explained further in chapter 7).

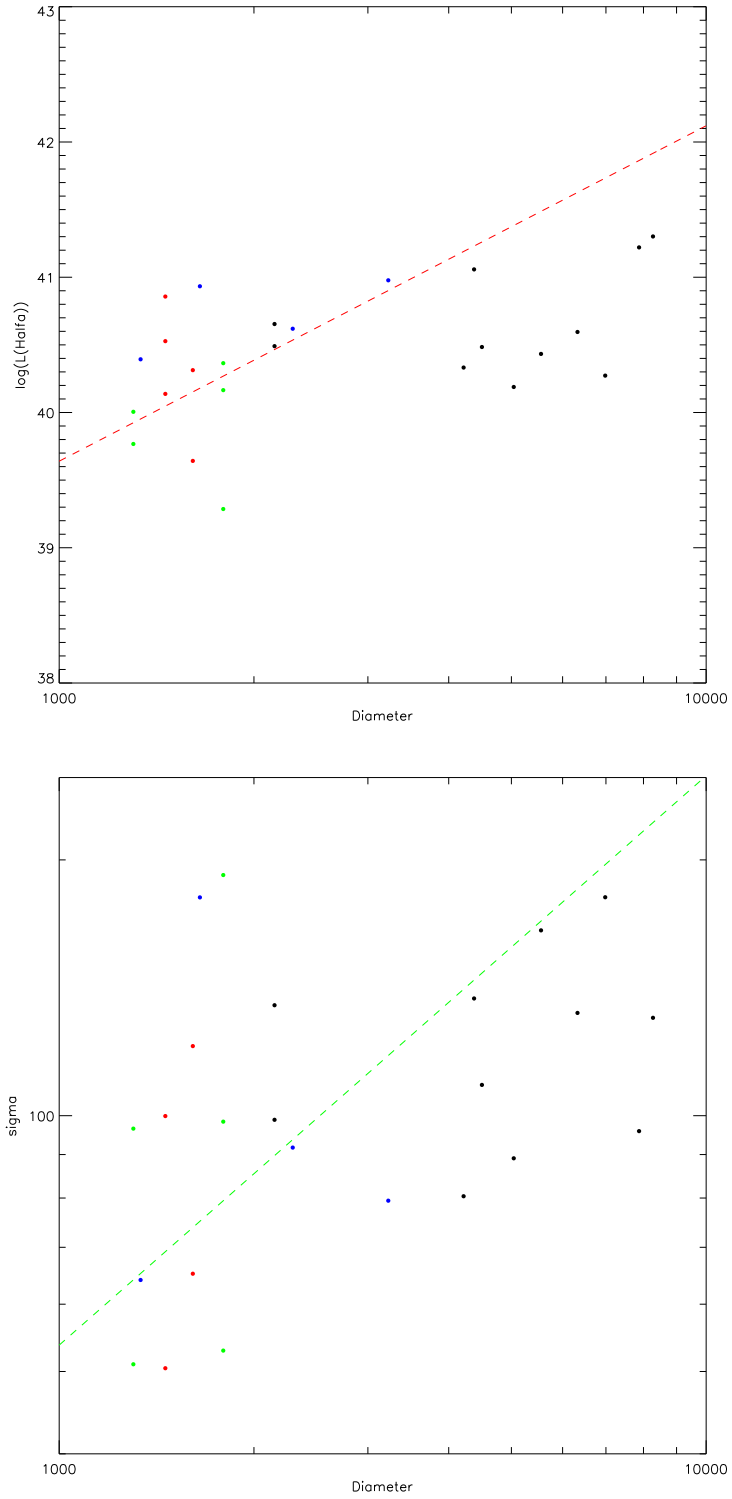

Figure 6.10: L(Hα) and σ versus the diameter for the sample of galaxies in our sample observed with ISIS at WHT. The overploted red line in the panel a is our scaling relation determined from the photometric data in our sample at low redshift. In panel b the overploted green line is the scaling relations from Fuentes-Masip et al. (2000). Black points are the whole galaxies, blue points are sub regions in galaxies which can be deblended spectroscopically but not photometrically, and red points are star-forming regions in galaxies detected photometrically and spectroscopically.

Chapter 7

Conclusions

The main aim of this thesis work is to study star-forming galaxies at different redshift to relate the star formation and their host galaxies in a common scheme. We attempt also to shed some light on the mechanisms driving the star formation in galaxies with cosmic time. At high redshift, the Ultra Deep Field images, obtained mainly with the HST, showed for the first time, morphologies not previously seen in the local universe. These morphologies are mainly dominated by large and massive star-forming regions with masses of $10^7 - 10^{10} M_\odot$ and sizes of a few kpc. In the local universe, the giant star-forming region are only a few pc of size with masses of the order of $10^4 - 10^6 M_\odot$. Throughout this thesis, we have tried to bridge the gap between the high - and low - redshift knowledge by presenting a series of new results on the properties of starburst galaxies (including the star-forming regions and the underlying host galaxy) at low and intermediate redshift. We reminder this study as fundamental to understand the formation and evolution of galaxies during the last 7 Gyr.

7.1 Starburst galaxies in COSMOS at $z < 0.5$ (*Chapter* 2 *and Chapter* 3)

In chapter 2 we used an spectroscopic sample of starburst galaxies from the zCOSMOS survey at $(0.1 < z < 0.5)$, to calibrate a taylor-made color-color diagram to extent our sample to galaxies with only photometric data available. We detected 220 galaxies at $(0 < z < 0.5)$ with a mass range $10^7 - 10^{10} M_\odot$ and different morphologies. The latter were defined according to their star-forming regions as: Sknot for galaxies with just one star forming region without diffuse light, Sknot+diffuse for galaxies with one star-forming region embeded in the more diffuse light, and Mknot for galaxies with two or more star-forming regions embedded in the more diffuse light. In chapter 3 we studied the properties of the star-forming regions of the galaxies in this "low redshift" sample. From our analysis we determined different parameters like: mass, Hα luminosity, Star Formation Rate, distance to the center, etc, for the entire galaxy and the individual knots of star formation. The masses for individual knots in Sknot+diffuse and Mknots galaxies vary with the distance to the center of the galaxy, increasing their mass the closer to the center they are. The masses of the knots are typically one order of magnitude below that of the host galaxy, with a peak at $10^{7.7} M_\odot$. The surface SFR and surface mass density do not show any footprint of their particular location within the galaxy. Based on the prediction of recent numerical simulations, we suggest that most of the clumps in Sknot+diffuse and Mknot/clumpy galaxies have been produced by violent disk instabilities. In this scenario, large and massive clumps at the galaxy centers would be the end-product of the coalescence of surviving smaller clumps from the outskirts.

In chapter 3 we have characterized the sample of starburst galaxies presented in chapter 2. This

represent a well defined sample in the redshift range ($0 < z < 0.5$). In order to characterize the morphology of the star-forming regions in our sample of galaxies we perform an isophotal analysis of the HST/ACS high spatial resolution images. From this analysis we classify the starburst galaxies in COSMOS ($z < 0.5$) as Sknot galaxies, Sknot+diffuse galaxies, and Mknots galaxies, whether they consist of a single knot of star formation, a single knot surrounded by diffuse emission, or several knots of star formation, respectively.

The stellar masses of the knots were calculated using photometric data from the COSMOS database. The masses for individual knots in Sknot+diffuse and Mknots galaxies vary with the distance to the center of the galaxy, increasing their mass the closer to the center they are. Masses of knots are typically one order of magnitude below that of the host galaxy, the mean is $10^{8.4}$M$_\odot$ (see Fig. 3.12). The specific characteristics of the starburst knots as a function of their distance to the center of their host galaxy are similar. The surface SFR and surface mass do not show any footprint of their particular location in the galaxy.

Even though the observational criteria to define clumps differs from different authors, and no direct comparison with other published papers can be done, we have made the exercise to define a "clumpy fraction". This parameter, defined in section 3.2.1, gives a value of f_{clumpy}=0.24, which is higher than other studies (e.g. Murata et al. 2014, f_{clumpy}=0.08). The reasons for this difference might be in the different mass ranges of the samples, and the precise criteria to identify starburst galaxies and star-formation clumps, as we showed in section 3.2.1.

The fraction of clumpy galaxies is a prediction of the numerical simulations. It is expected to first increase with redshift until $z > 4$ where simulations predict less clumpy and more compact star-forming galaxies than at lower redshifts (Ceverino et al. 2015). This is consistent with UV observations of bright clumps in high-z galaxies (Guo et al. 2015), where they found the fraction of clumpy galaxies 0.6 with stellar masses of log(M/M$_\odot$)=9-10 in the redshift range z = 0.5-3 (see also Elmegreen et al. (2007) and Tadaki et al. (2014)). From this work the clumpy fraction drops down to 0.24 at $z < 0.5$, for the starbursts in COSMOS, which have a typical stellar mass of 10^8 M$_\odot$. Our result therefore would also agree with the expected trend in the fraction of clumpy galaxies with z predicted by the numerical simulations.

Different properties of the knots, with respect to the absolute $B-$band magnitude of their host galaxies in our sample were compared with local and high-redshift galaxies (Elmegreen et al. 2013). We found that the clump surface density and clump mass versus host galaxy B-band absolute magnitude have a slope between those for the local and high-redshift sample, implying that for a given absolute $B-$band magnitude of the galaxy, the mass and surface density of the knots of the sample of this paper have higher values than those of clumps in local spirals, and lower than those found in high-redshift massive star-forming regions.

Sknot galaxies ($\sim$38%) show photometric structural properties that differ from star-forming knots in the other classes of galaxies (Sknot+diffuse and Mknots). Sknot galaxies have lower surface-brightness and lie in the dwarf spheroidal, dwarf irregular and elliptical regions in the surface-brightness versus absolute magnitude (M_B and M_V) diagrams. The possibility of an evolutionary trend among different dwarf systems was already proposed by Papaderos et al. (1996), and we suggest that Sknot galaxies in COSMOS may be examples of a transitional phase between BCD starbursts and dwarf spheroidals.

7.2 Starburst galaxies in COSMOS at $0.3 < z < 0.9$ (*Chapter* 4)

In this chapter we enlarge the sample of intermediate redshift starburst galaxies in COSMOS up to $z \sim 0.9$ (spectroscopy) and $z \sim 0.57$ (photometry). To this aim, we adapted the methodology of chapter 2 to deal with a new set of emission lines more suitable to this redshift range. After a careful study of the main properties of the starburst galaxies and their star-forming clumps, we found that they follow the same trends shown by the low-redshift sample, i.e., the most massve clumps with

the highest SFR are found close to the galaxy center. We also derive the LF of starburst galaxies in the redshift range $0 < z < 0.57$. We found an evolution of the faint-end slope being flatter for starburst galaxies at higher redshift.

In this chapter, we have extended the previous sample of starburst galaxies described in chapters 2 and 3 up to redshift $z \sim 0.57$. To this aim, we have developed, characterized, a calibrated a new intermediate band color-color diagnostic diagram based on the [OIII] and D4000 features of the galaxy spectra.

We found a new sample of 1152 starburst galaxies in the redshift ranges comprising $0.32 \geq z \geq 0.38$, $0.38 < z \geq 0.44$, $0.44 < z \geq 0.50$, and $0.5 < z \geq 0.57$. The redshift gaps are due to the non-continous coverage of the wavelength range by the SUBARU intermediate-band filters. The physical properties of the starburst galaxies such as stellar mass have been derived obtaining similar values as those presented for the low-redshift sample presented in chapter 3.

A careful morphological classification of the starburst galaxies have been carried out finding 424, 429, and 126 single knot (Sknot), single knot + diffuse light (Sknot+diff), and 126 multiple knot (Mknots) galaxies, respectively. The properties of the individual star-forming knots in our sample of starburst galaxies have also been derived. We found similar trends in the mass vs. galactocentric distance for both sample at low and intermediate redshift, with more massive knots lying in the center of the galaxies.

The LF of starburst galaxies throughout our redshift range was also derived. We found that the number density of our sources is not high enough to constraint the values of $\phi_\star$ and $M_\star$ associated to the Schechter function. However, we are able to constraint the faint-end slope (α) of the LF. We found that α flattens with the redshift, moving from $\alpha \sim -1.9$ at low redshift ($0 < z < 0.28$) to $\alpha \sim -1.36$ at $0.5 < z < 0.57$. These results are in agreement with the redshift evolution of the LF for the whole population of galaxies, and even more interestingly, they are compatible with previous result on the evolution of the number density of starburst galaxies (Liu et al. 2008).

we found a negative trend of f_{clumpy} with the redshift. This result is in disagreement with previous work that found and increase on the negative fraction of clumpy galaxies with redshift. Nevertheless, we conclude that the observed trend is biased by a resolution effect. At intermediate redshift ($z \sim 0.6$) our limitations resolution (PDF of HST/ACS) is ~ 600 pc whereas ay low redshift ($z < 0.27$) this value is as low as 100 pc. Therefore, at intermediate redshift we are not able to resolve small and close clumps into various systems. Accounting for this effect and imposing a size limits of the knots > 600 pc we found a constante trend of f_{clumpy}. This constancy is in good agreement with previous works in the redshift range probed by our sample.

7.3 The host galaxy of the starburst in COSMOS (*Chapter* 5)

In chapter 5 we used the high spatial resolution images in the F814W−*band*, obtained with the ACS camera in the HST available in the COSMOS database, to study the light distribution of the host galaxies in these systems. We performed a 2D analysis of the surface brightness using GALFIT fitting a Sersic profile after a careful removal of the starburst contribution. We found that the Sersic index for Sknot galaxies span a wide range of values from $0 \geq n \geq 4$. However, Sknot+diffuse and Mknot show a narrower distribution with a clear peak at $n \sim 1$. Therefore, we suggest that starburst galaxies with an extended morphology are characterized by an underlying disk-like structure.

The host galaxy in Sknot+diffuse and Mknots is well described by an exponential profile typical of a galaxy disk. Sknot galaxies are fit with a wide range of n values, including n=4 which corresponds to an exponential distribution as that for an elliptical-like galaxy. It is important however to emphasize that Sknot galaxies emission includes the host and the burst. As we have not been able to separate both light distribution (see chapters 2 and 3), the fit can not be interpreted as for the Mknots and Sknot+diffuse galaxies samples.

7.4 Star formation feedback and scaling relations(*Chapter* 6)

We estimated the mechanical luminosity using Starburst 99 (Leitherer et al. 1999) assuming an instantaneous star formation law, for Sknot galaxies. We compared the L_{mech} with the size for these galaxies, and using the threshold line derived when using gas cooling from a gas in collisional ionization equilibrium and gas and dust cooling (Tenorio-Tagle et al. 2010), we located these galaxies in the different hydrodynamical regimes. Considering the scenario of gas and dust cooling by dust produced by SN mechanism, we found that 63% of Sknot galaxies are candidates to be in a bimodal regime.

The L(Hα) versus size of star-forming regions have been investigated by several authors, searching for an universal relation. Taking the benefit of the excellent spatial resolution provided by the HST images, we have built the L(Hα) versus size for all individual knots of the 220 galaxies of our catalogue. We obtain a slope of 2.48 $\pm$ 0.05. This is a value similar to 2.5 obtained by Fuentes-Masip et al. (2000) for local, resolved giant HII regions measured with the Fabry-Perot technique. Note, however, that this value differs from the 2.78 slope given by Wisnioski et al. (2012), in which the authors include high-redshift galaxies. The spatial resolution in Fuentes-Masip et al. (2000) and this work allow us to have a good confidence in the results. For high- redshift galaxies the resolution is worse and can include errors in the measurements, which cannot be quantified.

Chapter 8

Future Work

This PhD thesis presents an extensive analysis of the incidence and properties of starburst galaxies in the redshift range $0 < z < 0.9$. A well-defined starburst sample, drawn from the COSMOS survey, was selected and analyzed using the high quality photometric data available for this cosmological field using both ground- and space-based telescopes.

The current work demonstrates how the development of new methodologies and the application of taylor-made algorithms are fundamental to optimize the extraction of information in photometric datasets. In particular, we have made evident how narrow-, and/or intermediate-band filters can be used to measure physical properties otherwise only accessible through spectroscopic data.

Thoroughout this thesis we have discussed how photometric data is "cheaper" in terms of telescope time than spectroscopy. This is a fundamental advantage of photometry when dealing with statistically significant samples. Nevertheless, in chapter 6 we also introduced the importance of high-spectral resolution spectroscopy to understand the physical processes behind the star formation modes and its evolution with cosmic time. The use of spectroscopic datasets represent the main research line of my future research.

The current PhD has been carried out within the environment of the ESTALLIDOS [1] research group. ESTALLIDOS is founded by the Spanish government and it is currently formed by 50 members in three main nodes (Tenerife, Madrid, and Granada). Furthermore, ESTALLIDOS contribute to the development of frontier technology and, in particular, of two new spectrographs WEAVE and MEGARA to be mounted on the William Herschel Telescope (WHT) and the Gran Telescopio Canarias (GTC), respectively. During my PhD I have participated in the science groups defining the first science to be done with these instruments that is tightly related to my research expertise.

The targets (galaxies) identified as starburst in the COSMOS field up to z=1 will be those to be observed within the programs for WEAVE and MEGARA. The detailed study carried out in my Phd work by means of the high spatial resolution data of the HST allows for a secure observing strategy. In my work I have obtained the precise coordinates and parameters - luminosity, size, SFR, etc. - of the star-forming knots in the - more than 1000 galaxies - catalogued in COSMOS. Like this we have all the information needed to go for targets with particular characteristics, for example - extreme SFR - or compactness or luminosity and due to use the future instrumentation, both at the WHT and GTC for the best suite case ofr our science.

Moreover in chapter 6 we also present preliminary make result to seek for the factibility of the cases for the megara and weave with the targets identified in COSMOS. The result is positive and then, and after to the work of my thesis we can go forward with targets well defined, science already argued and proven that the observations will be successfully in whatever case.

[1] http://www.iac.es/proyecto/consolider-ingenio-gtc/

In the following I will briefly describe the main research lines and technical aspects I plan to follow up with both instruments and that will be my future work result within ESTALLIDOS collaboration.

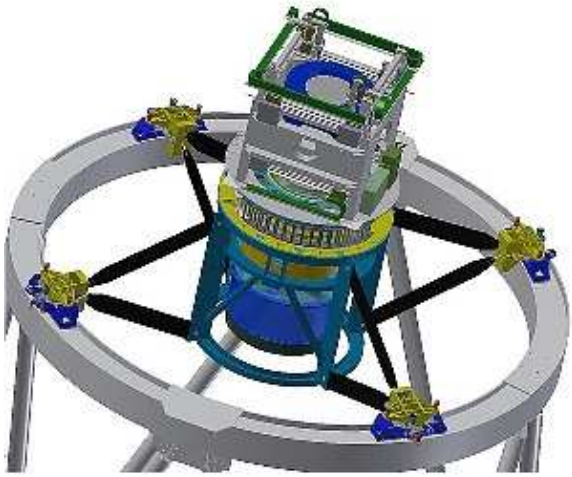

Figure 8.1: WEAVE is a new wide-field multi-object spectrograph proposed for the primary focus of the William Herschel Telescope at the Roque de los Muchachos Observatory, and it is currently under construction supported by the Severo Ochoa program (ref: http://www.ing.iac.es/weave/).

8.1 WEAVE. Scaling relations in starburst galaxies up to $z \sim 1$

It is important to emphasize the fact that there are no many spectrographs with high resolution spectroscopy mounted at 8-10 m class telescopes and the empirical results rely on emission lines, which are not resolved. Going back to the pioneering works in the 80-90, when the first correlations were explored, much effort was devoted to identify both the actual line-width and the definition of the optical size to correlate with. A number of reasons can modify the line profile, broadening it and producing a convolved non-resolved wide emission line. At low redshift a number of studies show clearly that winds and superwinds resulting from the SN and massive stars produce line splitting and asymmetries. The clear conclusion from the detailed study of resolved nearby objects is that good spectral resolution spectroscopy (above $R = 10000$ in $H\alpha$) is needed to get emission line profiles measurements if they are to be used in the scaling laws (see e,g., Martínez-Delgado et al. 2007; Munoz-Tunon et al. 1995, 1996; Telles et al. 2001). In a more recent work, Bordalo & Telles (2011) have explored the $L(H\beta) - \sigma$ correlation and its systematic errors using a nearby sample selected from the Terlevich et al. (1991) spectrophotometric catalogue of HII galaxies ($0 < z < 0.08$). They conclude that considering only the objects with clearly Gaussian profiles in their emission lines, they obtain something close to an $L(H\alpha) \propto \sigma^4$ relation with an rms scatter of $\delta log L(H\alpha) \sim 0.30$.

Apart from their intrinsic physical meaning (see chapter 1), the empirical laws relating the line-width and the size or luminosity have been frequently used for understanding high z objects that cannot be resolved. For instance, Wisnioski et al. (2012) studied the scaling relations of star-forming regions at high and low redshift to understand if they evolve with cosmic time. They claimed that by bringing together multiple studies from the literature, measured in a self-consistent way, the spectrum of HII regions form relatively consistent relationships between size, luminosity and

velocity dispersion, which can be extended to include high-redshift clumps. The scaling relationships observed have implications for how star-forming regions form in the changing cosmic environment.

In this thesis we have also approach the problem of estimating the scaling relation of starburst galaxies at high redshift. We have obtained a new relation between L(Hα) and size (r) which is in accordance with that obtained in giant HII regions and disagree with the more recent obtained using a high z sample (see chapter 6)

A central issue is the validity of the empirical correlations, of size and luminosity versus their supersonic line widths for local star forming galaxies and high-redshift galaxies. For this, spectroscopy of good spectral resolution $R > 10000$ in the optical range to map the hydrogen recombination lines are needed.

Also, for non-spatially resolved starburst, the emission can result from the integral along the line-of-sight of more than one burst. The analysis of the emission lines with good spectral resolution is the only observational approach that may allow for pinpointing it.

In this Phd work we have explored further the validity of the scale relations L versus σ for a subsample of the starburst galaxies catalogued in COSMOS. These galaxies were observed by jean of high spatial resolution spectroscopy and the fit to the different kinematiccal components were carried out (see chapter 6).

The resulting scaling relation of luminosity and σ seems to agree with that already reported in previous works for giant HII regions of nearby galaxies (see Fuentes-Masip et al. 2000; Telles et al. 2001) (see chapters 6 and 7).

In the case where the emission lines are multiple, it is the case which is narrower and less intense that one that leads to the appropriate result. This frames further that the starburst clumps are evolving in the so call positive feedback mode and much of the mass and energy is used to promote further star formation (see discussion chapter 6). The result shown in the thesis is a xxxxxxx are aimed at taking full advance of the capability of weave, with mean configuration we will be able to observe all the clumps catalogued in chapters 2 and 3, which are perfectly automatized so that can be easily targeted with the multiple spectroscopy at the WHT. Note also that our study was carried out at the WHT and with a similar instrumental (ISIS).

8.1.1 Future Work using WEAVE

Our proposal for WEAVE aims at:

1. Accurately determine scaling relations for starburst galaxies up to $z \sim 1$.
   (a) A detailed analysis of the resolved nebular emission lines, identifying and separating different kinematical components, will be performed.
   (b) Ancillary databases (e.g., HST images) providing good spatial resolution will be used to measure sizes and luminosities.
   (c) Revisit the physical mechanisms behind the scaling relations.
      i. Study the virial hypothesis in the light of the new results.
      ii. Compare the scaling relations with the state-of-the-art cosmological simulations forming (or triggering) starbursts in galaxies (e.g., galaxy mergers or inflowing cool flows).
   (d) Identify extreme and compact star forming galaxies up to z 1.

8.1.2 The sample

WEAVE will represent a revolution in the field of multi-object spectroscopy mainly because of two characteristics: i) the large number of fibers ($\sim$1000) that can be simultaneously placed over a large field-of-view (3.1 square degrees) and ii) the unprecedented high spectral resolution ($R \sim 20000$).

This project seeks to combine these unique features to provide a new view on the physical processes driving the evolution of star forming galaxies with cosmic time. Our target sample has been drawn from one of the five premium fields observed with HST, the COSMOS field. The COSMOS survey is the largest field-of-view ever cover by the HST representing the ideal framework to study galaxy evolution reducing the effects of cosmic variance. The field-of-view covered by the COSMOS survey is ~ 2.4 square degrees, therefore matching well the WEAVE field-of-view, and allowing an optimal allocation of fibers.

In a our study (Hinojosa-Goñi et al. 2016, submitted) we have identify a sample of starburst galaxies in the COSMOS survey by using the huge multiwavelength database on the survey provided by different telescopes and facilities such as: SUBARU, HST, SPITZER, etc. Our selection methodology is based on the simultaneous measurement of two colours medium-band excess. We have made use of the SUBARU medium-band photometry available for the COSMOS sample to compute colour excess around $H\alpha$ and OIII for galaxies with $z < 0.5$. For a second sample (Hinojosa-Goñi et al. 2016, in preparation) we have identified starburst galaxies in the COSMOS survey at $0.5 < z < 1$, this search was done using also the SUBARU medium-band photometry available in COSMOS, to compute for this sample the colour excess around the [OIII] amission line and the Balmer jump. Moreover, the proposed methodology was tested against the spectroscopic measurement obtained for a subsample of galaxies by ZCOSMOS. We found that all our target galaxies are actually star-forming galaxies with prominent emission-lines.

8.2 MEGARA. Star Formation Feedback in Massive systems at different redshifts.

MEGARA [2] is an IFU system designed to be installed at GTC. The instrument is about to be commissioned and installed at the telescope in 2016.

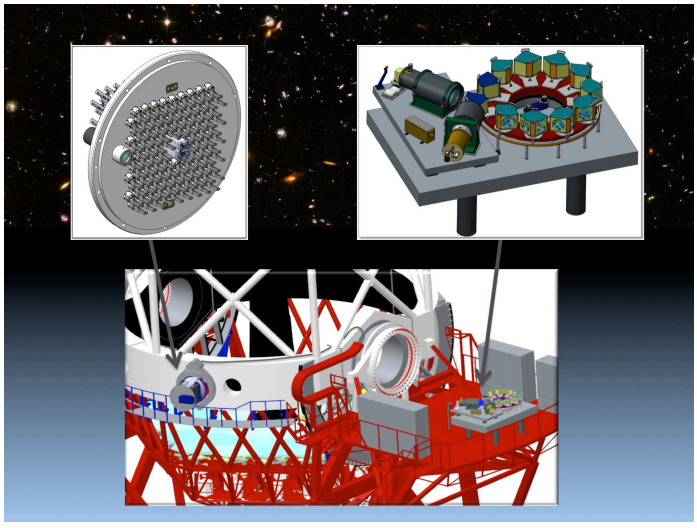

Figure 8.2: A 3D drawing of the two main elements of MEGARA installed at the GTC, the focal unit in a folded-cass station and the spectrograph in a nasmyth platform, both conected by the fibre bundle.

[2] http://www.gtc.iac.es/instruments/megara/megara.php

8.2.1 Future Work using MEGARA

The hydrodynamical models that are described in chapters 1 and 6 predict that massive assembling galaxies with large star formation rates are likely to evolve in a positive star formation feedback condition (Silich et al. 2010), either in the bimodal or in the gravitationally bound regime. Large and massive clumps of star formation have been detected in more than half of the resolved $z > 1$ galaxies in the Hubble Ultra Deep Field (UDF Elmegreen et al. 2005). These star-forming entities are found in galaxies at all distances in the range $0.07 < z < 5$. They have sizes of about 2 kpc and masses often larger than $10^8 M_\odot$. They are so luminous that dominate the appearance of their host galaxies at optical wavelengths. Massive clumps like these are usually found in types not observed locally, including chain galaxies and their face-on counterparts, clump-cluster galaxies.

Photometric observations of these objects have been interpreted within the context of the models of galaxy evolution. They support a model in which star formation occurs primarily in highly turbulent disks by gravitational instabilities having a Jeans mass of $\sim 10^8 M_\odot$ and a length of several kpc. Clump clusters are considered as examples of star-forming disks at their earliest stage, and maybe also initial seeds for spiral galaxies and, through mergers, spheroids as well (Elmegreen et al. 2005; Elmegreen & Elmegreen 2006; Bournaud et al. 2007; Elmegreen et al. 2007). These starforming galaxies have so far been studied through broadband images from the HST.

Paraphrasing Förster Schreiber et al. (2006), "Much of our current knowledge about high redshift galaxies rests on relatively crude broad-band photometric information, rarely on integrated spectra probing their restframe UV emission. As a result, very little is known about the dynamical and detailed physical properties of high-redshift galaxies". Details of the physical and dynamical properties of massive star-forming clumps can only be understood after analyzing the clump spectra. In order to model and understand the various feedback mechanisms (e.g. Tenorio-Tagle et al. 2007, 2010; Silich et al. 2010; Tenorio-Tagle et al. 2013, and references therein), it is important to determine the kinematics and physical state of the gas in the clumps. The spectroscopic observations provided by MEGARA will represent a necessary and definitive step forward in our knowledge of these objects and feedback processes. The basic questions we plan to answer are: Do the clumps show ionized-gas features? Do they show signs of negative feedback (e.g. shells, chimneys, winds)? Are they coeval star formation events or the result of continuous star formation? Are there cases of positive star-formation feedback? The 300 Myr upper-limit for the age of the clumps reported by Elmegreen et al. (2005) based on photometric studies justifies referring to them as ongoing massive starbursts. Whether or not emission-line features exist is crucial for their fate and evolution. Instantaneous star formation would lead to ionizing radiation for only a few tens of Myr, and the SN era is less than 50 Myr, whereas in the case of continuously decaying star formation these parameters would depend on the characteristic time scale of the star formation event. Clump ages and precise masses are needed in order to understand and parameterize the star-formation mechanism and in particular the star-formation feedback.

Using MEGARA we will be able to detect, resolve and characterize spectroscopically the targets and analyze their physical state. First we will confirm that they are massive young systems showing emission line features. Then, with a precise determination of their redshift we will derive their star-formation history and look for the presence of different velocity components that will enable us to determine their hydrodynamic state. The combination of the high spectral resolution of MEGARA together with the GTC collecting area will make possible to acquire the observations required to conclusively derive the feedback parameter.

8.2.2 Sample and observing strategy

So far, most of the work carried out in order to understand the physical properties of these massive clumps of star formation have been done using only photometric data and using surveys available in the southern hemisphere. Therefore, the need for a large and well-defined sample of clump-cluster

galaxies in the northern hemisphere is clear, as it is the need for accurate spectroscopic observations in order to analyze their physical properties.

In order to fill this gap we have produced in this thesis a well-defined sample of massive clumps of star formation observable with GTC. The kpc-size star-forming clumps were extracted from the COSMOS database. In order to map the $H\alpha$ emission line in the wavelength range provided by MEGARA we restrict our sample to galaxies with redshifts $0.1 < z < 0.3$, resulting in 220 starburst galaxies.

It is worth to notice that the typical projected size of these object spans a few arcseconds, typically they fall in the range between 1 to 6 arcsec matching perfectly into the dimensions of the MEGARA SCB, with a FOV of 10×8 arcsec^2. In addition, due to the number density calculated for these objects in COSMOS ($\sim$2 objects/MEGARA MOS FOV) the 92 positioners that can be located in the outer $3.5{\times}3.5$ arcmin^2 will allow us to highly increase the number of spectroscopically confirmed clump-cluster galaxies without increasing the total exposure time.

Even if no spatial information about these sources will be obtained, taking into account that no clump cluster galaxies have been spectroscopically observed up to now, this work will represent a cornerstone in the analysis of these objects.

We plan to obtain spectroscopy for a subsample of $\sim$100 candidate clump cluster galaxies using MEGARA at GTC. We will first use the SCB equipped with the LR-R, or LR-I VPHs (depending on the estimated redshift of the object) in order to detect one or several of the most relevant emission lines expected to be present in these galaxies, e.g., [OII]#3727Å, [OIII]#5007Å, $H\alpha$, [NII]#6583Å, [SII]##6716,6731ÅÅwith enough S/N, and perform a basic spectral analysis. The spectral resolution of these configurations is $R \sim 6000$, which give us a velocity resolution of $\sim$50 km s^{-1} (FWHM). Using the MEGARA Exposure Time Calculator (ETC) we estimate that we should be able to reach the continuum flux of our objects with $S/N > 5$ with an exposure time ranging from 10 min to 1 hour depending on the target magnitude. We note that the size of the ACS footprint is comparable to the FOV covered by the MEGARA MOS (3.5×3.5 arcmin^2). Using the MEGARA ETC assuming a seeing FWHM of 0.8", airmass=1.2, and a grey night, we will reach the continuum with $S/N > 5$ per Åwith integration times of 10 min, 30 min, and 1 hour for galaxies with $20 < i < 21$, $21 < i < 22$, and $22 < i < 23$, respectively.

In addition, for a small subsample (10 objects) of galaxies covering the parameter space (as measured by the LR observations described above), we aim at obtaining integral-field high resolution spectroscopy. We will use the SCB to resolve spectroscopically (FWHM$\sim$21 km/s) and spatially (<1 kpc/resolution element) the line emission for the most massive clumps present in the galaxies of the sample. The resolved emission line profiles of the star-forming clumps in this galaxy will be analyzed looking for the presence of a single or a double component in thevelocity space that will give us important insights on the hydrodynamical state of this object. In addition, by spatially resolving the different clumps using integral field spectroscopy we will obtain information on possible spatial differences where positive/negative feedback takes place.

We will determine which feedback regime applies to each clump and find the net contribution of the clumps to the enrichment of the interstellar medium. We will use the MEGARA IFU SCB (10x8 arcsec2) with the MR-R, MR-I or MR-Z VPHs (depending on the galaxy redshift). This instrumental configuration gives us a spectral resolution of R$\sim$14,400. Using the MEGARA ETC and assuming a seeing FWHM of 0.8", airmass=1.2, and the mean surface brightness of the object $\mu_i \sim 23$, we find S/N$\sim$10 in the H' continuum with an integration time of $\sim$2 hours.

Appendix A

Appendix A: Main parameters for galaxies in our sample

Main parameters for galaxies in our sample found in Chapter 2.

Table A.1: Main parameters for galaxies in our sample.

Object	RA	DEC	z_{phot}	m(F814W)	M(F814W)	R_{lum}	$U-B$	$B-V$	$V-K$	$V-i$	log(L(Hα))	SFR	log(L[OIII])	EW(Hα)	EW([OIII])	SB	Ellipticity	Mass	G
(1)	(2)	(3)	(4)	(5)	(6)	(7)	(8)	(9)	(10)	(11)	(12)	(13)	(14)	(15)	(16)	(17)	(18)	(19)	(20)
COSMOS-001	149.459	2.275	0.271	22.66	-17.33	1.559	0.49 ± 0.05	0.00 ± 0.03	0.41 ± 0.04	1.28 ± 0.45	40.56 ± 0.00	0.289	40.60 ± 0.01	759	769	1.18	0.69	28.72	0.14
COSMOS-002	149.480	2.455	0.019	22.93	-17.45	2.242	0.37 ± 0.05	0.38 ± 0.06	-0.26 ± 1.05	0.29 ± 0.02	40.70 ± 0.03	0.393	39.49 ± 0.18	231	308	1.06	0.62	0.11	0.13
COSMOS-003	149.489	1.682	0.245	22.05	-17.75	2.219	0.64 ± 0.05	0.39 ± 0.06	0.05 ± 0.09	0.62 ± 0.04	39.95 ± 0.05	0.070	39.80 ± 0.09	87	136	0.14	0.38	46.42	0.14
COSMOS-004	149.495	2.483	0.264	23.16	-16.78	1.533	0.79 ± 0.10	0.41 ± 0.06	0.45 ± 0.05	0.29 ± 0.05	39.69 ± 0.01	0.039	39.86 ± 0.01	118	170	3.86	0.03	15.94	0.11
COSMOS-005	149.496	2.482	0.264	21.79	-18.15	3.037	0.50 ± 0.10	0.34 ± 0.06	99.0 ± 99.0	0.34 ± 0.82	40.16 ± 0.00	0.114	40.47 ± 0.00	93	181	0.04	0.75	52.81	0.12
COSMOS-006	149.506	2.351	0.265	21.69	-18.26	2.888	0.70 ± 0.10	0.46 ± 0.03	0.15 ± 0.03	0.43 ± 0.04	40.27 ± 0.00	0.148	40.32 ± 0.00	124	125	0.04	0.77	83.68	0.18
COSMOS-007	149.520	2.788	0.263	23.10	-16.83	1.654	0.61 ± 0.07	0.34 ± 0.07	0.36 ± 0.04	1.39 ± 0.20	39.83 ± 0.01	0.053	39.91 ± 0.01	107	112	2.92	0.20	31.20	0.14
COSMOS-008	149.530	1.590	0.159	24.48	-14.48	0.641	0.65 ± 0.07	0.28 ± 0.07	0.08 ± 0.35	99.0 ± 99.0	39.08 ± 0.02	0.010	38.80 ± 0.02	109	59	462.11	0.13	5.50	0.15
COSMOS-009	149.546	2.818	0.062	22.38	-14.64	0.658	0.68 ± 0.07	0.23 ± 0.04	0.42 ± 0.03	0.26 ± 0.05	38.42 ± 0.01	0.002	38.95 ± 0.01	27	109	3.49	0.68	2.18	0.15
COSMOS-010	149.547	2.334	0.135	22.71	-15.78	1.154	0.88 ± 0.07	0.37 ± 0.04	0.66 ± 0.25	0.92 ± 0.48	38.53 ± 0.39	0.003	38.93 ± 0.13	173	108	2.41	0.61	8.39	0.14
COSMOS-011	149.548	2.185	0.264	21.33	-18.61	2.793	0.59 ± 0.07	0.11 ± 0.07	0.65 ± 1.02	0.96 ± 0.43	40.78 ± 0.00	0.477	41.03 ± 0.00	351	567	0.02	0.58	98.78	0.13
COSMOS-012	149.565	2.824	0.010	99.00	99.00	99.00	0.71 ± 0.07	0.24 ± 0.03	0.80 ± 0.51	0.30 ± 0.05	37.96 ± 0.00	0.001	37.58 ± 0.00	114	55	99.00	99.00	0.22	0.16
COSMOS-013	149.567	2.083	0.264	23.21	-16.73	1.435	0.67 ± 0.07	0.31 ± 0.02	-0.01 ± 0.05	0.45 ± 0.25	39.62 ± 0.01	0.033	39.85 ± 0.01	114	181	4.93	0.37	20.33	0.11
COSMOS-014	149.567	1.891	0.383	22.47	-18.15	2.514	0.46 ± 0.07	0.44 ± 0.04	0.42 ± 0.07	0.09 ± 0.03	40.83 ± 0.01	0.530	99.0 ± 99.0	208	132	0.29	0.42	98.58	0.20
COSMOS-015	149.567	2.354	0.425	99.00	99.00	99.00	0.39 ± 0.07	0.47 ± 0.05	0.37 ± 0.02	0.36 ± 0.14	40.63 ± 0.04	0.341	99.0 ± 99.0	93	145	99.00	99.00	0.00	99.00
COSMOS-016	149.574	2.445	0.264	22.61	-17.32	1.701	0.56 ± 0.07	0.34 ± 0.04	0.47 ± 0.21	0.24 ± 0.02	39.92 ± 0.01	0.066	40.05 ± 0.01	135	154	0.90	0.43	33.72	0.14
COSMOS-017	149.589	2.572	0.161	22.83	-16.22	1.188	0.69 ± 0.07	0.28 ± 0.05	-0.32 ± 0.99	0.26 ± 0.05	39.40 ± 0.08	0.020	39.73 ± 0.04	134	121	3.02	0.30	4.12	0.11
COSMOS-018	149.592	2.566	0.276	22.77	-17.24	1.733	0.62 ± 0.07	0.31 ± 0.06	0.29 ± 0.04	0.90 ± 0.45	40.38 ± 0.03	0.188	40.05 ± 0.04	200	183	1.24	0.64	24.42	0.09
COSMOS-019	149.601	1.623	0.066	21.26	-15.89	1.142	0.74 ± 0.07	0.22 ± 0.05	0.31 ± 0.52	0.31 ± 0.04	38.92 ± 0.00	0.006	39.26 ± 0.00	34	86	0.09	0.68	6.18	0.16
COSMOS-020	149.605	2.163	0.267	22.72	-17.25	1.368	0.32 ± 0.07	-0.27 ± 0.02	0.47 ± 0.06	0.67 ± 0.07	40.47 ± 0.01	0.230	40.56 ± 0.01	682	884	1.74	0.14	33.36	0.20
COSMOS-021	149.608	2.477	0.183	22.67	-16.62	1.636	0.67 ± 0.07	0.37 ± 0.05	0.87 ± 0.76	0.79 ± 0.27	40.04 ± 0.04	0.087	39.03 ± 0.23	95	140	1.09	0.68	7.84	0.12
COSMOS-022	149.610	2.270	0.031	23.77	-11.78	0.213	0.46 ± 0.07	0.20 ± 0.05	99.0 ± 99.0	0.24 ± 0.03	38.51 ± 0.01	0.003	38.30 ± 0.01	266	184	814.82	0.20	0.16	0.06
COSMOS-023	149.610	1.889	0.264	24.93	-15.01	0.698	0.55 ± 0.07	0.45 ± 0.04	0.29 ± 0.02	-0.02 ± 0.18	39.37 ± 0.02	0.018	39.53 ± 0.02	113	140	1100.62	0.83	10.42	0.11
COSMOS-024	149.630	1.698	0.010	23.95	-9.17	0.055	0.31 ± 0.07	-0.20 ± 0.05	0.35 ± 0.08	0.16 ± 0.04	37.92 ± 0.00	0.001	38.01 ± 0.00	604	800	18456.70	0.74	0.01	0.14
COSMOS-025	149.631	2.441	0.241	23.98	-15.79	1.348	0.68 ± 0.07	0.38 ± 0.03	99.0 ± 99.0	1.58 ± 0.40	39.48 ± 0.01	0.024	39.83 ± 0.01	113	167	33.09	0.92	6.25	0.09
COSMOS-026	149.633	2.372	0.436	22.41	-18.43	2.771	0.38 ± 0.07	0.37 ± 0.03	2.71 ± 0.62	0.39 ± 0.07	40.28 ± 0.08	0.152	99.0 ± 99.0	89	124	0.21	0.20	171.47	0.22
COSMOS-027	149.644	2.026	0.353	21.72	-18.69	2.616	0.36 ± 0.07	0.37 ± 0.05	0.04 ± 0.04	0.03 ± 0.01	40.96 ± 0.02	0.725	39.90 ± 0.11	190	186	0.05	0.27	116.04	0.11
COSMOS-028	149.650	2.797	0.162	99.00	99.00	99.00	0.61 ± 0.07	0.30 ± 0.05	-0.04 ± 0.94	0.65 ± 0.05	39.45 ± 0.01	0.022	39.44 ± 0.01	114	101	99.00	99.00	9.10	0.13
COSMOS-029	149.654	2.342	0.342	20.09	-20.11	4.921	1.50 ± 0.07	1.19 ± 0.05	0.32 ± 0.06	-0.14 ± 1.27	39.67 ± 0.06	0.037	99.0 ± 99.0	183	208	0.00	0.24	1847.00	0.64
COSMOS-030	149.662	2.281	0.642	22.91	-16.94	1.752	0.67 ± 0.07	0.31 ± 0.05	99.0 ± 99.0	0.21 ± 0.04	40.19 ± 0.03	0.122	40.40 ± 0.02	443	477	1.67	0.80	93.88	0.32
COSMOS-031	149.676	2.218	0.264	23.57	-16.36	1.541	0.49 ± 0.07	0.33 ± 0.05	0.04 ± 0.05	0.52 ± 0.05	39.58 ± 0.01	0.030	39.62 ± 0.01	127	120	9.92	0.89	16.44	0.08
COSMOS-032	149.681	1.613	0.466	21.43	-19.50	5.307	0.41 ± 0.07	0.33 ± 0.03	99.0 ± 99.0	0.73 ± 0.49	41.15 ± 0.07	1.129	99.0 ± 99.0	791	121	0.01	0.73	451.11	0.22
COSMOS-033	149.691	2.425	0.264	23.63	-16.31	1.625	0.59 ± 0.07	0.39 ± 0.03	0.10 ± 0.20	99.0 ± 99.0	39.42 ± 0.01	0.021	39.62 ± 0.01	79	112	10.10	0.40	12.14	0.07
COSMOS-034	149.694	2.486	0.179	24.44	-14.65	0.843	0.76 ± 0.07	0.29 ± 0.03	0.05 ± 0.04	0.58 ± 0.31	39.34 ± 0.09	0.017	39.41 ± 0.08	106	138	242.05	0.56	5.31	0.07
COSMOS-035	149.700	2.609	0.234	23.42	-16.29	1.101	0.58 ± 0.07	0.36 ± 0.04	0.15 ± 0.03	0.06 ± 0.03	39.66 ± 0.01	0.036	39.61 ± 0.01	171	109	13.56	0.29	17.57	0.09
COSMOS-036	149.705	2.284	0.037	25.92	-10.01	0.103	0.47 ± 0.07	0.11 ± 0.05	0.29 ± 0.06	0.42 ± 0.13	38.02 ± 0.01	0.001	37.70 ± 0.02	113	64	490114.03	0.26	0.22	0.12
COSMOS-037	149.714	2.299	0.234	21.70	-18.11	2.216	0.61 ± 0.07	0.31 ± 0.05	0.47 ± 0.06	0.08 ± 0.04	40.19 ± 0.03	0.123	40.02 ± 0.06	123	104	0.06	0.06	56.19	0.14
COSMOS-038	149.722	1.803	0.021	22.91	-17.56	2.767	0.48 ± 0.07	0.47 ± 0.05	99.0 ± 99.0	0.98 ± 0.22	40.93 ± 0.94	0.669	99.0 ± 99.0	1485	197	0.67	0.46	0.33	0.13
COSMOS-039	149.722	2.577	0.128	22.44	-16.08	0.689	0.41 ± 0.07	0.71 ± 0.04	-0.26 ± 0.56	0.40 ± 0.03	40.22 ± 0.00	0.130	40.19 ± 0.00	609	601	3.62	0.04	4.30	0.27
COSMOS-040	149.732	2.045	0.265	23.69	-16.25	1.765	0.56 ± 0.07	0.43 ± 0.03	-0.28 ± 0.03	0.27 ± 0.58	39.55 ± 0.01	0.028	39.72 ± 0.01	83	118	9.94	0.86	19.69	0.09
COSMOS-041	149.732	1.699	0.065	20.50	-16.63	1.425	0.76 ± 0.07	0.19 ± 0.03	0.31 ± 0.06	0.19 ± 0.04	38.84 ± 0.00	0.005	39.33 ± 0.00	20	74	0.01	0.77	8.17	0.15
COSMOS-042	149.734	2.333	0.172	25.11	-13.93	0.815	0.81 ± 0.07	0.30 ± 0.05	99.0 ± 99.0	0.40 ± 0.01	38.84 ± 0.26	0.006	37.79 ± 2.81	173	190	1224.86	0.84	3.89	0.06
COSMOS-043	149.746	2.590	0.246	21.91	-17.90	2.398	0.63 ± 0.07	0.25 ± 0.06	0.98 ± 0.36	0.28 ± 0.03	40.44 ± 0.00	0.215	40.53 ± 0.00	269	245	0.09	0.65	42.83	0.13
COSMOS-044	149.747	2.661	0.225	20.80	-18.78	3.163	0.77 ± 0.07	0.32 ± 0.05	-0.15 ± 0.42	0.81 ± 0.64	40.77 ± 0.01	0.469	39.37 ± 0.27	237	113	0.00	0.71	131.91	0.16
COSMOS-045	149.758	2.395	0.261	22.68	-17.24	2.363	1.36 ± 0.07	0.10 ± 0.05	0.23 ± 0.03	0.63 ± 0.65	39.89 ± 0.01	0.062	39.94 ± 0.01	89	101	0.53	0.90	31.18	0.13
COSMOS-046	149.759	2.079	0.133	21.86	-16.74	1.317	0.71 ± 0.07	0.26 ± 0.04	-0.94 ± 0.83	0.30 ± 0.04	40.06 ± 0.01	0.090	39.57 ± 0.04	108	115	0.26	0.43	11.39	0.14
COSMOS-047	149.768	2.479	0.265	23.05	-16.90	1.901	0.58 ± 0.07	0.44 ± 0.05	0.38 ± 0.03	0.44 ± 0.05	39.54 ± 0.01	0.027	39.82 ± 0.01	72	135	1.94	0.82	18.26	0.15
COSMOS-048	149.769	1.933	0.354	22.20	-18.27	2.654	0.37 ± 0.07	0.40 ± 0.06	0.24 ± 0.35	0.38 ± 0.29	40.65 ± 0.03	0.353	39.99 ± 0.08	154	124	0.14	0.58	95.71	0.13
COSMOS-049	149.771	2.173	0.046	99.00	99.00	99.00	0.54 ± 0.07	0.02 ± 0.04	-0.66 ± 1.21	0.12 ± 0.03	38.42 ± 0.01	0.002	38.05 ± 0.01	195	93	99.00	99.00	0.19	0.08
COSMOS-050	149.773	2.434	0.264	22.72	-17.22	1.816	0.64 ± 0.07	0.47 ± 0.04	-0.45 ± 0.51	-0.16 ± 0.98	39.78 ± 0.01	0.047	39.92 ± 0.01	98	142	0.99	0.48	34.38	0.18
COSMOS-051	149.776	2.299	0.130	24.59	-13.97	0.560	0.63 ± 0.07	0.31 ± 0.05	0.31 ± 0.05	0.09 ± 0.04	38.68 ± 0.01	0.004	39.23 ± 0.01	36	164	772.15	0.87	3.33	0.12
COSMOS-052	149.778	2.341	0.069	23.48	-13.77	0.464	0.73 ± 0.07	0.10 ± 0.05	0.28 ± 1.05	-0.14 ± 1.21	38.15 ± 0.01	0.001	38.22 ± 0.01	43	60	88.22	0.45	0.35	0.07
COSMOS-053	149.779	2.448	0.310	22.63	-17.59	2.260	0.41 ± 0.07	0.31 ± 0.05	-0.09 ± 0.04	0.54 ± 0.04	40.24 ± 0.03	0.137	39.75 ± 0.10	95	87	0.53	0.28	46.77	0.11
COSMOS-054	149.781	2.632	0.233	25.93	-13.89	0.635	0.60 ± 0.07	0.30 ± 0.05	0.24 ± 0.02	0.83 ± 0.37	39.85 ± 0.05	0.055	39.15 ± 0.30	161	110	13198.90	0.23	30.75	0.13
COSMOS-055	149.781	2.050	0.722	24.14	-16.31	1.505	0.49 ± 0.07	0.46 ± 0.09	0.04 ± 0.30	0.28 ± 0.04	39.62 ± 2.20	0.033	99.0 ± 99.0	105	105	37.92	0.34	273.68	0.43
COSMOS-056	149.786	1.821	0.135	23.58	-15.05	0.865	0.69 ± 0.07	0.27 ± 0.04	0.38 ± 0.04	0.35 ± 0.03	39.19 ± 0.01	0.012	39.56 ± 0.01	68	202	31.72	0.92	2.71	0.11
COSMOS-057	149.789	2.418	0.265	22.53	-17.42	1.871	0.60 ± 0.07	0.46 ± 0.04	1.32 ± 0.28	0.78 ± 0.37	39.87 ± 0.01	0.059	40.15 ± 0.01	118	204	0.61	0.41	22.66	0.10
COSMOS-058	149.790	1.929	0.046	99.00	99.00	99.00	0.74 ± 0.07	0.25 ± 0.04	0.32 ± 0.05	0.12 ± 0.04	39.01 ± 0.00	0.008	38.98 ± 0.00	100	112	99.00	99.00	2.24	0.14
COSMOS-059	149.796	1.944	0.425	22.58	-18.26	2.995	0.40 ± 0.07	0.40 ± 0.05	0.37 ± 0.05	0.63 ± 0.32	40.45 ± 0.12	0.221	99.0 ± 99.0	83	189	0.26	0.54	98.62	0.19
COSMOS-060	149.797	1.883	0.264	22.20	-17.74	2.168	0.58 ± 0.07	0.32 ± 0.02	99.0 ± 99.0	3.45 ± 0.14	40.12 ± 0.01	0.103	40.28 ± 0.01	159	220	0.21	0.51	48.28	0.14
COSMOS-061	149.804	1.893	0.265	21.13	-18.81	3.491	0.60 ± 0.07	0.42 ± 0.03	0.49 ± 0.04	1.00 ± 0.06	40.23 ± 0.00	0.134	40.29 ± 0.00	96	105	0.01	0.80	113.74	0.17
COSMOS-062	149.812	2.192	0.010	99.00	99.00	99.00	0.71 ± 0.07	0.16 ± 0.04	1.13 ± 0.40	0.52 ± 0.19	37.72 ± 0.00	0.000	37.39 ± 0.00	99	54	99.00	99.00	0.11	0.16
COSMOS-063	149.816	2.258	0.233	23.05	-16.66	1.366	0.58 ± 0.07	0.34 ± 0.02	1.41 ± 0.24	0.22 ± 0.02	39.74 ± 0.01	0.043	39.55 ± 0.01	172	75	3.75	0.61	11.50	0.06

Table A.1: continued.

Object	RA	DEC	z_{phot}	m(F814W)	M(F814W)	R_{lum}	$U-B$	$B-V$	$V-K$	$V-i$	log(L(Hα))	SFR	log(L[OIII])	EW (Hα)	EW([OIII])	SB	Ellipticity	Mass	G
(1)	(2)	(3)	(4)	(5)	(6)	(7)	(8)	(9)	(10)	(11)	(12)	(13)	(14)	(15)	(16)	(17)	(18)	(19)	(20)
COSMOS-064	149.833	1.763	0.210	27.12	-12.32	0.310	0.69 ± 0.07	0.35 ± 0.05	0.85 ± 0.22	0.35 ± 0.35	40.03 ± 0.04	0.084	99.0 ± 99.0	86	94	864296.94	0.45	33.18	0.18
COSMOS-065	149.838	1.684	0.366	24.49	-15.97	1.343	0.47 ± 0.07	0.60 ± 0.02	-0.03 ± 0.26	0.92 ± 0.37	40.10 ± 0.14	0.101	39.03 ± 0.55	537	93	108.64	0.73	91.56	0.28
COSMOS-066	149.840	2.152	0.010	21.58	-18.90	3.021	0.38 ± 0.07	0.31 ± 0.02	0.11 ± 0.22	0.19 ± 0.03	40.77 ± 0.06	0.466	40.27 ± 0.05	367	169	0.03	0.57	0.13	0.16
COSMOS-067	149.845	2.467	0.264	23.93	-16.00	1.180	0.52 ± 0.07	0.26 ± 0.03	3.64 ± 0.48	0.31 ± 0.03	39.65 ± 0.01	0.036	39.97 ± 0.01	149	269	38.85	0.19	13.06	0.05
COSMOS-068	149.849	1.792	0.265	21.22	-18.72	4.156	0.50 ± 0.07	0.35 ± 0.05	0.26 ± 0.04	0.82 ± 0.30	40.35 ± 0.00	0.177	40.48 ± 0.00	113	129	0.01	0.47	98.85	0.13
COSMOS-069	149.855	2.655	0.264	23.80	-16.14	1.399	0.54 ± 0.07	0.41 ± 0.04	1.02 ± 0.37	0.46 ± 0.03	39.62 ± 0.01	0.033	39.94 ± 0.01	95	188	20.38	0.30	11.30	0.18
COSMOS-070	149.857	2.246	0.025	23.28	-17.15	2.007	0.42 ± 0.07	0.47 ± 0.04	0.25 ± 0.05	0.81 ± 0.27	40.67 ± 0.86	0.373	39.51 ± 0.15	496	198	2.97	0.87	0.35	0.14
COSMOS-071	149.862	2.069	0.423	22.21	-18.54	3.381	0.36 ± 0.07	0.34 ± 0.03	0.09 ± 1.13	0.24 ± 0.03	40.80 ± 0.07	0.500	99.0 ± 99.0	544	92	0.09	0.81	125.91	0.17
COSMOS-072	149.862	1.995	0.046	25.13	-11.26	0.189	1.11 ± 0.07	0.24 ± 0.04	-0.01 ± 0.04	-0.15 ± 0.72	37.82 ± 0.02	0.001	37.68 ± 0.03	93	99	23748.30	0.46	0.18	0.09
COSMOS-073	149.878	1.785	0.265	23.01	-16.94	2.077	0.55 ± 0.07	0.37 ± 0.03	0.27 ± 0.06	0.11 ± 0.03	40.07 ± 0.00	0.093	40.27 ± 0.00	81	118	1.48	0.58	62.00	0.14
COSMOS-074	149.881	1.889	0.302	22.44	-17.79	2.699	0.45 ± 0.07	0.36 ± 0.03	99.0 ± 99.0	0.44 ± 0.18	40.20 ± 0.03	0.125	39.68 ± 0.12	106	98	0.24	0.22	66.45	0.17
COSMOS-075	149.883	1.994	0.245	25.60	-14.20	0.696	2.27 ± 0.07	0.35 ± 0.03	0.12 ± 0.06	-0.37 ± 0.86	39.65 ± 0.03	0.036	39.78 ± 0.01	298	309	5151.98	0.27	27.56	0.29
COSMOS-076	149.892	2.766	0.064	27.03	-10.06	0.117	0.63 ± 0.07	0.13 ± 0.03	1.13 ± 0.58	99.0 ± 99.0	38.68 ± 0.01	0.004	39.03 ± 0.01	59	145	4901600.00	0.63	1.22	0.14
COSMOS-077	149.896	2.466	0.245	24.01	-15.78	1.163	0.50 ± 0.07	0.38 ± 0.16	0.12 ± 0.56	0.44 ± 0.03	39.34 ± 0.02	0.017	39.19 ± 0.02	113	55	47.91	0.71	10.34	0.12
COSMOS-078	149.904	2.279	0.264	21.62	-18.32	2.518	0.66 ± 0.07	0.36 ± 0.05	99.0 ± 99.0	0.19 ± 0.03	40.49 ± 0.00	0.244	40.37 ± 0.00	217	141	0.04	0.22	101.76	0.19
COSMOS-079	149.905	2.834	0.264	22.45	-17.49	1.813	0.61 ± 0.06	0.43 ± 0.03	0.45 ± 0.04	0.20 ± 0.02	40.12 ± 0.01	0.104	40.08 ± 0.01	152	126	0.53	0.06	49.73	0.17
COSMOS-080	149.915	2.477	0.234	22.65	-17.06	1.691	0.49 ± 0.06	0.15 ± 0.05	0.92 ± 0.43	0.36 ± 0.57	40.10 ± 0.01	0.100	40.25 ± 0.01	251	266	0.99	0.57	9.39	0.07
COSMOS-081	149.916	2.477	0.233	22.21	-17.64	2.321	0.59 ± 0.06	0.43 ± 0.05	0.24 ± 0.02	0.14 ± 0.04	40.12 ± 0.04	0.104	39.74 ± 0.09	103	87	0.19	0.87	36.86	0.14
COSMOS-082	149.918	1.856	0.233	20.32	-19.53	4.310	0.52 ± 0.06	-0.12 ± 0.09	0.14 ± 0.05	0.71 ± 0.38	41.41 ± 0.00	2.035	41.56 ± 0.00	312	553	0.00	0.49	147.15	0.15
COSMOS-083	149.930	2.835	0.247	23.00	-16.81	1.346	0.27 ± 0.06	-0.13 ± 0.10	1.21 ± 0.41	1.02 ± 1.23	40.47 ± 0.01	0.230	40.63 ± 0.00	1082	1101	3.48	0.68	-NaN	0.25
COSMOS-084	149.931	2.084	0.178	21.58	-17.60	2.066	0.51 ± 0.06	0.22 ± 0.05	0.27 ± 0.05	0.41 ± 0.07	40.29 ± 0.00	0.153	39.84 ± 0.00	207	64	0.06	0.75	16.62	0.13
COSMOS-085	149.942	1.988	0.269	22.28	-17.67	3.109	0.56 ± 0.06	0.45 ± 0.04	0.31 ± 1.07	0.26 ± 0.03	39.86 ± 0.07	0.057	40.06 ± 0.04	86	95	0.12	0.90	35.66	0.13
COSMOS-086	149.943	2.095	0.234	22.18	-17.55	1.894	0.52 ± 0.06	0.33 ± 0.06	0.45 ± 0.12	0.94 ± 0.75	39.82 ± 0.06	0.052	38.98 ± 0.46	111	81	0.27	0.24	42.86	0.13
COSMOS-087	149.951	1.975	0.351	23.07	-17.49	2.469	0.43 ± 0.06	0.54 ± 0.39	-0.16 ± 0.03	0.34 ± 0.04	40.28 ± 0.05	0.152	39.35 ± 0.30	89	92	1.21	0.49	48.02	0.18
COSMOS-088	149.960	2.417	0.245	22.99	-16.81	1.552	0.43 ± 0.06	-0.01 ± 0.03	0.17 ± 0.29	99.0 ± 99.0	40.22 ± 0.01	0.132	40.35 ± 0.01	408	385	2.52	0.35	15.21	0.11
COSMOS-089	149.964	1.707	0.010	99.00	99.00	99.00	0.50 ± 0.06	0.17 ± 0.02	1.20 ± 0.94	0.13 ± 0.04	38.33 ± 0.00	0.002	38.49 ± 0.00	251	387	99.00	99.00	0.08	0.15
COSMOS-090	149.972	2.144	0.265	22.51	-17.43	2.071	0.56 ± 0.06	0.42 ± 0.02	0.19 ± 0.04	2.32 ± 0.47	39.71 ± 0.01	0.041	39.98 ± 0.01	73	125	0.48	0.56	30.74	0.13
COSMOS-091	149.991	2.606	0.246	22.60	-17.21	2.111	0.52 ± 0.06	0.24 ± 0.06	99.0 ± 99.0	0.72 ± 0.22	39.96 ± 0.01	0.073	39.94 ± 0.01	163	106	0.56	0.94	13.97	0.09
COSMOS-092	149.991	1.865	0.346	22.57	-17.83	2.463	0.36 ± 0.06	0.50 ± 0.01	0.02 ± 0.05	1.24 ± 0.31	40.43 ± 0.03	0.214	39.58 ± 0.17	110	106	0.39	0.22	45.15	0.14
COSMOS-093	149.992	1.806	0.488	22.57	-18.37	3.757	0.44 ± 0.06	0.44 ± 0.07	0.34 ± 0.04	0.19 ± 0.04	40.01 ± 0.54	0.081	99.0 ± 99.0	109	112	0.16	0.94	196.11	0.32
COSMOS-094	149.994	1.817	0.264	22.79	-17.15	1.710	0.50 ± 0.06	0.30 ± 0.03	0.91 ± 0.31	0.29 ± 0.03	39.70 ± 0.01	0.040	39.88 ± 0.01	89	126	1.33	0.26	25.11	0.14
COSMOS-095	149.998	1.923	0.265	99.00	99.00	99.00	0.47 ± 0.06	0.31 ± 0.07	0.37 ± 0.02	0.29 ± 0.45	39.33 ± 0.01	0.017	39.72 ± 0.01	76	156	99.00	99.00	9.70	0.08
COSMOS-096	150.003	2.626	0.247	24.10	-15.71	1.076	0.49 ± 0.06	0.44 ± 0.07	1.04 ± 0.14	0.12 ± 0.03	39.63 ± 0.01	0.033	39.65 ± 0.01	142	107	68.84	0.42	6.70	0.09
COSMOS-097	150.005	2.295	0.220	99.00	99.00	99.00	0.55 ± 0.06	0.07 ± 0.05	0.10 ± 0.99	0.30 ± 0.34	40.85 ± 0.03	0.561	40.43 ± 0.02	202	179	99.00	99.00	52.99	0.17
COSMOS-098	150.005	2.295	0.219	99.00	99.00	99.00	0.71 ± 0.06	0.37 ± 0.06	0.05 ± 0.04	0.19 ± 0.03	40.49 ± 0.03	0.242	39.62 ± 0.12	128	93	99.00	99.00	66.82	0.18
COSMOS-099	150.012	1.792	0.264	24.67	-15.27	0.857	0.49 ± 0.06	0.52 ± 0.03	0.43 ± 0.52	0.77 ± 0.18	39.37 ± 0.01	0.019	39.66 ± 0.01	79	141	402.07	0.42	16.06	0.17
COSMOS-100	150.013	2.193	0.246	22.32	-17.48	2.149	0.59 ± 0.06	0.29 ± 0.03	0.14 ± 0.06	0.11 ± 0.44	40.33 ± 0.00	0.171	40.13 ± 0.00	175	80	0.29	0.90	101.75	0.19
COSMOS-101	150.019	2.136	0.160	99.00	99.00	99.00	0.73 ± 0.06	0.34 ± 0.05	99.0 ± 99.0	0.20 ± 0.03	37.99 ± 2.04	0.001	39.51 ± 0.05	289	342	99.00	99.00	0.00	99.00
COSMOS-102	150.020	2.136	0.160	99.00	99.00	99.00	0.73 ± 0.06	0.34 ± 0.10	0.20 ± 0.02	99.0 ± 99.0	39.41 ± 0.01	0.020	39.53 ± 0.01	88	112	99.00	99.00	11.59	0.17
COSMOS-103	150.024	2.269	0.246	21.35	-18.39	2.521	0.54 ± 0.06	0.22 ± 0.04	0.24 ± 0.04	0.21 ± 0.04	40.22 ± 0.03	0.132	40.13 ± 0.05	125	91	0.02	0.37	132.74	0.20
COSMOS-104	150.028	2.379	0.010	99.00	99.00	99.00	0.46 ± 0.06	-0.05 ± 0.07	0.50 ± 0.18	0.47 ± 0.52	37.97 ± 0.00	0.001	37.59 ± 0.00	144	67	99.00	99.00	0.10	0.16
COSMOS-105	150.042	1.896	0.332	23.09	-17.26	2.632	0.44 ± 0.06	0.51 ± 0.02	99.0 ± 99.0	99.0 ± 99.0	40.27 ± 0.05	0.146	39.64 ± 0.15	234	98	1.11	0.77	49.61	0.12
COSMOS-106	150.045	2.210	0.233	24.00	-15.70	1.037	0.61 ± 0.06	0.37 ± 0.03	0.48 ± 0.03	-0.76 ± 0.86	39.43 ± 0.01	0.021	39.26 ± 0.01	118	60	58.15	0.55	10.76	0.16
COSMOS-107	150.045	1.969	0.359	26.14	-14.34	0.785	0.54 ± 0.06	0.55 ± 0.02	0.26 ± 0.04	-0.26 ± 0.03	40.12 ± 0.14	0.105	39.39 ± 0.23	332	80	14193.80	0.57	60.75	0.26
COSMOS-108	150.047	2.196	0.186	22.77	-16.52	1.196	0.86 ± 0.06	0.51 ± 0.07	0.97 ± 0.46	0.34 ± 0.05	39.80 ± 0.04	0.050	99.0 ± 99.0	95	85	2.59	0.33	23.77	0.19
COSMOS-109	150.055	2.550	0.264	23.66	-16.28	1.792	0.49 ± 0.06	0.25 ± 0.05	0.94 ± 0.16	-0.09 ± 0.04	39.77 ± 0.01	0.047	39.90 ± 0.01	170	196	8.91	0.91	15.71	0.06
COSMOS-110	150.067	2.322	0.124	22.29	-16.10	0.930	0.83 ± 0.06	0.38 ± 0.08	0.28 ± 0.07	99.0 ± 99.0	39.70 ± 0.02	0.040	38.59 ± 0.28	96	124	1.42	0.38	9.76	0.18
COSMOS-111	150.073	2.098	0.265	21.76	-18.18	3.062	0.56 ± 0.06	0.41 ± 0.04	2.16 ± 0.35	0.30 ± 0.07	40.09 ± 0.00	0.096	40.29 ± 0.01	105	161	0.04	0.96	73.83	0.18
COSMOS-112	150.077	2.009	0.059	23.84	-13.08	0.302	0.38 ± 0.06	0.37 ± 0.06	-0.32 ± 0.03	0.40 ± 0.04	38.58 ± 0.01	0.003	38.94 ± 0.01	144	451	474.55	0.65	0.62	0.13
COSMOS-113	150.079	2.637	0.264	22.03	-17.88	3.120	0.63 ± 0.06	0.45 ± 0.06	-0.69 ± 0.63	99.0 ± 99.0	40.07 ± 0.04	0.093	40.24 ± 0.03	131	90	0.07	0.97	55.14	0.15
COSMOS-114	150.082	2.082	0.233	22.30	-17.53	2.431	0.65 ± 0.06	0.45 ± 0.05	-0.50 ± 0.04	0.00 ± 0.06	39.81 ± 0.07	0.051	39.33 ± 0.23	173	97	0.21	0.62	31.77	0.16
COSMOS-115	150.087	1.962	0.162	23.36	-15.63	1.212	0.72 ± 0.06	0.22 ± 0.06	0.25 ± 0.03	99.0 ± 99.0	39.28 ± 0.01	0.015	39.21 ± 0.01	91	68	9.84	0.72	3.22	0.06
COSMOS-116	150.088	2.394	0.041	25.34	-10.81	0.151	0.85 ± 0.06	0.19 ± 0.03	0.27 ± 0.30	0.34 ± 0.05	37.87 ± 0.02	0.001	37.87 ± 0.02	87	158	60099.60	0.74	0.14	0.05
COSMOS-117	150.090	2.231	0.071	24.68	-12.63	0.262	0.68 ± 0.06	0.36 ± 0.02	-0.69 ± 1.09	0.57 ± 0.31	38.56 ± 0.01	0.003	38.34 ± 0.02	118	92	4388.31	0.33	0.77	0.08
COSMOS-118	150.091	2.419	0.265	23.01	-16.94	2.325	0.63 ± 0.06	0.46 ± 0.03	0.33 ± 0.04	1.08 ± 0.41	39.95 ± 0.01	0.071	40.20 ± 0.01	89	148	1.19	0.50	62.52	0.18
COSMOS-119	150.103	1.924	0.264	22.82	-17.12	1.514	0.71 ± 0.06	0.41 ± 0.04	0.85 ± 0.43	0.75 ± 0.04	39.80 ± 0.01	0.050	39.76 ± 0.01	127	110	1.79	0.21	27.35	0.16
COSMOS-120	150.103	1.923	0.265	22.67	-17.28	2.349	0.61 ± 0.06	0.43 ± 0.04	0.34 ± 0.04	0.28 ± 0.03	39.77 ± 0.01	0.046	39.92 ± 0.01	85	112	0.53	0.44	36.36	0.18
COSMOS-121	150.106	1.905	0.322	23.14	-17.17	2.497	0.48 ± 0.06	0.40 ± 0.03	0.15 ± 0.06	0.42 ± 0.04	40.51 ± 0.06	0.258	39.49 ± 0.17	302	146	1.38	0.15	34.27	0.13
COSMOS-122	150.109	2.224	0.349	27.00	-13.56	0.473	0.33 ± 0.06	0.36 ± 0.05	0.34 ± 0.06	99.0 ± 99.0	40.51 ± 0.09	0.254	39.57 ± 0.14	361	102	280297.00	0.34	105.96	0.26
COSMOS-123	150.112	2.430	0.426	21.83	-18.90	4.008	0.44 ± 0.06	0.54 ± 0.03	99.0 ± 99.0	0.25 ± 0.04	40.66 ± 0.02	0.364	99.0 ± 99.0	150	92	0.03	0.59	261.94	0.30
COSMOS-124	150.115	2.817	0.160	23.20	-15.77	0.979	0.66 ± 0.06	0.33 ± 0.02	1.30 ± 0.35	0.01 ± 0.05	39.31 ± 0.01	0.016	39.53 ± 0.01	105	178	10.34	0.80	5.10	0.07
COSMOS-125	150.116	1.951	0.265	20.48	-19.46	4.138	0.46 ± 0.06	-0.13 ± 0.05	0.02 ± 0.04	99.0 ± 99.0	41.20 ± 0.01	1.252	41.49 ± 0.00	588	558	0.00	0.41	144.90	0.19
COSMOS-126	150.119	2.565	0.265	22.99	-16.95	1.444	0.53 ± 0.06	0.34 ± 0.04	0.28 ± 0.05	99.0 ± 99.0	39.72 ± 0.01	0.041	39.83 ± 0.01	103	121	2.97	0.17	28.15	0.17

Table A.1: continued.

Object	RA	DEC	z_{phot}	m(F814W)	M(F814W)	R_{lum}	$U-B$	$B-V$	$V-K$	$V-i$	log(L(Hα))	SFR	log(L[OIII])	EW (Hα)	EW([OIII])	SB	Ellipticity	Mass	G
(1)	(2)	(3)	(4)	(5)	(6)	(7)	(8)	(9)	(10)	(11)	(12)	(13)	(14)	(15)	(16)	(17)	(18)	(19)	(20)
COSMOS-127	150.122	2.246	0.232	25.23	-14.47	0.759	0.61 ± 0.06	0.38 ± 0.16	1.94 ± 0.29	0.38 ± 0.16	39.16 ± 0.01	0.011	39.23 ± 0.01	73	66	1835.92	0.84	4.02	0.07
COSMOS-128	150.123	1.614	0.162	20.90	-18.10	2.142	0.79 ± 0.06	0.34 ± 0.06	-0.18 ± 1.03	0.17 ± 0.02	40.19 ± 0.00	0.122	40.13 ± 0.00	111	95	0.01	0.29	59.89	0.17
COSMOS-129	150.126	2.410	0.264	23.50	-16.44	1.522	0.51 ± 0.06	0.38 ± 0.05	0.38 ± 0.03	99.0 ± 99.0	39.62 ± 0.01	0.033	39.79 ± 0.01	117	164	8.54	0.31	16.24	0.08
COSMOS-130	150.134	1.956	0.380	21.96	-18.65	3.276	0.38 ± 0.06	0.40 ± 0.04	1.07 ± 0.17	0.13 ± 0.04	40.90 ± 0.02	0.625	99.0 ± 99.0	208	96	0.05	0.47	184.55	0.17
COSMOS-131	150.136	2.647	0.025	22.10	-18.40	3.253	0.35 ± 0.06	0.44 ± 0.18	0.91 ± 0.21	0.26 ± 0.34	40.74 ± -0.07	0.430	39.69 ± 0.15	736	245	0.08	0.46	0.42	0.16
COSMOS-132	150.138	2.440	0.305	22.49	-17.77	2.507	0.44 ± 0.06	0.37 ± 0.02	0.23 ± 0.02	0.03 ± 0.03	40.49 ± 0.02	0.245	39.80 ± 0.09	143	133	0.31	0.72	53.88	0.13
COSMOS-133	150.145	2.356	0.351	22.77	-17.65	2.000	0.25 ± 0.06	0.53 ± 0.04	-0.07 ± 0.02	0.34 ± 0.49	40.38 ± 0.44	0.192	99.0 ± 99.0	1314	104	0.92	0.47	150.75	0.28
COSMOS-134	150.146	1.928	0.406	99.00	99.00	99.00	0.39 ± 0.06	0.41 ± 0.02	0.17 ± 0.21	0.12 ± 0.04	40.14 ± 0.06	0.108	99.0 ± 99.0	136	88	99.00	99.00	87.05	0.13
COSMOS-135	150.146	2.003	0.050	20.89	-15.68	0.870	0.60 ± 0.06	0.14 ± 0.09	0.28 ± 0.04	99.0 ± 99.0	39.43 ± 0.00	0.021	39.34 ± 0.00	141	129	0.07	0.75	4.52	0.17
COSMOS-136	150.146	1.718	0.232	23.30	-16.39	1.313	0.54 ± 0.06	0.31 ± 0.08	-0.07 ± 1.31	0.34 ± 0.23	39.71 ± 0.01	0.041	39.54 ± 0.01	157	77	7.31	0.77	14.46	0.12
COSMOS-137	150.149	2.020	0.265	20.04	-19.91	3.938	0.54 ± 0.06	0.22 ± 0.02	0.19 ± 0.06	0.37 ± 0.08	41.10 ± 0.01	0.997	41.31 ± 0.01	311	243	0.00	0.64	410.20	0.18
COSMOS-138	150.152	2.518	0.264	99.00	99.00	99.00	0.63 ± 0.06	0.40 ± 0.02	0.28 ± 0.06	0.26 ± 0.01	40.25 ± 0.00	0.141	40.38 ± 0.00	119	151	99.00	99.00	106.36	0.18
COSMOS-139	150.158	2.859	0.173	23.21	-15.91	1.279	0.59 ± 0.06	0.34 ± 0.04	0.19 ± 1.47	-0.42 ± 0.82	39.73 ± 0.01	0.042	39.40 ± 0.01	222	96	6.24	0.74	4.09	0.11
COSMOS-140	150.163	2.710	0.138	99.00	99.00	99.00	0.70 ± 0.06	0.59 ± 0.18	99.0 ± 99.0	0.06 ± 0.03	40.00 ± 0.00	0.079	40.49 ± 0.00	162	620	99.00	99.00	9.24	0.17
COSMOS-141	150.168	1.719	0.173	20.80	-18.46	2.109	0.67 ± 0.06	0.26 ± 0.06	0.34 ± 0.05	-0.62 ± 0.37	40.61 ± 0.01	0.320	39.85 ± 0.06	117	97	0.01	0.43	0.00	0.18
COSMOS-142	150.179	2.256	0.217	23.13	-16.45	1.318	0.63 ± 0.06	0.28 ± 0.05	0.18 ± 1.21	-0.39 ± 0.02	39.83 ± 0.05	0.053	38.89 ± 0.43	116	84	4.83	0.68	16.18	0.13
COSMOS-143	150.190	2.023	0.074	21.48	-15.91	0.977	0.41 ± 0.06	0.30 ± 0.09	0.34 ± 0.03	-0.26 ± 0.55	39.66 ± 0.00	0.036	39.45 ± 0.00	206	146	0.20	0.29	4.70	0.19
COSMOS-144	150.199	1.713	0.264	99.00	99.00	99.00	0.56 ± 0.06	0.32 ± 0.02	0.96 ± 0.26	0.23 ± 0.04	40.05 ± 0.00	0.089	40.35 ± 0.00	74	142	99.00	99.00	76.57	0.15
COSMOS-145	150.211	2.449	0.654	22.70	-17.25	1.655	0.53 ± 0.06	0.25 ± 0.02	0.20 ± 0.02	0.12 ± 0.04	40.14 ± 0.03	0.109	40.50 ± 0.01	323	383	1.14	0.59	82.14	0.37
COSMOS-146	150.216	2.729	0.166	23.33	-15.71	1.043	0.71 ± 0.06	0.46 ± 0.05	0.14 ± 0.03	-0.21 ± 0.15	39.20 ± 0.01	0.013	39.20 ± 0.01	94	92	12.34	0.17	3.99	0.10
COSMOS-147	150.228	2.150	0.174	21.91	-17.22	2.100	0.65 ± 0.06	0.41 ± 0.01	-0.41 ± 1.20	-0.54 ± 0.74	40.20 ± 0.00	0.125	39.80 ± 0.01	222	94	0.12	0.70	22.56	0.15
COSMOS-148	150.230	2.237	0.117	22.86	-15.43	0.935	0.68 ± 0.06	0.50 ± 0.03	0.22 ± 0.05	0.22 ± 0.02	39.94 ± 0.03	0.069	37.94 ± 0.92	315	393	5.17	0.74	4.15	0.14
COSMOS-149	150.234	2.022	0.073	24.09	-13.27	0.430	0.76 ± 0.06	0.30 ± 0.03	0.26 ± 1.20	0.14 ± 0.02	37.98 ± 0.01	0.001	38.22 ± 0.01	25	58	420.14	0.29	0.91	0.12
COSMOS-150	150.237	1.862	0.304	22.30	-17.93	2.737	0.47 ± 0.06	0.48 ± 0.05	0.90 ± 1.17	0.12 ± 0.04	40.45 ± 0.03	0.221	39.78 ± 0.10	177	121	0.17	0.48	65.42	0.15
COSMOS-151	150.237	2.194	0.392	99.00	99.00	99.00	0.30 ± 0.06	0.42 ± 0.05	-0.35 ± 0.32	0.00 ± 0.04	39.82 ± 0.08	0.052	99.0 ± 99.0	128	116	99.00	99.00	86.33	0.10
COSMOS-152	150.239	2.647	0.265	21.73	-18.22	2.362	0.60 ± 0.06	0.38 ± 0.03	99.0 ± 99.0	2.18 ± 0.43	40.30 ± 0.00	0.158	40.18 ± 0.01	164	114	0.06	0.76	73.84	0.17
COSMOS-153	150.241	2.838	0.264	23.95	-15.99	1.367	0.62 ± 0.06	0.41 ± 0.05	0.35 ± 0.03	0.44 ± 0.07	39.65 ± 0.01	0.035	39.63 ± 0.01	161	135	29.95	0.41	19.16	0.18
COSMOS-154	150.262	1.686	0.164	23.98	-15.04	0.874	0.76 ± 0.06	0.43 ± 0.06	1.00 ± 0.23	-0.48 ± 0.23	39.06 ± 0.01	0.009	39.40 ± 0.01	88	198	79.15	0.52	2.89	0.08
COSMOS-155	150.265	1.903	0.020	23.92	-10.69	0.104	0.34 ± 0.06	0.15 ± 0.06	1.59 ± 1.42	-0.06 ± 0.06	37.88 ± 0.01	0.001	37.87 ± 0.01	284	304	4867.72	0.15	0.03	0.06
COSMOS-156	150.265	2.161	0.066	99.00	99.00	99.00	0.72 ± 0.06	0.18 ± 0.03	0.33 ± 0.03	0.44 ± 0.02	39.28 ± 0.00	0.015	39.64 ± 0.00	30	82	99.00	99.00	19.08	0.18
COSMOS-157	150.273	2.566	0.137	23.35	-15.31	0.797	0.58 ± 0.06	0.55 ± 0.05	0.39 ± 0.03	-0.12 ± 0.52	39.35 ± 0.01	0.018	39.74 ± 0.01	192	467	22.02	0.42	1.68	0.13
COSMOS-158	150.275	2.587	0.264	23.12	-16.82	1.573	0.58 ± 0.06	0.42 ± 0.03	0.48 ± 0.47	-0.38 ± 0.03	39.68 ± 0.01	0.038	39.89 ± 0.01	104	154	3.37	0.47	22.65	0.13
COSMOS-159	150.276	2.014	0.266	24.23	-15.72	1.578	0.56 ± 0.06	0.43 ± 0.03	99.0 ± 99.0	0.42 ± 0.08	39.52 ± 0.01	0.026	39.76 ± 0.01	77	124	42.88	0.63	11.02	0.09
COSMOS-160	150.279	2.173	0.264	23.11	-16.83	1.543	0.64 ± 0.06	0.38 ± 0.03	0.80 ± 0.28	0.63 ± 0.31	39.78 ± 0.01	0.048	39.87 ± 0.01	129	151	3.40	0.17	22.75	0.10
COSMOS-161	150.284	2.755	0.229	22.28	-17.39	2.289	0.52 ± 0.06	0.16 ± 0.05	0.43 ± 0.04	0.51 ± 0.23	39.98 ± 0.17	0.076	39.97 ± 0.05	1154	168	0.23	0.97	10.77	0.12
COSMOS-162	150.287	2.625	0.282	22.19	-17.87	2.813	0.49 ± 0.06	0.22 ± 0.03	0.95 ± 0.35	1.07 ± 0.55	40.67 ± 0.02	0.370	40.07 ± 0.05	201	155	0.12	0.74	44.64	0.09
COSMOS-163	150.290	2.838	0.449	21.75	-19.15	4.147	0.37 ± 0.06	0.38 ± 0.04	0.56 ± 0.04	-0.04 ± 0.03	40.51 ± 0.07	0.258	99.0 ± 99.0	145	102	0.02	0.69	258.13	0.14
COSMOS-164	150.295	2.347	0.246	21.21	-18.60	2.189	0.44 ± 0.06	-0.17 ± 0.13	0.96 ± 0.43	-0.42 ± 0.03	41.00 ± 0.00	0.794	41.26 ± 0.00	686	940	0.02	0.48	65.02	0.17
COSMOS-165	150.301	2.169	0.129	23.05	-15.49	0.980	0.62 ± 0.06	0.69 ± 0.07	0.14 ± 0.04	0.73 ± 0.18	39.53 ± 0.01	0.027	39.52 ± 0.01	228	266	7.35	0.54	2.24	0.13
COSMOS-166	150.333	2.279	0.136	22.48	-16.17	1.372	0.52 ± 0.06	-0.03 ± 0.03	0.36 ± 0.57	0.10 ± 0.02	39.57 ± 0.01	0.029	39.43 ± 0.01	117	96	1.01	0.76	5.50	0.18
COSMOS-167	150.341	2.380	0.541	22.97	-16.13	1.368	0.64 ± 0.06	0.38 ± 0.05	0.30 ± 0.09	1.33 ± 0.53	39.57 ± 0.05	0.029	38.90 ± 0.22	200	240	3.14	0.79	51.23	0.19
COSMOS-168	150.358	2.189	0.129	23.32	-15.22	0.968	0.75 ± 0.06	0.41 ± 0.05	0.23 ± 0.07	-0.07 ± 0.04	39.14 ± 0.01	0.011	39.01 ± 0.01	85	77	13.98	0.79	2.06	0.14
COSMOS-169	150.362	2.467	0.135	99.00	99.00	99.00	0.74 ± 0.06	0.19 ± 0.04	0.80 ± 0.88	0.23 ± 0.06	39.75 ± 0.00	0.045	39.60 ± 0.01	101	86	99.00	99.00	10.96	0.13
COSMOS-170	150.367	2.490	0.162	99.00	99.00	99.00	0.59 ± 0.06	0.20 ± 0.07	0.25 ± 0.02	0.14 ± 0.08	39.33 ± 0.01	0.017	39.15 ± 0.01	107	63	99.00	99.00	4.74	0.10
COSMOS-171	150.371	2.179	0.488	22.41	-18.51	3.613	0.34 ± 0.06	0.41 ± 0.03	0.11 ± 0.03	0.18 ± 0.03	40.34 ± 0.06	0.172	37.92 ± 1.73	146	81	0.12	0.78	162.34	0.20
COSMOS-172	150.381	2.019	0.430	22.89	-17.86	2.923	0.34 ± 0.06	0.42 ± 0.06	0.41 ± 0.05	0.75 ± 0.30	40.07 ± 0.07	0.094	99.0 ± 99.0	94	80	0.57	0.76	76.90	0.16
COSMOS-173	150.395	2.072	0.159	99.00	99.00	99.00	0.71 ± 0.06	0.27 ± 0.03	0.37 ± 0.04	-0.20 ± 0.22	40.25 ± 0.00	0.139	40.12 ± 0.00	89	62	99.00	99.00	93.40	0.17
COSMOS-174	150.396	2.334	0.234	23.71	-16.00	1.199	0.74 ± 0.06	0.52 ± 0.09	0.40 ± 0.92	-0.14 ± 0.02	39.44 ± 0.02	0.022	39.08 ± 0.02	160	50	22.59	0.25	10.78	0.15
COSMOS-175	150.407	1.928	0.232	20.77	-18.91	2.914	0.64 ± 0.06	0.30 ± 0.03	1.38 ± 0.54	99.0 ± 99.0	39.57 ± 0.17	0.029	40.34 ± 0.03	114	104	0.00	0.53	104.88	0.13
COSMOS-176	150.409	2.212	0.160	21.55	-17.42	2.055	0.68 ± 0.06	0.30 ± 0.03	0.41 ± 0.05	1.10 ± 0.10	39.73 ± 0.00	0.042	39.74 ± 0.00	93	85	0.05	0.87	18.42	0.15
COSMOS-177	150.411	2.209	0.168	21.69	-17.38	1.866	0.66 ± 0.06	0.68 ± 0.04	1.42 ± 0.42	1.23 ± 0.54	40.42 ± 0.00	0.208	40.71 ± 0.00	399	705	0.09	0.13	13.71	0.17
COSMOS-178	150.413	2.423	0.062	22.14	-18.55	3.403	0.35 ± 0.06	0.36 ± 0.04	0.07 ± 0.04	0.72 ± 0.05	40.98 ± 0.04	0.756	40.11 ± 0.08	404	331	0.08	0.18	6.33	0.14
COSMOS-179	150.418	1.879	0.166	21.92	-17.22	1.816	0.66 ± 0.06	0.34 ± 0.06	0.36 ± 0.02	1.28 ± 0.53	39.81 ± 0.05	0.051	39.86 ± 0.04	142	123	0.16	0.85	16.93	0.12
COSMOS-180	150.431	1.778	0.265	21.73	-18.21	2.657	0.48 ± 0.06	0.09 ± 0.07	0.13 ± 0.04	-0.00 ± 0.03	40.57 ± 0.00	0.291	40.85 ± 0.00	288	498	0.05	0.72	35.37	0.11
COSMOS-181	150.447	2.660	0.221	21.93	-17.65	2.676	0.65 ± 0.06	0.29 ± 0.03	99.0 ± 99.0	-0.27 ± 0.76	40.09 ± 0.03	0.097	99.0 ± 99.0	107	84	0.07	0.30	33.48	0.13
COSMOS-182	150.450	2.407	0.020	24.34	-10.27	0.099	0.69 ± 0.06	0.42 ± 0.04	0.06 ± 0.05	0.24 ± 0.03	37.69 ± 0.01	0.000	36.97 ± 0.03	221	74	13983.90	0.41	0.07	0.05
COSMOS-183	150.498	2.262	0.264	23.14	-16.80	1.901	0.66 ± 0.06	0.39 ± 0.04	1.71 ± 1.18	99.0 ± 99.0	39.86 ± 0.01	0.057	40.11 ± 0.01	142	232	2.41	0.78	25.74	0.10
COSMOS-184	150.505	2.728	1.149	24.72	-14.80	0.979	0.41 ± 0.06	0.26 ± 0.07	99.0 ± 99.0	0.24 ± 0.05	39.78 ± 0.07	0.047	99.0 ± 99.0	183	143	342.30	0.60	7466.50	0.78
COSMOS-185	150.515	2.339	0.168	23.42	-15.65	1.029	0.68 ± 0.06	0.37 ± 0.07	0.06 ± 1.24	0.33 ± 0.03	39.38 ± 0.01	0.019	39.28 ± 0.01	135	95	15.49	0.81	3.11	0.08
COSMOS-186	150.517	2.117	0.303	21.39	-18.83	3.573	0.57 ± 0.06	0.44 ± 0.09	1.18 ± 0.02	-0.03 ± 0.36	40.08 ± 0.06	0.095	39.69 ± 0.10	121	106	0.01	0.61	28.51	0.10
COSMOS-187	150.526	2.348	0.065	99.00	99.00	99.00	0.55 ± 0.06	0.03 ± 0.08	2.88 ± 0.03	1.11 ± 0.33	38.30 ± 0.01	0.002	38.74 ± 0.01	31	93	99.00	99.00	0.71	0.07
COSMOS-188	150.533	1.928	0.159	22.49	-16.46	1.320	0.71 ± 0.06	0.37 ± 0.12	0.28 ± 0.04	0.33 ± 0.03	39.69 ± 0.01	0.039	39.85 ± 0.01	172	204	1.13	0.67	5.70	0.14
COSMOS-189	150.533	2.181	0.231	22.48	-17.21	2.368	0.58 ± 0.06	0.22 ± 0.06	-0.05 ± 0.02	-0.17 ± 0.20	39.68 ± 0.01	0.038	39.93 ± 0.01	90	125	0.34	0.65	16.79	0.10

Table A.1: continued.

Object	RA	DEC	z_{phot}	m(F814W)	M(F814W)	R_{lum}	$U-B$	$B-V$	$V-K$	$V-i$	log(L(Hα))	SFR	log(L[OIII])	EW (Hα)	EW([OIII])	SB	Ellipticity	Mass	G
(1)	(2)	(3)	(4)	(5)	(6)	(7)	(8)	(9)	(10)	(11)	(12)	(13)	(14)	(15)	(16)	(17)	(18)	(19)	(20)
COSMOS-190	150.534	1.818	0.063	22.73	-14.33	0.419	0.26 ± 0.06	0.31 ± 0.05	0.32 ± 0.02	0.84 ± 0.55	38.97 ± 0.01	0.007	38.64 ± 0.01	185	107	19.10	0.50	2.38	0.10
COSMOS-191	150.535	2.456	0.264	22.83	-17.11	2.098	0.50 ± 0.06	0.24 ± 0.06	-0.30 ± 0.35	0.67 ± 0.04	39.88 ± 0.01	0.060	40.31 ± 0.01	114	374	0.96	0.17	32.05	0.06
COSMOS-192	150.538	2.597	0.422	22.83	-17.90	2.580	0.48 ± 0.06	0.55 ± 0.09	0.32 ± 0.05	0.08 ± 0.02	40.39 ± 0.03	0.192	99.0 ± 99.0	151	124	0.64	0.38	109.97	0.29
COSMOS-193	150.558	1.778	0.265	23.19	-16.75	1.914	0.55 ± 0.06	0.27 ± 0.05	0.44 ± 0.04	0.04 ± 0.05	39.89 ± 0.01	0.061	40.10 ± 0.01	161	262	2.68	0.69	17.42	0.09
COSMOS-194	150.571	2.581	0.173	23.72	-15.41	1.211	0.77 ± 0.06	0.42 ± 0.06	-0.06 ± 0.04	-0.03 ± 0.01	39.29 ± 0.01	0.015	39.15 ± 0.01	96	65	22.29	0.98	4.27	0.13
COSMOS-195	150.574	2.572	0.264	23.42	-16.52	1.415	0.49 ± 0.06	0.33 ± 0.07	99.0 ± 99.0	1.00 ± 0.35	39.57 ± 0.01	0.029	39.93 ± 0.01	128	262	8.30	0.53	7.67	0.06
COSMOS-196	150.575	2.581	0.042	23.61	-12.59	0.321	0.54 ± 0.06	0.50 ± 0.05	99.0 ± 99.0	0.14 ± 0.04	38.97 ± 0.01	0.007	39.25 ± 0.00	342	747	246.80	0.71	0.30	0.18
COSMOS-197	150.592	2.586	0.334	23.23	-17.11	2.271	0.35 ± 0.06	0.26 ± 0.03	0.19 ± 0.30	99.0 ± 99.0	40.67 ± 0.04	0.371	39.68 ± 0.12	360	164	2.08	0.91	29.92	0.12
COSMOS-198	150.593	2.527	0.539	21.88	-17.18	1.528	0.72 ± 0.06	0.57 ± 0.07	0.46 ± 0.07	0.10 ± 0.05	39.87 ± 0.03	0.059	38.36 ± 0.95	172	199	0.21	0.52	249.90	0.15
COSMOS-199	150.594	2.422	0.015	23.88	-10.12	0.075	0.32 ± 0.06	0.55 ± 0.10	-0.14 ± 0.02	-0.05 ± 0.28	38.44 ± 0.00	0.002	38.58 ± 0.00	547	946	8393.08	0.73	0.06	0.16
COSMOS-200	150.597	1.771	0.290	25.63	-14.58	1.002	0.48 ± 0.06	0.43 ± 0.05	0.02 ± 0.02	0.28 ± 0.05	40.03 ± 0.05	0.084	39.52 ± 0.14	233	89	2662.15	0.20	15.90	0.08
COSMOS-201	150.603	1.688	0.246	22.35	-17.45	1.794	0.54 ± 0.06	0.06 ± 0.07	0.18 ± 0.06	0.01 ± 0.05	40.51 ± 0.00	0.257	40.65 ± 0.00	403	439	0.44	0.15	39.39	0.10
COSMOS-202	150.611	1.627	0.274	23.38	-16.63	1.595	0.50 ± 0.06	0.38 ± 0.19	99.0 ± 99.0	-0.08 ± 0.04	39.58 ± 0.01	0.030	39.67 ± 0.01	89	103	5.90	0.52	14.18	0.06
COSMOS-203	150.622	1.817	0.236	22.94	-16.78	2.073	1.63 ± 0.06	-0.24 ± 0.06	99.0 ± 99.0	0.02 ± 0.03	39.56 ± 0.01	0.029	40.83 ± 0.00	70	547	1.28	0.74	30.02	0.19
COSMOS-204	150.638	2.815	0.221	21.28	-18.28	2.251	0.56 ± 0.06	0.26 ± 0.03	0.08 ± 0.02	-0.15 ± 0.04	40.68 ± 0.01	0.380	39.92 ± 0.06	184	131	0.02	0.34	45.37	0.10
COSMOS-205	150.643	2.388	0.265	23.24	-16.70	1.459	0.49 ± 0.06	0.33 ± 0.05	0.72 ± 0.02	0.78 ± 0.60	39.54 ± 0.01	0.027	39.73 ± 0.01	101	138	5.17	0.52	19.70	0.09
COSMOS-206	150.671	1.990	0.135	24.90	-13.73	0.406	0.72 ± 0.06	0.56 ± 0.05	-0.02 ± 0.32	0.33 ± 0.29	38.68 ± 0.02	0.004	38.90 ± 0.02	50	104	3013.74	0.27	6.29	0.11
COSMOS-207	150.674	2.424	0.353	21.69	-18.81	2.882	0.30 ± 0.06	0.41 ± 0.07	99.0 ± 99.0	0.18 ± 0.03	40.93 ± 0.02	0.679	40.09 ± 0.07	174	113	0.04	0.79	107.83	0.10
COSMOS-208	150.677	2.506	0.040	99.00	99.00	99.00	1.58 ± 0.06	0.47 ± 0.04	0.21 ± 0.08	0.20 ± 0.03	38.73 ± 0.01	0.004	38.54 ± 0.01	274	472	99.00	99.00	1.54	0.19
COSMOS-209	150.681	2.806	0.264	21.62	-18.32	2.778	0.59 ± 0.06	0.37 ± 0.06	99.0 ± 99.0	0.30 ± 0.33	40.27 ± 0.00	0.148	40.29 ± 0.00	124	112	0.03	0.76	50.80	0.11
COSMOS-210	150.694	2.678	0.065	22.82	-14.31	0.505	0.67 ± 0.06	0.36 ± 0.07	99.0 ± 99.0	0.17 ± 0.03	38.63 ± 0.01	0.003	38.99 ± 0.01	58	162	16.12	0.40	1.47	0.13
COSMOS-211	150.696	2.321	0.062	22.98	-14.04	0.513	0.74 ± 0.06	0.29 ± 0.08	0.85 ± 0.23	0.16 ± 0.04	38.28 ± 0.01	0.002	38.67 ± 0.01	34	100	22.91	0.55	1.36	0.08
COSMOS-212	150.697	2.170	0.164	22.84	-16.18	1.189	0.68 ± 0.06	0.49 ± 0.03	0.26 ± 0.03	99.0 ± 99.0	39.41 ± 0.01	0.020	39.69 ± 0.01	91	163	3.10	0.53	8.88	0.14
COSMOS-213	150.697	1.939	0.265	23.58	-16.37	0.430	0.45 ± 0.06	0.37 ± 0.04	0.34 ± 0.05	99.0 ± 99.0	39.84 ± 0.01	0.054	40.07 ± 0.01	70	112	128.18	0.73	22.28	0.10
COSMOS-214	150.714	2.692	0.133	22.90	-15.70	0.856	0.82 ± 0.06	0.48 ± 0.06	99.0 ± 99.0	0.20 ± 0.16	38.99 ± 0.01	0.008	39.65 ± 0.01	37	212	6.77	0.28	3.46	0.13
COSMOS-215	150.725	1.798	0.129	21.61	-16.93	1.299	0.52 ± 0.06	0.58 ± 0.06	0.15 ± 0.05	0.33 ± 0.04	40.31 ± 0.00	0.162	40.45 ± 0.00	460	759	0.15	0.41	5.78	0.27
COSMOS-216	150.726	2.387	0.047	99.00	99.00	99.00	0.68 ± 0.06	0.20 ± 0.05	-0.18 ± 0.05	99.0 ± 99.0	38.95 ± 0.00	0.007	38.71 ± 0.01	122	81	99.00	99.00	1.41	0.15
COSMOS-217	150.733	2.534	0.050	25.51	-11.06	0.213	0.79 ± 0.06	0.25 ± 0.03	99.0 ± 99.0	99.0 ± 99.0	38.11 ± 0.01	0.001	37.92 ± 0.02	85	72	44901.70	0.35	0.31	0.07
COSMOS-218	150.748	2.718	0.046	24.95	-11.44	0.236	0.70 ± 0.06	0.32 ± 0.09	0.22 ± 1.04	0.20 ± 0.06	38.30 ± 0.01	0.002	38.19 ± 0.01	93	97	10176.30	0.75	0.60	0.07
COSMOS-219	150.755	1.827	0.302	25.89	-14.32	0.836	0.49 ± 0.06	0.59 ± 0.05	0.27 ± 0.04	0.14 ± 0.06	39.95 ± 0.05	0.070	39.28 ± 0.24	87	87	7043.97	0.53	28.71	0.16
COSMOS-220	150.783	2.748	0.176	99.00	99.00	99.00	0.64 ± 0.06	0.35 ± 0.05	-0.60 ± 1.29	0.62 ± 0.50	40.09 ± 0.00	0.097	39.80 ± 0.01	205	100	99.00	99.00	9.93	0.14

(1) Object name (ordered by RA), (2) RA, (3) DEC, (4) Redshift, (5) F814W magnitude, (6) F814W absolute magnitude, (7) Luminous radius (kpc), (8) U-B, (9) B-V, (10) V-K, (11) V-i, (12) Hα luminosity, (13) SFR, (14) [OIII] luminosity, (15) Hα equivalent width (Å), (16) [OIII] equivalent width (Å), (17) surface brightness (erg s^{-1} cm^{-2} $Å^{-1}$) ($\times 10^{-24}$), (18) Ellipticity, (19) Mass ($\times 10^{7}$ $M_{\odot}$) and (20) G factor. For parameters where it was not possible to do an estimation, we give the value -99.0.

Appendix B

Appendix B: Main parameters for knots in our sample

Table B.1: Main parameters for knots.

Galaxy	Class	Diffuse Luminosity ergs s^{-1} ($\times 10^{37}$)	Knot	log(Hα) ergs s^{-1}	Mass $M_\odot$ ($\times 10^8$)	Distance to centre (pc)	Radius (pc)	Ellipticity
(1)	(2)	(3)	(4)	(5)	(6)	(7)	(8)	(9)
COSMOS-001	1	0	1	40.6	2.5	0	1349	0.7
COSMOS-002	1.5	564.00	1	39.1	0.1	1168	542	0.5
COSMOS-003	1.5	35.59	1	40.0	6.9	115	1704	0.4
COSMOS-004	1	0	1	39.7	5.6	0	1331	0.0
COSMOS-005	4	4179.34	1	38.9	0.5	2945	618	0.6
			2	38.9	0.4	980	431	0.8
			3	38.8	0.4	2288	483	0.4
			4	38.6	0.2	441	284	0.2
COSMOS-006	2	2744.70	1	39.8	7.9	1132	1226	0.4
			2	39.2	2.2	2867	686	0.8
COSMOS-007	1	0	1	39.8	6.0	0	1437	0.2
COSMOS-008	1	0	1	39.1	1.2	0	588	0.1
COSMOS-009	1	0	1	38.4	0.5	0	641	0.7
COSMOS-010	1.5	0.11	1	39.3	2.3	488	1046	0.6
COSMOS-011	3	9819.92	1	39.6	2.0	774	493	0.5
			2	39.2	0.9	745	345	0.2
			3	39.1	0.7	1319	331	0.5
COSMOS-012	2	128.86	1	99.0	0.0	275	41	0.5
			2	99.0	0.0	38	41	0.3
COSMOS-013	1	0	1	39.6	5.9	0	1246	0.4
COSMOS-014	1	0	1	40.8	7.3	0	2064	0.4
COSMOS-016	1	0	1	39.9	5.3	0	1477	0.4
COSMOS-017	1	0	1	39.4	1.4	0	1086	0.3
COSMOS-018	1	0	1	40.4	4.8	0	1496	0.6
COSMOS-019	2	1773.15	1	99.0	0.1	1484	281	0.5
			2	99.0	0.3	53	390	0.4
COSMOS-020	1	0	1	40.5	1.8	0	1186	0.1
COSMOS-021	4	169.72	1	38.6	0.1	1134	391	0.1
			2	38.6	0.1	807	429	0.6
			3	38.4	0.1	668	365	0.6

Table B.1: continued.

Galaxy	Class	Diffuse Luminosity ergs s^{-1} ($\times 10^{37}$)	Knot	log(Hα) ergs s^{-1}	Mass $M_\odot$ ($\times 10^8$)	Distance to center (pc)	Radius (pc)	Ellipticity
(1)	(2)	(3)	(4)	(5)	(6)	(7)	(8)	(9)
			4	38.2	0.0	845	301	0.6
COSMOS-022	1	0	1	38.5	0.0	0	212	0.2
COSMOS-023	1	0	1	39.4	1.2	0	606	0.8
COSMOS-024	1.5	0.04	1	99.0	0.0	30	35	0.3
COSMOS-025	1.5	26.40	1	38.3	0.3	1493	433	0.2
COSMOS-026	1	0	1	40.3	22.8	0	2220	0.2
COSMOS-027	1	0	1	41.0	3.2	0	2189	0.3
COSMOS-028	4	58333.77	1	39.9	2.9	3206	1624	0.4
			2	39.0	0.4	4474	616	0.5
			3	38.6	0.2	4976	545	0.6
			4	38.3	0.1	5809	378	0.6
COSMOS-029	1	0	1	39.7	1542.1	0	4189	0.2
COSMOS-030	1.5	284.76	1	39.0	0.7	954	477	0.4
COSMOS-031	1.5	67.78	1	38.9	0.6	987	602	0.9
COSMOS-032	2	4803.41	1	40.3	14.4	1076	1999	0.7
			2	39.3	1.8	6214	1066	0.4
COSMOS-033	1.5	14.83	1	39.2	1.8	0	1045	0.3
COSMOS-034	1.5	4.33	1	38.2	0.1	194	479	0.3
COSMOS-035	1	0	1	39.7	3.9	0	970	0.3
COSMOS-036	2	0.12	1	99.0	0.0	315	140	0.3
			2	99.0	0.0	155	113	0.3
COSMOS-037	1	0	1	40.2	8.7	0	1941	0.1
COSMOS-038	1.5	528.62	1	39.3	0.3	1950	784	0.5
COSMOS-039	1	0	1	40.2	0.7	0	644	0.0
COSMOS-040	1.5	42.02	1	38.7	0.7	614	752	0.7
COSMOS-041	1.5	4903.34	1	99.0	1.2	369	607	0.7
COSMOS-042	1.5	0.70	1	38.0	0.1	892	525	0.6
COSMOS-043	1.5	2333.31	1	39.6	4.2	678	882	0.6
COSMOS-044	1.5	11.98	1	40.5	23.3	910	2689	0.7
COSMOS-045	1.5	383.59	1	39.2	2.4	271	932	0.9

Table B.1: continued.

Galaxy	Class	Diffuse Luminosity ergs s^{-1} ($\times 10^{37}$)	Knot	log(Hα) ergs s^{-1}	Mass $M_\odot$ ($\times 10^8$)	Distance to center (pc)	Radius (pc)	Ellipticity
(1)	(2)	(3)	(4)	(5)	(6)	(7)	(8)	(9)
COSMOS-046	1	0	1	40.1	2.9	0	1227	0.4
COSMOS-047	1	0	1	39.5	3.9	0	1650	0.8
COSMOS-048	1	0	1	40.7	2.8	0	2208	0.6
COSMOS-049	1	0	1	38.4	0.0	0	503	0.5
COSMOS-050	1	0	1	39.8	10.3	0	1577	0.5
COSMOS-051	1.5	1.58	1	37.9	0.1	530	242	0.6
COSMOS-052	1	0	1	38.1	0.1	0	449	0.4
COSMOS-053	1	0	1	40.2	1.2	0	1921	0.3
COSMOS-054	2	174.66	1	38.9	0.3	261	536	0.7
			2	38.5	0.2	2479	427	0.5
COSMOS-055	1	0	1	39.6	24.2	0	1255	0.3
COSMOS-056	3	13.63	1	38.0	0.1	419	253	0.7
			2	38.0	0.1	618	222	0.2
			3	37.9	0.1	978	229	0.3
COSMOS-057	1	0	1	39.9	4.7	0	1623	0.4
COSMOS-058	2	975.98	1	99.0	0.0	878	148	0.3
			2	99.0	0.0	746	118	0.4
COSMOS-059	1	0	1	40.4	9.0	0	2403	0.5
COSMOS-060	1	0	1	40.1	6.4	0	1882	0.5
COSMOS-061	1.5	11953.53	1	40.1	9.4	747	1302	0.4
COSMOS-062	3	45.93	1	99.0	0.0	176	61	0.4
			2	99.0	0.0	64	43	0.7
			3	99.0	0.0	56	46	0.4
COSMOS-063	1	0	1	39.7	2.9	0	1205	0.6
COSMOS-064	1.5	99.0	1	99.0	0.7	502	915	0.2
COSMOS-065	1.5	174.96	1	39.6	3.1	11560	1908	0.7
COSMOS-066	1	0	1	40.8	2.3	0	2512	0.6
COSMOS-067	1	0	1	39.7	2.7	0	1025	0.2
COSMOS-068	2	15257.92	1	38.6	0.5	4741	843	0.4
			2	39.8	3.1	1373	1322	0.2

Table B.1: continued.

Galaxy	Class	Diffuse Luminosity ergs s^{-1} ($\times 10^{37}$)	Knot	log(Hα) ergs s^{-1}	Mass $M_\odot$ ($\times 10^8$)	Distance to center (pc)	Radius (pc)	Ellipticity
(1)	(2)	(3)	(4)	(5)	(6)	(7)	(8)	(9)
COSMOS-069	1.5	3.99	1	39.6	1.6	273	1766	0.5
COSMOS-070	1.5	77.18	1	39.4	0.6	1032	1223	0.3
COSMOS-071	2	1929.06	1	39.6	2.2	0	909	0.7
			2	39.2	0.8	2454	570	0.4
COSMOS-072	1	0	1	37.8	0.1	0	186	0.5
COSMOS-073	3	3086.70	1	39.6	1.9	506	1427	0.6
			2	38.4	0.2	5230	686	0.3
			3	38.3	0.2	5165	668	0.4
COSMOS-074	1.5	106.65	1	39.9	1.7	833	1757	0.2
COSMOS-075	1.5	2.99	1	38.9	0.3	259	1002	0.6
COSMOS-076	1.5	29.11	1	99.0	0.0	156	203	0.2
COSMOS-077	1	0	1	39.3	1.4	0	1019	0.7
COSMOS-078	1	0	1	40.5	19.7	0	2186	0.2
COSMOS-079	1	0	1	40.1	11.8	0	1574	0.1
COSMOS-080	1	0	1	40.1	4.0	0	1491	0.6
COSMOS-081	1.5	70.78	1	39.9	5.4	486	1649	0.8
COSMOS-082	3	67132.45	1	39.1	0.9	2195	614	0.3
			2	40.4	10.6	601	878	0.6
			3	38.8	0.3	2430	230	0.5
COSMOS-083	2	38.51	1	39.4	1.6	329	588	0.4
			2	38.5	0.2	1075	286	0.1
COSMOS-084	3	8762.42	1	38.7	0.2	2408	522	0.3
			2	39.1	0.4	1031	288	0.7
			3	39.0	0.3	487	284	0.8
COSMOS-085	4	1455.03	1	38.1	0.2	6363	505	0.5
			2	38.6	0.2	3555	510	0.7
			3	39.1	0.7	2154	865	0.1
			4	38.8	0.4	369	629	0.8
COSMOS-86	1	0	1	39.8	4.7	0	1667	0.2
COSMOS-87	1	0	1	40.3	4.3	0	2038	0.5

Table B.1: continued.

Galaxy	Class	Diffuse Luminosity ergs s^{-1} ($\times 10^{37}$)	Knot	log(Hα) ergs s^{-1}	Mass $M_\odot$ ($\times 10^8$)	Distance to center (pc)	Radius (pc)	Ellipticity
(1)	(2)	(3)	(4)	(5)	(6)	(7)	(8)	(9)
COSMOS-88	1	0	1	40.2	3.4	0	1361	0.3
COSMOS-89	4	255.92	1	99.0	0.0	545	93	0.4
			2	99.0	0.0	13	54	0.2
			3	99.0	0.0	423	54	0.2
			4	99.0	0.0	92	21	0.1
COSMOS-90	1.5	177.62	1	39.6	3.6	122	952	0.5
COSMOS-91	3	605.30	1	38.2	0.2	1653	293	0.1
			2	38.8	0.5	1072	353	0.6
			3	38.7	0.5	116	347	0.7
COSMOS-92	1	0	1	40.4	2.9	0	2061	0.2
COSMOS-93	1.5	2101.88	1	39.4	4.2	1461	754	0.8
COSMOS-94	1	0	1	39.7	2.3	0	1485	0.3
COSMOS-95	1.5	35.12	1	38.4	0.2	3596	686	0.3
COSMOS-96	1	0	1	39.6	1.6	0	942	0.4
COSMOS-97	2	51715.19	1	39.8	2.2	1929	1148	0.6
			2	39.8	0.3	8545	414	0.3
COSMOS-98	2	6020.30	1	38.9	0.6	3543	504	0.9
			2	38.9	0.4	1998	400	0.3
COSMOS-99	1	0	1	39.4	1.0	0	744	0.4
COSMOS-100	2	498.85	1	40.0	5.8	2972	2062	0.9
			2	40.0	1.4	3140	1037	0.6
COSMOS-102	1.5	26.12	1	99.0	0.0	845	313	0.1
COSMOS-103	1	0	1	40.2	5.1	0	2219	0.4
COSMOS-104	4	30.91	1	99.0	0.0	22	47	0.2
			2	99.0	0.0	171	40	0.4
			3	99.0	0.0	58	31	0.6
			4	99.0	0.0	159	40	0.4
COSMOS-105	1.5	594.04	1	39.8	1.4	716	1912	0.8
COSMOS-106	1	0	1	39.4	1.1	0	915	0.6
COSMOS-107	3	140.06	1	39.1	0.9	767	1313	0.5

Table B.1: continued.

Galaxy	Class	Diffuse Luminosity ergs s^{-1} ($\times 10^{37}$)	Knot	log(Hα) ergs s^{-1}	Mass $M_\odot$ ($\times 10^8$)	Distance to center (pc)	Radius (pc)	Ellipticity
(1)	(2)	(3)	(4)	(5)	(6)	(7)	(8)	(9)
			2	38.5	0.2	2599	530	0.5
			3	38.4	0.2	1904	530	0.5
COSMOS-108	1	0	1	39.8	4.5	0	1081	0.3
COSMOS-109	2	43.56	1	38.5	0.4	505	655	0.7
			2	38.5	0.4	1475	578	0.4
COSMOS-110	1	0	1	39.7	2.2	0	874	0.4
COSMOS-111	1.5	2251.62	1	39.8	4.9	122	1529	0.9
COSMOS-112	1.5	0.00	1	99.0	0.1	141	558	0.4
COSMOS-113	4	2834.22	1	38.6	0.6	4334	683	0.2
			2	38.5	0.4	4072	546	0.2
			3	38.5	0.4	2657	492	0.3
			4	39.1	1.2	436	802	0.8
COSMOS-114	1.5	1846.58	1	39.0	0.8	715	559	0.8
COSMOS-115	1	0	1	39.3	0.9	0	1111	0.7
COSMOS-116	1.5	0.03	1	99.0	0.0	24	101	0.6
COSMOS-117	1	0	1	38.6	0.4	0	253	0.3
COSMOS-118	1.5	313.69	1	39.0	1.0	1098	851	0.5
COSMOS-119	1	0	1	39.8	5.7	0	1315	0.2
COSMOS-120	1.5	120.92	1	39.7	4.4	1158	1767	0.5
COSMOS-121	1.5	190.74	1	39.1	0.5	704	909	0.2
COSMOS-122	1.5	25.00	1	39.0	0.1	346	805	0.3
COSMOS-123	1.5	5472.28	1	40.0	5.6	821	1375	0.4
COSMOS-124	1.5	139.00	1	37.9	0.1	647	181	0.6
COSMOS-125	4	20582.32	1	40.4	5.5	1479	1613	0.7
			2	39.5	0.7	2603	668	0.4
			3	38.4	0.1	3948	392	0.4
			4	39.6	1.0	3909	825	0.7
COSMOS-126	1	0	1	39.7	2.5	0	1253	0.2
COSMOS-127	1	0	1	39.2	1.2	0	670	0.8
COSMOS-128	1	0	1	40.2	2.7	0	1964	0.3

Table B.1: continued.

Galaxy	Class	Diffuse Luminosity ergs s^{-1} ($\times 10^{37}$)	Knot	log(Hα) ergs s^{-1}	Mass $M_\odot$ ($\times 10^8$)	Distance to center (pc)	Radius (pc)	Ellipticity
(1)	(2)	(3)	(4)	(5)	(6)	(7)	(8)	(9)
COSMOS-129	1	0	1	39.6	3.7	0	1322	0.3
COSMOS-130	1	0	1	40.9	4.4	0	2689	0.5
COSMOS-131	2	2405.32	1	38.9	0.1	2600	664	0.0
			2	38.9	0.5	1074	907	0.4
COSMOS-132	2	660.17	1	39.6	0.6	873	948	0.8
			2	39.6	0.1	1919	373	0.3
COSMOS-133	1	0	1	40.4	3.7	0	1672	0.5
COSMOS-134	3	429.55	1	39.6	1.6	1132	1853	0.7
			2	38.8	0.3	5118	987	0.6
			3	38.8	0.3	3778	899	0.6
COSMOS-135	2	4558.17	1	99.0	0.1	302	213	0.6
			2	99.0	0.0	643	123	0.9
COSMOS-136	1.5	27.66	1	39.2	2.3	458	1014	0.8
COSMOS-137	1.5	127.31	1	40.9	7.5	2050	3134	0.7
COSMOS-138	1	0	1	40.3	11.0	0	2013	0.4
COSMOS-139	1.5	100.13	1	38.6	0.2	197	457	0.7
COSMOS-140	4	83670.61	1	40.1	4.4	3889	2337	0.2
			2	39.7	1.6	3997	1295	0.4
			3	39.5	0.9	2316	600	0.4
			4	38.9	0.3	4948	419	0.3
COSMOS-141	1	0	1	40.6	0.0	0	1908	0.4
COSMOS-142	1	0	1	39.8	2.5	0	1171	0.7
COSMOS-143	3	1140.49	1	99.0	0.1	472	173	0.4
			2	99.0	0.2	418	222	0.1
			3	99.0	0.0	737	114	0.1
COSMOS-144	4	3982.06	1	39.1	0.8	2942	987	0.4
			2	39.0	0.7	2638	1039	0.2
			3	39.0	0.6	2378	734	0.1
			4	39.0	0.6	1347	734	0.8
COSMOS-145	1	0	1	40.1	11.2	0	1437	0.6

Table B.1: continued.

Galaxy	Class	Diffuse Luminosity ergs s^{-1} ($\times 10^{37}$)	Knot	log(Hα) ergs s^{-1}	Mass $M_\odot$ ($\times 10^8$)	Distance to center (pc)	Radius (pc)	Ellipticity
(1)	(2)	(3)	(4)	(5)	(6)	(7)	(8)	(9)
COSMOS-146	1.5	38.93	1	38.8	0.7	85	512	0.5
COSMOS-147	1.5	1685.18	1	39.3	0.9	1137	548	0.2
COSMOS-148	1.5	130.88	1	38.4	0.2	531	213	0.2
COSMOS-149	1.5	0.29	1	99.0	0.1	41	337	0.3
COSMOS-150	1	0	1	38.0	3.0	0	2327	0.5
COSMOS-151	2	1154.40	1	40.2	2.5	9466	3447	0.8
			2	40.2	0.9	1816	2092	0.5
COSMOS-152	1	0	1	40.3	14.9	0	2050	0.8
COSMOS-153	1	0	1	39.7	5.2	0	1187	0.4
COSMOS-154	1	0	1	39.1	1.0	0	800	0.5
COSMOS-155	1	0	1	37.9	0.0	0	104	0.2
COSMOS-156	4	102269.29	1	99.0	0.3	1160	328	0.4
			2	99.0	0.1	411	47	0.2
			3	99.0	0.1	2132	219	0.3
			4	99.0	0.1	1674	135	0.3
COSMOS-157	1	0	1	39.4	0.4	0	741	0.4
COSMOS-158	1	0	1	39.7	4.8	0	1366	0.5
COSMOS-159	1.5	9.31	1	38.8	0.3	826	848	0.4
COSMOS-160	1	0	1	39.8	6.6	0	1340	0.2
COSMOS-161	2	778.43	1	38.8	0.3	2272	501	0.8
			2	38.8	1.0	2379	870	0.4
COSMOS-162	2	1825.36	1	39.3	0.7	1670	770	0.4
			2	39.3	0.5	1436	660	0.6
COSMOS-163	1.5	8221.43	1	39.9	5.3	1175	983	0.5
COSMOS-164	1	0	1	41.0	9.9	0	1918	0.5
COSMOS-165	1.5	0.08	1	39.2	0.6	249	877	0.5
COSMOS-166	2	353.85	1	38.4	0.2	565	316	0.3
			2	38.4	0.3	1068	452	0.6
COSMOS-167	2	192.92	1	38.4	0.3	705	304	0.6
			2	38.4	0.2	978	279	0.8

Table B.1: continued.

Galaxy	Class	Diffuse Luminosity ergs s^{-1} ($\times 10^{37}$)	Knot	log(Hα) ergs s^{-1}	Mass $M_\odot$ ($\times 10^8$)	Distance to center (pc)	Radius (pc)	Ellipticity
(1)	(2)	(3)	(4)	(5)	(6)	(7)	(8)	(9)
COSMOS-168	1.5	10.20	1	38.9	0.6	503	787	0.8
COSMOS-169	2	94.49	1	38.8	0.6	643	295	0.2
			2	38.8	0.3	215	218	0.6
COSMOS-170	1.5	41.87	1	39.0	0.5	2132	1110	0.5
COSMOS-171	1.5	30.78	1	40.2	20.0	1408	2317	0.7
COSMOS-172	1.5	334.83	1	39.6	3.4	597	1319	0.7
COSMOS-173	4	115221.11	1	40.2	6.3	2644	1523	0.6
			2	40.2	5.8	828	1362	0.4
			3	39.3	0.7	4841	594	0.3
			4	39.1	0.5	2481	671	0.6
COSMOS-174	1	0	1	39.4	3.0	0	1057	0.3
COSMOS-175	1.5	32430.25	1	40.0	5.9	110	719	0.7
COSMOS-176	2	2285.74	1	38.7	0.3	2494	415	0.7
			2	38.7	1.3	341	727	0.7
COSMOS-177	2	1516.45	1	38.9	0.1	1469	438	0.3
			2	38.9	0.4	610	501	0.0
COSMOS-178	1.5	40.61	1	40.3	6.9	918	2450	0.2
COSMOS-179	2	212.17	1	39.7	2.4	199	1151	0.8
			2	39.7	0.1	2082	330	0.2
COSMOS-180	1.5	9172.64	1	39.4	1.3	614	427	0.0
COSMOS-181	2	3503.79	1	39.0	0.9	150	700	0.5
			2	39.0	0.1	1623	293	0.3
COSMOS-182	1	0	1	37.7	0.0	0	99	0.4
COSMOS-183	1.5	27.74	1	39.5	2.2	745	1270	0.7
COSMOS-184	1.5	21.42	1	38.5	6.0	328	639	0.5
COSMOS-185	1.5	4.01	1	39.1	0.8	578	876	0.8
COSMOS-186	1.5	33499.50	1	99.0	0.6	432	1247	0.1
COSMOS-187	1.5	1.99	1	99.0	0.0	1009	111	0.2
COSMOS-188	1.5	21.65	1	39.5	1.1	583	949	0.6
COSMOS-189	2	1166.68	1	38.5	0.4	1965	455	0.4

Table B.1: continued.

Galaxy	Class	Diffuse Luminosity ergs s^{-1} ($\times 10^{37}$)	Knot	log(Hα) ergs s^{-1}	Mass $M_\odot$ ($\times 10^8$)	Distance to center (pc)	Radius (pc)	Ellipticity
(1)	(2)	(3)	(4)	(5)	(6)	(7)	(8)	(9)
			2	38.5	0.3	1004	279	0.2
COSMOS-190	1	0	1	39.0	0.1	0	408	0.5
COSMOS-191	1.5	0.97	1	39.9	3.2	821	2261	0.1
COSMOS-192	1	0	1	40.4	12.5	0	2092	0.4
COSMOS-193	2	58.82	1	39.2	1.5	661	957	0.4
			2	39.2	0.3	1706	480	0.4
COSMOS-194	1.5	29.21	1	38.2	0.2	1986	398	0.4
COSMOS-195	1	0	1	39.6	1.0	0	1228	0.5
COSMOS-196	1.5	1.72	1	99.0	0.0	214	163	0.2
COSMOS-197	1.5	338.70	1	38.7	0.1	3045	523	0.4
COSMOS-198	1	0	1	39.9	4.5	0	1396	0.5
COSMOS-199	1.5	0.07	1	99.0	0.0	29	35	0.2
COSMOS-200	3	8.40	1	39.3	0.9	191	1727	0.1
			2	38.7	0.2	3013	730	0.2
			3	38.5	0.2	4518	631	0.5
COSMOS-201	1.5	0.66	1	40.0	7.0	581	2115	0.3
COSMOS-202	1	0	1	39.6	1.5	0	1378	0.5
COSMOS-203	1.5	665.27	1	39.2	6.7	909	932	0.6
COSMOS-204	1	0	1	40.7	8.9	0	2003	0.3
COSMOS-205	1	0	1	39.5	2.7	0	1266	0.5
COSMOS-206	1	0	1	38.7	1.0	0	378	0.3
COSMOS-207	1.5	1149.78	1	40.2	2.3	429	1511	0.8
COSMOS-208	1.5	1.33	1	99.0	0.1	144	176	0.6
COSMOS-209	1	0	1	40.3	10.6	0	2413	0.8
COSMOS-210	1	0	1	38.6	0.6	0	491	0.4
COSMOS-211	1.5	38.77	1	99.0	0.0	295	134	0.5
COSMOS-212	1	0	1	39.4	1.5	0	1088	0.5
COSMOS-213	1.5	1532.84	1	39.2	0.8	274	940	0.7
COSMOS-214	1	0	1	39.0	0.8	0	798	0.3
COSMOS-215	1	0	1	40.3	1.1	0	1213	0.4

Table B.1: continued.

Galaxy	Class	Diffuse Luminosity ergs s^{-1} ($\times 10^{37}$)	Knot	log(Hα) ergs s^{-1}	Mass $M_\odot$ ($\times 10^8$)	Distance to center (pc)	Radius (pc)	Ellipticity
(1)	(2)	(3)	(4)	(5)	(6)	(7)	(8)	(9)
COSMOS-216	2	440.66	1	99.0	0.0	1269	164	0.2
			2	99.0	0.0	783	128	0.2
COSMOS-217	1.5	0.40	1	99.0	0.0	29	329	0.4
COSMOS-218	1	0	1	38.3	0.1	0	232	0.8
COSMOS-219	1.5	13.43	1	38.7	0.2	693	881	0.5
COSMOS-220	1.5	63.05	1	38.1	0.1	3993	323	0.4

(1) Object name (ordered by RA), (2) knots classification, (3) Diffuse luminosity, (4) Knots number, (5) Hα luminosity, (6) Mass, (7) distance to the center of the galaxy, (8) Knot radius and (9) Knot ellipticity. For parameters where it was not possible to do an estimation, we give the value -99.0.

Appendix C

Appendix C: Main parameters for galaxies in our sample at intermediate redshift

Main parameters for galaxies in our sample found in Chapter 4.

Table C.1: Main parameters for starburst galaxies at intermediate redshift]. (1) Target name, (2) RA, (3), DEC, (4) Redshift, and (5) Mass

Object	**RA**	**DEC**	$\mathbf{z}_{phot}$	Mass ($\times 10^8 M_\odot$)
(1)	(2)	(3)	(4)	(5)
COSMOS-0221	149.447	2.225	0.423	56.424
COSMOS-0222	149.451	2.459	0.502	32.049
COSMOS-0223	149.462	1.671	0.478	92.751
COSMOS-0224	149.464	2.590	0.556	43.907
COSMOS-0225	149.467	1.864	0.486	25.406
COSMOS-0226	149.468	2.301	0.423	54.008
COSMOS-0227	149.469	2.014	0.448	17.969
COSMOS-0228	149.471	1.690	0.503	29.258
COSMOS-0229	149.473	1.673	0.615	108.550
COSMOS-0230	149.474	2.578	0.446	19.252
COSMOS-0231	149.480	2.419	0.349	41.188
COSMOS-0232	149.480	2.455	0.336	19.966
COSMOS-0233	149.481	2.092	0.352	26.494
COSMOS-0234	149.483	1.995	0.758	255.010
COSMOS-0235	149.491	1.852	0.548	102.330
COSMOS-0236	149.494	1.861	0.556	31.468
COSMOS-0237	149.494	1.876	0.448	102.850
COSMOS-0238	149.495	2.527	0.557	24.942
COSMOS-0239	149.495	1.947	0.447	50.045
COSMOS-0240	149.495	1.870	0.555	23.010
COSMOS-0241	149.495	1.739	0.542	60.977
COSMOS-0242	149.495	2.703	0.484	194.400

Continued on next page

Table C.1 – *Continued from previous page*

Object	**RA**	**DEC**	$\mathbf{z}_{phot}$	Mass ($\times 10^8 M_\odot$)
				$M_\odot$
(1)	(2)	(3)	(4)	(5)
COSMOS-0243	149.496	1.877	0.554	166.440
COSMOS-0244	149.497	1.693	0.447	10.721
COSMOS-0245	149.497	2.135	0.423	66.796
COSMOS-0246	149.500	2.149	0.485	31.382
COSMOS-0247	149.500	2.547	0.469	7.289
COSMOS-0248	149.504	1.788	0.485	23.999
COSMOS-0249	149.504	1.811	0.545	132.450
COSMOS-0250	149.505	2.095	0.555	17.597
COSMOS-0251	149.506	2.860	0.485	35.596
COSMOS-0252	149.508	1.772	0.566	41.684
COSMOS-0253	149.511	1.889	0.553	232.210
COSMOS-0254	149.512	1.872	0.550	238.070
COSMOS-0255	149.515	2.432	0.444	23.964
COSMOS-0256	149.517	2.452	0.352	11.149
COSMOS-0257	149.518	2.425	0.556	68.554
COSMOS-0258	149.518	2.120	0.485	20.979
COSMOS-0259	149.519	1.956	0.558	30.566
COSMOS-0260	149.520	2.679	0.498	47.652
COSMOS-0261	149.522	1.657	0.366	42.579
COSMOS-0262	149.522	2.393	0.438	65.780
COSMOS-0263	149.523	2.283	0.422	730.470
COSMOS-0264	149.523	2.308	0.555	29.028
COSMOS-0265	149.527	2.121	0.564	51.711
COSMOS-0266	149.529	2.234	0.557	55.474
COSMOS-0267	149.529	2.333	0.552	60.633
COSMOS-0268	149.529	2.607	0.486	14.596
COSMOS-0269	149.531	1.994	0.485	145.590
COSMOS-0270	149.531	2.134	0.425	87.635
COSMOS-0271	149.531	2.565	0.352	57.044
COSMOS-0272	149.534	2.332	0.507	28.351
COSMOS-0273	149.534	2.832	0.502	12.774
COSMOS-0274	149.540	1.733	0.552	35.624
COSMOS-0275	149.540	1.890	0.554	67.127
COSMOS-0276	149.542	2.541	0.487	94.168
COSMOS-0277	149.542	2.456	0.486	41.388
COSMOS-0278	149.542	1.736	0.557	23.560
COSMOS-0279	149.542	2.547	0.450	21.532
COSMOS-0280	149.544	2.408	0.556	24.393
COSMOS-0281	149.546	2.695	0.423	30.868
COSMOS-0282	149.548	2.346	0.436	52.377
COSMOS-0283	149.548	2.482	0.486	93.653
COSMOS-0284	149.549	2.106	0.435	17.882
COSMOS-0285	149.551	2.706	0.422	29.612
COSMOS-0286	149.551	2.444	0.422	64.351

Continued on next page

Table C.1 – *Continued from previous page*

Object	**RA**	**DEC**	$\mathbf{z}_{phot}$	Mass ($\times 10^8 M_\odot$) $M_\odot$
(1)	(2)	(3)	(4)	(5)
COSMOS-0287	149.551	1.892	0.501	53.213
COSMOS-0288	149.554	2.460	0.375	201.600
COSMOS-0289	149.556	1.602	0.393	8.940
COSMOS-0290	149.556	2.823	0.423	6.101
COSMOS-0291	149.556	1.723	0.563	50.918
COSMOS-0292	149.558	2.336	0.484	11.664
COSMOS-0293	149.559	2.568	0.484	10.891
COSMOS-0294	149.561	2.072	0.486	114.580
COSMOS-0295	149.562	2.494	0.482	166.440
COSMOS-0296	149.562	2.103	0.675	133.300
COSMOS-0297	149.564	2.145	0.424	11.354
COSMOS-0298	149.564	2.514	0.486	38.771
COSMOS-0299	149.564	1.904	0.488	27.361
COSMOS-0300	149.565	2.818	0.556	42.991
COSMOS-0301	149.567	1.891	0.384	58.931
COSMOS-0302	149.568	2.101	0.557	72.738
COSMOS-0303	149.568	2.218	0.504	21.462
COSMOS-0304	149.569	1.889	0.486	33.715
COSMOS-0305	149.573	1.687	0.554	50.279
COSMOS-0306	149.574	1.688	0.484	28.165
COSMOS-0307	149.575	2.124	0.354	11.060
COSMOS-0308	149.582	2.642	0.424	15.886
COSMOS-0309	149.583	1.785	0.545	24.415
COSMOS-0310	149.583	1.777	0.763	478.830
COSMOS-0311	149.584	1.660	0.569	43.004
COSMOS-0312	149.585	2.560	0.834	504.800
COSMOS-0313	149.586	2.774	0.557	255.510
COSMOS-0314	149.587	2.270	0.430	12.493
COSMOS-0315	149.589	2.705	0.406	7.000
COSMOS-0316	149.589	2.700	0.394	25.145
COSMOS-0317	149.590	2.569	0.557	28.174
COSMOS-0318	149.590	2.700	0.487	30.156
COSMOS-0319	149.591	1.724	0.557	40.385
COSMOS-0320	149.595	2.489	0.354	16.518
COSMOS-0321	149.596	1.980	0.557	41.184
COSMOS-0322	149.598	1.995	0.502	15.303
COSMOS-0323	149.598	2.426	0.511	47.284
COSMOS-0324	149.598	2.028	0.487	4.902
COSMOS-0325	149.603	1.753	0.557	33.079
COSMOS-0326	149.604	1.992	0.702	493.100
COSMOS-0327	149.604	1.850	0.486	61.784
COSMOS-0328	149.604	2.475	0.431	26.495
COSMOS-0329	149.604	2.517	0.559	21.003
COSMOS-0330	149.607	1.870	0.762	*******

Continued on next page

Table C.1 – *Continued from previous page*

Object	**RA**	**DEC**	$\mathbf{z}_{phot}$	Mass ($\times 10^8 M_\odot$)
				$M_\odot$
(1)	(2)	(3)	(4)	(5)
COSMOS-0331	149.608	2.167	0.676	632.270
COSMOS-0332	149.609	2.238	0.552	102.990
COSMOS-0333	149.612	2.543	0.408	28.323
COSMOS-0334	149.614	2.118	0.556	62.338
COSMOS-0335	149.615	2.524	0.508	79.154
COSMOS-0336	149.617	2.833	0.366	23.836
COSMOS-0337	149.617	1.628	0.423	37.353
COSMOS-0338	149.618	2.585	0.553	196.380
COSMOS-0339	149.620	1.661	0.352	41.478
COSMOS-0340	149.621	1.719	0.735	*******
COSMOS-0341	149.621	1.826	0.560	19.794
COSMOS-0342	149.622	1.874	0.555	46.272
COSMOS-0343	149.622	2.698	0.552	4.879
COSMOS-0344	149.623	1.633	0.559	34.072
COSMOS-0345	149.628	2.151	0.555	54.413
COSMOS-0346	149.629	2.191	0.701	559.100
COSMOS-0347	149.629	2.192	0.701	818.390
COSMOS-0348	149.632	2.138	0.328	42.473
COSMOS-0349	149.633	2.372	0.440	74.893
COSMOS-0350	149.633	2.144	0.485	50.848
COSMOS-0351	149.636	2.599	0.366	24.470
COSMOS-0352	149.643	2.338	0.497	206.850
COSMOS-0353	149.644	2.026	0.341	66.606
COSMOS-0354	149.646	2.304	0.564	13.167
COSMOS-0355	149.646	2.374	0.485	23.043
COSMOS-0356	149.646	1.629	0.551	23.827
COSMOS-0357	149.652	2.582	0.365	14.066
COSMOS-0358	149.653	2.229	0.556	27.668
COSMOS-0359	149.656	2.362	0.868	233.450
COSMOS-0360	149.656	2.733	0.423	84.912
COSMOS-0361	149.660	1.751	0.485	13.040
COSMOS-0362	149.663	2.607	0.487	30.632
COSMOS-0363	149.664	1.610	0.360	50.568
COSMOS-0364	149.669	2.827	0.607	102.140
COSMOS-0365	149.669	2.039	0.494	37.422
COSMOS-0366	149.670	1.973	0.486	38.685
COSMOS-0367	149.672	2.474	0.357	26.466
COSMOS-0368	149.672	2.193	0.507	15.959
COSMOS-0369	149.673	2.462	0.427	22.921
COSMOS-0370	149.674	1.657	0.424	24.778
COSMOS-0371	149.675	1.967	0.837	358.080
COSMOS-0372	149.677	1.609	0.488	200.990
COSMOS-0373	149.677	2.602	0.544	66.174
COSMOS-0374	149.679	2.288	0.423	67.772

Continued on next page

Table C.1 – *Continued from previous page*

Object	**RA**	**DEC**	$\mathbf{z}_{phot}$	Mass ($\times 10^8 M_\odot$) $M_\odot$
(1)	(2)	(3)	(4)	(5)
COSMOS-0375	149.679	2.171	0.449	12.457
COSMOS-0376	149.682	1.613	0.464	201.200
COSMOS-0377	149.685	1.674	0.555	48.428
COSMOS-0378	149.686	1.901	0.350	20.260
COSMOS-0379	149.688	2.040	0.486	60.070
COSMOS-0380	149.689	2.328	0.555	73.343
COSMOS-0381	149.690	1.637	0.486	57.148
COSMOS-0382	149.693	1.785	0.486	42.873
COSMOS-0383	149.693	1.784	0.485	118.010
COSMOS-0384	149.694	1.817	0.449	11.226
COSMOS-0385	149.697	2.247	0.554	78.398
COSMOS-0386	149.697	2.468	0.349	35.561
COSMOS-0387	149.702	2.102	0.556	50.668
COSMOS-0388	149.704	2.023	0.550	36.069
COSMOS-0389	149.710	2.697	0.485	30.903
COSMOS-0390	149.712	1.616	0.635	172.440
COSMOS-0391	149.712	2.572	0.615	102.920
COSMOS-0392	149.713	2.282	0.486	33.525
COSMOS-0393	149.713	2.108	0.558	65.357
COSMOS-0394	149.713	2.527	0.552	28.531
COSMOS-0395	149.722	1.803	0.354	38.524
COSMOS-0396	149.724	1.641	0.498	53.815
COSMOS-0397	149.725	2.655	0.486	65.553
COSMOS-0398	149.726	2.522	0.551	113.370
COSMOS-0399	149.726	2.737	0.487	71.652
COSMOS-0400	149.731	2.016	0.647	163.080
COSMOS-0401	149.731	2.086	0.547	30.479
COSMOS-0402	149.731	2.022	0.410	23.829
COSMOS-0403	149.731	1.790	0.320	11.626
COSMOS-0404	149.732	2.452	0.484	39.559
COSMOS-0405	149.732	2.445	0.372	63.761
COSMOS-0406	149.732	2.240	0.709	288.320
COSMOS-0407	149.732	2.293	0.746	199.450
COSMOS-0408	149.734	2.591	0.492	138.700
COSMOS-0409	149.736	2.004	0.556	25.650
COSMOS-0410	149.736	2.220	0.486	39.659
COSMOS-0411	149.737	1.977	0.509	27.997
COSMOS-0412	149.741	1.675	0.556	54.561
COSMOS-0413	149.743	2.819	0.497	43.391
COSMOS-0414	149.745	2.750	0.345	27.565
COSMOS-0415	149.745	2.466	0.343	63.498
COSMOS-0416	149.748	2.689	0.377	143.020
COSMOS-0417	149.758	2.330	0.450	5.733
COSMOS-0418	149.759	2.792	0.485	160.110

Continued on next page

Table C.1 – *Continued from previous page*

Object	**RA**	**DEC**	$\mathbf{z}_{phot}$	Mass ($\times 10^8 M_\odot$)
				$M_\odot$
(1)	(2)	(3)	(4)	(5)
COSMOS-0419	149.760	2.704	0.486	72.710
COSMOS-0420	149.761	1.775	0.790	753.180
COSMOS-0421	149.761	1.725	0.558	144.690
COSMOS-0422	149.762	2.005	0.439	15.202
COSMOS-0423	149.763	2.149	0.510	13.027
COSMOS-0424	149.765	2.695	0.535	10.066
COSMOS-0425	149.769	2.547	0.549	18.113
COSMOS-0426	149.769	2.835	0.556	94.931
COSMOS-0427	149.769	1.933	0.354	50.959
COSMOS-0428	149.770	2.391	0.712	184.720
COSMOS-0429	149.770	2.130	0.485	37.260
COSMOS-0430	149.771	2.804	0.555	437.600
COSMOS-0431	149.772	1.620	0.558	48.705
COSMOS-0432	149.772	2.026	0.661	183.300
COSMOS-0433	149.772	1.717	0.664	392.730
COSMOS-0434	149.773	2.698	0.556	70.574
COSMOS-0435	149.775	2.292	0.745	281.190
COSMOS-0436	149.776	2.324	0.558	40.182
COSMOS-0437	149.777	1.707	0.423	40.813
COSMOS-0438	149.781	2.673	0.449	15.047
COSMOS-0439	149.781	2.849	0.358	36.773
COSMOS-0440	149.782	2.591	0.484	19.129
COSMOS-0441	149.782	1.638	0.543	308.130
COSMOS-0442	149.787	2.846	0.546	43.776
COSMOS-0443	149.788	2.626	0.560	42.824
COSMOS-0444	149.789	1.630	0.555	303.580
COSMOS-0445	149.790	2.597	0.440	19.720
COSMOS-0446	149.790	2.046	0.677	228.770
COSMOS-0447	149.791	1.934	0.556	20.529
COSMOS-0448	149.792	2.589	0.485	94.178
COSMOS-0449	149.795	2.160	0.677	293.100
COSMOS-0450	149.796	1.944	0.437	63.502
COSMOS-0451	149.797	2.834	0.511	25.196
COSMOS-0452	149.797	2.528	0.447	30.568
COSMOS-0453	149.798	2.531	0.487	57.116
COSMOS-0454	149.799	2.830	0.489	73.238
COSMOS-0455	149.799	2.178	0.352	15.702
COSMOS-0456	149.800	2.345	0.557	150.880
COSMOS-0457	149.802	2.184	0.557	32.389
COSMOS-0458	149.803	2.184	0.556	127.920
COSMOS-0459	149.804	1.897	0.483	86.830
COSMOS-0460	149.806	2.657	0.366	34.907
COSMOS-0461	149.806	2.500	0.484	69.593
COSMOS-0462	149.807	2.179	0.551	15.162

Continued on next page

Table C.1 – *Continued from previous page*

Object	**RA**	**DEC**	$\mathbf{z}_{phot}$	Mass ($\times 10^8 M_\odot$) $M_\odot$
(1)	(2)	(3)	(4)	(5)
COSMOS-0463	149.808	2.593	0.484	32.958
COSMOS-0464	149.808	2.658	0.441	46.082
COSMOS-0465	149.808	1.637	0.449	49.748
COSMOS-0466	149.808	1.647	0.556	19.959
COSMOS-0467	149.812	2.196	0.484	28.121
COSMOS-0468	149.813	2.169	0.501	16.179
COSMOS-0469	149.816	2.513	0.423	56.117
COSMOS-0470	149.818	2.458	0.741	*******
COSMOS-0471	149.818	1.983	0.356	40.390
COSMOS-0472	149.818	2.863	0.427	47.498
COSMOS-0473	149.819	2.300	0.825	207.100
COSMOS-0474	149.819	1.782	0.547	68.707
COSMOS-0475	149.820	1.747	0.509	45.825
COSMOS-0476	149.820	2.305	0.422	18.147
COSMOS-0477	149.820	2.866	0.428	36.595
COSMOS-0478	149.823	1.638	0.543	198.340
COSMOS-0479	149.824	2.590	0.560	42.886
COSMOS-0480	149.825	2.194	0.553	18.737
COSMOS-0481	149.825	2.095	0.556	11.119
COSMOS-0482	149.825	2.576	0.351	32.438
COSMOS-0483	149.828	2.033	0.428	24.387
COSMOS-0484	149.830	2.721	0.549	50.742
COSMOS-0485	149.831	2.848	0.333	17.703
COSMOS-0486	149.831	2.393	0.487	21.634
COSMOS-0487	149.833	1.674	0.556	65.056
COSMOS-0488	149.834	1.590	0.490	18.525
COSMOS-0489	149.835	2.261	0.743	206.100
COSMOS-0490	149.837	1.802	0.486	139.770
COSMOS-0491	149.839	2.592	0.556	23.131
COSMOS-0492	149.839	2.591	0.504	52.243
COSMOS-0493	149.840	2.152	0.355	84.168
COSMOS-0494	149.841	2.087	0.688	165.360
COSMOS-0495	149.842	1.605	0.554	51.146
COSMOS-0496	149.842	2.106	0.557	44.296
COSMOS-0497	149.843	2.196	0.343	30.980
COSMOS-0498	149.843	1.736	0.487	50.475
COSMOS-0499	149.848	1.823	0.446	132.630
COSMOS-0500	149.849	2.301	0.344	51.153
COSMOS-0501	149.850	1.829	0.486	55.499
COSMOS-0502	149.851	2.481	0.422	84.046
COSMOS-0503	149.851	2.447	0.497	39.459
COSMOS-0504	149.852	2.673	0.407	99.321
COSMOS-0505	149.853	2.789	0.598	75.239
COSMOS-0506	149.853	2.748	0.568	228.190

Continued on next page

Table C.1 – *Continued from previous page*

Object	**RA**	**DEC**	$\mathbf{z}_{phot}$	Mass ($\times 10^8 M_\odot$)
				$M_\odot$
(1)	(2)	(3)	(4)	(5)
COSMOS-0507	149.853	2.747	0.553	19.417
COSMOS-0508	149.853	2.403	0.668	453.490
COSMOS-0509	149.853	2.210	0.479	45.625
COSMOS-0510	149.854	1.861	0.497	53.950
COSMOS-0511	149.854	2.759	0.480	152.100
COSMOS-0512	149.854	1.655	0.351	46.392
COSMOS-0513	149.856	2.651	0.486	102.970
COSMOS-0514	149.857	1.630	0.556	54.631
COSMOS-0515	149.857	2.478	0.492	24.192
COSMOS-0516	149.857	2.246	0.345	25.525
COSMOS-0517	149.857	1.970	0.424	14.385
COSMOS-0518	149.860	1.759	0.736	227.680
COSMOS-0519	149.862	2.069	0.417	69.366
COSMOS-0520	149.862	1.737	0.551	29.103
COSMOS-0521	149.863	2.069	0.423	50.219
COSMOS-0522	149.865	2.168	0.603	165.140
COSMOS-0523	149.866	1.964	0.431	7.580
COSMOS-0524	149.871	1.785	0.560	24.335
COSMOS-0525	149.871	2.001	0.766	511.490
COSMOS-0526	149.871	1.727	0.555	8.146
COSMOS-0527	149.872	1.962	0.423	42.615
COSMOS-0528	149.872	1.964	0.428	17.881
COSMOS-0529	149.873	1.945	0.550	329.280
COSMOS-0530	149.873	1.943	0.555	41.425
COSMOS-0531	149.873	1.670	0.429	13.869
COSMOS-0532	149.875	1.731	0.619	180.240
COSMOS-0533	149.875	1.910	0.547	45.111
COSMOS-0534	149.876	2.438	0.426	154.930
COSMOS-0535	149.876	2.649	0.551	110.350
COSMOS-0536	149.878	2.374	0.550	162.440
COSMOS-0537	149.878	1.665	0.423	54.348
COSMOS-0538	149.879	1.765	0.556	35.455
COSMOS-0539	149.880	1.812	0.552	48.364
COSMOS-0540	149.881	2.664	0.442	30.961
COSMOS-0541	149.882	2.614	0.763	793.300
COSMOS-0542	149.882	2.740	0.554	67.283
COSMOS-0543	149.884	2.407	0.427	69.974
COSMOS-0544	149.885	1.833	0.870	710.370
COSMOS-0545	149.885	2.505	0.552	175.120
COSMOS-0546	149.887	2.244	0.486	54.544
COSMOS-0547	149.888	2.653	0.351	10.557
COSMOS-0548	149.890	2.063	0.556	20.977
COSMOS-0549	149.892	2.426	0.350	21.084
COSMOS-0550	149.892	2.129	0.634	136.490

Continued on next page

Table C.1 – *Continued from previous page*

Object	**RA**	**DEC**	$\mathbf{z}_{phot}$	Mass ($\times 10^8 M_\odot$) $M_\odot$
(1)	(2)	(3)	(4)	(5)
COSMOS-0551	149.893	1.767	0.542	79.209
COSMOS-0552	149.894	1.704	0.449	14.950
COSMOS-0553	149.895	2.696	0.485	29.028
COSMOS-0554	149.896	2.172	0.350	70.790
COSMOS-0555	149.899	1.815	0.556	66.161
COSMOS-0556	149.901	2.674	0.485	24.894
COSMOS-0557	149.902	2.184	0.774	*******
COSMOS-0558	149.904	2.491	0.556	82.388
COSMOS-0559	149.904	1.896	0.407	25.101
COSMOS-0560	149.905	2.436	0.424	30.834
COSMOS-0561	149.905	2.555	0.488	57.242
COSMOS-0562	149.909	2.027	0.509	27.021
COSMOS-0563	149.910	2.576	0.438	19.802
COSMOS-0564	149.911	1.824	0.556	22.201
COSMOS-0565	149.912	2.631	0.509	45.952
COSMOS-0566	149.912	2.049	0.488	36.962
COSMOS-0567	149.913	2.282	0.354	37.670
COSMOS-0568	149.916	2.689	0.557	53.882
COSMOS-0569	149.917	2.726	0.407	41.305
COSMOS-0570	149.917	2.252	0.856	264.260
COSMOS-0571	149.920	2.429	0.570	112.120
COSMOS-0572	149.921	2.488	0.429	97.167
COSMOS-0573	149.922	2.156	0.557	94.484
COSMOS-0574	149.923	2.138	0.350	17.909
COSMOS-0575	149.923	2.618	0.501	31.125
COSMOS-0576	149.924	2.696	0.557	161.970
COSMOS-0577	149.925	1.972	0.423	43.224
COSMOS-0578	149.927	1.662	0.389	16.604
COSMOS-0579	149.930	2.642	0.556	286.110
COSMOS-0580	149.930	2.641	0.510	60.025
COSMOS-0581	149.934	1.909	0.422	26.053
COSMOS-0582	149.935	2.792	0.507	27.563
COSMOS-0583	149.935	2.802	0.399	83.003
COSMOS-0584	149.937	2.793	0.509	36.509
COSMOS-0585	149.937	2.295	0.485	27.762
COSMOS-0586	149.938	2.497	0.553	147.190
COSMOS-0587	149.938	2.716	0.552	86.611
COSMOS-0588	149.939	2.496	0.556	37.392
COSMOS-0589	149.941	2.375	0.556	37.299
COSMOS-0590	149.943	1.830	0.511	57.367
COSMOS-0591	149.943	1.700	0.559	67.197
COSMOS-0592	149.946	2.742	0.557	47.823
COSMOS-0593	149.946	2.162	0.554	53.992
COSMOS-0594	149.946	2.757	0.556	25.662

Continued on next page

Table C.1 – *Continued from previous page*

Object	**RA**	**DEC**	$\mathbf{z}_{phot}$	Mass ($\times 10^8 M_\odot$)
				$M_\odot$
(1)	(2)	(3)	(4)	(5)
COSMOS-0595	149.947	2.459	0.782	686.210
COSMOS-0596	149.951	2.647	0.485	67.160
COSMOS-0597	149.952	1.736	0.559	67.848
COSMOS-0598	149.952	2.172	0.423	69.589
COSMOS-0599	149.952	2.588	0.566	90.030
COSMOS-0600	149.953	2.478	0.422	13.127
COSMOS-0601	149.953	1.774	0.739	486.190
COSMOS-0602	149.954	2.790	0.796	*******
COSMOS-0603	149.956	2.294	0.731	202.180
COSMOS-0604	149.958	2.282	0.487	100.380
COSMOS-0605	149.959	2.180	0.361	25.425
COSMOS-0606	149.961	2.072	0.393	8.026
COSMOS-0607	149.965	1.943	0.422	11.142
COSMOS-0608	149.967	1.969	0.422	21.111
COSMOS-0609	149.967	2.440	0.423	230.650
COSMOS-0610	149.968	2.660	0.429	26.864
COSMOS-0611	149.968	1.617	0.557	49.860
COSMOS-0612	149.968	2.567	0.447	94.750
COSMOS-0613	149.968	1.617	0.554	65.074
COSMOS-0614	149.971	1.773	0.480	47.446
COSMOS-0615	149.973	2.522	0.484	11.241
COSMOS-0616	149.977	2.382	0.439	33.109
COSMOS-0617	149.977	2.646	0.550	52.387
COSMOS-0618	149.978	2.357	0.547	93.680
COSMOS-0619	149.978	2.460	0.497	26.462
COSMOS-0620	149.978	1.964	0.422	72.379
COSMOS-0621	149.979	2.586	0.555	245.700
COSMOS-0622	149.980	2.322	0.352	94.079
COSMOS-0623	149.983	2.520	0.422	7.930
COSMOS-0624	149.983	1.872	0.485	37.258
COSMOS-0625	149.985	1.776	0.486	51.104
COSMOS-0626	149.986	2.327	0.849	865.190
COSMOS-0627	149.988	2.225	0.352	12.285
COSMOS-0628	149.989	1.638	0.776	548.690
COSMOS-0629	149.989	2.409	0.485	34.678
COSMOS-0630	149.991	2.456	0.436	117.030
COSMOS-0631	149.991	1.865	0.341	33.265
COSMOS-0632	149.992	1.806	0.465	92.128
COSMOS-0633	149.993	1.960	0.495	11.457
COSMOS-0634	149.993	2.403	0.350	19.753
COSMOS-0635	149.993	1.911	0.558	16.747
COSMOS-0636	149.993	1.872	0.485	43.415
COSMOS-0637	149.995	1.713	0.573	353.680
COSMOS-0638	149.998	2.230	0.551	22.200

Continued on next page

Table C.1 – *Continued from previous page*

Object	**RA**	**DEC**	$\mathbf{z}_{phot}$	Mass ($\times 10^8 M_\odot$) $M_\odot$
(1)	(2)	(3)	(4)	(5)
COSMOS-0639	150.000	2.326	0.508	6.413
COSMOS-0640	150.000	2.456	0.422	35.151
COSMOS-0641	150.000	2.469	0.437	48.771
COSMOS-0642	150.001	2.184	0.334	18.304
COSMOS-0643	150.002	2.170	0.556	31.311
COSMOS-0644	150.004	1.674	0.557	30.702
COSMOS-0645	150.004	1.607	0.448	10.685
COSMOS-0646	150.004	1.760	0.446	15.692
COSMOS-0647	150.008	2.186	0.479	251.460
COSMOS-0648	150.011	2.662	0.511	18.832
COSMOS-0649	150.011	1.741	0.557	52.831
COSMOS-0650	150.012	2.640	0.546	57.532
COSMOS-0651	150.015	2.457	0.497	18.028
COSMOS-0652	150.016	2.223	0.557	15.076
COSMOS-0653	150.017	1.648	0.471	8.000
COSMOS-0654	150.018	2.049	0.872	799.190
COSMOS-0655	150.020	2.607	0.483	9.630
COSMOS-0656	150.021	1.766	0.831	701.630
COSMOS-0657	150.021	1.640	0.487	115.690
COSMOS-0658	150.022	1.604	0.557	96.657
COSMOS-0659	150.022	1.802	0.500	14.405
COSMOS-0660	150.025	2.062	0.343	16.762
COSMOS-0661	150.026	2.498	0.445	7.300
COSMOS-0662	150.028	2.047	0.329	16.016
COSMOS-0663	150.030	2.284	0.330	6.032
COSMOS-0664	150.031	2.285	0.347	5.300
COSMOS-0665	150.032	2.144	0.639	161.040
COSMOS-0666	150.032	1.936	0.557	76.512
COSMOS-0667	150.036	1.991	0.408	15.932
COSMOS-0668	150.040	2.584	0.555	125.830
COSMOS-0669	150.041	1.956	0.430	10.784
COSMOS-0670	150.042	2.208	0.436	25.712
COSMOS-0671	150.042	2.125	0.340	39.097
COSMOS-0672	150.043	2.798	0.428	68.262
COSMOS-0673	150.044	2.678	0.511	14.223
COSMOS-0674	150.047	2.139	0.731	246.850
COSMOS-0675	150.048	2.295	0.491	50.563
COSMOS-0676	150.049	2.805	0.559	68.740
COSMOS-0677	150.049	2.068	0.559	145.030
COSMOS-0678	150.049	2.440	0.435	425.110
COSMOS-0679	150.050	2.240	0.602	717.200
COSMOS-0680	150.052	2.595	0.696	385.520
COSMOS-0681	150.054	1.962	0.556	187.990
COSMOS-0682	150.055	2.888	0.426	5.692

Continued on next page

Table C.1 – *Continued from previous page*

Object	**RA**	**DEC**	$\mathbf{z}_{phot}$	Mass ($\times 10^8 M_\odot$)
				$M_\odot$
(1)	(2)	(3)	(4)	(5)
COSMOS-0683	150.057	2.778	0.406	19.174
COSMOS-0684	150.060	1.878	0.488	21.439
COSMOS-0685	150.060	1.974	0.336	17.386
COSMOS-0686	150.062	2.342	0.484	20.995
COSMOS-0687	150.065	1.866	0.499	25.929
COSMOS-0688	150.067	1.939	0.430	39.415
COSMOS-0689	150.067	2.359	0.668	221.280
COSMOS-0690	150.068	2.703	0.423	61.991
COSMOS-0691	150.070	2.258	0.543	19.940
COSMOS-0692	150.074	2.748	0.492	37.108
COSMOS-0693	150.077	1.720	0.556	28.125
COSMOS-0694	150.077	1.930	0.540	75.724
COSMOS-0695	150.079	2.013	0.556	29.476
COSMOS-0696	150.080	2.164	0.541	171.270
COSMOS-0697	150.080	1.937	0.438	117.980
COSMOS-0698	150.080	1.722	0.428	365.510
COSMOS-0699	150.081	1.968	0.556	19.894
COSMOS-0700	150.081	1.937	0.438	47.614
COSMOS-0701	150.081	1.686	0.559	100.540
COSMOS-0702	150.082	2.647	0.556	81.543
COSMOS-0703	150.084	1.881	0.554	38.054
COSMOS-0704	150.084	2.720	0.426	74.514
COSMOS-0705	150.087	2.369	0.353	9.544
COSMOS-0706	150.087	2.309	0.688	184.340
COSMOS-0707	150.088	2.377	0.441	20.153
COSMOS-0708	150.088	2.151	0.551	52.487
COSMOS-0709	150.089	1.808	0.521	318.060
COSMOS-0710	150.090	1.634	0.326	19.856
COSMOS-0711	150.092	2.702	0.405	33.168
COSMOS-0712	150.092	1.810	0.557	62.402
COSMOS-0713	150.094	2.504	0.752	*******
COSMOS-0714	150.094	1.910	0.844	305.920
COSMOS-0715	150.095	2.206	0.422	12.838
COSMOS-0716	150.096	1.694	0.555	23.255
COSMOS-0717	150.096	2.673	0.349	16.435
COSMOS-0718	150.096	2.558	0.436	75.486
COSMOS-0719	150.096	1.656	0.556	93.436
COSMOS-0720	150.100	2.020	0.555	37.945
COSMOS-0721	150.101	2.775	0.447	15.680
COSMOS-0722	150.101	1.641	0.331	3.299
COSMOS-0723	150.102	1.655	0.557	26.400
COSMOS-0724	150.102	2.826	0.550	21.924
COSMOS-0725	150.103	2.844	0.697	485.170
COSMOS-0726	150.103	2.390	0.485	39.208

Continued on next page

Table C.1 – *Continued from previous page*

Object	**RA**	**DEC**	$\mathbf{z}_{phot}$	Mass ($\times 10^8 M_\odot$) $M_\odot$
(1)	(2)	(3)	(4)	(5)
COSMOS-0727	150.103	1.766	0.498	46.190
COSMOS-0728	150.106	1.905	0.322	20.049
COSMOS-0729	150.106	2.508	0.498	32.380
COSMOS-0730	150.106	1.960	0.435	42.256
COSMOS-0731	150.107	2.456	0.478	67.765
COSMOS-0732	150.107	2.367	0.352	197.940
COSMOS-0733	150.109	2.224	0.372	56.043
COSMOS-0734	150.110	2.842	0.422	5.153
COSMOS-0735	150.110	2.018	0.487	173.460
COSMOS-0736	150.111	2.254	0.777	482.970
COSMOS-0737	150.112	2.430	0.409	107.660
COSMOS-0738	150.112	2.533	0.731	246.060
COSMOS-0739	150.112	2.881	0.344	8.822
COSMOS-0740	150.113	2.687	0.560	26.578
COSMOS-0741	150.113	2.363	0.485	34.874
COSMOS-0742	150.115	2.773	0.452	56.572
COSMOS-0743	150.116	1.597	0.554	187.860
COSMOS-0744	150.118	2.791	0.498	44.002
COSMOS-0745	150.118	2.024	0.499	36.647
COSMOS-0746	150.118	1.752	0.447	14.529
COSMOS-0747	150.119	2.416	0.837	950.480
COSMOS-0748	150.119	2.545	0.495	25.822
COSMOS-0749	150.120	1.789	0.555	54.748
COSMOS-0750	150.120	1.979	0.549	38.462
COSMOS-0751	150.120	1.680	0.486	48.445
COSMOS-0752	150.120	2.036	0.485	11.689
COSMOS-0753	150.121	2.525	0.516	88.506
COSMOS-0754	150.122	2.462	0.351	76.006
COSMOS-0755	150.123	2.857	0.557	16.978
COSMOS-0756	150.125	2.722	0.499	92.772
COSMOS-0757	150.125	1.668	0.542	36.844
COSMOS-0758	150.125	2.732	0.505	14.362
COSMOS-0759	150.126	1.719	0.560	58.064
COSMOS-0760	150.126	2.735	0.423	50.657
COSMOS-0761	150.128	1.626	0.488	68.464
COSMOS-0762	150.128	2.737	0.423	52.812
COSMOS-0763	150.129	2.070	0.351	10.095
COSMOS-0764	150.130	2.315	0.552	20.739
COSMOS-0765	150.130	1.603	0.496	75.701
COSMOS-0766	150.131	1.700	0.444	8.865
COSMOS-0767	150.132	2.299	0.487	76.808
COSMOS-0768	150.133	2.629	0.726	347.050
COSMOS-0769	150.134	1.956	0.384	85.694
COSMOS-0770	150.136	2.647	0.361	46.610

Continued on next page

Table C.1 – *Continued from previous page*

Object	**RA**	**DEC**	$\mathbf{z}_{phot}$	Mass ($\times 10^8 M_\odot$)
				$M_\odot$
(1)	(2)	(3)	(4)	(5)
COSMOS-0771	150.138	2.421	0.339	11.635
COSMOS-0772	150.141	2.652	0.350	7.631
COSMOS-0773	150.141	2.012	0.485	21.629
COSMOS-0774	150.143	2.208	0.847	533.980
COSMOS-0775	150.144	2.358	0.517	90.441
COSMOS-0776	150.144	1.789	0.731	*******
COSMOS-0777	150.145	2.356	0.343	92.493
COSMOS-0778	150.145	2.096	0.727	209.390
COSMOS-0779	150.146	1.928	0.399	52.119
COSMOS-0780	150.147	2.231	0.552	32.213
COSMOS-0781	150.147	2.612	0.554	43.786
COSMOS-0782	150.148	1.759	0.568	238.830
COSMOS-0783	150.149	2.692	0.506	19.877
COSMOS-0784	150.152	1.765	0.436	7.684
COSMOS-0785	150.153	1.609	0.552	22.986
COSMOS-0786	150.153	2.556	0.696	200.730
COSMOS-0787	150.154	1.850	0.671	465.010
COSMOS-0788	150.155	1.584	0.555	55.997
COSMOS-0789	150.156	2.697	0.438	37.458
COSMOS-0790	150.156	2.146	0.475	68.271
COSMOS-0791	150.156	2.624	0.408	4.255
COSMOS-0792	150.158	2.515	0.502	77.475
COSMOS-0793	150.159	1.714	0.541	93.187
COSMOS-0794	150.160	2.035	0.558	13.490
COSMOS-0795	150.161	2.551	0.485	21.584
COSMOS-0796	150.162	2.023	0.621	167.680
COSMOS-0797	150.163	2.258	0.349	13.388
COSMOS-0798	150.163	2.733	0.490	46.292
COSMOS-0799	150.164	2.457	0.354	12.621
COSMOS-0800	150.164	1.838	0.583	276.450
COSMOS-0801	150.165	2.363	0.423	22.891
COSMOS-0802	150.165	2.064	0.496	96.058
COSMOS-0803	150.165	2.228	0.485	18.088
COSMOS-0804	150.165	2.213	0.449	20.915
COSMOS-0805	150.166	1.706	0.484	21.205
COSMOS-0806	150.167	1.945	0.484	18.637
COSMOS-0807	150.168	2.762	0.498	53.723
COSMOS-0808	150.168	1.598	0.487	55.565
COSMOS-0809	150.168	2.393	0.504	22.259
COSMOS-0810	150.168	2.211	0.489	21.503
COSMOS-0811	150.170	1.599	0.559	108.190
COSMOS-0812	150.171	2.114	0.558	46.897
COSMOS-0813	150.173	1.826	0.512	60.951
COSMOS-0814	150.174	2.419	0.507	23.858

Continued on next page

Table C.1 – *Continued from previous page*

Object	**RA**	**DEC**	$\mathbf{z}_{phot}$	Mass ($\times 10^8 M_\odot$) $M_\odot$
(1)	(2)	(3)	(4)	(5)
COSMOS-0815	150.174	2.626	0.498	28.061
COSMOS-0816	150.174	2.626	0.500	17.474
COSMOS-0817	150.174	2.153	0.679	91.554
COSMOS-0818	150.175	2.436	0.672	159.110
COSMOS-0819	150.175	1.706	0.363	47.577
COSMOS-0820	150.176	2.014	0.553	*******
COSMOS-0821	150.178	2.019	0.560	16.739
COSMOS-0822	150.183	1.829	0.556	803.160
COSMOS-0823	150.184	2.578	0.426	132.660
COSMOS-0824	150.185	1.778	0.486	120.260
COSMOS-0825	150.185	1.778	0.451	5.650
COSMOS-0826	150.185	2.420	0.557	76.810
COSMOS-0827	150.186	1.759	0.499	49.109
COSMOS-0828	150.188	1.843	0.554	27.899
COSMOS-0829	150.188	1.764	0.556	63.755
COSMOS-0830	150.193	1.923	0.347	20.541
COSMOS-0831	150.193	2.213	0.665	148.400
COSMOS-0832	150.199	2.338	0.387	30.484
COSMOS-0833	150.201	2.865	0.486	20.609
COSMOS-0834	150.203	2.047	0.475	232.400
COSMOS-0835	150.203	2.484	0.555	23.642
COSMOS-0836	150.206	1.782	0.472	122.190
COSMOS-0837	150.209	2.813	0.433	17.621
COSMOS-0838	150.209	2.313	0.748	137.780
COSMOS-0839	150.211	2.814	0.431	48.702
COSMOS-0840	150.211	2.494	0.559	52.620
COSMOS-0841	150.211	2.603	0.558	30.537
COSMOS-0842	150.212	1.790	0.551	39.387
COSMOS-0843	150.215	2.126	0.498	23.460
COSMOS-0844	150.215	2.852	0.438	19.675
COSMOS-0845	150.217	2.061	0.547	33.721
COSMOS-0846	150.217	1.991	0.559	35.906
COSMOS-0847	150.217	2.134	0.353	16.519
COSMOS-0848	150.218	2.465	0.674	267.010
COSMOS-0849	150.219	1.786	0.557	33.577
COSMOS-0850	150.219	1.782	0.557	24.103
COSMOS-0851	150.222	2.354	0.599	229.300
COSMOS-0852	150.225	1.734	0.489	26.361
COSMOS-0853	150.227	2.774	0.486	10.388
COSMOS-0854	150.228	2.037	0.743	698.560
COSMOS-0855	150.230	2.670	0.335	85.556
COSMOS-0856	150.231	2.049	0.830	220.390
COSMOS-0857	150.232	2.009	0.371	91.029
COSMOS-0858	150.233	1.815	0.555	141.050

Continued on next page

Table C.1 – *Continued from previous page*

Object	**RA**	**DEC**	$\mathbf{z}_{phot}$	Mass ($\times 10^8 M_\odot$)
				$M_\odot$
(1)	(2)	(3)	(4)	(5)
COSMOS-0859	150.233	1.917	0.447	12.916
COSMOS-0860	150.234	2.170	0.469	26.406
COSMOS-0861	150.234	2.498	0.354	14.562
COSMOS-0862	150.236	2.246	0.487	31.110
COSMOS-0863	150.236	2.369	0.558	61.725
COSMOS-0864	150.236	1.651	0.552	38.004
COSMOS-0865	150.237	2.728	0.556	94.589
COSMOS-0866	150.238	2.237	0.497	10.614
COSMOS-0867	150.240	2.215	0.351	46.798
COSMOS-0868	150.242	1.827	0.621	130.400
COSMOS-0869	150.243	2.713	0.422	12.531
COSMOS-0870	150.245	2.224	0.727	490.050
COSMOS-0871	150.246	2.353	0.468	51.563
COSMOS-0872	150.246	1.842	0.485	27.691
COSMOS-0873	150.247	2.344	0.327	16.068
COSMOS-0874	150.250	2.291	0.486	7.811
COSMOS-0875	150.254	1.942	0.556	126.290
COSMOS-0876	150.254	2.318	0.555	39.703
COSMOS-0877	150.255	1.849	0.557	25.996
COSMOS-0878	150.256	1.850	0.557	47.114
COSMOS-0879	150.256	1.736	0.423	75.033
COSMOS-0880	150.258	2.233	0.565	37.615
COSMOS-0881	150.259	2.562	0.351	81.188
COSMOS-0882	150.259	1.981	0.550	23.759
COSMOS-0883	150.260	1.697	0.560	62.682
COSMOS-0884	150.261	1.615	0.504	29.652
COSMOS-0885	150.261	2.010	0.557	42.710
COSMOS-0886	150.261	2.756	0.558	24.777
COSMOS-0887	150.261	2.021	0.638	203.660
COSMOS-0888	150.261	1.788	0.636	116.760
COSMOS-0889	150.263	2.018	0.430	24.840
COSMOS-0890	150.264	2.385	0.729	534.900
COSMOS-0891	150.266	2.383	0.376	64.233
COSMOS-0892	150.267	2.345	0.498	107.800
COSMOS-0893	150.269	2.333	0.750	218.490
COSMOS-0894	150.269	2.113	0.663	103.870
COSMOS-0895	150.270	1.704	0.510	19.757
COSMOS-0896	150.271	2.340	0.352	49.423
COSMOS-0897	150.271	1.711	0.538	13.272
COSMOS-0898	150.274	1.779	0.350	28.904
COSMOS-0899	150.274	2.167	0.741	467.800
COSMOS-0900	150.275	2.050	0.552	42.856
COSMOS-0901	150.278	2.163	0.500	21.489
COSMOS-0902	150.279	1.684	0.554	29.671

Continued on next page

Table C.1 – *Continued from previous page*

Object	**RA**	**DEC**	$\mathbf{z}_{phot}$	Mass ($\times 10^8 M_\odot$) $M_\odot$
(1)	(2)	(3)	(4)	(5)
COSMOS-0903	150.280	2.439	0.484	100.090
COSMOS-0904	150.283	1.856	0.549	91.229
COSMOS-0905	150.286	1.624	0.595	78.086
COSMOS-0906	150.287	2.097	0.556	13.697
COSMOS-0907	150.290	2.838	0.456	138.790
COSMOS-0908	150.291	1.985	0.551	173.050
COSMOS-0909	150.291	1.617	0.502	9.557
COSMOS-0910	150.292	2.231	0.422	17.372
COSMOS-0911	150.292	2.046	0.712	237.020
COSMOS-0912	150.293	1.641	0.552	71.408
COSMOS-0913	150.293	1.994	0.484	32.911
COSMOS-0914	150.294	1.755	0.557	50.771
COSMOS-0915	150.295	2.439	0.557	85.908
COSMOS-0916	150.296	1.630	0.554	89.010
COSMOS-0917	150.297	2.571	0.422	42.057
COSMOS-0918	150.302	2.273	0.484	25.927
COSMOS-0919	150.303	2.571	0.500	35.896
COSMOS-0920	150.305	2.682	0.741	272.970
COSMOS-0921	150.306	1.792	0.555	43.543
COSMOS-0922	150.306	2.329	0.430	15.337
COSMOS-0923	150.307	2.344	0.485	47.024
COSMOS-0924	150.308	1.872	0.447	44.998
COSMOS-0925	150.309	2.189	0.490	44.638
COSMOS-0926	150.310	2.686	0.423	48.639
COSMOS-0927	150.310	1.690	0.502	14.265
COSMOS-0928	150.312	2.734	0.484	4.489
COSMOS-0929	150.314	2.402	0.666	458.840
COSMOS-0930	150.316	2.378	0.365	92.234
COSMOS-0931	150.317	2.073	0.485	47.647
COSMOS-0932	150.318	1.923	0.724	576.710
COSMOS-0933	150.320	2.118	0.423	47.619
COSMOS-0934	150.324	2.598	0.556	18.736
COSMOS-0935	150.324	2.841	0.333	69.371
COSMOS-0936	150.324	2.489	0.497	315.020
COSMOS-0937	150.327	1.910	0.367	125.660
COSMOS-0938	150.328	2.535	0.557	28.597
COSMOS-0939	150.328	2.670	0.539	3.740
COSMOS-0940	150.328	2.620	0.548	40.179
COSMOS-0941	150.328	2.338	0.484	18.621
COSMOS-0942	150.328	2.614	0.489	65.502
COSMOS-0943	150.328	2.802	0.484	8.390
COSMOS-0944	150.328	2.177	0.850	549.200
COSMOS-0945	150.329	1.827	0.811	600.240
COSMOS-0946	150.329	1.667	0.348	52.074

Continued on next page

Table C.1 – *Continued from previous page*

Object	**RA**	**DEC**	$\mathbf{z}_{phot}$	Mass ($\times 10^8 M_\odot$)
				$M_\odot$
(1)	(2)	(3)	(4)	(5)
COSMOS-0947	150.330	1.791	0.422	11.018
COSMOS-0948	150.331	1.880	0.839	273.190
COSMOS-0949	150.331	2.140	0.560	40.868
COSMOS-0950	150.333	2.417	0.350	151.700
COSMOS-0951	150.333	1.637	0.527	57.259
COSMOS-0952	150.337	1.914	0.367	28.730
COSMOS-0953	150.337	2.012	0.434	24.244
COSMOS-0954	150.338	1.843	0.559	36.583
COSMOS-0955	150.339	1.685	0.446	17.312
COSMOS-0956	150.340	2.755	0.485	21.680
COSMOS-0957	150.341	2.380	0.171	4.755
COSMOS-0958	150.341	2.739	0.423	53.745
COSMOS-0959	150.346	2.307	0.350	19.982
COSMOS-0960	150.347	2.677	0.528	282.280
COSMOS-0961	150.348	2.637	0.360	117.520
COSMOS-0962	150.348	2.636	0.367	44.497
COSMOS-0963	150.349	2.284	0.592	425.530
COSMOS-0964	150.349	1.878	0.553	37.600
COSMOS-0965	150.349	2.352	0.489	21.378
COSMOS-0966	150.350	2.276	0.464	96.557
COSMOS-0967	150.350	2.652	0.750	*******
COSMOS-0968	150.351	2.196	0.553	53.101
COSMOS-0969	150.351	2.762	0.795	*******
COSMOS-0970	150.352	2.132	0.351	19.406
COSMOS-0971	150.352	1.937	0.427	25.048
COSMOS-0972	150.353	1.781	0.559	65.962
COSMOS-0973	150.354	2.726	0.555	35.538
COSMOS-0974	150.354	2.735	0.451	81.601
COSMOS-0975	150.356	2.222	0.347	6.931
COSMOS-0976	150.356	2.263	0.556	22.594
COSMOS-0977	150.356	1.975	0.353	69.355
COSMOS-0978	150.356	2.580	0.406	12.520
COSMOS-0979	150.358	1.847	0.488	41.660
COSMOS-0980	150.358	2.145	0.555	28.278
COSMOS-0981	150.358	2.660	0.661	334.040
COSMOS-0982	150.360	2.642	0.485	18.441
COSMOS-0983	150.360	1.615	0.509	26.043
COSMOS-0984	150.361	2.367	0.448	52.442
COSMOS-0985	150.362	2.131	0.552	33.110
COSMOS-0986	150.362	1.806	0.499	10.231
COSMOS-0987	150.363	1.919	0.559	77.031
COSMOS-0988	150.364	2.181	0.486	18.896
COSMOS-0989	150.365	2.125	0.553	38.182
COSMOS-0990	150.366	1.794	0.473	130.700

Continued on next page

Table C.1 – *Continued from previous page*

Object	**RA**	**DEC**	$\mathbf{z}_{phot}$	Mass ($\times 10^8 M_\odot$) $M_\odot$
(1)	(2)	(3)	(4)	(5)
COSMOS-0991	150.366	2.755	0.448	37.200
COSMOS-0992	150.366	2.402	0.486	94.988
COSMOS-0993	150.366	2.795	0.423	13.239
COSMOS-0994	150.367	1.793	0.497	88.028
COSMOS-0995	150.367	2.035	0.422	181.290
COSMOS-0996	150.369	2.687	0.420	52.049
COSMOS-0997	150.369	2.213	0.423	7.978
COSMOS-0998	150.370	2.179	0.460	63.116
COSMOS-0999	150.371	2.273	0.558	19.171
COSMOS-1000	150.374	2.610	0.673	127.370
COSMOS-1001	150.374	2.687	0.487	51.928
COSMOS-1002	150.376	2.001	0.555	101.590
COSMOS-1003	150.376	2.145	0.354	68.781
COSMOS-1004	150.376	2.197	0.485	50.439
COSMOS-1005	150.376	2.779	0.500	78.198
COSMOS-1006	150.376	1.676	0.484	44.875
COSMOS-1007	150.379	1.728	0.484	17.238
COSMOS-1008	150.379	2.454	0.499	83.241
COSMOS-1009	150.380	2.718	0.484	11.677
COSMOS-1010	150.381	2.380	0.486	12.338
COSMOS-1011	150.381	2.495	0.389	149.460
COSMOS-1012	150.381	2.019	0.415	45.511
COSMOS-1013	150.381	1.592	0.485	26.503
COSMOS-1014	150.383	2.812	0.424	67.152
COSMOS-1015	150.383	2.372	0.851	266.450
COSMOS-1016	150.385	2.030	0.558	15.524
COSMOS-1017	150.386	1.983	0.426	34.524
COSMOS-1018	150.388	1.735	0.561	13.286
COSMOS-1019	150.389	2.837	0.816	351.090
COSMOS-1020	150.390	2.005	0.461	*******
COSMOS-1021	150.390	1.914	0.844	628.400
COSMOS-1022	150.390	2.421	0.344	97.835
COSMOS-1023	150.391	1.910	0.352	36.631
COSMOS-1024	150.391	2.570	0.557	46.595
COSMOS-1025	150.391	1.812	0.448	86.217
COSMOS-1026	150.392	2.603	0.826	224.180
COSMOS-1027	150.394	2.741	0.484	36.635
COSMOS-1028	150.394	2.579	0.499	35.811
COSMOS-1029	150.394	2.046	0.582	569.670
COSMOS-1030	150.395	1.666	0.405	23.222
COSMOS-1031	150.395	1.891	0.558	97.010
COSMOS-1032	150.396	1.837	0.697	195.370
COSMOS-1033	150.396	2.508	0.553	30.429
COSMOS-1034	150.396	2.428	0.561	76.767

Continued on next page

Table C.1 – *Continued from previous page*

Object	**RA**	**DEC**	$\mathbf{z}_{phot}$	Mass ($\times 10^8 M_\odot$)
				$M_\odot$
(1)	(2)	(3)	(4)	(5)
COSMOS-1035	150.401	2.744	0.428	50.059
COSMOS-1036	150.402	2.667	0.611	409.710
COSMOS-1037	150.403	2.154	0.556	153.020
COSMOS-1038	150.405	2.643	0.667	136.260
COSMOS-1039	150.406	2.386	0.619	139.780
COSMOS-1040	150.409	1.956	0.448	20.081
COSMOS-1041	150.412	1.728	0.560	57.834
COSMOS-1042	150.413	2.423	0.401	183.090
COSMOS-1043	150.414	2.683	0.556	125.820
COSMOS-1044	150.414	2.086	0.556	19.300
COSMOS-1045	150.415	2.593	0.408	6.503
COSMOS-1046	150.416	1.982	0.556	64.101
COSMOS-1047	150.417	2.711	0.484	72.261
COSMOS-1048	150.417	1.984	0.451	35.745
COSMOS-1049	150.418	1.841	0.834	749.150
COSMOS-1050	150.419	2.578	0.555	64.602
COSMOS-1051	150.420	2.587	0.826	744.490
COSMOS-1052	150.422	2.204	0.422	64.169
COSMOS-1053	150.422	2.521	0.447	11.347
COSMOS-1054	150.423	2.614	0.555	164.900
COSMOS-1055	150.424	2.586	0.426	28.150
COSMOS-1056	150.426	2.097	0.492	21.992
COSMOS-1057	150.427	2.348	0.507	70.047
COSMOS-1058	150.428	1.934	0.496	75.399
COSMOS-1059	150.430	1.858	0.557	37.699
COSMOS-1060	150.430	2.013	0.501	22.493
COSMOS-1061	150.432	1.984	0.555	27.096
COSMOS-1062	150.432	1.912	0.366	41.371
COSMOS-1063	150.433	2.611	0.557	311.360
COSMOS-1064	150.433	2.564	0.408	22.703
COSMOS-1065	150.434	2.832	0.448	54.684
COSMOS-1066	150.434	2.563	0.407	93.691
COSMOS-1067	150.435	1.915	0.500	121.580
COSMOS-1068	150.437	2.533	0.486	41.491
COSMOS-1069	150.438	1.636	0.423	89.143
COSMOS-1070	150.438	2.738	0.487	58.132
COSMOS-1071	150.439	2.759	0.500	43.549
COSMOS-1072	150.439	1.832	0.499	51.148
COSMOS-1073	150.444	2.431	0.497	13.819
COSMOS-1074	150.445	2.540	0.353	54.225
COSMOS-1075	150.445	2.134	0.556	43.444
COSMOS-1076	150.445	2.697	0.369	20.064
COSMOS-1077	150.446	2.812	0.487	22.642
COSMOS-1078	150.447	2.558	0.405	33.308

Continued on next page

Table C.1 – *Continued from previous page*

Object	**RA**	**DEC**	$\mathbf{z}_{phot}$	Mass ($\times 10^8 M_\odot$) $M_\odot$
(1)	(2)	(3)	(4)	(5)
COSMOS-1079	150.448	2.558	0.394	42.452
COSMOS-1080	150.448	2.780	0.501	32.056
COSMOS-1081	150.450	2.753	0.465	151.610
COSMOS-1082	150.450	2.580	0.429	75.534
COSMOS-1083	150.450	2.729	0.556	27.795
COSMOS-1084	150.450	1.718	0.424	27.623
COSMOS-1085	150.454	1.943	0.431	4.953
COSMOS-1086	150.456	1.581	0.485	56.009
COSMOS-1087	150.459	2.071	0.435	32.686
COSMOS-1088	150.460	2.390	0.487	46.962
COSMOS-1089	150.460	2.233	0.487	83.947
COSMOS-1090	150.460	2.026	0.485	62.781
COSMOS-1091	150.461	2.347	0.373	40.211
COSMOS-1092	150.461	2.079	0.553	130.930
COSMOS-1093	150.463	2.155	0.499	11.434
COSMOS-1094	150.464	2.045	0.509	19.407
COSMOS-1095	150.469	2.543	0.408	25.050
COSMOS-1096	150.469	1.984	0.351	66.086
COSMOS-1097	150.469	2.034	0.552	75.020
COSMOS-1098	150.471	2.544	0.483	8.021
COSMOS-1099	150.472	2.778	0.488	40.559
COSMOS-1100	150.474	1.616	0.422	31.185
COSMOS-1101	150.476	2.625	0.425	14.473
COSMOS-1102	150.476	1.888	0.830	*******
COSMOS-1103	150.477	2.574	0.361	36.890
COSMOS-1104	150.481	2.624	0.485	40.920
COSMOS-1105	150.484	2.066	0.506	38.506
COSMOS-1106	150.484	2.634	0.422	39.092
COSMOS-1107	150.484	1.712	0.558	25.274
COSMOS-1108	150.485	1.939	0.552	18.335
COSMOS-1109	150.486	2.590	0.816	*******
COSMOS-1110	150.487	2.732	0.490	57.142
COSMOS-1111	150.488	2.454	0.744	269.800
COSMOS-1112	150.488	2.827	0.545	47.387
COSMOS-1113	150.491	1.978	0.409	26.344
COSMOS-1114	150.491	2.839	0.432	103.960
COSMOS-1115	150.493	2.623	0.350	14.145
COSMOS-1116	150.494	2.399	0.559	53.556
COSMOS-1117	150.497	2.495	0.672	163.780
COSMOS-1118	150.498	2.156	0.557	28.525
COSMOS-1119	150.499	1.771	0.488	118.000
COSMOS-1120	150.499	1.866	0.526	52.996
COSMOS-1121	150.501	1.811	0.700	161.620
COSMOS-1122	150.502	2.102	0.556	151.410

Continued on next page

Table C.1 – *Continued from previous page*

Object	**RA**	**DEC**	$\mathbf{z}_{phot}$	Mass ($\times 10^8 M_\odot$)
				$M_\odot$
(1)	(2)	(3)	(4)	(5)
COSMOS-1123	150.502	2.095	0.558	31.724
COSMOS-1124	150.502	2.505	0.569	19.388
COSMOS-1125	150.504	1.756	0.542	333.230
COSMOS-1126	150.509	2.210	0.671	140.760
COSMOS-1127	150.510	2.217	0.473	114.110
COSMOS-1128	150.511	2.789	0.422	35.712
COSMOS-1129	150.512	2.608	0.555	53.509
COSMOS-1130	150.512	1.970	0.490	25.114
COSMOS-1131	150.512	1.822	0.423	9.552
COSMOS-1132	150.516	2.047	0.557	52.210
COSMOS-1133	150.516	1.685	0.793	671.460
COSMOS-1134	150.516	2.211	0.824	613.800
COSMOS-1135	150.517	1.876	0.540	108.180
COSMOS-1136	150.517	1.982	0.462	31.524
COSMOS-1137	150.517	2.172	0.589	293.160
COSMOS-1138	150.518	2.237	0.394	26.123
COSMOS-1139	150.521	2.624	0.486	304.090
COSMOS-1140	150.522	2.548	0.553	164.160
COSMOS-1141	150.523	1.947	0.556	14.467
COSMOS-1142	150.524	2.666	0.449	18.571
COSMOS-1143	150.528	2.294	0.556	51.773
COSMOS-1144	150.530	1.713	0.556	22.121
COSMOS-1145	150.531	1.774	0.558	51.856
COSMOS-1146	150.534	2.045	0.433	25.661
COSMOS-1147	150.535	2.858	0.485	32.911
COSMOS-1148	150.536	2.089	0.502	20.840
COSMOS-1149	150.536	2.757	0.486	120.260
COSMOS-1150	150.536	2.038	0.544	10.441
COSMOS-1151	150.537	2.391	0.560	44.384
COSMOS-1152	150.537	2.472	0.487	21.537
COSMOS-1153	150.538	1.760	0.447	28.287
COSMOS-1154	150.538	2.597	0.412	78.260
COSMOS-1155	150.542	2.653	0.451	13.743
COSMOS-1156	150.543	2.447	0.508	49.852
COSMOS-1157	150.543	2.343	0.425	28.085
COSMOS-1158	150.544	1.961	0.557	38.341
COSMOS-1159	150.544	2.274	0.485	32.430
COSMOS-1160	150.549	1.963	0.555	26.563
COSMOS-1161	150.550	2.340	0.362	23.360
COSMOS-1162	150.551	2.509	0.661	362.520
COSMOS-1163	150.552	2.542	0.493	70.165
COSMOS-1164	150.552	2.130	0.557	50.010
COSMOS-1165	150.553	2.345	0.365	85.386
COSMOS-1166	150.554	2.430	0.450	19.120

Continued on next page

Table C.1 – *Continued from previous page*

Object	**RA**	**DEC**	$\mathbf{z}_{phot}$	Mass ($\times 10^8 M_\odot$) $M_\odot$
(1)	(2)	(3)	(4)	(5)
COSMOS-1167	150.555	2.649	0.557	66.213
COSMOS-1168	150.557	2.839	0.428	18.288
COSMOS-1169	150.557	2.137	0.558	16.725
COSMOS-1170	150.558	2.433	0.491	179.570
COSMOS-1171	150.559	2.776	0.497	112.640
COSMOS-1172	150.560	2.443	0.751	373.610
COSMOS-1173	150.560	2.099	0.554	23.269
COSMOS-1174	150.561	1.754	0.486	22.603
COSMOS-1175	150.561	2.668	0.553	41.148
COSMOS-1176	150.562	1.732	0.531	10.309
COSMOS-1177	150.563	2.150	0.556	34.852
COSMOS-1178	150.564	2.627	0.498	11.627
COSMOS-1179	150.567	2.809	0.350	28.597
COSMOS-1180	150.569	2.123	0.556	31.831
COSMOS-1181	150.569	2.763	0.428	32.406
COSMOS-1182	150.570	2.159	0.422	28.270
COSMOS-1183	150.571	1.983	0.422	109.380
COSMOS-1184	150.571	2.312	0.422	12.324
COSMOS-1185	150.572	2.664	0.554	35.911
COSMOS-1186	150.575	2.619	0.449	6.619
COSMOS-1187	150.575	2.019	0.326	6.533
COSMOS-1188	150.576	2.457	0.557	55.238
COSMOS-1189	150.576	2.608	0.550	115.060
COSMOS-1190	150.577	2.634	0.465	9.240
COSMOS-1191	150.579	2.215	0.484	26.420
COSMOS-1192	150.582	2.667	0.851	*******
COSMOS-1193	150.583	2.266	0.496	35.757
COSMOS-1194	150.583	2.189	0.555	42.550
COSMOS-1195	150.585	2.826	0.490	250.230
COSMOS-1196	150.586	2.412	0.763	979.500
COSMOS-1197	150.587	2.614	0.490	114.420
COSMOS-1198	150.588	2.246	0.508	67.545
COSMOS-1199	150.589	2.605	0.550	63.434
COSMOS-1200	150.592	2.164	0.553	22.495
COSMOS-1201	150.592	1.654	0.484	10.415
COSMOS-1202	150.592	2.428	0.565	155.010
COSMOS-1203	150.592	2.586	0.330	23.969
COSMOS-1204	150.593	2.527	0.168	11.657
COSMOS-1205	150.600	2.038	0.485	32.840
COSMOS-1206	150.601	2.483	0.485	14.569
COSMOS-1207	150.605	2.734	0.508	25.003
COSMOS-1208	150.606	2.408	0.358	14.855
COSMOS-1209	150.606	1.721	0.498	51.619
COSMOS-1210	150.608	2.607	0.557	44.810

Continued on next page

Table C.1 – *Continued from previous page*

Object	**RA**	**DEC**	$\mathbf{z}_{phot}$	Mass ($\times 10^8 M_\odot$)
				$M_\odot$
(1)	(2)	(3)	(4)	(5)
COSMOS-1211	150.608	2.237	0.485	27.009
COSMOS-1212	150.609	2.772	0.556	240.920
COSMOS-1213	150.610	2.600	0.485	16.752
COSMOS-1214	150.611	2.129	0.483	66.382
COSMOS-1215	150.611	2.440	0.509	129.160
COSMOS-1216	150.612	2.197	0.566	66.530
COSMOS-1217	150.612	2.225	0.551	52.413
COSMOS-1218	150.612	2.210	0.555	40.684
COSMOS-1219	150.612	2.530	0.502	8.952
COSMOS-1220	150.612	1.932	0.560	49.516
COSMOS-1221	150.620	2.769	0.502	12.060
COSMOS-1222	150.621	2.827	0.484	35.149
COSMOS-1223	150.621	2.780	0.484	104.340
COSMOS-1224	150.621	2.322	0.448	18.103
COSMOS-1225	150.623	1.608	0.410	22.249
COSMOS-1226	150.626	2.417	0.497	111.380
COSMOS-1227	150.629	2.079	0.556	120.190
COSMOS-1228	150.629	2.060	0.448	34.612
COSMOS-1229	150.630	2.360	0.556	107.530
COSMOS-1230	150.631	2.662	0.506	162.550
COSMOS-1231	150.631	2.366	0.450	19.082
COSMOS-1232	150.631	2.755	0.501	83.680
COSMOS-1233	150.632	2.382	0.484	18.568
COSMOS-1234	150.633	2.302	0.486	80.912
COSMOS-1235	150.636	2.834	0.556	60.431
COSMOS-1236	150.637	2.323	0.423	51.476
COSMOS-1237	150.637	2.717	0.496	167.390
COSMOS-1238	150.638	2.530	0.552	228.350
COSMOS-1239	150.639	2.391	0.511	41.023
COSMOS-1240	150.643	2.344	0.503	438.570
COSMOS-1241	150.644	2.735	0.556	111.540
COSMOS-1242	150.644	1.719	0.434	14.828
COSMOS-1243	150.646	2.678	0.789	642.190
COSMOS-1244	150.647	2.071	0.555	114.930
COSMOS-1245	150.648	1.683	0.547	39.991
COSMOS-1246	150.648	1.818	0.357	36.603
COSMOS-1247	150.651	2.474	0.502	118.960
COSMOS-1248	150.651	2.271	0.448	42.549
COSMOS-1249	150.652	2.209	0.485	50.054
COSMOS-1250	150.653	2.173	0.487	40.536
COSMOS-1251	150.653	2.023	0.423	9.952
COSMOS-1252	150.654	2.665	0.487	51.122
COSMOS-1253	150.655	2.474	0.437	36.823
COSMOS-1254	150.658	1.899	0.485	39.294

Continued on next page

Table C.1 – *Continued from previous page*

Object	**RA**	**DEC**	$\mathbf{z}_{phot}$	Mass ($\times 10^8 M_\odot$) $M_\odot$
(1)	(2)	(3)	(4)	(5)
COSMOS-1255	150.660	2.549	0.352	111.840
COSMOS-1256	150.661	2.582	0.484	44.060
COSMOS-1257	150.662	2.657	0.557	55.460
COSMOS-1258	150.667	2.384	0.436	22.758
COSMOS-1259	150.670	1.981	0.424	28.072
COSMOS-1260	150.671	2.318	0.428	178.110
COSMOS-1261	150.673	2.447	0.489	42.939
COSMOS-1262	150.673	2.807	0.512	31.046
COSMOS-1263	150.674	2.319	0.430	18.436
COSMOS-1264	150.674	2.424	0.360	68.630
COSMOS-1265	150.675	1.947	0.448	246.370
COSMOS-1266	150.677	2.310	0.555	66.708
COSMOS-1267	150.677	2.738	0.541	220.350
COSMOS-1268	150.678	2.273	0.488	16.465
COSMOS-1269	150.680	2.197	0.557	157.110
COSMOS-1270	150.680	2.831	0.546	224.100
COSMOS-1271	150.681	2.396	0.501	27.065
COSMOS-1272	150.681	2.337	0.486	25.602
COSMOS-1273	150.681	2.035	0.557	170.240
COSMOS-1274	150.683	1.947	0.434	80.052
COSMOS-1275	150.684	2.297	0.436	8.393
COSMOS-1276	150.685	1.725	0.450	31.096
COSMOS-1277	150.685	2.292	0.486	226.330
COSMOS-1278	150.685	2.258	0.485	73.618
COSMOS-1279	150.692	1.639	0.511	40.131
COSMOS-1280	150.692	2.633	0.484	46.772
COSMOS-1281	150.693	2.041	0.443	40.670
COSMOS-1282	150.693	2.037	0.485	290.650
COSMOS-1283	150.696	1.702	0.553	28.639
COSMOS-1284	150.699	2.541	0.485	36.616
COSMOS-1285	150.701	2.341	0.447	11.532
COSMOS-1286	150.703	2.817	0.551	24.153
COSMOS-1287	150.703	2.596	0.485	72.333
COSMOS-1288	150.704	1.651	0.487	72.881
COSMOS-1289	150.705	2.028	0.427	43.620
COSMOS-1290	150.705	1.717	0.570	68.062
COSMOS-1291	150.706	1.701	0.558	84.740
COSMOS-1292	150.708	2.392	0.485	173.870
COSMOS-1293	150.714	2.197	0.553	55.834
COSMOS-1294	150.716	2.206	0.549	328.810
COSMOS-1295	150.716	1.815	0.486	15.019
COSMOS-1296	150.717	2.775	0.431	27.848
COSMOS-1297	150.719	2.558	0.330	17.024
COSMOS-1298	150.719	2.407	0.485	65.874

Continued on next page

Table C.1 – *Continued from previous page*

Object	**RA**	**DEC**	$\mathbf{z}_{phot}$	Mass ($\times 10^8 M_\odot$) $M_\odot$
(1)	(2)	(3)	(4)	(5)
COSMOS-1299	150.721	1.809	0.321	75.895
COSMOS-1300	150.721	1.849	0.553	29.223
COSMOS-1301	150.722	1.892	0.487	38.522
COSMOS-1302	150.722	2.442	0.556	54.234
COSMOS-1303	150.722	1.976	0.553	317.870
COSMOS-1304	150.723	2.829	0.554	129.520
COSMOS-1305	150.727	1.796	0.826	675.400
COSMOS-1306	150.727	2.434	0.491	29.860
COSMOS-1307	150.727	2.363	0.486	63.706
COSMOS-1308	150.731	1.769	0.541	176.200
COSMOS-1309	150.732	1.845	0.556	216.720
COSMOS-1310	150.736	2.561	0.460	5.801
COSMOS-1311	150.738	2.408	0.332	11.871
COSMOS-1312	150.738	2.552	0.556	50.201
COSMOS-1313	150.741	2.410	0.555	51.925
COSMOS-1314	150.741	2.212	0.549	41.810
COSMOS-1315	150.745	2.410	0.353	19.550
COSMOS-1316	150.750	2.366	0.502	68.858
COSMOS-1317	150.756	1.832	0.438	5.616
COSMOS-1318	150.756	2.023	0.422	27.599
COSMOS-1319	150.757	2.414	0.351	109.630
COSMOS-1320	150.758	2.750	0.542	68.666
COSMOS-1321	150.763	1.741	0.422	142.750
COSMOS-1322	150.765	2.417	0.822	468.500
COSMOS-1323	150.774	2.399	0.350	39.443

References

1987, Nature, 326, 219

Abraham, R. G., Tanvir, N. R., Santiago, B. X., et al. 1996, MNRAS, 279, L47

Aguerri, J. A. L., Elias-Rosa, N., Corsini, E. M., & Muñoz-Tuñón, C. 2005, A&A, 434, 109

Alongi, M., Bertelli, G., Bressan, A., & Chiosi, C. 1991, A&A, 244, 95

Amorín, R., Aguerri, J. A. L., Muñoz-Tuñón, C., & Cairós, L. M. 2009, A&A, 501, 75

Amorín, R., Pérez-Montero, E., Vílchez, J. M., & Papaderos, P. 2012, ApJ, 749, 185

Amorín, R., Sommariva, V., Castellano, M., et al. 2014, A&A, 568, L8

Amorín, R. O., Muñoz-Tuñón, C., Aguerri, J. A. L., Cairós, L. M., & Caon, N. 2007, A&A, 467, 541

Arsenault, R. & Roy, J.-R. 1988, A&A, 201, 199

Athanassoula, E., Morin, S., Wozniak, H., et al. 1990, MNRAS, 245, 130

Aumer, M., Burkert, A., Johansson, P. H., & Genzel, R. 2010, ApJ, 719, 1230

Avni, Y. & Bahcall, J. N. 1980, ApJ, 235, 694

Baggett, W. E., Baggett, S. M., & Anderson, K. S. J. 1998, AJ, 116, 1626

Bastian, N. & Goodwin, S. P. 2006, MNRAS, 369, L9

Bell, E. F. & de Jong, R. S. 2001, ApJ, 550, 212

Bell, E. F., Naab, T., McIntosh, D. H., et al. 2006, ApJ, 640, 241

Benítez, N., Moles, M., Aguerri, J. A. L., et al. 2009, ApJ, 692, L5

Bergvall, N. & Östlin, G. 2002, A&A, 390, 891

Blanton, M. R. & Roweis, S. 2007, AJ, 133, 734

Bordalo, V. & Telles, E. 2011, ApJ, 735, 52

Bournaud, F. & Elmegreen, B. G. 2009, ApJ, 694, L158

Bournaud, F., Elmegreen, B. G., & Elmegreen, D. M. 2007, ApJ, 670, 237

Bruzual, G. & Charlot, S. 2003, MNRAS, 344, 1000

Byun, Y. I. & Freeman, K. C. 1995, ApJ, 448, 563

Cairós, L. M., Caon, N., García-Lorenzo, B., et al. 2007, ApJ, 669, 251

Cairós, L.-M., Caon, N., Muñoz-Tuñón, C., & Vílchez, J. M. 2000, in Astronomical Society of the Pacific Conference Series, Vol. 215, Cosmic Evolution and Galaxy Formation: Structure, Interactions, and Feedback, ed. J. Franco, L. Terlevich, O. López-Cruz, & I. Aretxaga, 52

Cairós, L. M., Caon, N., Papaderos, P., et al. 2009a, ApJ, 707, 1676

Cairós, L. M., Caon, N., Papaderos, P., et al. 2003, ApJ, 593, 312

Cairós, L. M., Caon, N., Zurita, C., et al. 2010, A&A, 520, A90

Cairós, L. M., Caon, N., Zurita, C., et al. 2009b, A&A, 507, 1291

Cairós, L. M., Vílchez, J. M., González Pérez, J. N., Iglesias-Páramo, J., & Caon, N. 2001, ApJS, 133, 321

Caon, N., Cairós, L. M., Aguerri, J. A. L., & Muñoz-Tuñón, C. 2005, ApJS, 157, 218

Caon, N., Capaccioli, M., & D'Onofrio, M. 1993, MNRAS, 265, 1013

Capak, P., Aussel, H., Ajiki, M., et al. 2007, ApJS, 172, 99

Ceverino, D., Dekel, A., Mandelker, N., et al. 2012, MNRAS, 420, 3490

Ceverino, D., Dekel, A., Tweed, D., & Primack, J. 2015, MNRAS, 447, 3291

Chabrier, G. 2003, PASP, 115, 763

Chávez, R., Terlevich, E., Terlevich, R., et al. 2012, MNRAS, 425, L56

Chu, Y.-H. & Kennicutt, Jr., R. C. 1994, Ap&SS, 216, 253

Ciotti, L. 1991, A&A, 249, 99

Conselice, C. J., Chapman, S. C., & Windhorst, R. A. 2003, ApJ, 596, L5

Cowie, L. L., Hu, E. M., & Songaila, A. 1995, AJ, 110, 1576

Daddi, E., Bournaud, F., Walter, F., et al. 2010, ApJ, 713, 686

de Jong, R. S. 1996, A&AS, 118, 557

de Vaucouleurs, G. 1948, Annales d'Astrophysique, 11, 247

de Vaucouleurs, G. 1953, MNRAS, 113, 134

Dekel, A., Birnboim, Y., Engel, G., et al. 2009, Nature, 457, 451

Dekel, A. & Silk, J. 1986, ApJ, 303, 39

Doublier, V., Caulet, A., & Comte, G. 2001, A&A, 367, 33

Elmegreen, B. G. & Elmegreen, D. M. 2006, ApJ, 650, 644

Elmegreen, B. G., Elmegreen, D. M., Fernandez, M. X., & Lemonias, J. J. 2009, ApJ, 692, 12

Elmegreen, B. G., Elmegreen, D. M., Sánchez Almeida, J., et al. 2013, ApJ, 774, 86

Elmegreen, D. M., Elmegreen, B. G., & Hirst, A. C. 2004a, ApJ, 604, L21

Elmegreen, D. M., Elmegreen, B. G., Ravindranath, S., & Coe, D. A. 2007, ApJ, 658, 763

Elmegreen, D. M., Elmegreen, B. G., Rubin, D. S., & Schaffer, M. A. 2005, ApJ, 631, 85

Elmegreen, D. M., Elmegreen, B. G., & Sheets, C. M. 2004b, ApJ, 603, 74

Förster Schreiber, N. M., Genzel, R., Lehnert, M. D., et al. 2006, ApJ, 645, 1062

Förster Schreiber, N. M., Shapley, A. E., Genzel, R., et al. 2011, ApJ, 739, 45

Freedman, W. L., Madore, B. F., Scowcroft, V., et al. 2012, ApJ, 758, 24

Freeman, K. C. 1970, ApJ, 160, 811

Fuentes-Masip, O., Muñoz-Tuñón, C., Castañeda, H. O., & Tenorio-Tagle, G. 2000, AJ, 120, 752

Gallagher, J. S. & Hunter, D. A. 1983, ApJ, 274, 141

Garn, T. & Best, P. N. 2010, MNRAS, 409, 421

Genzel, R., Newman, S., Jones, T., et al. 2011, ApJ, 733, 101

Graham, A., Lauer, T. R., Colless, M., & Postman, M. 1996, ApJ, 465, 534

Graham, A. W., Driver, S. P., Petrosian, V., et al. 2005, AJ, 130, 1535

Graham, A. W. & Guzmán, R. 2003, AJ, 125, 2936

Guo, Y., Ferguson, H. C., Bell, E. F., et al. 2014, ArXiv e-prints

Guo, Y., Ferguson, H. C., Bell, E. F., et al. 2015, ApJ, 800, 39

Guo, Y., Giavalisco, M., Ferguson, H. C., Cassata, P., & Koekemoer, A. M. 2012, ApJ, 757, 120

Gutiérrez, L., Beckman, J. E., & Buenrostro, V. 2011, AJ, 141, 113

Ilbert, O., Capak, P., Salvato, M., et al. 2009, ApJ, 690, 1236

Ilbert, O., Salvato, M., Capak, P., et al. 2008, in Astronomical Society of the Pacific Conference Series, Vol. 399, Panoramic Views of Galaxy Formation and Evolution, ed. T. Kodama, T. Yamada, & K. Aoki, 169

James, P. A. 1994, MNRAS, 269, 176

Jedrzejewski, R. I. 1987, MNRAS, 226, 747

Jones, T. A., Swinbank, A. M., Ellis, R. S., Richard, J., & Stark, D. P. 2010, MNRAS, 404, 1247

Kennicutt, Jr., R. C. 1998, in Astronomical Society of the Pacific Conference Series, Vol. 142, The Stellar Initial Mass Function (38th Herstmonceux Conference), ed. G. Gilmore & D. Howell, 1

Kereš, D., Katz, N., Weinberg, D. H., & Davé, R. 2005, MNRAS, 363, 2

Kewley, L. J., Dopita, M. A., Sutherland, R. S., Heisler, C. A., & Trevena, J. 2001, ApJ, 556, 121

Kewley, L. J., Geller, M. J., & Jansen, R. A. 2004, AJ, 127, 2002

Khosroshahi, H. G., Wadadekar, Y., & Kembhavi, A. 2000, ApJ, 533, 162

Kniazev, A. Y., Pustilnik, S. A., Grebel, E. K., Lee, H., & Pramskij, A. G. 2004, ApJS, 153, 429

Koekemoer, A. M., Aussel, H., Calzetti, D., et al. 2007, ApJS, 172, 196

Kormendy, J. & Bender, R. 2012, ApJS, 198, 2

Kunth, D., Maurogordato, S., & Vigroux, L. 1988, A&A, 204, 10

Larson, R. B. 1981, MNRAS, 194, 809

Lauer, T. R., Ajhar, E. A., Byun, Y.-I., et al. 1995, AJ, 110, 2622

Leitherer, C., Ortiz Otálvaro, P. A., Bresolin, F., et al. 2010, ApJS, 189, 309

Leitherer, C., Schaerer, D., Goldader, J. D., et al. 1999, ApJS, 123, 3

L'Huillier, B., Combes, F., & Semelin, B. 2012, A&A, 544, A68

Lilly, S. J., Le Fèvre, O., Renzini, A., et al. 2007, ApJS, 172, 70

Liu, C. T., Capak, P., Mobasher, B., et al. 2008, ApJ, 672, 198

Loose, H.-H. & Thuan, T. X. 1986, ApJ, 309, 59

Lotz, J. M., Madau, P., Giavalisco, M., Primack, J., & Ferguson, H. C. 2006, ApJ, 636, 592

Madau, P., Pozzetti, L., & Dickinson, M. 1998, ApJ, 498, 106

Martínez-Delgado, I., Tenorio-Tagle, G., Muñoz-Tuñón, C., Moiseev, A. V., & Cairós, L. M. 2007, AJ, 133, 2892

Melnick, J. 1979, ApJ, 228, 112

Melnick, J. & Quintana, H. 1981, A&AS, 44, 87

Melnick, J., Terlevich, R., & Moles, M. 1988, MNRAS, 235, 297

Melnick, J., Terlevich, R., & Terlevich, E. 2000, MNRAS, 311, 629

Méndez-Abreu, J., Aguerri, J. A. L., Corsini, E. M., & Simonneau, E. 2008, A&A, 478, 353

Miyauchi-Isobe, N., Maehara, H., & Nakajima, K. 2010, Publications of the National Astronomical Observatory of Japan, 13, 9

Monreal-Ibero, A., Colina, L., Arribas, S., & García-Marín, M. 2007, A&A, 472, 421

Morales-Luis, A. B., Sánchez Almeida, J., Aguerri, J. A. L., & Muñoz-Tuñón, C. 2011, ApJ, 743, 77

Moustakas, J., Kennicutt, Jr., R. C., & Tremonti, C. A. 2006, ApJ, 642, 775

Munoz-Tunon, C., Gavryusev, V., & Castoneda, H. O. 1995, AJ, 110, 1630

Munoz-Tunon, C., Tenorio-Tagle, G., Castaneda, H. O., & Terlevich, R. 1996, AJ, 112, 1636

Munoz-Tunon, C., Vilchez, J. M., & Castaneda, H. O. 1993, A&A, 278, 364

Murata, K. L., Kajisawa, M., Taniguchi, Y., et al. 2014, ApJ, 786, 15

Noeske, K. G., Papaderos, P., Cairós, L. M., & Fricke, K. J. 2003, A&A, 410, 481

Noeske, K. G., Papaderos, P., Cairós, L. M., & Fricke, K. J. 2005, A&A, 429, 115

Overzier, R. A., Heckman, T. M., Tremonti, C., et al. 2009, ApJ, 706, 203

Papaderos, P., Guseva, N. G., Izotov, Y. I., & Fricke, K. J. 2008, A&A, 491, 113

Papaderos, P., Loose, H.-H., Thuan, T. X., & Fricke, K. J. 1996, A&AS, 120, 207

Peng, C. Y., Ho, L. C., Impey, C. D., & Rix, H.-W. 2002, AJ, 124, 266

Peng, C. Y., Ho, L. C., Impey, C. D., & Rix, H.-W. 2010, AJ, 139, 2097

Prieto, M., Aguerri, J. A. L., Varela, A. M., & Muñoz-Tuñón, C. 2001, A&A, 367, 405

Puech, M. 2010, MNRAS, 406, 535

Rhodes, J. D., Massey, R. J., Albert, J., et al. 2007, ApJS, 172, 203

Riess, A. G., Macri, L., Casertano, S., et al. 2011, ApJ, 730, 119

Rozas, M., Richer, M. G., López, J. A., Relaño, M., & Beckman, J. E. 2006, A&A, 455, 539

Sánchez Almeida, J., Elmegreen, B. G., Muñoz-Tuñón, C., & Elmegreen, D. M. 2014, A&A Rev., 22, 71

Sánchez Almeida, J., Muñoz-Tuñón, C., Elmegreen, D. M., Elmegreen, B. G., & Méndez-Abreu, J. 2013, ApJ, 767, 74

Scannapieco, E., Ferrara, A., & Madau, P. 2002, ApJ, 574, 590

Schechter, P. 1976, ApJ, 203, 297

Schmidt, M. 1968, ApJ, 151, 393

Sersic, J. L. 1968, Atlas de galaxias australes

Shaw, M. A. & Gilmore, G. 1989, MNRAS, 237, 903

Silich, S., Tenorio-Tagle, G., & Muñoz-Tuñón, C. 2007, ApJ, 669, 952

Silich, S., Tenorio-Tagle, G., Muñoz-Tuñón, C., et al. 2010, ApJ, 711, 25

Simard, L. 1998, in Astronomical Society of the Pacific Conference Series, Vol. 145, Astronomical Data Analysis Software and Systems VII, ed. R. Albrecht, R. N. Hook, & H. A. Bushouse, 108

Sobral, D., Smail, I., Best, P. N., et al. 2013, MNRAS, 428, 1128

Swinbank, A. M., Webb, T. M., Richard, J., et al. 2009, MNRAS, 400, 1121

Tacconi, L. J., Genzel, R., Neri, R., et al. 2010, Nature, 463, 781

Tadaki, K.-i., Kodama, T., Tanaka, I., et al. 2014, ApJ, 780, 77

Telles, E., Muñoz-Tuñón, C., & Tenorio-Tagle, G. 2001, ApJ, 548, 671

Telles, E. & Terlevich, R. 1993, Ap&SS, 205, 49

Telles, E. & Terlevich, R. 1995, MNRAS, 275, 1

Tenorio-Tagle, G., Munoz-Tunon, C., & Cid-Fernandes, R. 1996, ApJ, 456, 264

Tenorio-Tagle, G., Munoz-Tunon, C., & Cox, D. P. 1993, ApJ, 418, 767

Tenorio-Tagle, G., Silich, S., Martínez-González, S., et al. 2013, ApJ, 778, 159

Tenorio-Tagle, G., Silich, S., Rodríguez-González, A., & Muñoz-Tuñón, C. 2005, ApJ, 628, L13

Tenorio-Tagle, G., Wünsch, R., Silich, S., Muñoz-Tuñón, C., & Palouš, J. 2010, ApJ, 708, 1621

Tenorio-Tagle, G., Wünsch, R., Silich, S., & Palouš, J. 2007, ApJ, 658, 1196

Terlevich, R. & Melnick, J. 1981, MNRAS, 195, 839

Terlevich, R., Melnick, J., Masegosa, J., Moles, M., & Copetti, M. V. F. 1991, A&AS, 91, 285

van den Bergh, S., Abraham, R. G., Ellis, R. S., et al. 1996, AJ, 112, 359

Vázquez, G. A. & Leitherer, C. 2005, ApJ, 621, 695

Wadadekar, Y., Robbason, B., & Kembhavi, A. 1999, AJ, 117, 1219

Wisnioski, E., Glazebrook, K., Blake, C., et al. 2012, MNRAS, 422, 3339

Wünsch, R., Tenorio-Tagle, G., Palouš, J., & Silich, S. 2008, ApJ, 683, 683

Wuyts, S., Förster Schreiber, N. M., Genzel, R., et al. 2012, ApJ, 753, 114

Young, C. K. & Currie, M. J. 1994, MNRAS, 268, L11